STRUCTURAL AND BIOCHEMICAL STUDIES OF THE HUMAN TWO PORE DOMAIN POTASSIUM CHANNEL K2P1

by

Alexandria Nuesa Miller

A Dissertation

Presented to the Faculty of the Louis V. Gerstner, Jr.

Graduate School of Biomedical Sciences,

Memorial Sloan-Kettering Cancer Center

in Partial Fulfillment of the Requirements for the Degree of

Doctor of Philosophy

New York, NY

April, 2013

_____
Stephen B. Long, PhD
Dissertation Mentor

_____April 5, 2013____
Date

ABSTRACT

Potassium (K^+) channels are the largest family of ion channels in eukaryotes with over 70 genes in humans. They have diverse functional roles including controlling the firing duration and frequency of actions potentials in neurons and regulating water retention in the kidneys. K^+ channels are highly-selective for K^+ over other monovalent cations, can conduct K^+ at rates approaching 10^8 ions per second and, like other ion channels, switch between conductive (open) and non-conductive (closed) states through a process called gating.

Two pore domain (K_{2P}) potassium channels, originally called K^+ background or leak channels, represent a subclass of K^+ channels that function to establish and maintain the resting potential in eukaryotic cells. This process primes cells for diverse responses such as action potentials in excitatory cells and cell signaling cascades, which can direct growth and motility in non-excitable cell types. K_{2P} channels have been shown to be gated by a range of cell stimuli and pharmacological agents including temperature, pH, polyunsaturated fatty acids, mechanical stress, and anesthetics. Not surprisingly, it is proposed that they are involved in physiological processes such as pain perception and anesthetic modulation. Structural studies of K_{2P} channels would not only provide insight into how K_{2P} channels are gated by these stimuli, but also may suggest strategies for the generation of K_{2P} specific drugs.

In the present work, I focused on both structural and biochemical studies of human $K_{2P}1$, a member of the K_{2P} family. I demonstrated, through biochemical studies of purified human $K_{2P}1$, that the channel is dimeric and is glycosylated at residue asparagine 95. This glycosylation mutant was used for subsequent biochemical and structural studies of $K_{2P}1$. Several limited proteolysis experiments and $K_{2P}1$ sequence analyses were performed to identify a core unit of human $K_{2P}1$. A human $K_{2P}1$ N95Q truncation mutant, containing residues 22-303, was generated

from these studies and successfully crystallized. Further truncation to the C-terminus and refinement strategies produced crystals of human $K_{2P}1$ N95Q 22-288 that diffracted to 3.4 Å resolution.

The $K_{2P}1$ crystal structure reveals a number of features that may have general implications on K_{2P} channel selectivity, gating and conductivity. A large extracellular domain is positioned above the extracellular entryway and creates an ion pathway with two side portals that can accommodate hydrated K^+ ions. The coordination of K^+ ions within the $K_{2P}1$ selectivity filter recapitulates the four-fold symmetry that is present in other K^+ channel structures. However, the non-covalent interactions surrounding the $K_{2P}1$ filter deviates from what has been previously observed and is two-fold symmetric, which may facilitate outer pore gating. An amphipathic C helix runs parallel to the cytosolic face of the membrane. Its connection and proximity to inner helices, which line the pore and form the activation gate of other K^+ channels, suggests that the C helix may be involved in inner helical gating. Finally, the $K_{2P}1$ pore is exposed to the lipid bilayer through openings in the intramembrane molecular surface, accommodating electron density that we attribute to lipid or detergent alkyl chains. We speculate that this may be an access point for endogenous lipids as well as lipophilic compounds such as tetrahexylammonium (THexA), recently shown to be a K_{2P} channel inhibitor.

The human $K_{2P}1$ structure defines the molecular architecture of the K_{2P} channel family, lays a foundation for further investigation of how K_{2P} channels are regulated by diverse stimuli, and provides insight for the development of K_{2P}-specific therapies. Future work to determine a high-resolution structure of $K_{2P}1$ is ongoing with the hopes of addressing key questions that still remain unanswered, such as the role of the $K_{2P}1$ selectivity filter in outer pore gating.

ACKNOWLEDGMENTS

I would like to thank the many people who have made this thesis possible: Steve Long, for the support and guidance that he has provided throughout my graduate career. I am finishing my Ph. D. as someone who is more enthusiastic and intrigued about scientific questions and challenges than I was when I started graduate school. I am also more confident with my ability to think independently about my work. For these reasons, I am truly grateful to Steve for taking me on as one of his first graduate students. I am also indebted to the members of the Long lab: Melinda Diver, Xiaowei Hou, Veronica Kane Dickson, and Leanne Pedi. I have had the pleasure of working with these folks throughout my time at the Sloan-Kettering Institute and am forever thankful for both the scientific and personal support that they have given me.

My advisory committee, Morgan Huse and Chris Lima, and Stew Shuman, who has been on both my advance to candidacy and thesis exam committees. The insightful questions that these folks posed to me were not only helpful for advancing my progress on my research project, but also allowed me to recognize weak points in my knowledge or my overall experimental strategy. I left these meetings always reminded of what I needed to improve on to mature as a scientist, and will be always grateful for their teaching and guidance through my graduate training.

The MSKCC proteomics and monoclonal antibody core, Hediye Erdjument-Bromage, Frances Weis-Garcia, Olivera Grbovic, Paul Montanez and S. Lloyd Bourne, who assisted me with some of the work presented in this thesis. The directors of the X-ray Methods in Structural Biology Course at Cold Spring Harbor Laboratory for giving me the opportunity to learn a bit about X-ray crystallography. The NSLS staff for providing technical assistance on the X25 and X29 beamlines.

TABLE OF CONTENTS

LIST OF TABLES

LIST OF FIGURES

AA	Arachadonic acid
ACMA	9-amino-6-chloro-2-methoxyacridine
AD	Anomalous dispersion/scattering
BK	Big conductance calcium-activated potassium channels, $K_{Ca}1$
CCCP	Carbonyl cyanide m-chlorophenyl hydrazone
CMC	Critical micelle concentration
CNS	Central nervous system
DTT	Dithiothreitol
EG	Ethylene glycol
Fab	Fragment, antigen binding region of an antibody
FSEC	Fluorescence-detection size exclusion chromatography
IR	Isomorphous replacement
I-V	Current-voltage
LORR	Loss of righting reflex response
LTWR	Loss of tail-pinch withdrawal response
lysoPL	Lysophospholipids
KcsA	*S. lividans* homolog of *Shaker* channel
K_V	Voltage-gated potassium channel
K_{Ca}	Calcium-activated potassium channel
K_{IR}	Inward-rectifying potassium channel
K_{2P}	Two pore domain potassium channel
M	Transmembrane segment
mAb	Monoclonal antibody
MIRAS	Multiple isomorphous replacement with anomalous dispersion/scattering
MPD	2-methyl-2,4-pentanediol

MR	Molecular replacement
MthK	*M. autotrophicum* homolog of K_{Ca}
MTS	Methanethiosulfonate
QA	Quaternary ammonium
PEG	Polyethylene glycol
PL	Phospholipids
PNS	Peripheral nervous system
PUFA	Polyunsaturated fatty acids
SAD	Single anomalous dispersion/scattering
SDS-PAGE	Sodium dodecyl sulfate polyacrylamide gel electrophoresis
SEC	Size exclusion chromatography
Shab	*D. melanogaster* homolog of K_V2 subfamily
Shaker	*D. melanogaster* homolog of K_V1 subfamily
Shal	*D. melanogaster* homolog of K_V4 subfamily
Shaw	*D. melanogaster* homolog of K_V3 subfamily
SK	Small conductance calcium-activated potassium channels, $K_{Ca}2$
TASK-1	Two pore domain potassium channel $K_{2P}3$
TCEP	Tris(2-carboxyethyl)phosphine
TEA	Tetraethylammonium
THexA	Tetrahexylammonium
TOctA	Tetraoctylammonium
TPenA	Tetrapentylammonium
TRAAK	Two pore domain potassium channel $K_{2P}4$
TREK-1	Two pore domain potassium channel $K_{2P}2$
TWIK-1	Two pore domain potassium channel $K_{2P}1$

CHAPTER 1

1.   INTRODUCTION

1.1.   Transport across the cell membrane

The cell membrane defines the boundaries of the cell. An essential role of the cell membrane is to provide a barrier against passive diffusion of molecules to and from the extracellular environment (Alberts, 2008). In particular, polar molecules are restricted to pass due to the hydrophobic composition of the cell membrane. By providing a barrier, the cell membrane also permits the asymmetrical distribution of molecules between the intracellular and extracellular compartments. Since polar molecules cannot diffuse through the membrane, transport proteins embedded in the membrane facilitate their movement across the lipid bilayer (Alberts, 2008).

Membrane transport proteins facilitate the movement of a specific class of polar molecules and some are selective for a molecule within this class (Alberts, 2008; Kandel et al., 2012). Polar molecules in biological systems include ions (small charged polar molecules), sugars, amino acids (large uncharged polar molecules), and water (small uncharged polar molecules). In addition, all transport proteins are multipass integral membrane proteins that are comprised both hydrophobic and hydrophilic residues. Hydrophobic regions of transport proteins typically interact with the lipid bilayer whereas hydrophilic portions are positioned away from the membrane environment, forming a hydrophilic core within the bilayer. As a result, the hydrophilic core typically interacts with the polar molecule of interest, shielding it from the membrane hydrophobic environment (Alberts, 2008; Kandel et al., 2012).

Transporters and channels comprise the two major classes of membrane transport proteins (Figure 1.1). The majority of transporters bind the polar molecule of interest on one side of the
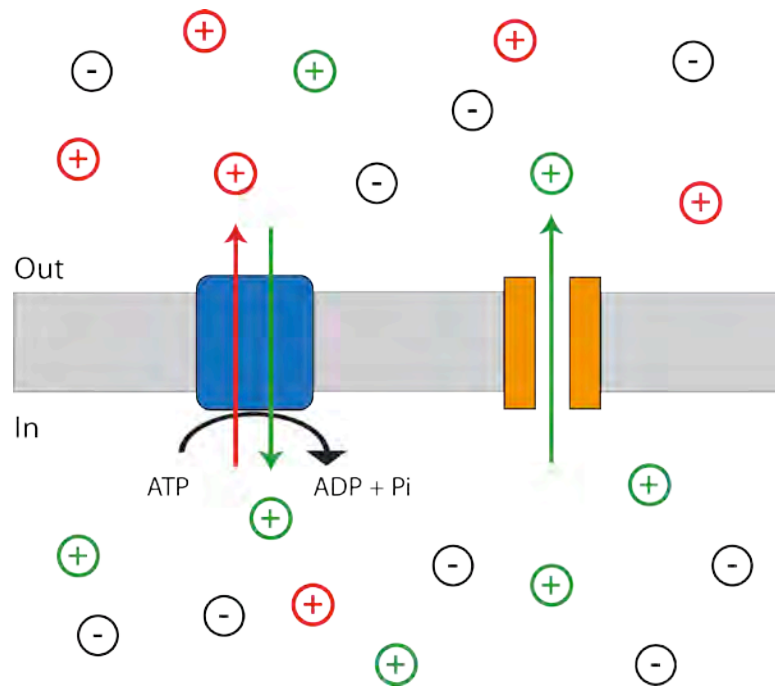
Figure 1.1: Schematic of two major classes of membrane transport proteins. Channels (orange) facilitate movement of a polar molecule or molecules (green cations) across the bilayer through an aqueous pore. Transporters (cyan) shuttle polar molecules from one side of the membrane to the other by undergoing a series of conformational changes. Channels are only capable of performing passive transport, which requires a chemical gradient of the polar molecule, but no energy consumption. Transporters, on the other hand, are capable of performing both active and passive transport, and obtain energy for active transport through ATP hydrolysis or by co-transportation of a second polar molecule down its chemical gradient.

membrane, undergo a number of conformational changes, and release the molecule on the other side of the membrane (Jardetzky, 1966; Lauger, 1979). Channels, on the other hand, select for the polar molecule of interest and facilitate its movement through an aqueous pore within the membrane (Hille, 1971).

The distribution of molecules between the cytosol and the extracellular space is asymmetric and this creates chemical gradients that provide the driving force for movement of polar molecules into or out of the cell (Figure 1.2) (Alberts, 2008). Movement of a polar molecule down its electrochemical gradient (see below) is defined as passive transport, or facilitated diffusion. In contrast, active transport involves the movement of a polar molecule against its chemical gradient and requires energy (e.g. from the hydrolysis of ATP or from the co-transportation of a second polar molecule down its chemical gradient). Transporters are capable of facilitating both active and passive diffusion whereas channels only perform passive transport (Alberts, 2008). The majority of channels that have been identified are involved in transporting inorganic, charged ions across the membrane.

1.2. Ion channels

Ion channels perform passive transport by mediating the movement of an ion down its electrochemical gradient. The electrochemical gradient is generated from the electrical potential of ions across the membrane and the chemical gradient of the ion (Hodgkin and Huxley, 1952).

1.2.1. Membrane potential and ion distribution at rest

For the majority of cells, the electrical potential across the membrane at rest, or the resting potential, is maintained with negative voltage inside the cell relative to outside (Kandel et al., 2012; Wright, 2004). The negative resting potential is primarily established by the action of two membrane transport proteins: sodium/potassium pumps (Na^+/K^+ pumps) and potassium leak

3
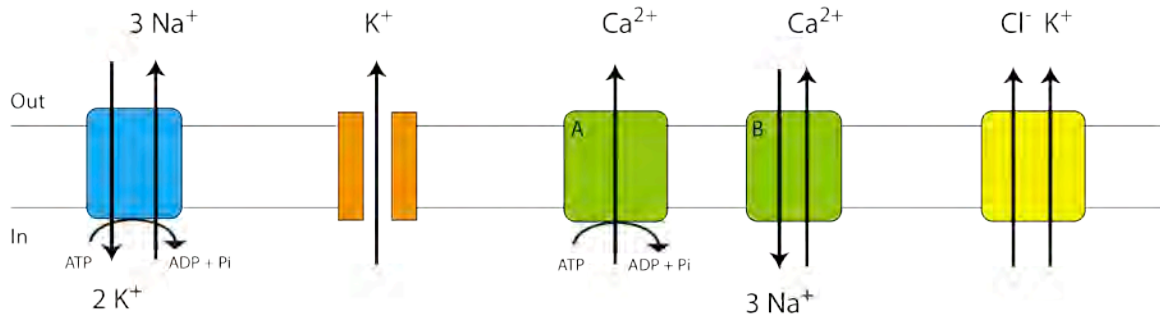
Figure 1.2: Distribution of Na^+, K^+, Ca^{2+} and Cl^- ions at rest is regulated by a number of important channels and transporters. The Na^+/K^+ pump (cyan) establishes Na^+ and K^+ cellular gradients, with a higher concentration of Na^+ outside of the cell relative to the inside and a higher concentration of K^+ inside the cell relative to the outside. The Na^+/K^+ pump performs active transport and requires energy, in the form of ATP hydrolysis. The stoichiometry of Na^+ and K^+ transport through the Na^+/K^+ pump is 3Na:2K. The initial Na^+ and K^+ gradients established by the Na^+/K^+ pump are required for setting up all subsequent ionic gradients. K^+ efflux through K^+ leak channels (orange) establish the negative resting potential in cells. The Ca^{2+} gradient is established by two transporters (green), PMCA (A) and NCX (B). Both PCMA and NCX require energy (ATP hydrolysis and Na^+ influx, respectively) to transport Ca^{2+} up its chemical gradient. In mature neurons, the Cl^- gradient is primarily established by KCC2 (yellow), which couples Cl^- and K^+ efflux. Extracellular (out) and intracellular (in) are denoted.

4

channels (K$^+$ leak channel) (Seyfarth, 2006; Skou, 1957). A chemical gradient is first generated by Na$^+$/K$^+$ pumps, with high concentrations of sodium (Na$^+$) and potassium (K$^+$) ions on the exterior and interior of the cell, respectively. Then, the efflux of K$^+$ through K$^+$ leak channels results in a movement of positive change out of the cell, hyperpolarizing the cell. The overall outcome is the asymmetric chemical distribution of Na$^+$ and K$^+$ ions as well as a negative electrical gradient (see also 1.6.1 Theoretical electrophysiological properties of K$^+$ leak channels) (Table 1.1) (Figure 1.2) (Kandel et al., 2012; Wright, 2004).

The distribution of calcium (Ca^{2+}) and chloride (Cl$^-$) ions in the cell is also asymmetric, with a high concentration of both ions outside the cell with respect to the inside (Table 1.1) (Figure 1.2). For Ca^{2+}, this is achieved through the action of two transporters: the plasma membrane ATPase (PMCA) and the Na$^+$/Ca^{2+} exchanger (NCX) (Brini and Carafoli, 2011). PMCA transports Ca^{2+} from the cytosol to the extracellular space through hydrolysis of ATP (Brini and Carafoli, 2011). The Na$^+$ concentration gradient established by the Na$^+$/K$^+$ pump is required for Ca^{2+} efflux through NCX since this movement is coupled to Na$^+$ influx (Table 1.1) (Figure 1.2) (Brini and Carafoli, 2011). Likewise, the Cl$^-$ gradient in mature neurons is primarily established by Cl$^-$ K$^+$ symporter 5 (KCC2), a transport protein which couples Cl$^-$ efflux with K$^+$ efflux by again utilizing the K$^+$ gradient generated by the Na$^+$/K$^+$ pump (Table 1.1) (Figure 1.2) (Blaesse et al., 2009).

1.2.2. Properties of ion channels

Some ion channels are capable of conducting ions at rates up to 10^8 ions per second, approaching the diffusion limit of ion arrival at the mouth of the pore (Hille, 2001; Kandel et al., 2012). In addition, ion channels often select for a specific ion. The region of the channel that is responsible for ion selection is called the selectivity filter (Hille, 1971). Selection is based on the chemical

Ion	Extracellular concentration (mM)	Intracellular concentration (mM)
Na^+	150	15
K^+	3	150
Ca^{2+}	1.2	1×10^{-4}
Cl^-	130	8

Table 1.1: Distribution of ions at rest in the cell (Hille, 2001).

properties of the ion, including charge and size of the ion, as well as coordination geometry of the ion in water. Finally, ion channels have the ability to open and close through a mechanism called gating (Kandel et al., 2012). Ion channel gating is regulated by a variety of stimuli. For instance, voltage-gated ion channels open and closed in response to changes in voltage across the plasma membrane whereas ligand-gated ion channels open upon binding of a neurotransmitter, ion, nucleotide or lipid moiety. For detailed descriptions of ion channel conductance, selectivity and gating based on insights from K^+ channel structures, see 1.3.1 K^+ channel selectivity and 1.3.2 K^+ channel gating.

1.2.3. Function of ion channels

Ion channels are highly abundant in the central and peripheral nervous systems (CNS and PNS, respectively) and are essential for cell communication and sensory and motor responses (Hille, 2001; Kandel et al., 2012). In the CNS, ion channels produce and propagate nerve impulses, or action potentials, as waves along neuronal axons. They control the release of vesicles into the synapse and are abundant at the post-synaptic junction for enhancing or inhibiting the initiation of an action potential. Visual and auditory stimuli from the PNS are transmitted to the CNS through electrical impulses produced by ion channels. Ion channels also give rise to and regulate muscle contraction. Numerous diseases have been associated with genetic abnormalities that result in defects in muscle ion channel function (Jurkat-Rott and Lehmann-Horn, 2005).

Ion channels also play important roles in non-excitable cell types. For instance, Ca^{2+} is an essential secondary messenger, regulating a variety of cellular functions such as proliferation, motility, gene expression and apoptosis. Store operated Ca^{2+} channels primarily mediate Ca^{2+} entry in non-excitable cells (Putney, 2011). In phagocytes, voltage-gated proton channels (H_V1 channels) counter the depolarizing and cytosolic acidification effects of reactive oxygen species

production, a process that is necessary for the degradation of ingested pathogens (Demaurex, 2012). H_V1 channels perform this role by expelling protons from the cytosol to the extracellular space (Demaurex, 2012). Ion channels also contribute to the regulation of cell volume homeostasis, protein degradation in endosomes, as well as to the secretion or reabsorption of ions in the kidney.

Many ion channels are categorized into four major groups based on their selectivity - Na^+, K^+, Ca^{2+} and Cl^- channels (Hille, 2001). Voltage-gated Na^+ and K^+ channels are essential for the generation of action potentials in neurons. Depolarization during an action potential is a result of Na^+ influx through voltage-gated Na^+ channels. Subsequently, K^+ efflux through voltage-gated K^+ channels (K_V channels) facilitates repolarization of the neuron back to the resting state (Hodgkin and Huxley, 1952). Voltage-gated Ca^{2+} channels are important for muscle contraction. For instance, the L-type Ca^{2+} channel $Ca_V1.2$ is responsible for sustaining action potentials in cardiac myocytes (Catterall et al., 2005; Nilius et al., 1985). Anionic Cl^- channels are important for cell hyperpolarization in the CNS and PNS and, therefore, have regulatory roles. For instance, $GABA_A$ and glycine receptors induce hyperpolarization at postsynaptic terminals, preventing neurons from firing an action potential (Coombs et al., 1955; Krnjevic and Schwartz, 1967; Werman et al., 1968). Likewise, ClC channels are responsible for setting and maintaining the resting potential in skeletal muscles (Steinmeyer et al., 1991). Unlike cation channels, anion channels typically are not selective for one anion; however, they often conduct Cl^- since this is an abundant anion in the cell. The remainder of this introduction will be focused on the K^+ channel superfamily.

1.3.   Principles of K^+ channel selectivity, gating and conductance from structural studies

K^+ channels represent the largest family of ion channels in eukaryotes with over 70 genes in humans (Hille, 2001). As expected, these channels have diverse roles depending on cell type and

context. In the CNS, it is well known that K^+ channels contribute to the resting membrane potential and modulate the duration and frequency of action potentials, whereas in the PNS, K^+ channels are important in skeletal and cardiac muscle contraction (Hille, 2001). In non-excitable cells, they are implicated in controlling cell volume, regulating water retention in the kidneys, as well as promoting the activation of lymphocytes (Hibino et al., 2010; Lewis and Cahalan, 1995; Patel et al., 2000). K^+ channels can be divided into three subfamilies based on membrane topology, sequence identity and biophysical characteristics: 1. voltage-gated (K_V) K^+ channels and Ca^{2+}-activated (K_{Ca}) K^+ channels, 2. inward-rectifying K^+ channels (K_{IR}) and 3. two pore domain K^+ channels (K_{2P}) (Figure 1.3) (Hille, 2001). A brief description of K_V / K_{Ca} and K_{IR} channels, and a more comprehensive description of K_{2P} channels, is provided in the following sections: 1.4 Voltage-gated K^+ channels and Ca^{2+}-activated K^+ channels, 1.5 Inward-rectifying K^+ channels, and 1.6 Two pore domain K^+ channels. Although each K^+ channel subfamily has distinct functions, all have conserved structural features that are essential for establishing K^+ selectivity, gating and conductance.

1.3.1. K^+ channel selectivity

K^+ selectivity is a highly conserved property among the K^+ channel superfamily. All K^+ channels possess a consensus amino acid sequence referred to as the filter sequence, Thr-x-Gly-Tyr-Gly-Asp with x representing an aliphatic residue (TxGYGD), which lines the channel pore and confers K^+ selectivity (Figure 1.4) (Doyle et al., 1998; Hille, 2001; Zhou et al., 2001b). As canonical K^+ channels assemble as tetramers and each monomer typically contains one filter sequence, four filter sequences are required to form the channel selectivity filter (Doyle et al., 1998; Hille, 2001; Zhou et al., 2001b). Each K^+ ion within the filter directly coordinates with eight carbonyl oxygen atoms contributed from the protein backbone or by threonine side-chains within the selectivity filter (Figure 1.4) (Morais-Cabral et al., 2001; Zhou and MacKinnon, 2004a; Zhou et al., 2001b; Zhou and MacKinnon, 2003). A high-resolution crystal structure of K^+

9
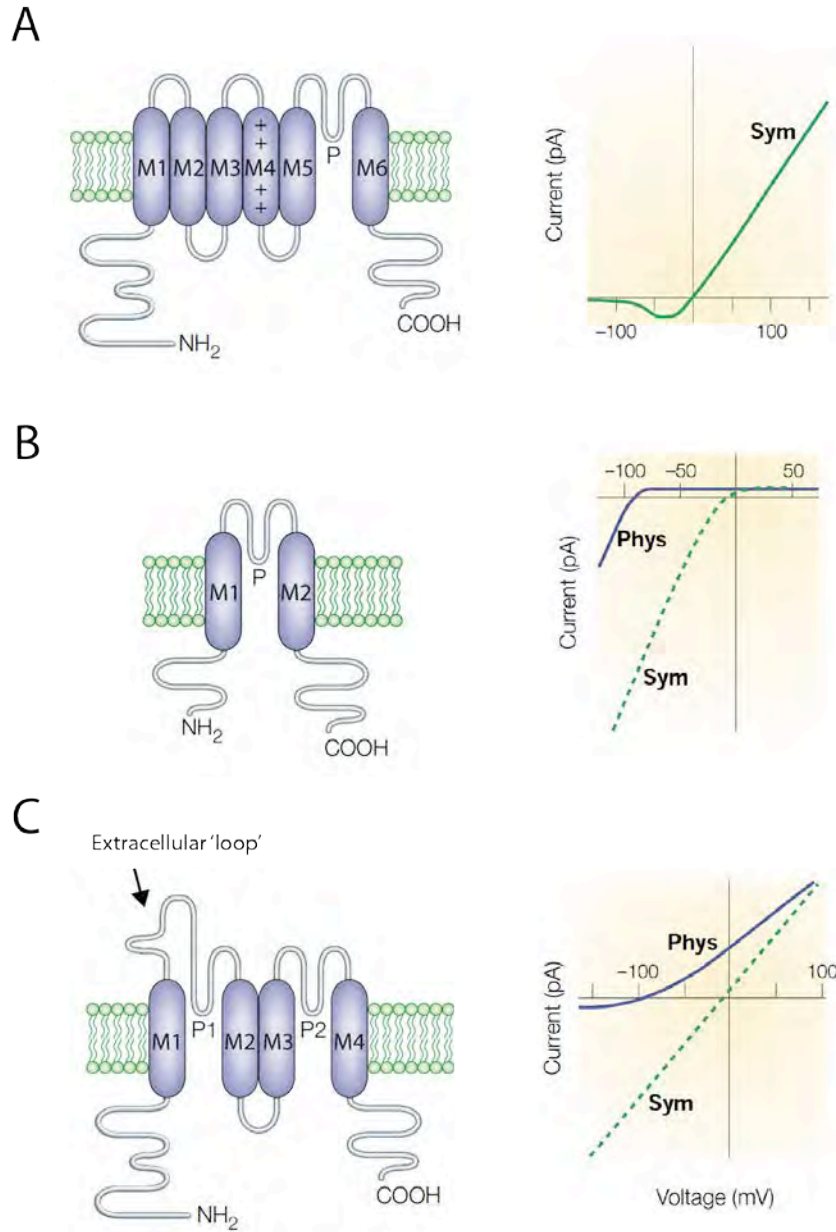
Figure 1.3: Membrane topology of K_V (A), K_{IR} (B) and K_{2P} (C) protomers with representative current-voltage (I-V) relationships in physiological (Phys) and symmetrical (Sym) K^+ conditions. A) K_V channel protomers consists of 6 transmembrane segments (M1-6) and 1 pore domain (P) and assemble as tetramers. K_V channel are voltage-dependent channels that are opened at depolarizing (as shown in figure) or hyperpolarizing membrane potentials and sense voltage changes through an arginine-rich segment within transmembrane segment 4 (M4). B) K_{IR} channels protomers consists of 2 transmembrane segments (M1-2) and 1 pore domain (P) and assemble as tetramers. They are non-conductive at depolarizing potentials above the equilibrium potential for K^+. C) K_{2P} protomers contain 4 transmembrane segments (M1-4) and 2 pore domains (P1-2) and assemble as dimers. K_{2P} protomers also contain an extended M1-P1 linker or extracellular 'loop'. Their I-V relationship best fits the prediction by the GHK current equation for background K^+ channels. Adapted by permission from Macmillan Publishers Ltd: Nature Reviews Neuroscience 2001 Mar;2(3):175-84, copyright 2001.
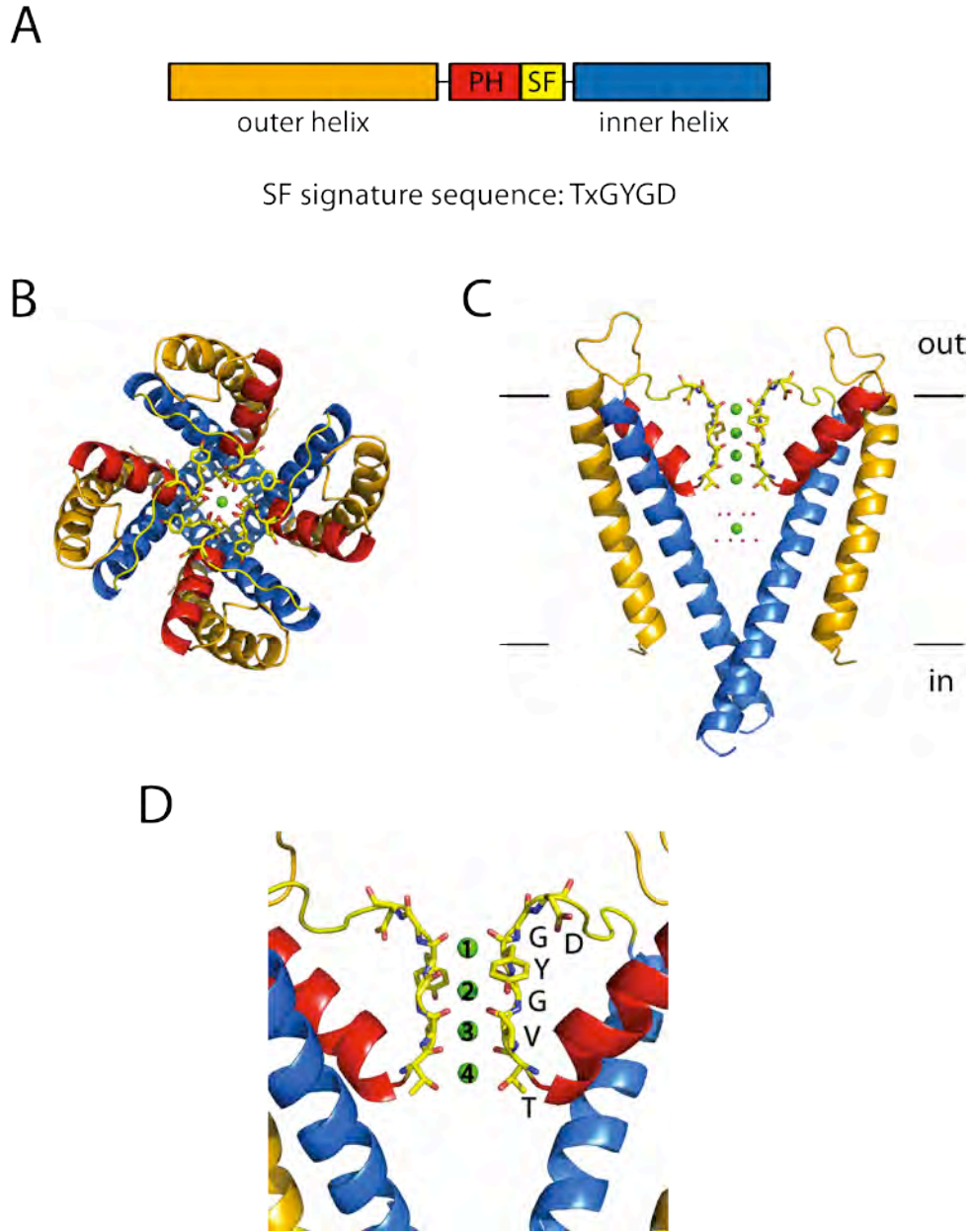
Figure 1.4: High-resolution crystal structure of *S. lividans* KcsA furthers our understanding of K^+ selection by the conserved K^+ channel selectivity filter sequence. A) Arrangement of helices and domains within a KcsA protomer. Outer helix, pore helix (PH), selectivity filter sequence (SF) and inner helix are colored orange, red, yellow and blue, respectively. Canonical SF signature residues are highlighted. B) Extracellular view of the crystal structure of tetrameric KcsA with channel pore in the center (PDB ID: 1K4C). KcsA was crystallized in high K^+ (200 mM), with K^+ ions colored green, and all other colors are similar to A. Residues within the filter are shown as sticks, highlighting the 4-fold symmetry. C) Side view of KcsA with two of the four protomers removed with selectivity filter, crystallized in a conductive configuration. Extracellular (out) and intracellular (in) regions are labeled with dashed lines denoting the lipid bilayer. Coloring similar to A and B. D) Close up of the KcsA selectivity filter from (C) with residues TVGYGD labeled. K^+ ions (green), labeled 1-4, are coordinated to backbone carbonyls, and threonine side chains, provided by these residues.

11

bound to the selectivity filter of KcsA, a bacterial potassium channel from *Streptomyces lividans*, depicts the coordination of these ions in an square-antiprismatic conformation (Figure 1.4, see also Figure 1.5) (Morais-Cabral et al., 2001; Zhou et al., 2001b; Zhou and MacKinnon, 2003; 2004b). In addition, a hydrated K^+ appears within the central cavity of the channel, and the waters surrounding the K^+ ion are coordinated in a similar manner (Figure 1.4, Figure 1.5) (Roux and MacKinnon, 1999; Zhou et al., 2001b; Zhou and MacKinnon, 2004b).

Although electron density for four K^+ binding sites are observed within the selectivity filter of the KcsA crystal structure, only two ions occupy the filter on average when KcsA is a conductive state (Figure 1.4, Figure 1.6) (Morais-Cabral et al., 2001; Zhou et al., 2001b; Zhou and MacKinnon, 2003). By numbering the ions from the extracellular space to the cytosol 1 to 4, K^+ ions are either found in positions 1 and 3 (1, 3 state) or 2 and 4 (2, 4 state) with water molecules occupying the empty positions in a conductive state (Figure 1.6). K^+ ion coordination in the 1, 3 or 2, 4 states was supported through a mutagenesis study of threonine 75 (T75), a residue within the KcsA filter that coordinates K^+ through its backbone carbonyl and side-chain hydroxyl group. Mutation of T75 to cysteine directly disrupted K^+ coordination at site 4. The electron density along the filter of the KcsA T75C crystals structure revealed a reduction of electron density in site 4, but also in site 2 (Zhou and MacKinnon, 2004a). This data suggested that 1. there are two states of K^+ coordination in the conducting conformation (the 1, 3 and the 2, 4 states), 2. that in wild-type KcsA, these states are energetically equivalent and 3. that the T75C mutant disrupts the energetic equilibrium, favoring the 1, 3 over the 2, 4 state (Zhou and MacKinnon, 2004a). In addition, K^+ occupancy in sites 1-4 has been estimated from direct measurements of thallium (Tl^+) occupancy from KcsA crystal structures with Tl^+, an electron-rich K^+ surrogate. The ~ 0.5 occupancy of K^+ in sites 1-4 supports the model of two energetically equivalent, 1, 3 and 2, 4 conductive states (Zhou and MacKinnon, 2003).
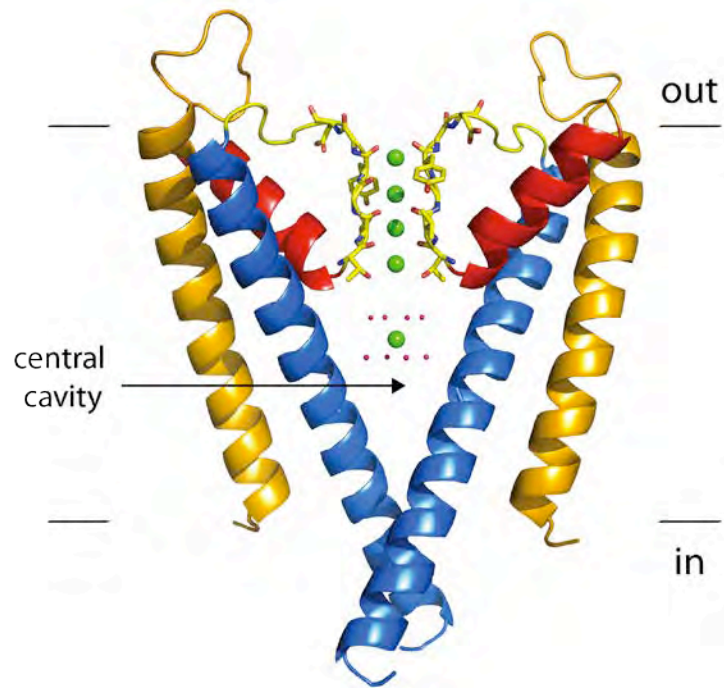
Figure 1.5: Ordered K$^+$ ion located in the central cavity of the *S. lividans* KcsA crystal structure. Side view of KcsA with two of four protomers removed (PDB ID: 1K4C). Extracellular and intracellular regions are labeled with lines denoting the lipid bilayer. Outer helix, selectivity filter sequence and inner helix are colored orange, yellow and blue, respectively. Pore helices (red) stabilize the K$^+$ ion (green) coordinated to 8 water molecules (pink) in an square-antiprismatic conformation within the central cavity (arrow).
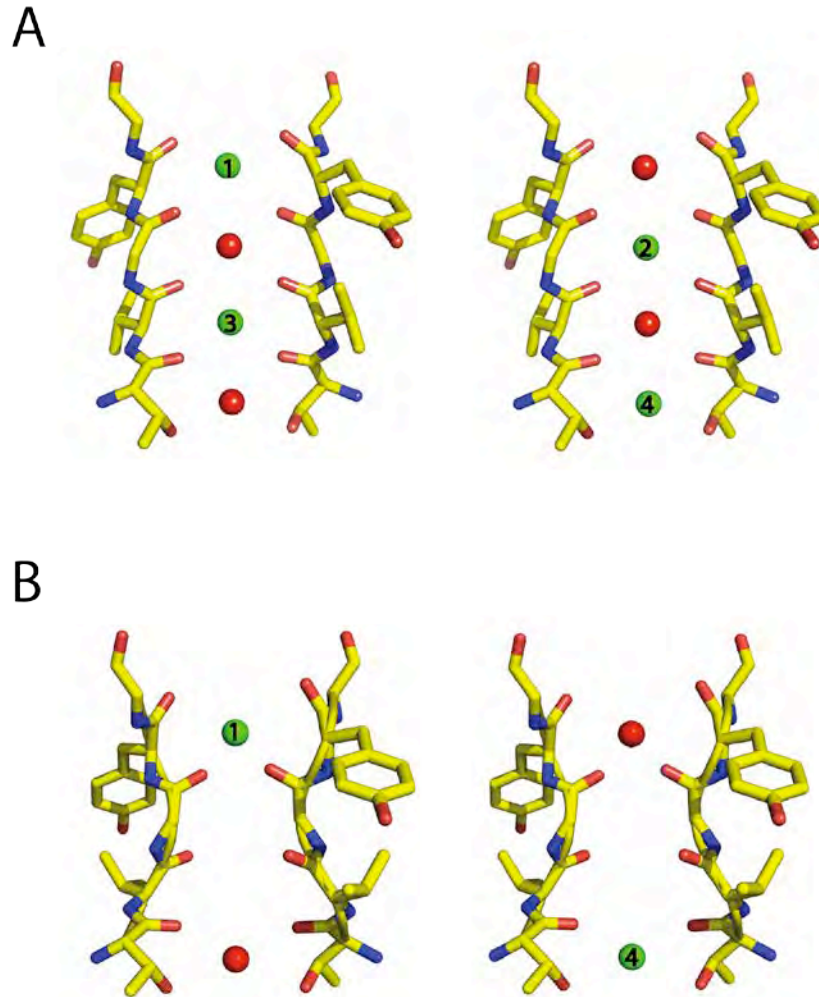
Figure 1.6: Physiological distribution of K^+ ions in both conductive and non-conductive configurations of the *S. lividans* KcsA selectivity filter. Selectivity filter from KcsA crystal structures exposed to high (A; PDB ID: 1K4C) and low (B; PDB ID: 1K4D) K^+ conditions. K^+ ions (green) are labeled from the extracellular to intracellular side, 1-4. A total of 4 and 2 K^+ ions are observed in the high K^+ (200 mM) and low K^+ (5 mM) KcsA selectivity filter structures, respectively. However, experimental evidence suggests that the conductive configuration (A) most likely switches from a 1, 3 to a 2, 4 state whereas the non-conductive configuration or collapsed filter (B) is occupied at either the 1 or 4 position (both represented above), with empty positions occupied by water molecules (red).

Interestingly, crystal structures of KcsA in 'low' K^+ (5 mM) or Tl^+ (25 mM) conditions resulted in a structural rearrangements, or collapse, of the selectivity filter, a feature referred to as the non-conductive conformation (Zhou et al., 2001b; Zhou and MacKinnon, 2003). In contrast to what is observed in 'high' K^+ (200 mM) or Tl^+ (160 mM) conditions, electron density for two K^+ binding sites are observed in the low K^+ structure at positions 1 and 4, with only one K^+ ion occupying the filter on average in a non-conductive state (Figure 1.6) (Zhou et al., 2001b; Zhou and MacKinnon, 2003). Evidence to support the distribution and quantity of K^+ ion within the KcsA selectivity filter was based on functional and structural studies using K^+ and rubidium (Rb^+) (Morais-Cabral et al., 2001; Zhou and MacKinnon, 2004a; Zhou et al., 2001b; Zhou and MacKinnon, 2003). Rb^+ is an ion with a larger ionic radius to K^+, but which can conduct through K^+ channels, including KcsA (LeMasurier et al., 2001; Morais-Cabral et al., 2001; Zhou and MacKinnon, 2004a). K^+ and Rb^+ currents measured from KcsA channels reconstituted into planar lipid bilayers revealed two conduction states (steep and linear) when KcsA K^+ or Rb^+ conductance was graphed as a function of ion concentration (Morais-Cabral et al., 2001; Zhou and MacKinnon, 2004a). The transition between steep and linear conduction state occurred at 30-50 mM K^+ and Rb^+. This correlated with a shift in the number of K^+ or Rb^+ ions coordinated to the filter in low (3-5 mM) versus high ($\geq$ 30 mM) ion conditions, as evaluated by measuring electron density along the filter from high-resolution KcsA crystal structures. Whereas electron density was detected in sites 1 and 4 in low K^+ or Rb^+ conditions, electron density was measured in sites 1, 3 and 4 for Rb^+ or sites 1-4 for K^+ ions in high ion conditions (Morais-Cabral et al., 2001).

Conversely, a high-resolution crystal structure of MthK, a bacterial K^+ channel isolated from *Methanobacterium autotrophicum*, revealed a filter in the conductive conformation in low K^+ conditions (Ye et al., 2010). Furthermore, MthK conducts Na^+ ions in the absence of K^+, lending further evidence to support the idea that the filter is in a conductive configuration (Ye et al.,

2010). This Na$^+$ conductance property in the absence of K$^+$ has also been reported for a variety of K$_V$ channels (Callahan and Korn, 1994; Korn and Ikeda, 1995; Ogielska and Aldrich, 1998; Starkus et al., 1997; 1998). The MthK structural and functional data suggest that the collapsed KcsA selectivity filter observed in low K$^+$ conditions is most likely a feature of only a subset of K$^+$ channels, which may be correlated with an inability of these channels to conduct Na$^+$ in the absence of K$^+$.

1.3.2. K$^+$ channel gating

Most of our overall knowledge of K$^+$ channel gating stems from electrophysiological studies of K$_v$ and K$_{IR}$ channels, as well as from features observed in several prokaryotic K$^+$ channel crystal structures (Cuello et al., 2010a; 2010b; Doyle et al., 1998; Hibino et al., 2010; Jiang et al., 2002; Yellen, 1998; Zhou et al., 2001b). Although additional mechanisms of gating have been identified in K$_V$ (N-type inactivation) and K$_{IR}$ channels (G loop gate), all K$^+$ channels contain two conserved structural regions of gating which are named the activation gate and the C-type inactivation gate, or outer pore gate (Hibino et al., 2010; Yellen, 1998).

The activation gate is formed by conformational movements of the inner transmembrane helices lining the ion conduction pore, which physically permits or obstruct K$^+$ conductance (M2 in KcsA) (Figure 1.7). Comparison of bacterial K$^+$ channel KcsA (closed) and MthK (open) crystal structures reveal a conserved glycine residue (Gly 99 in KcsA; Gly 83 in MthK) that acts as a hinge to facilitate bending of the inner helices (Figure 1.7) (Doyle et al., 1998; Jiang et al., 2002; Zhou et al., 2001b). This residue is conserved in most K$^+$ channels and in 'P-loop'-containing channels, including cyclic nucleotide-gated and voltage-gated Na$^+$ channels (Na$_v$) (Flynn et al., 2001; Jiang et al., 2002; Zhao et al., 2004). Gating hinge glycine mutagenesis studies with the *Drosophila melanogaster* Shaker channel, a K$_v$ homolog, demonstrate that an alanine substitution

16
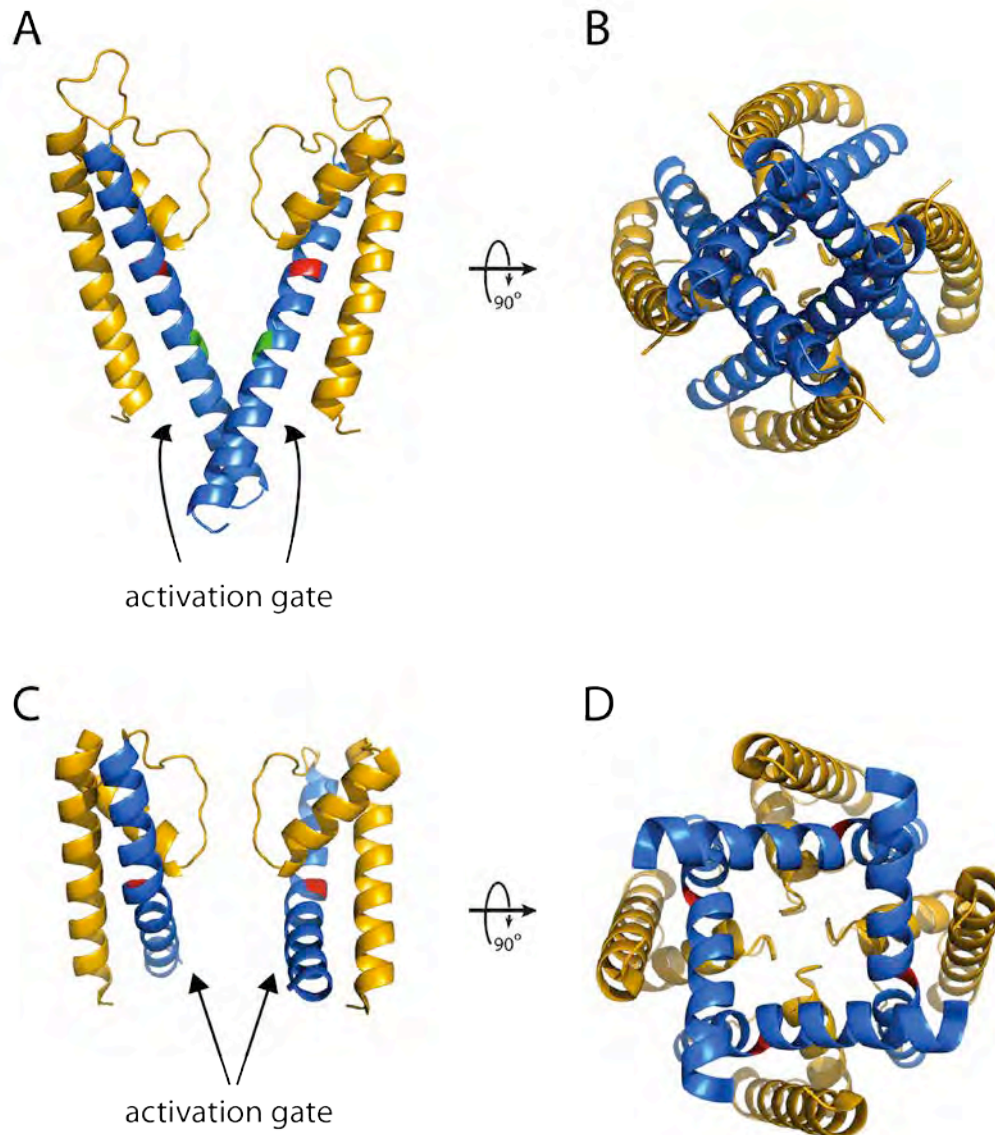
Figure 1.7: Comparison of *S. lividans* KcsA (closed; PDB ID: 1K4C) and *M. autotrophicum* MthK (open; PDB ID: 1LNQ) crystal structures, highlighting the inner helices (blue) that form the activation gate. Side (A) and intracellular (B) views of KcsA with closed inner helices, based on the diameter of the pore at the narrowest region (threonine 107, colored green). Side (C) and intracellular (D) views of MthK with open inner helices. Side views have two subunits removed for clarity. Outer helices are colored orange and gating glycine hinge (G99 in KcsA, G83 in MthK) is colored red.

stabilizes the closed, non-conductive conformation of the channel (Ding et al., 2005; Magidovich and Yifrach, 2004). In contrast, a proline substitution to the Shaker channel and to a bacterial Na_v channel appeared to stabilize the open conformation, as manifested by both channel opening at a more negative membrane potential and a slower rate of closure (Magidovich and Yifrach, 2004; Zhao et al., 2004). These functional and structural data demonstrate that the K^+ channel activation gate involves a large hinge movement of the inner helices that is facilitated by a conserved glycine residue.

In addition to the activation gate, a second gate is located within the extracellular region of the pore called the C-type inactivation gate or outer pore gate. Like the activation gate, the outer pore gate physically opens or closes the K^+ channel pore. However, the conformation changes to this gate are small and involve perturbations to the selectivity filter, as has been suggested through numerous functional studies and through recent crystal structures of a constitutively open KcsA mutant (Cuello et al., 2010a; Cuello et al., 2010b; Yellen, 1998). Interestingly, C-type inactivation, as interpreted from the KcsA mutant crystal structures, appears to involve constriction to the center the selectivity filter around valine 76 and glycine 77 (75 TVGYGD 80) and little perturbation to the outer mouth of the pore (Cuello et al., 2010b). This was a surprising observation since numerous functional studies of C-type inactivation with the Shaker channel have demonstrated that the largest movements to this gating apparatus occur on the extracellular side of the filter (Liu et al., 1996; Yellen et al., 1994).

One of these studies involved the generation of a cadmium (Cd^{2+}) binding site to the outer mouth of the Shaker channel pore. Cd^{2+} binding to the Shaker channel T449C mutant appeared to be state-dependent, with binding to the channel in the C-type inactivated state, and little to no binding the open state (Yellen et al., 1994). Furthermore, Yellen and colleagues demonstrated that Cd^{2+} promotes the transition to the C-type inactivated state with very low affinity (K_D

~ 9 mM), yet Cd^{2+} stabilized this state with high affinity (K_D = 0.2 μM) (Yellen et al., 1994). It was proposed from these findings that introduction of the cysteine mutant created a single binding site for Cd^{2+}, with all four cysteines coordinating to the ion, contributed from each protomer. Recently, a similar study was published with a KcsA mutant (Y82C) (Raghuraman et al., 2012). Unlike the Shaker channel, Cd^{2+} enhanced the rate of C-type inactivation in the micromolar range (K_D ~ 20 μM). In addition, the generation of a concatenated KcsA tetramer with two adjacent cysteines mutated demonstrated that the addition of 100 μM Cd^{2+} led to faster inactivation of the channel (τ_i = 250 ms) compared to the channel without Cd^{2+} (τ_i = 1100 ms). These channel inactivation values appear similar to those recorded for the KcsA Y82C mutant. This suggested that Cd^{2+} coordination, in the case of KcsA, involved only two cysteine residues and may highlight an inherent difference between KcsA the Shaker channels (Raghuraman et al., 2012).

In fact, it is possible that structural rearrangements observed as a result of C-type inactivated may vary slightly among K^+ channels. For instance, it has also been shown that a subset of K^+ channels that undergo C-type inactivation are able to conduct Na^+ ions in the absence of K^+ (Callahan and Korn, 1994; Korn and Ikeda, 1995; Starkus et al., 1997; 1998). Further structural information (e.g. crystal structures of other K^+ channels in a C-type inactivated state) will advance our understanding of this gating mechanism.

1.3.3. K^+ channel conductance

Some K^+ channels can conduct K^+ ions at rates up to 10^8 ions per second, or measured single channel conductance values of 200-300 pS (physiological K^+ concentration), as in the case of the big conductance K_{Ca} channels (BK channels; $K_{Ca}1$ channels) (Hille, 2001; Latorre et al., 1989). On average though, measurements of single channel conductance through eukaryotic K^+ channel can be estimated to be approximately 5-50 pS (Hille, 2001). The KcsA and MthK crystal structures provide us with an idea of how K^+ channels may accommodate fast rates of K^+

transport. As earlier discussed, K^+ selectivity is accomplished by residues within the selectivity filter sequence, which contribute backbone carbonyls and threonine side chain hydroxyl groups to coordination with dehydrated K^+ ions (Doyle et al., 1998; Zhou et al., 2001a).

Since dehydration is a necessary step for K^+ conduction, the significant free-energy cost of K^+ ion dehydration, 85 kcal/mol, must be minimized in order for K^+ channels to accommodate fast rates of conduction (Hille, 2001). K^+ coordination to the selectivity filter achieves this minimization since the selectivity filter carbonyls and threonine side chain hydroxyl groups are positioned such that the filter mimics K^+ coordination with water (Doyle et al., 1998; Zhou et al., 2001a). K^+ ion coordination within the KcsA selectivity filter is found in the 1, 3 state or 2, 4 state in the conductive configuration, with each ion coordinated to 8 carbonyls, and these two coordinated states are energetically equivalent (Figure 1.4, Figure 1.6) (Morais-Cabral et al., 2001; Zhou and MacKinnon, 2004a; Zhou et al., 2001b; Zhou and MacKinnon, 2003). Transition of ions between the 1, 3 and 2, 4 states requires a rearrangement in K^+ ion coordination within the filter. This rearrangement most likely results in an octahydryl coordination of the K^+ ion, contributed by four carbonyls from the filter and two water molecule that are either occupying the empty positions within the filter or surrounding the vestibules (Morais-Cabral et al., 2001).

KcsA selectivity filter coordination to ions with larger ionic radii, such as Rb^+, is different to what is observed for K^+, since only 3 of the 4 sites are occupied (positions 1, 3 and 4) (Morais-Cabral et al., 2001; Zhou and MacKinnon, 2003). In other words, Rb^+ does not share the energetically equivalent 1, 3 and 2, 4 states of K^+ filter coordination. Single channel recordings of KcsA further support this idea since the single channel conductance of KcsA in symmetrical Rb^+ conditions is lower compared to symmetrical K^+ conditions (LeMasurier et al., 2001). Coordination of smaller monovalent cations such as Na^+ to the filter is also not energetic favorable and, therefore, does not occur in physiological K^+ conditions. The process of K^+ ion

dehydration, coordination to the selectivity filter, transition between the 1, 3 and 2, 4 states, and hydration of filter-exiting ions in physiological K^+ conditions results in a maximum energy barrier of 2-4 kcal/mol, as determined from molecular dynamics free energy simulations (Berneche and Roux, 2001).

In addition to the selectivity filter, the opening of the activation gate also plays a role in supporting fast rate of K^+ channel conductance, as interpreted from the MthK crystal structure. Activation gate opening reduces the distance in which K^+ ions have to travel through the low dielectric membrane environment (Jiang et al., 2002). Comparison of the calculated electrostatic potentials for MthK and KcsA, as evaluated from the crystal structures, demonstrates that opening of the activation gate exposes the MthK intracellular region to the cytosol, raising the dielectric constant to ~80. As a result, this narrows the membrane diameter to ~12 Å, or the length of the selectivity filter, and contributes to fast channel conductance.

Although the selectivity filter and activation gate are conserved architectural features of K^+ channels, the measured single channel conductance between channels varies significantly. The MthK crystal structure spearheaded several mutagenesis studies to identify residues that influence K^+ channel conductance. Sequence analysis identified acidic residues located within the inner helix of K_{Ca}, such as MthK and BK channels, but not other K^+ channels, which enhance channel conductance for outward currents (Brelidze et al., 2003; Nimigean et al., 2003). Charge neutralization of these residues in mouse Slo1 (BK channel) diminished conductance whereas substitution of the analogous KcsA residue to glutamate enhanced channel conductance. The mechanism by which these acidic residues enhance channel conductance is through electrostatic attraction of K^+ ions to this region, as demonstrated by measuring single channel conductance in varying K^+ concentrations (Brelidze et al., 2003; Nimigean et al., 2003). These mutagenesis

studies suggest that residues within the inner helix are important for diversifying the conductance properties of K^+ channels.

1.4. Voltage-gated K^+ channels and Ca^{2+}-activated K^+ channels

K^+ channels can be classified into three subfamilies based on their membrane topology and functional characteristics (Hille, 2001). The largest subfamily of K^+ channels is comprised of K_V and K_{Ca} channels, which are voltage-dependent channels comprised of 6 transmembrane helices (M1-6), or 7 in the case of BK channels (M0-6), and 1 selectivity filter signature sequence (Figure 1.3) (Coetzee et al., 1999; Hille, 2001). Since one selectivity filter sequence is found in each monomer, K_V and K_{Ca} channels are tetrameric (Coetzee et al., 1999; Doyle et al., 1998). Furthermore, K_V and K_{Ca} channels have been shown to assemble as homotetramer and heterotetramers, which is presumably important for diversifying their functional properties (Coetzee et al., 1999; Doyle et al., 1998). In addition to the hallmark selectivity filter sequence, these channels also harbor an arginine-enriched segment (every 3rd residue) within M4, which is the channel voltage sensor (Figure 1.3) (Yellen, 1998). Another important structural feature that plays a role in fast inactivation of K_V channels is the N-terminus, which has been proposed to inactivate K_V channels by plugging the intracellular side of the pore through a ball-and-chain model (Yellen, 1998).

K_V and K_{Ca} channels make up over half of the total number of human K^+ channels currently identified and can be further divided into twelve (K_V1-12) and five (K_{Ca}1-5) classes, respectively, based on sequence homology (Coetzee et al., 1999). K_V channels have distinct electrophysiological properties that work collectively to fine-tune the number, duration and firing frequency of action potentials in neurons (Johnston et al., 2010). For instance, K_V1 and K_V4 channels, homologs of *D. melanogaster* Shaker and Shal channels, respectively, are sensitive to small depolarizations near to the resting potential (around -40 mV to -30 mV), proposed to be

important for regulating the number of action potentials fired during depolarization (Johnston et al., 2010). In contrast, K_V2 and K_V3 channels (*D. melanogaster* Shab and Shaw channels, respectively) require greater membrane depolarization (around 0 mV), and thus are important for repolarizing neurons after an action potential. K_V3 channels are activated quickly, typically before reaching the action potential plateau, and therefore are also important for modulating action potential firing and fast frequency by promoting repolarization. K_V2 channels have slower activation kinetics than K_V3 channels and consequently contribute additional K^+ currents (with K_V3) during the repolarization (Johnston et al., 2010).

K_{Ca} channel gating is modulated by changes in intracellular Ca^{2+} and, as a result, these channels are often co-expressed with voltage-gated Ca^{2+} channels. In the case of $K_{Ca}1$ channels (BK channels), gating is also voltage-dependent (Vergara et al., 1998). BK channels are expressed in a wide variety of tissues, with the highest abundance in the brain and smooth muscle-containing organs (Wu and Marx, 2010). Consequently, $K_{Ca}1$ channels have been shown to have essential functions in the cerebellum, vasculature, kidneys (adrenal glands) and bladder, as evaluated with $K_{Ca}1$-targeted knockout mice (Wu and Marx, 2010). $K_{Ca}1$ channels associate with tissue-specific auxiliary subunits (β1-4), which contribute to their functional diversity within different organs. Efflux of K^+ ions through Ca^{2+}-modulated $K_{Ca}1$ channels results in cell hyperpolarization, which reduces Ca^{2+} influx through voltage-gated Ca^{2+} channels. $K_{Ca}1$ are, therefore, often described as feedback regulators of voltage-gated Ca^{2+} channels (Vergara et al., 1998). Unlike BK channels, $K_{Ca}2$ channels, or small conductance K_{Ca} channels (SK channels), exhibit voltage-independent gating properties and play an essential role in excitable cells. SK channels are modulated by intracellular Ca^{2+} ions, but do not directly bind Ca^{2+}. Instead, SK channels are regulated by calmodulin binding through interaction with the SK channel C-terminus (Adelman et al., 2012). Interestingly, SK channel have also been localized in the dendritic spines of hippocampal CA1 neurons and have been reported to dampen AMPA receptor- and NMDA receptor-induced

excitatory post-synaptic potentials in these neurons, suggesting a role in learning and memory (Adelman et al., 2012).

1.5. Inward-rectifying K$^+$ channels

K_{IR} channels comprise a second subfamily of K$^+$ channels, which are structurally distinct from K_V and K_{Ca} channels since they harbor only 2 transmembrane segments (M1-2) and 1 selectivity filter signature sequence (Figure 1.3) (Hibino et al., 2010; Hille, 2001). As anticipated based on the K_{IR} molecular architecture, K_{IR} channels are not voltage-gated since they do not contain the voltage-sensing domain that is found in K_V and K_{Ca} channels. However, like K_V and K_{Ca} channels, K_{IR} channels are tetrameric complexes, which can assemble as functional homomers and heteromers (Hibino et al., 2010). All K_{IR} channels display inward rectification, with large measurable conductance below the equilibrium potential for K$^+$ ions (E_K) and very little conductance above the E_K (see 1.6.1 Theoretical electrophysiological properties of K$^+$ leak channels for explanation of E_K) (Figure 1.3). Interestingly, K_{IR} inward rectification is not associated with modulation to the channel gate. Instead, K_{IR} channels are able to minimize K$^+$ conductance at higher membrane potentials through a physical block of the ion pore by intracellular magnesium ions (Mg^{2+}) and/or polyamines (Lopatin et al., 1994; Matsuda et al., 1987).

A total of 15 K_{IR} channels have been identified in mammals that can be first grouped into 7 subfamilies based on their sequence similarity, and the 7 subfamilies can be categorized into 4 groups based on their functional characteristics. These groups are classical K_{IR} channels ($K_{IR}2$), G protein-gated K_{IR} channels ($K_{IR}3$), ATP-sensitive K_{IR} channels ($K_{IR}6$), and other K_{IR} channels ($K_{IR}1$, $K_{IR}4$, $K_{IR}5$, and $K_{IR}7$) (Hibino et al., 2010). Although all K_{IR} channels exhibit inward rectification, they do so to varying degrees. For instance, $K_{IR}2$ and $K_{IR}3$ channels are classified as strong inward rectifiers, whereas $K_{IR}4$ channels are intermediated inward rectifiers and $K_{IR}1$,

$K_{IR}5$, $K_{IR}6$ and $K_{IR}7$ channels are considered weak inward rectifiers. One molecular distinction, which dictates strong or weak inward rectification of K_{IR} channels by Mg^{2+} block, is a conserved residue within the inner helix (M2) of K_{IR} channels (Lu and MacKinnon, 1994; Stanfield et al., 1994; Wible et al., 1994). Strong inward rectifiers contain an aspartate at this position (e.g. aspartate 172 in human $K_{IR}2.1$), whereas weak inward rectifiers contain an asparagine. Mutation of this residue alters the affinity for Mg^{2+} and the magnitude of inward rectification through an electrostatic mechanism (Lu and MacKinnon, 1994; Stanfield et al., 1994; Wible et al., 1994).

Among their various physiological roles, $K_{IR}2$ channels are abundant in cardiac myocytes and are essential for dictating the kinetics of a cardiac action potential. $K_{IR}2.1$-2.3 channels control the resting membrane potential, they are responsible for sustaining the characteristic prolonged cardiac action potential, and also significantly contribute K^+ efflux during repolarization (Hibino et al., 2010). Andersen's syndrome, an autosomal dominant disorder associated with a cardiac arrhythmia phenotype in patients, is linked to mutations in $K_{IR}2.1$ (Plaster et al., 2001). In the nephron, $K_{IR}1.1$ channels are primarily localized to the thick ascending limb of the loop of Henle (TAL), the distal convoluted tubule, and the cortical collecting duct (Hibino et al., 2010). TAL cells are essential for reabsorbing 25% of Na^+ ions from the urine and this process is primarily regulated by the Na^+-K^+-$2Cl^-$ cotransporter (NKCC). $K_{IR}1.1$ and NKCC appear to be functionally coupled since $K_{IR}1.1$ channels are hypothesized to be necessary for balancing the K^+ influx introduced through the action of NKCC. $K_{IR}1.1$-mediated K^+ efflux results in an increase of extracellular K^+ ions, which, in turn, facilitates additional Na^+ reabsorption through NKCC (Hibino et al., 2010). In support of the role of $K_{IR}1.1$ in the nephron, $K_{IR}1.1$ knockout mice exhibit a Na^+, K^+ and Cl^- wasting phenotype similar to type II Bartter's syndrome (Lorenz et al., 2002).

1.6. Two pore domain K$^+$ channels

The third subfamily of K$^+$ channels are named two pore domain K$^+$ channels (K$_{2P}$), and these channels were originally classified as background or leak K$^+$ channels. K$_{2P}$ channels have a unique molecular architecture, which contains four transmembrane segments (M1-4) and 2 selectivity filter sequences (P1-2) (Figure 1.3) (Enyedi and Czirjak, 2010; Hille, 2001). Their topology suggests that the biological assembly of K$_{2P}$ channels is a dimer rather than a tetramer (Kollewe et al., 2009; Lesage et al., 1996b; Maingret et al., 2000a; Patel et al., 2000). A total of 15 human homologs have been identified and are grouped into a total of 6 subfamilies based on their sequence identity and functional properties (Table 1.2) (Enyedi and Czirjak, 2010; Goldstein et al., 2005). Overall, the individual physiological roles of K$_{2P}$ channels have not been fully elucidated due to a lack of K$_{2P}$-specific inhibitors and/or to the potential for compensatory or tantamount function of other K$_{2P}$ channels paralogs within a cell. However, the most studied of these channels are the TREK (K$_{2P}$2, K$_{2P}$4 and K$_{2P}$10) and TASK (K$_{2P}$3, K$_{2P}$9) subfamilies. Members of the TREK subfamily are gated by a diverse range of cell stimuli and pharmacological agents such as membrane stretch, temperature, pH, anesthetics and lipids (Enyedi and Czirjak, 2010; Honore, 2007). Electrophysiological and K$_{2P}$2 knockout mice studies suggest roles for these channels in neuroprotection, pain perception, depression and anesthetic modulation through a common mechanism of hyperpolarization and decreased cell excitability (Honore, 2007; Sabbadini and Yost, 2009b). TASK subfamily members are acid-sensitive channels, gated by changes to extracellular pH and anesthetics (Enyedi and Czirjak, 2010). They have a number of important physiological roles, including aldosterone production and secretion, which is important for K$^+$ secretion and Na$^+$ reabsorption in the kidney (Bayliss and Barrett, 2008; Sabbadini and Yost, 2009b). TASK channels best fit the model of a K$^+$ leak channel, as predicted for free ion flux through an open ion-selective pore by the Goldman-Hodgkin-Katz (GHK) constant field current equation (Figure 1.3) (Goldman, 1943; Hodgkin and Katz, 1949).

Subfamilies	Channel
TWIK	$K_{2P}1$ (TWIK-1)
	$K_{2P}6$ (TWIK-2)
	$K_{2P}7$
TREK	$K_{2P}2$ (TREK-1)
	$K_{2P}4$ (TRAAK)
	$K_{2P}10$ (TREK-2)
TASK	$K_{2P}3$ (TASK-1)
	$K_{2P}9$ (TASK-3)
	$K_{2P}15$ (TASK-5)
THIK	$K_{2P}12$ (THIK-2)
	$K_{2P}13$ (THIK-1)
TALK	$K_{2P}5$ (TASK-2)
	$K_{2P}16$ (TALK-1)
	$K_{2P}17$ (TALK-2)
TRESK	$K_{2P}18$ (TRESK)

Table 1.2: List of 15 human K_{2P} channels that are grouped into 6 subfamilies based on sequence identity and functional characteristics. Channels that are italicized have not been demonstrated to be functional in the literature. With the exception of $K_{2P}18$, all K_{2P} channels were cloned and screened by FSEC (see 2.3.1 Pre-crystallization screening of K_{2P} channels).

1.6.1. Theoretical electrophysiological properties of K$^+$ leak channels

As mentioned earlier, Na$^+$/K$^+$ pumps and K$^+$ leak channels are essential for establishing the electrical potential across the membrane at rest. Na$^+$/K$^+$ pumps are important for generating concentration gradients of both Na$^+$ and K$^+$ ions. The resulting asymmetrical distribution of K$^+$ ions, with a high concentration inside the cell, promotes K$^+$ efflux through K$^+$ leak channels. This K$^+$ efflux generates a negative electrical gradient, due to the positive charge moving out of the cell and the counter negative charge remaining inside. Therefore, K$^+$ efflux is dictated by the K$^+$ concentration gradient, established by Na$^+$/K$^+$ pumps, and the electrical gradient generated by both K$^+$ efflux and the total distribution of ions.

K$^+$ equilibrium is reached at the membrane potential, or the Nernst potential, where there is no net ion flux. In a hypothetical system in which the membrane is only permeable to K$^+$ ions, the Nernst potential can be simplified to the equilibrium potential for K$^+$ ions (E$_K$):

$$E_K = \frac{RT}{zF} \ln \frac{[K^+]_o}{[K^+]_i}$$

where R is the gas constant, T is the absolute temperature constant in kelvin, z is the charge of the ion (1, in the case of K$^+$) , F is Faraday constant and $[K^+]_o$ and $[K^+]_i$ are the K$^+$ ion concentrations outside and inside the cell, respectively. At physiological K$^+$ concentrations and temperature (37°C), E$_K$ is −98 mV and the resting potential for mammalian cells is between −60 to −90 mV. Not surprisingly, K$^+$ conductance has a significant contribution at rest since E$_K$ is close to resting potential, a phenomenon documented > 100 years ago (Seyfarth, 2006). Yet, the variability of resting potential in mammalian cells suggests that contribution is not limited to K$^+$, but may also include other ions such as Na$^+$ and Cl$^-$ (equilibrium potentials of +67 and −90 mV, respectively) (Hille, 2001).

Initial studies to elucidate the properties of ion permeation and selectivity through biological membranes were performed by Goldman, Hodgkin and Katz in the 1940's (Goldman, 1943; Hodgkin and Katz, 1949). One of the equations derived from these studies, called the GHK constant field current equation, is now viewed as an expression that can predict the non-linear current-voltage (I-V) relationship that is observed for leak channels (Hille, 2001). The non-linear I-V relationship, called rectification, is assumed to be a result of asymmetrical concentration of ions inside and outside of the cell exclusively. The other major assumptions that were made when deriving this equation were that 1. the membrane is a homogenous layer, 2. there is a constant electric field across the membrane, 3. ions crossing the membrane do so independently of one another (no interaction), and 4. current amplitude adjusts instantaneously to changes in membrane potential. The GHK current equation can be used to calculate the hypothetical current amplitude measured from an ion-selective leak channel as long as the permeability of ion S (P_S), the cytosolic and extracellular concentrations of ion S ($[S]_i$ and $[S]_o$, respectively), and the membrane potential are known (V_m):

$$I_S = P_S z_S{}^2 \frac{V_m F^2}{RT} \frac{[S]_i - [S]_o \exp(-\frac{z_S V_m F}{RT})}{1 - \exp(-\frac{z_S V_m F}{RT})}$$

Assuming that ions cross the membrane independently of one another, the equation above can be separated into two expressions of current efflux and influx of ion S:

$$I_S\ efflux = P_S z_S{}^2 \frac{V_m F^2}{RT} \frac{[S]_i}{1 - \exp(-\frac{z_S V_m F}{RT})}$$

$$I_S\ influx = P_S z_S{}^2 \frac{V_m F^2}{RT} \frac{[S]_o}{1 - \exp(\frac{z_S V_m F}{RT})}$$

29
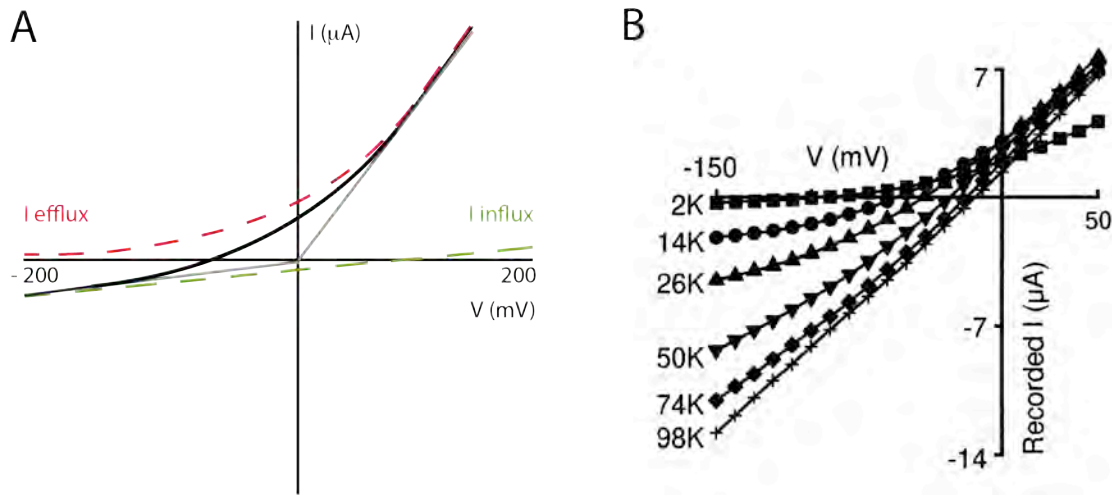
Figure 1.8: TASK channels best fit the GHK current equation prediction for a K^+ leak channel. (A) Theoretical I-V representation of K^+ (black curve) with an ~ 5-10 fold K^+ gradient, as predicted from the GHK current equations (I_K efflux, red dashed curve; I_K influx, green dashed curve). At larger negative and positive membrane potentials, the inward and outward current amplitudes become asymptotic to straight lines from the origin (gray lines). In symmetrical conditions, I_K efflux and influx become one line that passes through the origin. (B) I-V relationship of human TASK-1 ($K_{2P}3$) channels expressed in *Xenopus* oocytes. Whole-cell recordings of $K_{2P}3$ in various external concentrations of K^+ ions. Symmetrical conditions (98K) appear as a straight line, as predicted by the GHK current equation. Adapted by permission from Macmillan Publishers Ltd: EMBO 16(17): 5464-71 copyright 1997.

At large positive and negative membrane potentials (V_m), both I_S efflux and influx become

asymptotic to straight lines from the origin in an I-V curve (Figure 1.8). In this case, the equations

can be simplified to:

$$I_S \text{ efflux} = P_S z_S{}^2 \frac{V_m F^2}{RT} [S]_i \quad \text{for } V_m \gg 0$$

$$I_S \text{ influx} = P_S z_S{}^2 \frac{V_m F^2}{RT} [S]_o \quad \text{for } V_m \ll 0$$

Interestingly, the asymptotic lines converge to a straight line through the origin in the I-V curve

when the internal and external concentrations of S are equal. In this case, the channel

conductance (slope) is the same at all membrane potentials, corresponding to Ohm's law. From

the GHK current equation, the I-V relationship of a leak channel measured in symmetrical ionic

conditions should be linear, graphing as a straight line through the origin (Figure 1.3, Figure 1.8).

For a K^+-specific leak channel recorded in physiological K^+ conditions (non-symmetrical), one

would expect to measure an outward rectifying channel with an E_K at around -100 mV (Figure

1.8).

We now know that many of the assumptions made are not observed physiologically. The lipid

bilayer is made up of many components, including different types of phospholipids, cholesterol,

membrane-anchored proteins and transmembrane proteins including ion channels. The crystal

structures of KcsA demonstrated that channel pores have dipoles and charges that contribute to

local changes in the electric field (Doyle et al., 1998; Roux and MacKinnon, 1999). In addition,

the structure highlights the importance of K^+ charge repulsion within the selectivity filter as a

means to promote ion movement within this region (Doyle et al., 1998; Zhou et al., 2001b).

Despite the inaccurate assumptions, the GHK current equation is still able to predict the I-V

relationship of leak channels quite well. K_{2P} channels exhibit I-V relationships that are most

similar to the GHK current equation prediction compared with other K^+ channel families (Figure

similar to the GHK current equation prediction compared with other K^+ channel families (Figure 1.3). In particular, instantaneous currents measured from TASK channel subfamily members exhibit almost identical properties (Figure 1.8) (Duprat et al., 1997; Enyedi and Czirjak, 2010). I will now discuss the biophysical characteristics and physiological roles the two most extensively studied K_{2P} subfamilies, the TASK and TREK channels, and end the section with a description of $K_{2P}1$ (TWIK-1) channels, which is the focus of this thesis.

1.6.2. TASK channels: biophysical characteristics and physiological roles

TASK-1 ($K_{2P}3$), TASK-3 ($K_{2P}9$) and TASK-5 ($K_{2P}15$) are members of the TASK subfamily of K_{2P} channels, or TWIK-related Acid Sensitive K^+ channels. The first channels which were identified and characterized within this family were $K_{2P}3$ and $K_{2P}9$ channels, both of which exhibited electrophysiological properties that resemble leak K^+ channels as predicted by the GHK current equation (Duprat et al., 1997; Enyedi and Czirjak, 2010; Kim et al., 1999; 2000; Lopes et al., 2000; Rajan et al., 2000). In addition, both $K_{2P}3$ and $K_{2P}9$ channels are gated by extracellular acidosis and substitution of a histidine residue within the P1 selectivity filter sequence in both channels (TIGYG**H**; H98 for both $K_{2P}3$ and $K_{2P}9$) inhibits this regulation (Kim et al., 2000; Lopes et al., 2000; Lopes et al., 2001; Morton et al., 2003; Rajan et al., 2000). Interestingly, background K^+ channels had been proposed to be targets of anesthetic action for ~ 30 years ago (Franks and Lieb, 1988; Nicoll and Madison, 1982). After the molecular identification of the K_{2P} channel family in the mid-90's, it was demonstrated that $K_{2P}3$ and $K_{2P}9$ channels are modulated by inhalation anesthetics including halothane and isoflurane ($K_{2P}9$-specific), but not chloroform or diethyl either (Berg et al., 2004; Patel et al., 1999; Sirois et al., 2000; Talley and Bayliss, 2002).

Currently, $K_{2P}3$ and $K_{2P}9$ channels are the only K_{2P} family members that have been reported to assemble as both homomeric and heteromeric channels (Berg et al., 2004; Czirjak and Enyedi, 2002; Kang et al., 2004). Not surprisingly, $K_{2P}3$ and $K_{2P}9$ channel homomers and $K_{2P}3$-$K_{2P}9$

channel heteromers have distinct electrophysiological and pharmacological properties, as has been demonstrated through co-expression of both subunits, as well as with expression of a $K_{2P}3$-$K_{2P}9$ tandem heterodimer (Berg et al., 2004; Czirjak and Enyedi, 2002; Kang et al., 2004). Functional $K_{2P}3$-$K_{2P}9$ heteromers, as well as $K_{2P}3$ and $K_{2P}9$ homomers, have also been identified in somatic motor neurons and cerebellar granule cells (Berg et al., 2004; Kang et al., 2004). The existence of both homomers and heteromers of $K_{2P}3$ and $K_{2P}9$ is most likely important for providing functional diversity within this K_{2P} channel family and could play a role in fine tuning cellular responses to changes in extracellular pH.

More recent work with a $K_{2P}3/K_{2P}9$ double knockout mouse model has illuminated the physiological role of these channels. For example, both $K_{2P}3$ and $K_{2P}9$ are highly expressed in the outer layer of the adrenal glands (zona glomerulosa; ZG). One role of ZG cells is to facilitate the production and secretion of aldosterone, a hormone that is important for regulating K^+ secretion and Na^+ reabsorption in the kidney and, in turn, controlling blood pressure. Aldosterone secretion is enhanced by both extracellular acitification and activation of AT_1 (a G_q-coupled receptor) by angiotensin II, and both AT1 activation and acidosis have been shown to gate $K_{2P}3$ and $K_{2P}9$ channels (Czirjak et al., 2000). Furthermore, aldosterone production and secretion are regulated by Ca^{2+} entry through T-type Ca^{2+} channels (most likely candidate is $Ca_V3.2$ based on electrophysiological characteristics) (Hu et al., 2012). Since membrane depolarization is required for Ca^{2+} entry, maintenance of the resting potential by both $K_{2P}3$ and $K_{2P}9$ is also essential for this process (Czirjak et al., 2000). Although $K_{2P}3/K_{2P}9$ double knockout mice appear to have normal histological features, they have enhanced production and secretion of aldosterone (Davies et al., 2008). ZG cells are depolarized in the $K_{2P}3/K_{2P}9$ knockout mice. In addition, aldosterone production and secretion is enhanced in both high and low sodium diets in these mice, whereas aldosterone levels in the urine are elevated with low (angiotensin II production), but not high (no angiotensin II), sodium diets in wild-type mice (Davies et al., 2008). The mice exhibit a

phenotype similar to primary hyperaldosteronism, a condition which results in enhanced Na^+ reabsorption, K^+ excretion and, ultimately, hypertension.

Studies of anesthetic response by wild-type, $K_{2P}3$ knockout, and $K_{2P}9$ knockout mice have also been investigated. The overall response to the hypnotic and analgesic effects of halothane and isoflurane, as evaluated by the loss of righting reflex response (LORR) and loss of tail-pinch withdrawal response (LTWR) behavioral tests, appeared to be present, but minimal, for the $K_{2P}3$ and $K_{2P}9$ knockout mice (Linden et al., 2006; Linden et al., 2007). These results suggest that there may be other channels that contribute to the overall effects induced by halothane and isoflurane. However, these results do not exclude the possibility of compensatory effects of other K_{2P} channel family members. For example, $K_{2P}3$ knockout mice exhibit enhanced expression of other K_{2P} channels in the mouse forebrain, at least at the transcript level (Linden et al., 2006).

1.6.3. TREK channels: biophysical characteristics and physiological roles

The TREK channel family, which consists of TREK-1 ($K_{2P}2$), TREK-2 ($K_{2P}10$) and TRAAK ($K_{2P}4$) were the second family of K_{2P} channels identified (Bayliss and Barrett, 2008; Dedman et al., 2009; Enyedi and Czirjak, 2010; Honore, 2007). TREK channels exhibit mild outward ($K_{2P}2$) or inward ($K_{2P}4$, $K_{2P}10$) rectification in symmetrical K^+ conditions when recorded as single channels (Bang et al., 2000; Kim et al., 2001a; Patel et al., 1998). This mild rectification suggests a weak voltage dependency and, therefore, TREK channels do not fit the GHK current equation model.

TREK channels have been of considerable interest since they are highly responsive to thermo, mechanical and chemical stimuli (Bayliss and Barrett, 2008; Dedman et al., 2009; Enyedi and Czirjak, 2010; Honore, 2007). For instance, patch clamp studies of overexpressed $K_{2P}2$, $K_{2P}4$ or $K_{2P}10$ in *Xenopus* oocytes and mammalian cell lines demonstrated that current amplitudes are

enhanced when channels are recorded at elevated temperatures (37°C - 42°C versus 25°C) (Kang et al., 2005; Maingret et al., 2000a). Mechanical stress also modulates $K_{2P}2$, $K_{2P}4$ or $K_{2P}10$ activity, as demonstrated by studies utilizing 1. mechanical force (positive or negative pressure), 2. introduction of amphipaths that selectively integrate into the outer (trinitrophenol, lysolecithin) or inner (chlorpromazine) leaflets of the lipid bilayer, or 3. cell swelling (Bang et al., 2000; Lesage et al., 2000a; Lesage et al., 2000b; Maingret et al., 1999a; Patel et al., 1998). Furthermore, mechanical stimulation of TREK channels appears to be a direct effect since $K_{2P}2$, $K_{2P}4$ and $K_{2P}10$ mechanosensitivity was maintained in excised patches. In addition to membrane tension, TREK channels are also gated by lipids moieties embedded in the bilayer, including polyunsaturated fatty acids (PUFAs; e.g. arachadonic acid), phospholipids (PL), and lysophospholipids (lysoPLs) (Bang et al., 2000; Chemin et al., 2005a; Chemin et al., 2005b; Fink et al., 1998; Lesage et al., 2000b; Maingret et al., 2000b; Patel et al., 1998). Intracellular acidification ($K_{2P}2$, $K_{2P}10$) or alkalinization ($K_{2P}4$) has also been demonstrated to directly activate these channels since these effects are observed in inside-out patch configuration (Bang et al., 2000; Kim et al., 2001a; Lesage et al., 2000b; Maingret et al., 1999b). Finally, as has been demonstrated for TASK channels, $K_{2P}2$ and $K_{2P}10$ channels, but not $K_{2P}4$ channels, are also modulated by inhalation anesthetics (Lesage et al., 2000b; Patel et al., 1999).

Site-directed mutagenesis studies have been conducted on TREK channels to identify a region(s) of the channel that is important for sensing these modalities. Many of the studies suggest that the cytosolic C-terminus is an important region for modulation by these stimuli in both $K_{2P}2$ and $K_{2P}10$ channels, whereas modifications to the C-terminus of $K_{2P}4$ have no effect (Chemin et al., 2005b; Chemin et al., 2007; Honore et al., 2002; Kim et al., 2001a; Kim et al., 2001b; Maingret et al., 1999b; 2000b; Patel et al., 1998; Patel et al., 1999). Since response to heat, pH, and mechanical stress appear to converge on C-terminus, one hypothesis is that these modalities may modulate the TREK channel gate in a similar manner. However, it has been shown that combined

intracellular acidosis ($K_{2P}2$ and $K_{2P}10$) or alkalinization ($K_{2P}4$) and membrane stretch (negative pressure) results in synergistic activation of TREK channels, suggesting different mechanisms of action (Honore et al., 2002; Kim et al., 2001a; Kim et al., 2001b). Substitution of glutamate 306 (E306), located within the proximal C-terminus (residues 297-311) of $K_{2P}2$, results in a channel that is insensitive to intracellular acidification, but activated by membrane stretch (Figure 1.9). Likewise, a $K_{2P}2$ C-terminal truncation mutant that eliminates residues 312-411 ($K_{2P}2$ $\Delta100$; distal C-terminus) is insensitive to pressure, but is activated by protons (Figure 1.9) (Honore et al., 2002). Lipid modification and stretch also appear to have separate modes of action. PIP_2 stimulation of $K_{2P}2$ requires the presence of positively charged C-terminal residues within the proximal C-terminus, whereas deletion of the distal C-terminus has no effect (Figure 1.9) (Chemin et al., 2005b). Furthermore, $K_{2P}2$ modulation by lysophosphatidic acid does not require the C-terminus (Chemin et al., 2005a).

Evaluating the location of TREK channel expression can help to elucidate their physiological function. For instance, expression of TREK channels is abundant in the brain, with high expression of $K_{2P}2$ and $K_{2P}10$ in the dorsal striatum (caudate nucleus and putamen) and expression of $K_{2P}2$ and $K_{2P}4$ in the amygdala, regions of the brain that are essential for memory and emotional response (Heurteaux et al., 2006; Lesage et al., 2000b; Meadows et al., 2000; Medhurst et al., 2001; Reyes et al., 2000). Interestingly, $K_{2P}2$ knockout mice exhibit a depression-resistant phenotype, with increased serotonin (5-HT) neurotransmission and a decreased response to behavioral tests examining depression and stress (Heurteaux et al., 2006). $K_{2P}2$ knockout mice are also resistant to a variety of antidepressants, such as fluoxetine, paroxetine and amitriptyline. This phenotype was not matched in the $K_{2P}4$ knockout mice, which was surprising because 5-HT receptors (predominantly G protein-coupled receptors) are expressed within a region of the amygdala called the hippocampus. However, the lack of a depression-resistant phenotype in the $K_{2P}4$ knockout mice may be a result of $K_{2P}2$, but not $K_{2P}4$, regulation by G proteins

M4   proximal C-terminus   distal C-terminus

270   280   290   300   310   320   330   340

K₂P2 264 I E Y L D F Y K P V V W F W I L V G L A Y F A A V L S M I G D W L R V I S K K T K E E V G E F R A H A A E W T A N V T A E F K E T R R R L S V E I Y D K F Q R A T S 345

* ** ** * *

distal C-terminus

350   360   370   380   390   400

K₂P2 346 I K R K L S A E L A G N H N Q E L T P C R R T L S V N H L T S E R D V L P P L L K T E S I Y L N G L T P H C A G E E I A V I E N I K 411
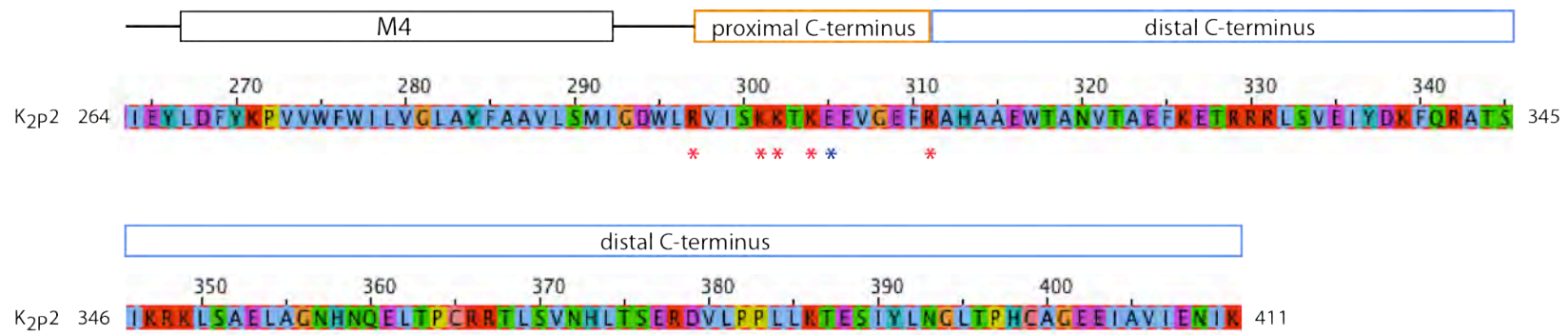
Figure 1.9: Modifications to the C-terminus of $K_{2P}2$ which alter gating. $K_{2P}2$ sequence with transmembrane segment 4 (M4), proximal C-terminus (orange) and distal C-terminus (blue) highlighted above. Asterisks denote residues located within the proximal C-terminus that are important for sensing intracellular acidification (E306, blue) and for interacting with PIP_2 (basic residues, red) (Chemin et al., 2005b; Honore et al., 2002).

(Heurteaux et al., 2006). The depression-resistant phenotype of the $K_{2P}2$ knockout mice suggests an important physiological role of $K_{2P}2$ in hyperpolarizing serotonergic neurons.

In addition to the brain, TREK channels are also found in dorsal root ganglion (DRG), a region comprised of afferent neurons located in the spine that are capable of sensing noxious stimuli and relaying this information to the brain (Alloui et al., 2006; Kang et al., 2005; Kang and Kim, 2006; Maingret et al., 2000a; Medhurst et al., 2001; Noel et al., 2009; Reyes et al., 2000; Talley et al., 2001). Nociceptive neurons in the DRG are able to respond to noxious stimuli, which include extreme cold and hot temperatures, mechanical stress, and tissue acidity (Chudler and Dong, 1995). These insults are activators of TREK channels, suggesting a direct role for these channels in regulating DRG neuronal firing (Honore, 2007). This hypothesis is supported by work with $K_{2P}2$ single knockout and $K_{2P}2$-$K_{2P}10$ double knockout mice, which demonstrate a role for cold and heat, mechanical (osmolarity), and chemical perception in the DRG through mouse behavioral studies and electrophysiological recordings from wild-type, Kcnk2 -/- and Kcnk2-Kcnk10 -/- DRG neurons and C-fibers (Alloui et al., 2006; Noel et al., 2009).

PUFAs and lysoPLs have been reported to be important for neuroprotection against cerebral insults such as ischemia and kainite- (glutamate receptor agonist) induced seizures in mice (Blondeau et al., 2002a; Blondeau et al., 2002b; Lauritzen et al., 2000). The proposed mechanism for neuroprotection is activation of PUFA-sensitive background K^+ channels within the TREK subfamily, which result in a reduction of the resting potential and reduced excitatory postsynaptic potentials (Lauritzen et al., 2000). Riluzole is a potent neuroprotectant that is a first-line drug for the treatment of amyotrophic lateral sclerosis. Like PUFAs, it is suggested that riluzole prevents neuronal hyperexcitability and has been shown to directly activate $K_{2P}2$, $K_{2P}4$ and $K_{2P}10$ channels (Duprat et al., 2000; Fink et al., 1998; Lesage et al., 2000b). Physiological evidence for a neuroprotective role of $K_{2P}2$ was demonstrated in $K_{2P}2$ knockout mice, which displayed increased

susceptibility to brain and spinal cord ischemia as well as to kainite- and pentylenetetrazol-(GABA$_A$ receptor antagonist) induced epileptic seizures (Heurteaux et al., 2004). Furthermore, whereas wild-type mice benefited by injection of linolenic acid (a PUFA) or lysophosphatidylcholine (a lysoPL) prior to kainite administration, with decreased seizure activity and mortality rates, K$_{2P}$2 knockout mice performed poorly with or without the lipid pre-treatment (Heurteaux et al., 2004). These results suggested a loss of neuroprotection by PUFAs and lysoPLs in the K$_{2P}$2 knockout mice.

Inhalation anesthetics, such as chloroform, halothane and isoflurane, have been demonstrated to activate K$_{2P}$2 and K$_{2P}$10 channels, but not K$_{2P}$4 channels, at clinically relevant concentrations (Patel et al., 1999). K$_{2P}$2 knockout mice were less sensitive to the hypnotic effects of chloroform, halothane, seroflurane and desflurane, with an increase in latency to LORR compared to wild-type animals (Heurteaux et al., 2004). These effects were restricted to inhalation anesthetics since K$_{2P}$2 knockout mice responded similarly to application of pentobarbital compared to wild-type mice (Heurteaux et al., 2004). These results suggest that K$_{2P}$2, and possibly K$_{2P}$10, channels are likely targets of inhalation anesthetics.

1.6.4. K$_{2P}$1 channel: biophysical characteristics and physiological roles

The K$_{2P}$1 (TWIK-1) channel was the first mammalian K$_{2P}$ channel identified, with widespread expression in both human and mouse tissue samples (Lesage et al., 1996a; Lesage and Lazdunski, 2000). K$_{2P}$1 is most abundant in the CNS, with high expression in the cerebellum, thalamus and cortex (Medhurst et al., 2000; Talley et al., 2001). K$_{2P}$1 nephron distribution has also been extensively examined in human, rat and rabbit, with high levels of expression in the TAL and distal tube (Cluzeaud et al., 1998; Levy et al., 2004; Orias et al., 1997). Although K$_{2P}$1 expression is widespread in multiple organisms, K$_{2P}$1 knockout mice exhibit minor abnormalities with the exception a renal phosphate and water retention reduction phenotype (Millar et al., 2006; Nie et

al., 2005; Sabbadini and Yost, 2009a). The modest phenotypes observed these mice may be the result of compensatory responses to the loss of $K_{2P}1$ from other K_{2P} family members.

Biochemical studies of $K_{2P}1$ have supported the idea that K_{2P} channels assemble as dimers rather than tetramers. Under non-reducing conditions by SDS-PAGE, $K_{2P}1$ migrates as both a monomer and a dimer (Lesage et al., 1996b). A cysteine residue within the extracellular 'loop' (C69) was thought to contribute to $K_{2P}1$ dimerization since a $K_{2P}1$ C69S mutant migrates as a monomer (Figure 1.3). This residue is conserved throughout the majority of the K_{2P} paralogs and it is not known whether the cysteine is necessary for dimerization and, ultimately, for channel function. In addition, initial biochemical work demonstrated that $K_{2P}1$ is N-glycosylated at asparagine 95 (N95) within the extracellular 'loop'. Wild-type $K_{2P}1$ separated as two monomeric bands in reducing conditions whereas an N-glycosylation mutant (N95A) or PNGase F-treated wild-type $K_{2P}1$ sample separated as one, lower molecular weight band (Lesage et al., 1996b).

Functional characterization by electrophysiological studies initially classified $K_{2P}1$ as a weak inward-rectifying channel. This conclusion was based on the I-V curve from $K_{2P}1$ macroscopic measurements in *Xenopus* oocytes recorded in symmetrical K^+ conditions (Lesage et al., 1996a). However, further biophysical characterization of $K_{2P}1$ was not performed until ~10 years later since others were unable to obtain K^+ currents attributable to $K_{2P}1$ upon heterologous expression in a variety of cell lines (Goldstein et al., 1998; Goldstein et al., 2001).

Although localized to the plasma membrane, one hypothesis was that $K_{2P}1$ channels may require an additional factor or subunit, or may be rapidly internalized. One proposed mechanism of $K_{2P}1$ 'silencing' came from experimental data suggesting that a lysine residue within the $K_{2P}1$ carboxy-terminus (K274) is SUMO conjugated (Plant et al., 2010; Rajan et al., 2005). Addition of the SUMO-specific protease, SENP-1, and mutagenesis of K274 to glutamate (K274E) enhanced

$K_{2P}1$ macroscopic current density (Plant et al., 2010; Rajan et al., 2005). These findings were initially questioned by Lesage and colleagues since the introduction of the conservative K274 to arginine (K274R) mutation, which should also abolish SUMO conjugation, did not significantly enhance $K_{2P}1$ current amplitude in their hands (Feliciangeli et al., 2007; Feliciangeli et al., 2010). However, Goldstein and colleagues were later able to demonstrate that $K_{2P}1$ current amplitude was enhanced with the K274R mutation (Plant et al., 2010). The discrepancies between these groups have yet to be resolved but most likely can be attributed to differences in experimental systems and conditions used.

A second proposed mechanism of $K_{2P}1$ 'silencing' was developed from initial observations of $K_{2P}1$ localization to the pericentriolar recycling compartment in mammalian kidney cell lines (Decressac et al., 2004). It was shown that mutation of a non-canonical clatherin-mediated endocytosis motif located on the $K_{2P}1$ C-terminus (I293/294) resulted in both $K_{2P}1$ localization to the plasma membrane and enhanced $K_{2P}1$ current amplitude (Chatelain et al., 2012; Feliciangeli et al., 2010). Interestingly, $K_{2P}1$ K274E does not affect $K_{2P}1$ trafficking *in vitro*, lending support to the idea that the K274E mutation alters $K_{2P}1$ gating through a charge effect or SUMO conjugation (Feliciangeli et al., 2010).

The $K_{2P}1$ K274E mutant exhibits different biophysical properties to what had been previously characterized. Single channel recordings of a $K_{2P}1$ K274E mutant channel in COS-7 cells resembled a K^+ leak channel as defined by the GHK constant field equation, with a linear I-V relationship in symmetrical K^+ conditions and outward rectification in physiological K^+ conditions (Rajan et al., 2005). In addition, $K_{2P}1$ K274E channel gating is regulated by extracellular pH through protonation of histidine 122 (H122). Mutagenesis of H122 to aspartic acid (H122D) results in a $K_{2P}1$ channel that is insensitive to acidification (Chatelain et al., 2012; Rajan et al., 2005).

A study of the $K_{2P}1$ K274E mutant demonstrated that K^+ selectivity is altered when exposed to low extracellular concentrations of K^+ (< 3mM), a condition that resembles hypokalemia, or low K^+ in the blood (Ma et al., 2011; Ma et al., 2012a; Ma et al., 2012b). Moderate (< 3 mM K^+) to severe (< 2.5 mM K^+) hypokalemia can result in heart rate abnormalities and potentially cardiac arrest (Ma et al., 2011; Rastegar and Soleimani, 2001). Interestingly, human cardiomyocytes that are exposed to hypokalemic conditions exhibit significant depolarized resting potentials (~ -50 mV), compared with what is typically measured (~ -80 mV) (Christe, 1983; Gurney and Manoury, 2009). Furthermore, Na^+ influx is proposed to contribute to this observed depolarization (Gadsby and Cranefield, 1977). The observation of $K_{2P}1$ altered selectivity in the presence of low extracellular K^+, and its abundance in human heart tissue, suggests a role for this channel in the heart. Threonine 118 (T118), located within the $K_{2P}1$ highly-conserved selectivity filter sequence, is a conserved isoleucine in all other K_{2P} channel family members. Substitution of T118 to isoleucine resulted in a channel that was K^+ selective in low extracellular concentrations of K^+ (Chatelain et al., 2012; Ma et al., 2011). Likewise, substitution of the analogous $K_{2P}9$ residue, isoleucine 94, to threonine results in a shift of the I-V curve to a more depolarized reversal potential in low extracellular K^+ conditions, as is observed for $K_{2P}1$ (Ma et al., 2011). These data suggest that $K_{2P}1$ selectivity filter residue T118 is responsible for 'sensing' changes to extracellular K^+.

Altered K^+ selectivity has also been documented for $K_{2P}1$ K274E channels exposed to low extracellular pH and H122 mutagenesis presented a similar phenotype to the T118 substitution (Chatelain et al., 2012; Ma et al., 2012b). The physiological role of $K_{2P}1$ altered selectivity in the presence of low extracellular pH is not fully understood, but may exhibit similar functional consequences to what has been observed for the TASK channel family (see 1.6.2 TASK channels: biophysical characteristics and physiological roles).

1.7. Aims and objectives of this thesis

K_{2P} channel gating is modulated by a diverse range of cell stimuli and pharmacological agents including temperature, pH, polyunsaturated fatty acids, mechanical stress, and anesthetics. Electrophysiological and K_{2P} knockout mice studies suggest roles for these channels in neuroprotection, pain perception and anesthetic modulation through a common mechanism of hyperpolarization and decreased cell excitability. In humans, missense mutations within a K_{2P} channel family member have been associated with typical familial migraine with aura (Andres-Enguix et al., 2012; Lafreniere et al., 2010). Although the therapeutic potential of K_{2P} channels is evident, our limited understanding of how K_{2P} channels gate and why this subfamily and not other K^{+} channels respond to these stimuli has attenuated progress towards K_{2P} channel drug discovery. Structural studies of K_{2P} channels would provide insight into K_{2P} channel gating and suggest strategies for drug design.

My thesis work aims to further our understanding of K_{2P} channel function through both structural and biochemical characterization of human $K_{2P}1$. Chapter 2 reports a series of biochemical studies that were performed with purified human $K_{2P}1$ in order to identify a structured core of $K_{2P}1$ that was suitable for protein crystallization. Chapter 3 describes human $K_{2P}1$ crystal refinement, derivatization, structural determination and a full description and interpretation of the human $K_{2P}1$ crystal structure. Chapter 4 describes preliminary experimental attempts to improve human $K_{2P}1$ crystal diffraction through manipulation of crystal growth conditions, crystal contacts, addition of an inhibitor, monovalent cation (Na^{+}) substitution, and the generation of $K_{2P}1$ monoclonal antibodies. Chapter 5 provides a summary of the work and future directions.

CHAPTER 2

2. BIOCHEMICAL STUDIES OF HUMAN K$_{2P}$1

2.1. Summary

An initial pre-crystallization strategy identified human K$_{2P}$1 as a potential candidate for purification and crystallization. Biochemical studies of human K$_{2P}$1 demonstrated that cysteine 69 forms a disulfide bridge, which most likely stabilizes the detergent-extracted channel. In addition, human K$_{2P}$1 is glycosylated at asparagine 95, as evaluated by generation of a mutant (N95Q) and by chemical removal of the glycan by N-Glycosidase F. The human K$_{2P}$1 N95Q mutant was used for a subtilisin limited proteolysis/mass spectroscopy experiment to identify a disordered region(s) of the channel. A C-terminal deletion of human K$_{2P}$1 N95Q (Δ303) was generated based on these results. Purification of human K$_{2P}$1 N95Q Δ303 in DDM unexpectedly resulted in the accumulation of a higher-order oligomer through non-specific disulfide bond formation with cysteine residues on the N-terminus. Mutation of the N-terminal cysteines or deletion of the N-terminus eliminated the formation of the higher-ordered oligomer. In addition, truncation to the N-terminus (N-terminus Δ22; human K$_{2P}$1 N95Q 22-303 construct) was demonstrated to be essential for protein crystallization.

2.2. Materials and Methods

2.2.1. Cloning of human K$_{2P}$ paralogs and K$_{2P}$1 orthologs

Genes of the human K$_{2P}$ paralogs and K$_{2P}$1 orthologs were amplified by PCR from human, mouse, rat, guinea pig, cow, chicken or pig cDNA libraries (BioChain) or from fully sequenced zebrafish or frog K$_{2P}$1 cDNA clones (Open Biosystems). PCR products (2 μg) were EcoRI/SalI or XhoI/PstI digested (1 μl, New England Biolabs) for 2 hours at 37°C. For HEK293-GT cell expression, digested product was ligated (Roche) into the pNGFP-EU and pCGFP-EU vectors for

generation of N- and C-terminal GFP-fusion proteins (Kawate and Gouaux, 2006) or into the pcDNA3.1$^+$ vector with a C-terminal YL1/2 antibody recognition sequence (Glu-Gly-Glu-Glu-Phe; EGEEF tag. For expression in *Pichia pastoris*, human $K_{2P}1$ was ligated into the EcoRI/AvrII cloning sites of a pICZ-C vector (Invitrogen Life Technologies) with an EGEEF tag or ligated into the EcoRI/SalI cloning sites of a modified pICZ-C vector for generation of N-terminal and C-terminal GFP-fusions (pZNAAV and pZCAAV vectors, respectively) (Figure 2.1). K_{2P} point mutations were introduced by site-directed mutagenesis, adapted from the QuikChange site-directed mutagenesis protocol (Stratagene). Briefly, complementary primers introducing a human $K_{2P}1$ point mutation were generated (Integrated DNA Technologies). Mutants were amplified by PCR from 12.5 ng of human $K_{2P}1$ plasmid template. PCR product was digested with DpnI (0.5 μl, New England Biolabs) for 2 hours at 37°C and transformed into competent *E. coli* for plasmid amplification. A *P. pastoris* codon optimized construct of human $K_{2P}1$ C10A N95Q Δ303 was chemically synthesized with EcoRI/AvrII restriction sites (GeneWiz).

2.2.2.   Fluorescence-detection size exclusion chromatography (FSEC) screening

HEK293-GT cells were seeded at $1x10^6$ (6 well plate) or $1x10^7$ (10 cm dish) cells at least 2 hours prior to transfection. Cells were transiently transfected with each construct (3 μg/well or 10 μg/dish) using Lipofectamine 2000 (6 μl/well, 20 μl/dish; Invitrogen Life Technologies). After 48 hours, cells were rinsed with chilled PBS and harvested by suspension in chilled PBS (2 ml/well, 7-10 ml/dish). Cells were divided into individual samples (500 μl/sample), pelleted by centrifugation at 1,000 x g for 5 min at 4°C, and resuspended in 150 μl of buffer containing: 150 mM KCl; 50 mM Tris, pH 7.5; 1:500 dilution of Protease Inhibitor Cocktail Set III, EDTA-free (PI Mix III; Calbiochem) and detergent (Table 2.1, Anatrace). Samples were solubilized by rotation at 4°C for 1 hour and the detergent-insoluble cell debris was pelleted by centrifugation at 20,000 x g for 1 hour at 4°C. The soluble fraction (supernatent) was collected (100 μl) and
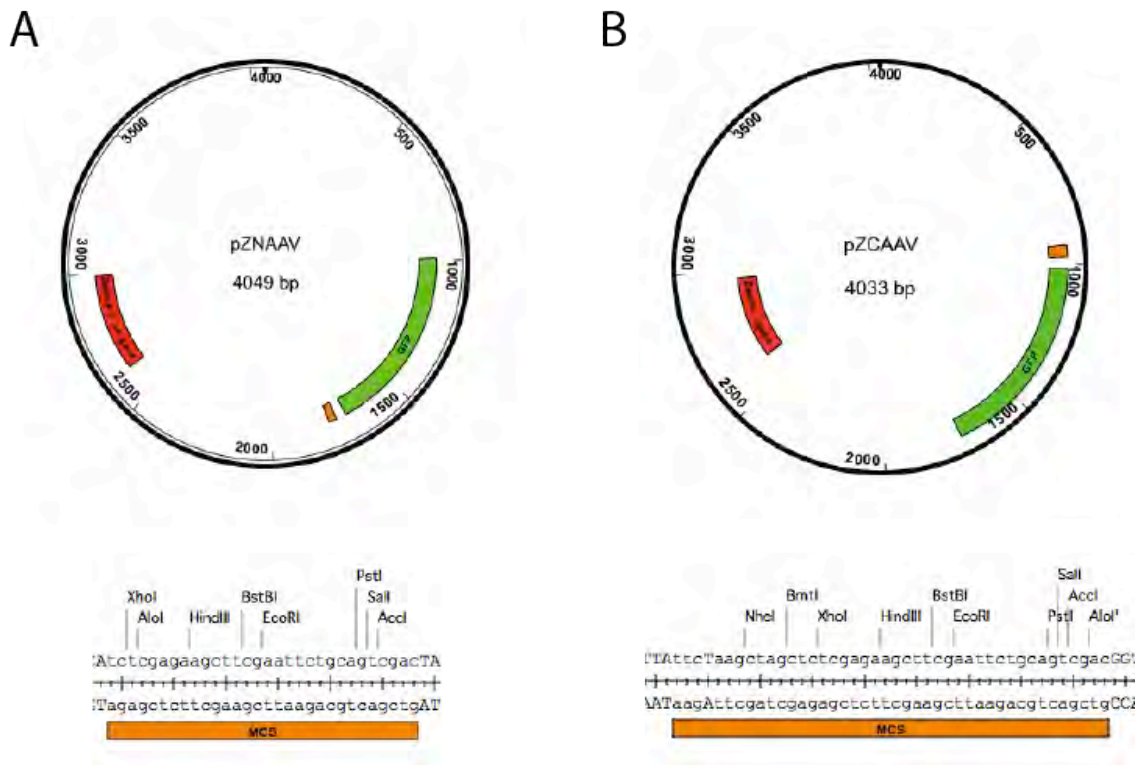
Figure 2.1: pZNAAV (A) and pZCAAV (B) plasmid maps and multiple cloning sites. Within the circular plasmid maps, multiple cloning site (orange), GFP (green) and zeocin resistance gene (red) are highlighted. Within the multiple cloning site (MCS), restriction endonuclease cleavage sites are denoted. Vector maps and multiple cloning site images were generated in the Lasergene SeqBuilder program by DNASTAR.

Name	Chemical Name	Concentration
DDM	n-Dodecyl-β-D-maltopyranoside	40 mM
DM	n-Decyl-β-D-maltopyranoside	40 mM
OM	n-Octyl-β-D-maltopyranoside	250 mM
OG	n-Octyl-β-D-glucopyranoside	250 mM
CYMAL-6	6-Cyclohexyl-1-hexyl-β-D-maltoside	40 mM
$C_{12}E_8$	Octaethylene glycol monododecyl ether	40 mM
LDAO	n-Dodecyl-N,N-dimethylamine-N-oxide	40 mM
FOS-12	n-Dodecylphosphocholine	40 mM
$C_{10}E_9$	Polyoxyethylene(9)decyl Ether	40 mM
$C_{10}E_6$	Polyoxyethylene(6)decyl Ether	40 mM
DHPC	1,2-Diheptanoyl-sn-glycero-4-phosphocholine	40 mM
Triton-X100	α-[4-(1,1,3,3-Tetramethylbutyl)phenyl]-w-hydroxy-poly(oxy-1,2-ethanediyl)	20 mM
CHAPS	3-[(3-Cholamidopropyl)dimethylammonio]-1-propanesulfonate	40 mM

Table 2.1: List of detergents that were incorporated into pre-crystallization screening by FSEC.

separated by FSEC (Superose 6, 10/300 GL; GE Healthcare) in buffer containing 150 mM KCl; 20 mM Tris, pH 7.5, 1 mM DDM (Kawate and Gouaux, 2006).

For extraction of K_{2P} channels in 'low KCl' conditions, cells were resuspended in 150 µl of 190 mM NaCl; 10 mM KCl; 50 mM Tris, pH 7.5; 1:500 dilution of PI Mix III and detergent (Table 2.1). After protein extraction, samples were separated by FSEC in buffer containing 190 mM NaCl; 10 mM KCl; 20 mM Tris, pH 7.5; 1 mM DDM.

2.2.3. Transformation of expression vectors into *P. pastoris*

DNA (20 µg) was linearized by PmeI digestion (5 µl, New England Biolabs) for 2 hours at 37°C. Afterwards, a sample of digested DNA was separated on a 1% agarose gel to verify linearization. If not fully linearized, additional PmeI (1 µl) was added and the sample was incubated for an additional hour at 37°C. Linearized DNA was purified and concentrated by ethanol precipitation. Sodium acetate, pH 5.5 (1/10 volume) and ethanol (2.5 x volume) were combined with linearized DNA and flash-cooled. DNA was pelleted by centrifugation at 20,000 x g for 1 hour at 4°C and rinsed 4x with cold 70% ethanol. Once dry, the pellet was vigorously resuspended in sterile water (10 µl) for 10 min.

P. pastoris (SMD1163H, a *pep4 prb1* protease deficient, His$^+$ strain; Invitrogen Life Technologies) was inoculated into YPD medium and grown overnight at 30°C with shaking. The next day, the OD_{600} was measured and an amount of cells equivalent to 10 ml of culture at an OD_{600} of 10 was pelleted at 2000 x g for 7 min. The pellet was resuspended in 30 ml of YPD medium, 6 ml of 1 M HEPES, pH 8.0 and 1 ml of 1 M dithiothreitol (DTT) and left to incubate at 30°C without shaking. Cells were pelleted at 2000 x g for 7 min at 4°C and resuspended in 1 M ice-cold sorbitol twice. After this process, the pellet was resuspended in ice-cold sorbitol (0.3 ml).

Competent *P. pastoris* (40 μl) and linearized DNA (20 μg) were combined in a chilled 0.2 cm electroporation cuvette (Bio-Rad) and placed on ice for 5 min. Cells were then pulsed once at 2 kV. Ice-cold sorbitol (1 M, 0.6 ml) was immediately added to the sample and was left to incubate at 30°C for 1 hour without shaking. YPD (0.5 ml) was then added to the sample and the cells were allowed to recover at 30°C for 1 hour with shaking. The cell suspension (0.25 ml) was spread onto YPDS plates containing 1-2 mg/ml of Zeocin (InvivoGen). Colonies grew after 4-6 days at 30°C.

2.2.4. Small- and large-scale growth and expression in *P. pastoris*

Colonies were selected and grown in a 96 well plate in YPD medium with 0.4 mg/ml Zeocin at 30°C for 24-48 hours. Clones were transferred to BMG medium (5 ml) with 0.1 mg/ml Zeocin at 30°C for 24 hours, shaking. Glycerol stocks for each clone were prepared.

For test expression: From a 5 ml BMG culture, cells were pelleted at 2000 x g for 5 min. Pellet was resuspended in 5 ml of BMM medium and expression was induced at 24°C for 24 hours. Cells were pelleted in microcentrifuge tubes at 5000 x g for 8 min, flash-cooled, and a metal ball cooled in liquid N_2 was added to each tube for cell lysis. Samples were stored at -80°C. The original media recipes contained 200 mM K^+, provided by potassium phosphate buffer. For tests of $K_{2P}1$ expression by elevating K^+ concentrations above 200 mM, varying concentrations of KCl (0-1M) were added to the growth (BMG) and induction (BMM) media. For tests of $K_{2P}1$ expression with K^+ concentration below 200 mM, varying concentrations of potassium phosphate (0-200 mM), pH 6.0 were combined with sodium phosphate buffer (0-200 mM), pH 6.0 so that the total concentration of buffer added to the growth and induction media was not altered. For tests of $K_{2P}1$ expression in the presence of $BaCl_2$, cells were initially grown in YPG (variation of YPD without dextrose and with glycerol) media and transferred to YPM (variation of YPD without dextrose and with methanol) in the presence of $BaCl_2$ (1 mM).

For expression in 1 L culture*: P. pastoris* was inoculated (~ 100 µl; glycerol stock) into 40 ml of YPD with 0.1 mg/ml Zeocin and grown for 24 hours at 30°C with shaking. *P. pastoris* cultures (~20 ml; OD_{600} between 10-20) were subsequently inoculated into 1 L of BMG and grown for 24 hours at 30°C with shaking. Cells were pelleted at 2000 x g for 10 min, resuspended in 1 L of BMM and expression was induced at 24°C for 24 hours. Cells were pelleted at 5000 x g for 15 min, flash-cooled and stored at -80°C.

For expression via fermentor: The fermenter vessel with first prepared with sterilized 5 mM $CaSO_4$, 100 mM K_2SO_4, 60 mM $MgSO_4$ and 0.05 g/ml of glycerol, which was followed by the addition of 10 mM $(NH_4)_2SO_4$, 6 mM sodium hexametaphosphate and trace metal salt solution (PTM_1, ~ 4 ml/L). Vessel was inoculated with 4 x 50 ml of cells at an OD_{600} measurement of 20. Cells were grown at 30°C with agitation between 500-800 rpm at pH 5 until the dissolved oxygen spiked, approximately 24 hours later. A 50% glycerol feed (600 ml, 18-22% feed rate), supplemented with PTM_1 (12 ml/L), was started the next day. Culture was incubated at 30°C with agitation between 700-800 rpm at pH 5 until the dissolved oxygen spiked, approximately 24 hours later. The next day, a 100% methanol feed (350 ml, 3 % feel rate for first hour, 7 % feed rate afterwards), supplemented with PTM_1 (12 ml/L) was started. Protein expression was induced at 24°C with agitation between 700-800 rpm at pH 5 for approximately 24 hours. Cells were pelleted at 5000 x g for 15 min, flash-cooled and stored at -80°C.

2.2.5. Mechanical cell lysis of *P. pastoris*

For test expression: Frozen cells (~0.25 g) in microcentrifuge tubes with steel balls were placed in an adaptor rack (Retsch) cooled in liquid N_2. The adaptor rack was placed in a mixer mill (Retsch) and cells were lysed for 1 min at 30 Hz. The adaptor rack was then cooled in liquid N_2 and the grinding step was repeated 3-4x. Lysed cells were stored at -80°C.

For 1 L and fermentor-grown *P. pastoris*: Frozen cells (6-150 g, small to large scale) were added to grinding jars (Retsch) cooled in liquid N_2. Grinding balls (Retsch) were added to the chamber and the jars were cooled for 5-10 min in liquid N_2. Grinding jars were placed in a mixer mill (MM) or planetary ball mill (PM; Retsch) and cells were lysed for 3 min at either 30 Hz (MM) or 400 rpm with 1 min intervals (PM). The grinding jar was then cooled in liquid N_2 for 5-7 min and the grinding step was repeated 4x (MM) or 6-8x (PM). Lysed cells were stored at -80°C.

2.2.6. Human $K_{2P}1$ protein purifications

Purification of EGEEF-tagged protein: Lysed cells were resuspended in buffer (6.3 ml buffer/g cells) containing 150 mM KCl; 10 mM sodium phosphate, pH 7.0; 0.1 mg/ml deoxyribonuclease I (DNAse I); 1:1000 dilution of PI mix III; 1 mM benzamidine (Sigma-Aldrich); and 0.5 mM 4-(2-Aminoethyl) benzenesulfonyl fluoride hydrochloride (AEBSF; Gold Biotechnology). Cell lysate was adjusted to pH 7.0 with 1 N KOH, 0.06 g DDM (Anatrace, solgrade) per 1 g of cells was added to the cell lysate, and the mixture was stirred at room temperature for 45 minutes to extract $K_{2P}1$ from the membranes. The sample was then centrifuged at 30,000 x g for 45 min at 12°C. CNBr-activated Sepharose resin (GE Healthcare) coupled to purified YL1/2 antibody, which recognizes a C-terminal alpha-tubulin epitope, was pre-equilibrated in 150 mM KCl and 10 mM sodium phosphate, pH 7.0 and directly added to filtered supernatant (Kilmartin et al., 1982). The sample was rotated for 1 hour at room temperature. Beads were collected on a column and washed with 5 column volumes of purification buffer: 150 mM KCl; 10 mM sodium phosphate, pH 7.0; and 3 mM DDM. Protein was eluted with buffer containing 150 mM KCl; 100 mM Tris, pH 7.5; 3 mM DDM; and 5 mM Asp-Phe peptide (Sigma-Aldrich) (Wehland et al., 1984). Protein was concentrated to ~ 8 mg/ml using a 50 kDa Amicon Ultra concentrator (Millipore) and further purified on a Superdex 200 gel filtration column (10/300 GL; GE Healthcare) in 150 mM KCl; 20 mM Tris-HCl, pH 7.5; and 5 mM DM (Anatrace, anagrade). A

fraction corresponding to K$_{2P}$1 was collected, protein concentration was measured and if required, the fraction was concentrated to the desired protein concentration using a 50 kDa Vivaspin-2 concentrator (Sartorius Stedim Biotech).

Purification of GFP-fusion protein: Lysed cells were resuspended in buffer (3.3 ml buffer/g cells) containing 150 mM KCl; 30 mM Tris-HCl, pH 8.5; 5 mM imidazole; 0.1 mg/ml DNAse I; 1:1000 dilution of PI mix III; 1 mM benzamidine; and 0.5 mM AEBSF. Cell lysate was adjusted to pH 8.5 with 1 N KOH, 0.05 g DDM (sol grade) per 1 g of cells was added to the cell lysate, and the mixture was stirred at room temperature for 45 minutes to extract K$_{2P}$1 from the membranes. The sample was then centrifuged at 30,000 x g for 45 min at 12°C. Cobalt affinity beads (Talon, BD Science) pre-equilibrated in 150 mM KCl and 30 mM Tris-HCl, pH 8.5 were added directly to filtered supernatent and rotated for 2 hours at room temperature. Beads were collected on a column, washed with 8 column volumes of buffer (150 mM KCl; 30 mM Tris-HCl, pH 8.5; 3 mM DDM, 5-10 mM imidazole) and protein was eluted with buffer containing 150 mM imidazole. PreScission protease (1:50 wt:wt), DTT (1 mM), and EDTA (1 mM) were added to the elution from the cobalt column and the protein was digested overnight at 4°C. The protein was concentrated to ~ 10 mg/ml using a 50 kDa Amicon Ultra concentrator and further purified on a Superdex 200 gel filtration column in 150 mM KCl; 20 mM Tris-HCl, pH 7.5; and detergent (anagrade) (see Table 2.2 for detergent concentrations used for large-scale purification) in the absence or presence of 0.1 mg/ml brain total lipid extract (Avanti Polar Lipids). The fraction corresponding to K$_{2P}$1 was concentrated to 5-13 mg/ml using a 50 kDa Vivaspin-2 concentrator (Sartorius Stedim Biotech), mixed 1:1 with crystallization solution and set up as hanging drops over reservoirs containing 0.1-0.5 ml of well solution in a 96 well or 24 well plate.

Detergent	Purification concentration	Screening concentration
DDM	3 mM	5 mM
DM	5 mM	5 mM
NM	10 mM	--
OM	30 mM	40 mM
OG	--	40 mM
CYMAL-6	5 mM	5 mM
$C_{12}E_8$	--	5 mM
LDAO	--	5 mM
FOS-12	--	5 mM
$C_{10}E_9$	--	5 mM
$C_{10}E_6$	--	5 mM
DHPC	--	5 mM
Triton-X100	--	5 mM
CHAPS	--	20 mM

Table 2.2: List of detergent concentrations used for $K_{2P}1$ purification and subsequent detergent screening concentrations with purified $K_{2P}1$.

2.2.7. Detergent stability experiments with purified protein

DDM-purified $K_{2P}1$ wild-type and C69S proteins were diluted 1:15 into buffer containing 150 mM KCl; 20 mM sodium phosphate, pH 7.5; 20 mM DTT and 1 of 13 detergents (Table 2.2). Samples were rotated for 4 hours at 4°C and separated by gel filtration (Superdex 200 column) equilibrated in buffer containing 150 mM KCl; 20 mM sodium phosphate, pH 7.5; 20 mM DTT and 1 mM DDM. Protein was detected by Trp fluorescence using FSEC.

2.2.8. Crosslinking experiments of $K_{2P}1$ from membranes and with purified protein

Preparation of samples: For detergent-extracted cell lysate, HEK293-GT cells (10 cm dish) were transiently transfected with human $K_{2P}1$ pNGFP-EU (10 μg/dish) using Lipofectamine 2000 (20 μl/dish). After 48 hours, cell were rinsed with chilled PBS and harvested by suspension in 1 ml of chilled PBS. Cells were divided into 2 individual samples (+/- DTT), pelleted by centrifugation at 1,000 x g for 5 min at 4°C and resuspended in 150 μL of buffer containing 190 mM NaCl; 10 mM KCl; 50 mM sodium phosphate, pH 7.5; 1:500 dilution of PI Mix III and 40 mM DDM with or without 20 mM DTT. Samples were solubilized by rotating at 4°C for 1 hour and detergent-insoluble cell debris was pelleted by centrifugation at 20,000 x g for 1 hour at 4°C. The soluble fraction (supernatent) was collected (100 μL) and separated by FSEC (Superose 6) in buffer containing 150 mM KCl; 20 mM sodium phosphate, pH 7.5; 1 mM DDM with or without 20 mM DTT (Kawate and Gouaux, 2006). The peak fraction for each sample was collected and diluted 1:10 in FSEC buffer for the crosslinking experiment.

For preparation of membrane fractions, HEK293-GT cells (10 cm dish) were transiently transfected with human $K_{2P}1$ wild-type, C69S mutant, or *C. elegans* $K_{2P}1$ pcDNA3.1$^+$ (10 μg/well), all with an EGEEF tag using Lipofectamine 2000 (20 μl/dish). After 48 hours, cell were rinsed with chilled PBS and harvested by suspension in 8 ml of membrane prep buffer: 150 mM KCl; 50 mM sodium phosphate, pH 7.5; and 1:500 dilution of PI Mix III. Sample was

split in half (4 ml x 2) and cells were sheared with a Dounce homogenizer (4x), followed by a brief sonication for 30 seconds. Cell debris was pelleted from sample by centrifugation at 2,500 x g for 10 min at 4°C and the supernatant was collected. This step was performed 3x. Cell membranes were then pelleted by ultracentrifugation at 100,000 x g for 1 hour at 4°C. Membrane prep buffer (500 μl) was added to the cell membrane pellet and the pellet was resuspended with a Dounce homogenizer (4x). Sample was diluted 1:2 in membrane prep buffer prior to crosslinking experiment.

Crosslinking with disuccinimidyl suberate (DSS): DSS (25 mM) was prepared in DMSO and four concentrations of DSS ranging from 25 μl - 2.5 mM were added to samples of interest. For purified protein (15-20 μg), only one concentration of DSS (2.5 mM) was tested due to the limited amount of sample. Samples were incubated with DSS for 30 minutes at room temperature. Tris, pH 7.5 (~30 mM) was then added to quench the reaction and the sample was incubated for an additional 15 minutes at room temperature. Samples were then diluted into NuPAGE LDS sample buffer (2x final concentration, Invitrogen) containing 250 mM DTT.

2.2.9. Test for glycosylation of human $K_{2P}1$

DDM-purified human $K_{2P}1$ (~ 1 mg/ml, 10 μl) was diluted into buffer containing 150 mM KCl; 20 mM sodium phosphate, pH 7.5; 3 mM DDM and incubated in the presence or absence of PNGase F (1 μl, 500 units/μl; New England Biolabs) and 50 mM sodium phosphate, pH 7.5 for 1 hour at 37°C. A sample of RNAse B (10 μg) in the presence or absence of PNGase F was also included as controls. Samples were quenched with dilution into NuPAGE LDS sample buffer (2x final concentration) containing 250 mM DTT.

2.2.10. Limited proteolysis experiments

Subtilisin limited proteolysis: Eight serial dilutions of subtilisin (Sigma-Aldrich) ranging from 4-

500 ng/µl were prepared in buffer containing: 150 mM KCl; 20 mM sodium phosphate, pH 7.5; 3 mM DDM; and 5 mM DTT. Dilutions of subtilicin (1 µl) were incubated with purified human $K_{2P}1$ N95Q ($\sim$ 1.25 mg/ml, 50 µl) for 40 min at room temperature. Reactions were quenched with 8.4 mM AEBSF for 10 min at room temperature and diluted into NuPAGE LDS sample buffer (2x final concentration) containing 250 mM DTT.

Limited proteolysis experiment with panel of proteases: A panel of eight proteases were evaluated (Table 2.3; Sigma-Aldrich). Proteases were diluted into buffer containing: 150 mM KCl; 20 mM Tris, pH 7.5; 5 mM DM; and 0.05 mg/ml synthetic phospholipid blend (60:20:20 wt% POPC:POPE:POPG; Avanti Polar Lipids). For subtilisin protease treatment, purified subtilisin was coupled to CNBr-activated Sepharose resin prior to use. Dilutions of each protease were incubated with purified human K_{2P} N95Q (60 µg) for 90 min at room temperature (Table 2.3). All reactions, except for Arg-C and subtilisin resin, were quenched with 14 mM AEBSF for 10 min at room temperature. PI mix III (1 µl) was added to quench each Arg-C protease sample. For subtilisin cleavage, resin was first removed and then the reaction was quenched with 14 mM AEBSF. Samples were then diluted into NuPAGE LDS sample buffer (2x final concentration) containing 250 mM DTT.

2.2.11. SDS-PAGE and Western blot

Samples were separated by SDS-PAGE using either 12% NuPAGE precast gels (Invitrogen) or 12% Tris-tricine gels (Schagger, 2006). For NuPAGE gels, SDS-PAGE samples were separated at 120-150 V, for 60-80 min. For Tris-tricine gels, SDS-PAGE samples were separated at 50 V for 30 min (stacking gel), then at 120 V for 60-75 min (separating gel). Gels were stained with Coomassie brilliant blue (1%; Sigma-Aldrich), prepared in solution containing 40% methanol and 7% acetic acid, and subsequently destained in the same solution without dye.

Protease	Concentration range (ng/µl)	Number of dilutions
Asp-N	0.4 - 3.6	3
Lys-C	0.5 - 7.5	3
Glu-C	0.5 - 7.5	3
Arg-C	0.5 - 7.5	3
Thrombin	10 - 90	3
Trypsin	0.2 - 20	5
Chymotrypsin	0.2 - 20	5
Subtilisin resin	0.2 - 4	5

Table 2.3: List of proteases and concentrations used for limited proteolysis experiment.

For western blots, samples were transferred to a PVDF membrane using a semi-dry transfer apparatus (BioRad). Transfer buffer contained: 192 mM glycine; 25 mM tris base; 25% methanol and 0.3% sodium dodecyl sulfate (SDS). PVDF membranes were soaked in 100% methanol for 30 seconds and subsequently rinsed with transfer buffer prior to setting up the transfer. Samples were transferred at 20 V for 40 min. The PVDF membrane was blocked for 1 hour at room temperature in TBS-T buffer (tris-buffered saline with 0.1% Tween 20) supplemented with 5% milk powder (TBS-T/block). The blot was incubated with rat YL1/2 primary antibody at a 1:10,000 dilution in TBS-T/block for 1 hour at room temperature. The membrane was rinsed 5x with TBS-T/block and incubated with HRP-goat anti-rat secondary antibody (Invitrogen) at 1:20,000 dilution in TBS-T/block for 1 hour at room temperature. The blot was rinsed 1x with TBS-T/block, 1x with TBS-T and 5x with TBS (no Tween 20). The membrane was developed with Immobilon Western Chemiluminescent HRP substrate (Millipore).

2.3. Results

2.3.1. Pre-crystallization screening of K_{2P} channels

My initial strategy was to identify stable, well-expressed human K_{2P} channel paralogs that were ideal candidates for purification and crystallization. Protein behavior was assessed by fluorescence-detection size-exclusion chromatography (FSEC), a pre-crystallization screening technique that utilizes GFP-fusion proteins to detect nanogram quantities of protein from cell lysate (Kawate and Gouaux, 2006). I generated N- and C-terminal GFP-fusion constructs for 14 of the 15 known human K_{2P} paralogs (Table 1.2). These constructs were expressed in HEK293-GT cells, and extracted in buffer containing 40 mM DDM. The soluble fraction was separated by FSEC to determine appropriate protein size (elution time), relative expression levels (fluorescence intensity) and monodispersity or stability (peak shape). From my initial screening, four candidates stood out as well-expressing and monodisperse: human $K_{2P}1$, $K_{2P}6$, $K_{2P}13$ and $K_{2P}17$ (Figure 2.2). I further evaluated stability by solubilizing the four candidates in a panel of
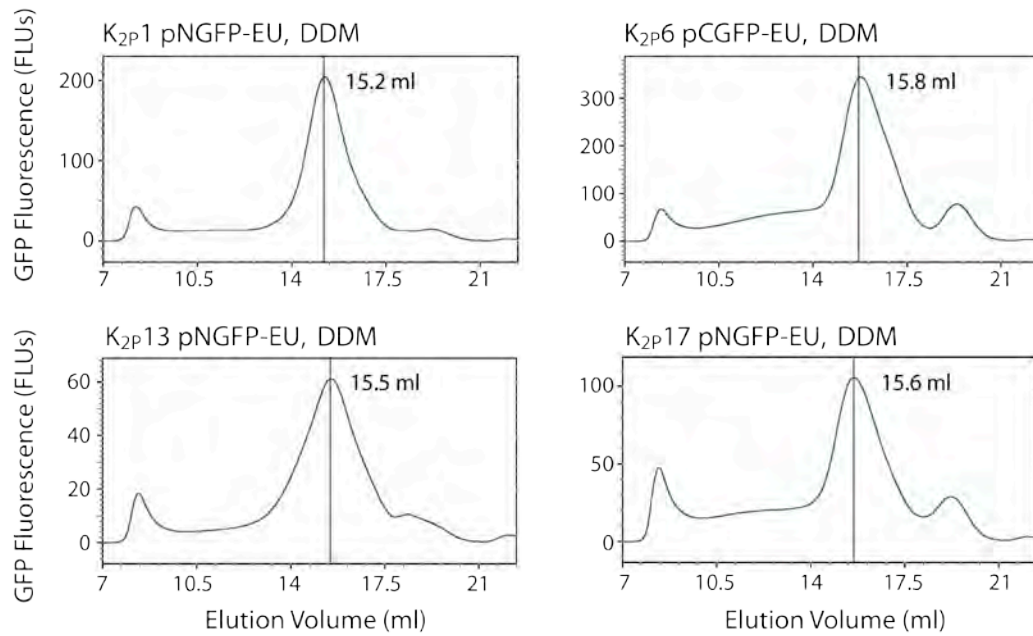
Figure 2.2: FSEC elution profiles for DDM-solubilized human $K_{2P}1$, K_{2P} 6, K_{2P} 13 and $K_{2P}17$ N-terminal (pNGFP-EU) or C-terminal (pCGFP-EU) GFP-fusion constructs expressed for 48 hours in HEK293-GT cells (Superose 6).
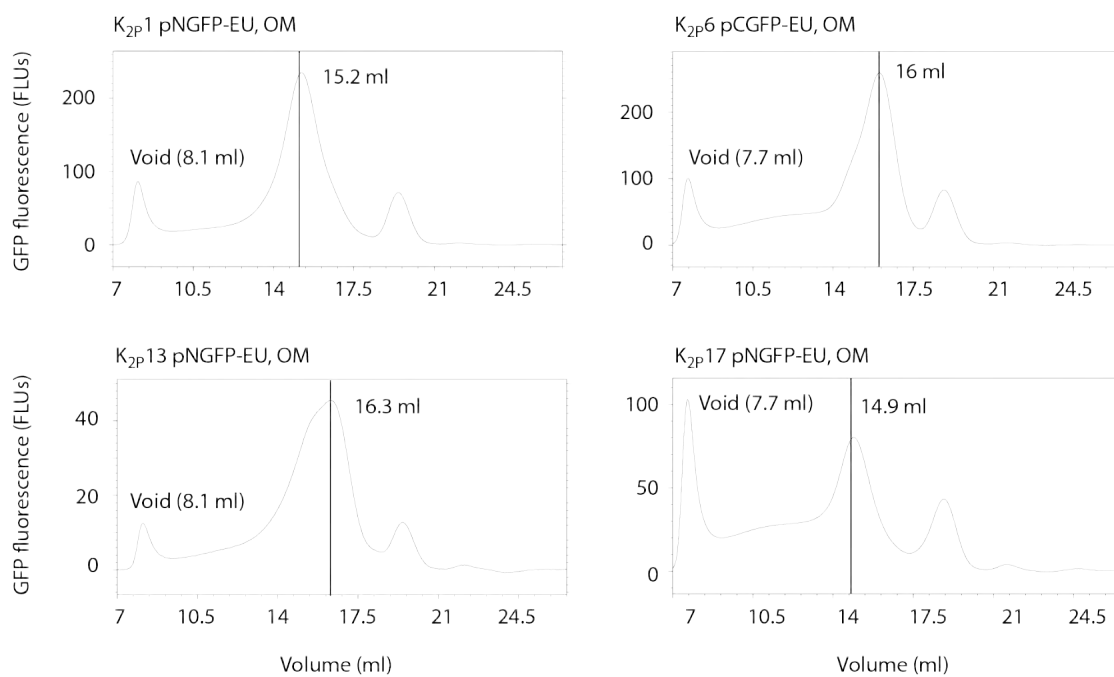
Figure 2.3: FSEC elution profiles for OM-solubilized human $K_{2P}1$, $K_{2P}6$, $K_{2P}13$ and $K_{2P}17$ N-terminal (pNGFP-EU) or C-terminal (pCGFP-EU) GFP-fusion constructs expressed for 48 hours in HEK293-GT cells (Superose 6).

13 detergents with varying hydrophilic head group moieties and alkyl chain length (Table 2.1). Human $K_{2P}1$ stood out from the detergent screening as the best candidate for purification and crystallization (Figure 2.3).

In an effort to identify other potential candidates, I screened 12 $K_{2P}1$ orthologs (Table 2.4). Similar to the human K_{2P} paralogs, the $K_{2P}1$ orthologs were cloned as N- and C-terminal GFP fusion proteins. Many of these clones, after extraction in DDM, appeared to have similar or less symmetrical elution profiles to human $K_{2P}1$. One of the orthologs screened was *Caenorhabditis elegans* $K_{2P}1$, which separates as a monodisperse, Gaussian peak by gel filtration, but unlike the other $K_{2P}1$ constructs tested, eluted at later volume (Figure 2.4). These results led us the question the oligomeric state of the detergent-extracted $K_{2P}1$.

2.3.2. Oligomeric state of human $K_{2P}1$

In order to evaluate the oligomeric state of $K_{2P}1$, I performed crosslinking experiments with both EGEEF-tagged human and *C. elegans* $K_{2P}1$ from detergent-extracted cell lysate and from membrane preparations of overexpressed $K_{2P}1$ in HEK293-GT cells. Crosslinking experiments were evaluated by YL1/2 western blot. Efforts to evaluate the $K_{2P}1$ oligomeric state from these sample preparations by western blot proved challenging since the YL1/2 antibody displayed cross-reactivity with other HEK293-expressed proteins.

Since both human and *C. elegans* $K_{2P}1$ were good candidates for purification and crystallization, I chose to express and purify these orthologs from *P. pastoris* in order to determine their expression level and monodispersity as well as to evaluate their oligomeric state(s) without the need for detection using an antibody. Large-scale purification of these two proteins was performed using a two-step protocol. After DDM extraction of $K_{2P}1$ from the membrane, the

K_{2P}1 Orthologs Cloned

Bos taurus	Cow
Caenorhabditis elegans	Roundworm
Cavia porcellus	Guinea Pig
Danio rerio	Zebrafish (x2)
Gallus gallus	Chicken
Mus musculus	Mouse
Oryctolagus cuniculus	Rabbit
Rattus norvegicus	Rat
Sus scrofa	Pig
Xeonpus laevis	African Clawed Frog (x2)

Table 2.4: List of $K_{2P}1$ orthologs cloned and screened by FSEC. Both *D. rerio* and *X. laevis* had 2 variants of $K_{2P}1$ annontated (x2), which were both cloned and tested.
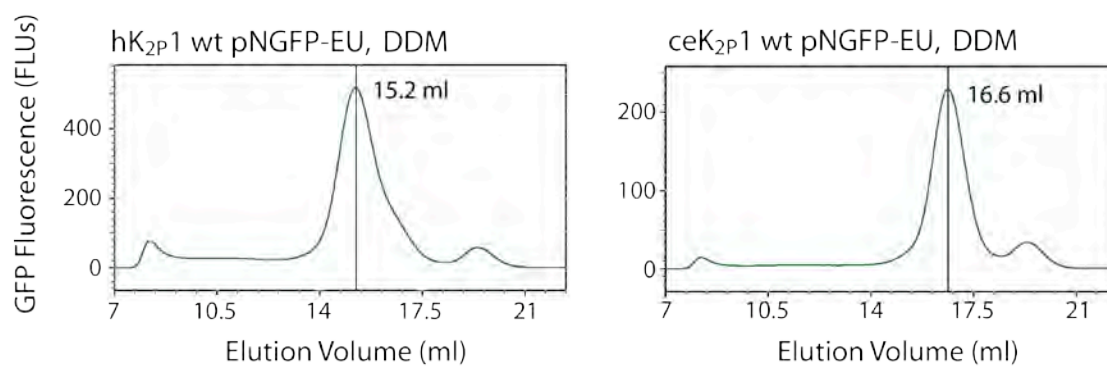
Figure 2.4: FSEC elution profiles for DDM-solubilzed human and *C. elegans* K$_{2P}$1 N-terminal (pNGFP-EU) GFP-fusion constructs expressed for 48 hours in HEK293-GT cells (Superose 6).

channel was initially purified using YL1/2 antibody affinity chromatography, followed by gel filtration chromatography (Figure 2.4). Reflecting what was observed by FSEC, human $K_{2P}1$ eluted at an earlier volume than *C. elegans* $K_{2P}1$, suggesting that the purified proteins had different oligomeric states. To evaluate the oligomeric state of the samples, crosslinking experiments were performed with the $K_{2P}1$ peak fraction from gel filtration. Disuccinimidyl suberate (DSS) was chosen as a suitable crosslinker since it is membrane permeable and may be able to access lysines located near the detergent interface. Human $K_{2P}1$ crosslinked as a dimer in the presence of DSS (10 mg/ml), whereas the DSS-treated *C. elegans* ortholog migrated as a monomer, as evaluated by SDS-PAGE (Figure 2.5). From these results, we chose to pursue the human $K_{2P}1$ ortholog since K_{2P} channels most likely assemble as dimers, as suggested by K_{2P} channel sequences containing two P domains and by published K_{2P} experimental data (Lesage et al., 1996b; Maingret et al., 2000a; Patel et al., 2000).

2.3.3. An intermolecular disulfide bridge stabilize human $K_{2P}1$

Cysteine 69 (C69), located within the extracellular domain of human $K_{2P}1$, has been reported to form an intermolecular disulfide bridge between two $K_{2P}1$ monomers (Lesage et al., 1996b). To assess whether C69 is important for assembly or stability, a human $K_{2P}1$ C69S mutant was generated for screening by FSEC (N-terminal GFP fusion construct), as well as for large-scale expression in *P. pastoris* (construct with an EGEEF epitope). For FSEC screening, both wild-type and C69S $K_{2P}1$ channels were expressed in HEK293-GT cells and extracted in DDM. Both the wild-type and C69S mutant elute at the same volume by FSEC, suggesting that the mutation did not alter the oligomeric state of the channel (Figure 2.6). Likewise, large-scale purification of the $K_{2P}1$ C69S mutant in DDM (3 mM) yielded protein that eluted at a similar volume to the wild-type channel by gel filtration. When subjected to DSS treatment, $K_{2P}1$ C69S crosslinked as a dimer as evaluated by SDS-PAGE (Figure 2.5). These results demonstrate that that $K_{2P}1$ C69 is not essential for channel assembly.
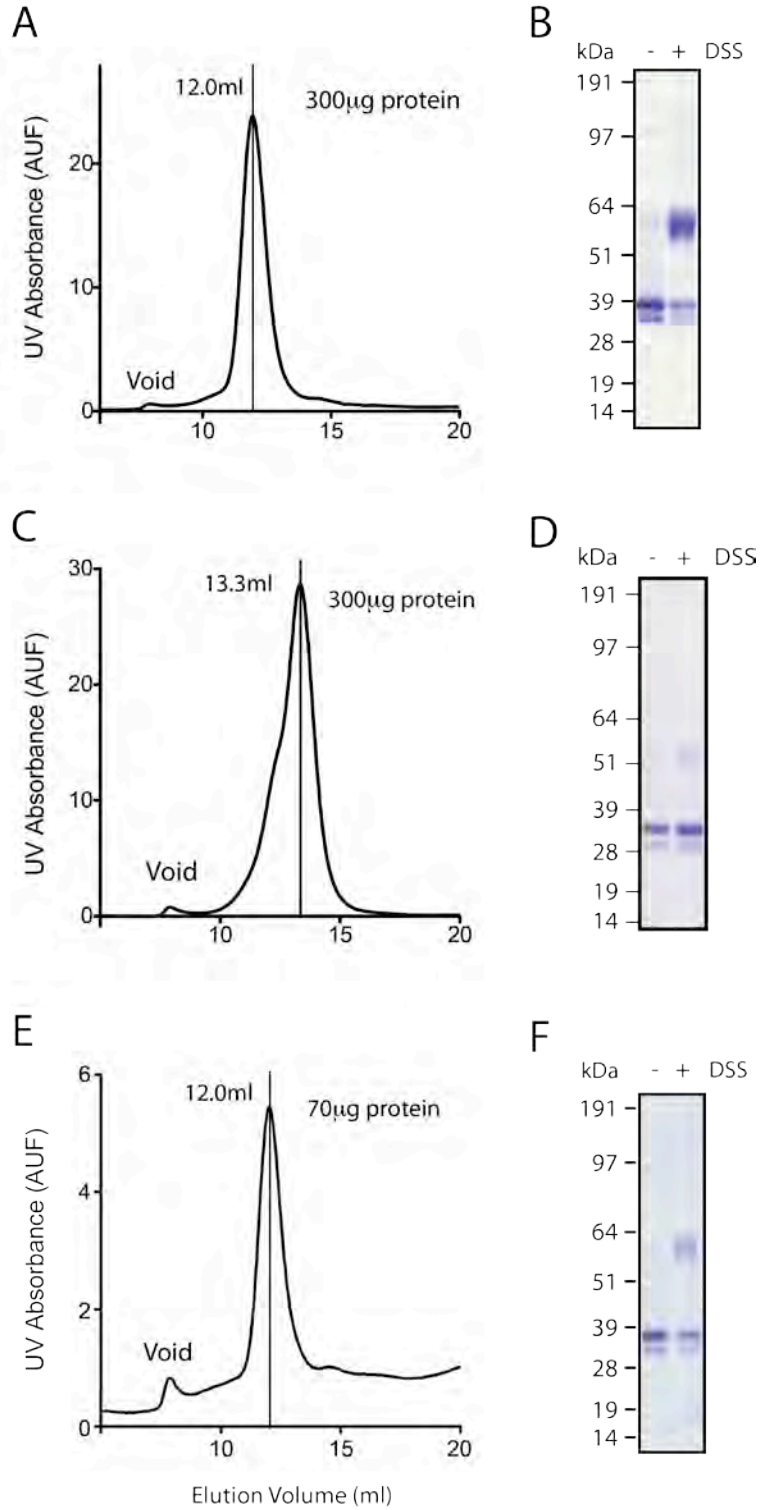
Figure 2.5: Oligomeric state of purified human K$_{2P}$1 (A, B), *C. elegans* K$_{2P}$1 (C, D), and human K$_{2P}$1 C69S mutant (E, F). Purified protein collected from gel filtration (A, C, E) was subjected to DSS treatment (+ DSS) and separated by SDS-PAGE (B, D, F) to evaluate the oligomeric state of the channel.
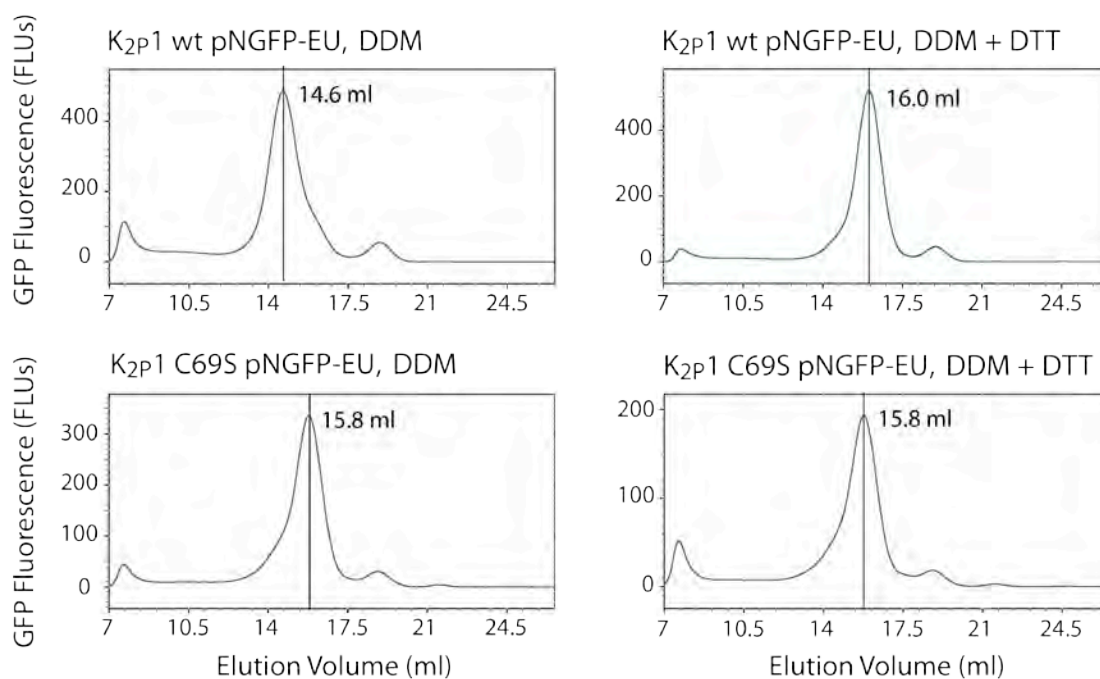
Figure 2.6: FSEC elution profiles for DDM-solubilzed human K$_{2P}$1 wild-type (wt) and C69S mutant N-terminal (pNGFP-EU) GFP-fusion constructs expressed for 48 hours in HEK293-GT cells (Superose 6). Samples were solubilized in buffer containing 10 mM KCl ('low KCl' condition) in the absence or presence of DTT (20 mM).

Inspection of the FSEC elution profiles of the $K_{2P}1$ wild-type and C69S mutant, however, suggested that the C69S mutant may be slightly less stable, with a broader shoulder to the right of the $K_{2P}1$ peak. This small discrepancy was exacerbated with extraction of $K_{2P}1$ in 'low KCl' conditions (10 mM KCl) since K^+ coordination to the selectivity filter stabilizes K^+ channels. Whereas wild-type $K_{2P}1$ eluted at 14.6 ml, the $K_{2P}1$ C69S mutant eluted at 15.8 ml, suggesting that the DDM-solubilized C69S mutant was in a different oligomeric state to the wild-type channel (Figure 2.6). Similar results were also observed with extraction of wild-type $K_{2P}1$ in the presence of 20 mM DTT in low KCl conditions. Furthermore, the elution volume of DTT-treated $K_{2P}1$ was similar to monomeric *C. elegans* $K_{2P}1$ in the absence or presence of DTT (Figure 2.4). Although $K_{2P}1$ C69 is not necessary for channel dimerization, this residue appears to be important for $K_{2P}1$ channel stability in detergent micelles.

2.3.4. N-linked glycosylation of human $K_{2P}1$

Both purified EGEEF-tagged wild-type human and *C. elegans* $K_{2P}1$ separate as two distinct molecular weight bands by SDS-PAGE, indicating that the channel is either proteolytically cleaved or post-translationally modified (Figure 2.5, Figure 2.7). $K_{2P}1$ proteolytic cleavage was evaluated by both YL1/2 western blot, which recognizes the C-terminal EGEEF tag, and Edman degradation. The two bands were detectable by western blot for both orthologs, and N-terminal peptide sequencing of the two bands indicated that both protein populations contained the same N-termini. It was evident from these results that $K_{2P}1$ must be post-translationally modified.

A search of the human $K_{2P}1$ sequence for known post-translational consensus motifs revealed one putative glycosylation and three phosphorylation sites (Lesage et al., 1996a; Lesage et al., 1996b). Since there was experimental evidence in the literature to support $K_{2P}1$ glycosylation at residue asparagine 95 (N95), $K_{2P}1$ glycosylation was evaluated by two methods: by addition of N-glycosidase F (PNGase F) to purified protein and by generation of a glutamine mutant (N95Q).
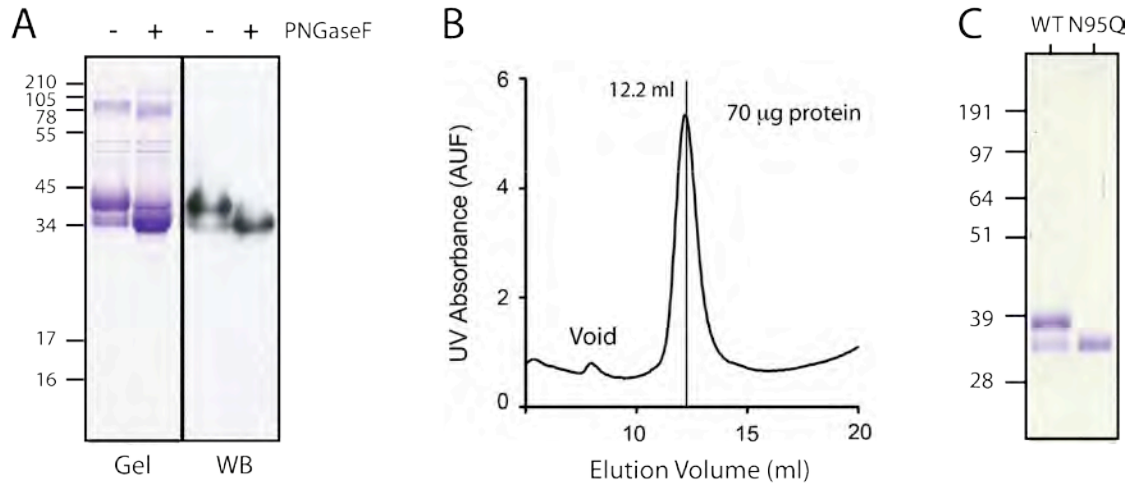
Figure 2.7: Human $K_{2P}1$ is glycosylated. (A) Separation of DDM-purified human $K_{2P}1$-EGEEF in the absence (-) or presence (+) of PNGaseF by SDS-PAGE, detected by coomassie staining and Y/L 1/2 western blot. (B) Gel filtration profile of DDM-purified human $K_{2P}1$ N95Q. (C) Separation of DDM-purified human $K_{2P}1$ (wt) and human $K_{2P}1$ N95Q (N95Q).

PNGase F is an amidase isolated from *Flavobacterium meningosepticum* that cleaves between N-acetylglucosamine and the asparagine side chain. Purified human $K_{2P}1$ was incubated with PNGase F, separated by SDS-PAGE and evaluated by both Coomassie staining and western blot with YL1/2 antibody since PNGase F separates at the same molecular weight as the $K_{2P}1$ higher molecular weight band (Figure 2.7). The $K_{2P}1$ higher molecular weight band is not present in the PNGase F-treated sample. In addition, the lower molecular weight band is much more predominant in the PNGase F-treated sample compared to the control sample, suggesting that the $K_{2P}1$ channel population corresponding to the upper molecular weight band is glycosylated.

These results were corroborated with a $K_{2P}1$ N95Q glycosylation mutant. Purified $K_{2P}1$ N95Q separate as one band by SDS-PAGE that corresponds with the $K_{2P}1$ wild-type lower molecular weight band (Figure 2.7). In addition, the SEC elution volume of $K_{2P}1$ N95Q shifted 0.2 ml to the right compared to both $K_{2P}1$ wild-type and C69S mutant, suggesting that the N95Q mutant has a smaller hydrodynamic radius due to the absence of the N-glycan. These data collectively demonstrate that $K_{2P}1$ N95 is glycosylated. Since heterogeneous glycosylation of $K_{2P}1$ is likely to be unfavorable for protein crystal growth, all subsequent constructs that were cloned and purified contained the N95Q mutation.

2.3.5. Identifying a structured 'core' of human $K_{2P}1$ by limited proteolysis

One strategy to promote protein crystallization is to identify a 'core,' or structured, unit of human $K_{2P}1$. I performed limited proteolysis of purified human $K_{2P}1$ N95Q with subtilisin (0-500 ng/μl), a non-specific protease, in order to survey the channel for a region(s) that is more susceptible to proteolytic cleavage, and thus less-structured. Protease-cleaved fragments were separated by SDS-PAGE and the gel was stained with Coomassie dye. Protein bands were excised from the gel (see Figure 2.8), digested with trypsin and analyzed by mass spectrometry by the MSKCC Proteomics Core Facility to map the site(s) of subtilisin cleavage (Figure 2.8). The peptides that
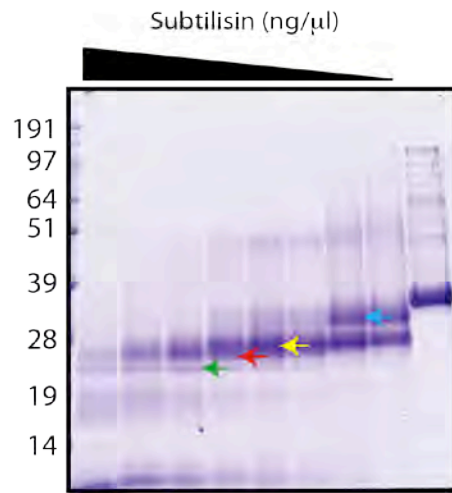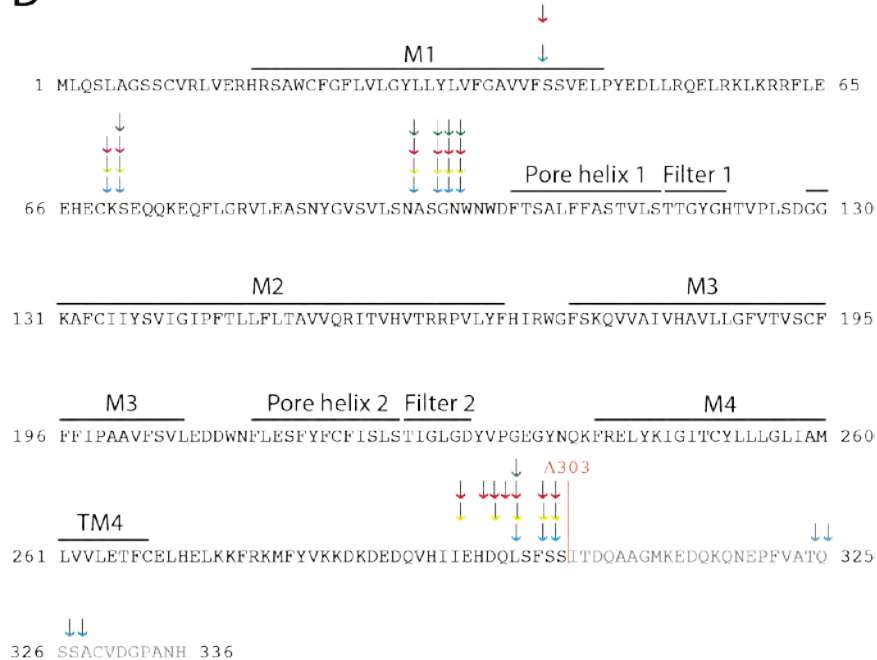
Figure 2.8: Subtilisin limited proteolysis (4-500 ng/µl) of DDM-purified human $K_{2P}1$ N95Q. (A) Coomassie-stained gel of human $K_{2P}1$ N95Q cleavage products from subtilisin limited proteolysis experiment. Four bands (blue, yellow, red and green arrows) were isolated for mass spectroscopy analysis. (B) Mapping of subtilisin cleavage sites identified by mass spectroscopy on the primary structure of human $K_{2P}1$ N95Q with transmembrane helices (M1-4), pore helices (Pore helix 1 and 2) and selectivity filter sequences (Filter 1 and 2) highlighted. Arrow colors denote the cleavage products identified for each band isolated in (A). The C-terminal deletion construct generated from these results is highlighted in orange (Δ303).

were identified by mass spectrometry were mapped onto the $K_{2P}1$ sequence (~ 35% coverage overall). Peptides that contained trypsin cleavage sites on both the N and C termini (tryptic peptides) were discarded, whereas peptides containing a non-specific cleavage site (subtilisin) were identified. Mass spectrometry results indicate that there are approximately three predominant peptides, or protease 'hot-spots' within human $K_{2P}1$: two are located within the $K_{2P}1$ extracellular 'loop' and the other at the C-terminus (Figure 2.8). An alignment of K_{2P} channels demonstrates that the C-terminus is not conserved, and no secondary structure is predicted in this region (Figure 2.9). From these results, a deletion construct that lacks a portion of the C-terminus, $\Delta 303$, was cloned and screened by FSEC. DDM-extracted human $K_{2P}1$ $\Delta 303$ has a Gaussian-like distribution similar to what was observed with wild-type $K_{2P}1$. From these results, a human $K_{2P}1$ $\Delta 303$ construct was generated in the N95Q mutant background for purification and crystallization.

2.3.6. Human $K_{2P}1$ N95Q $\Delta 303$ forms a higher-ordered oligomer via a non-specific disulfide linkage

Large-scale purification of DDM-purified $K_{2P}1$ N95Q $\Delta 303$ initially yielded protein that exhibited a monodisperse peak by SEC (Figure 2.10). However, the purified protein aggregated as a second population of higher molecular weight over time (Figure 2.10). This effect was exacerbated during purification of $K_{2P}1$ N95Q $\Delta 303$ in the shorter-chain detergent, DM, where the earlier protein population was observed during the purification by gel filtration. Interestingly, DM purification of $K_{2P}1$ N95Q $\Delta 303$ in the presence of 5 mM DTT appeared to reduce the size of gel filtration peak associated with the higher molecule weight population. These results were not observed during detergent screening of DDM-purified $K_{2P}1$ N95Q $\Delta 303$ by FSEC (Trp fluorescence) most likely because the purified channel had to be diluted (15-fold) for this experiment. This dilution was necessary to reduce the DDM concentration in the protein sample to below the critical micelle concentration (CMC) for detergent screening. From these results, it

P domain 1 =>

M1

outer helix 1

```
K2P1_(TWIK-1)   1  ------------------------------MLQSLAGSS-----CVRLVERHRSAWCF----GFL-VLGYLLYLVFGAVVFSSVELPYED  50
K2P6_(TWIK-2)   1  ---------------------------------------MRRGAL------LAGALAAYAAYLVLGALLVARLEGPREA  34
K2P7            1  ------------------------------------MGGLRPW----SRYGLL-VVAHLLALGLGAVVFQALEGPPAC  37
K2P2_(TREK-1)   1  ------------------MAAPDLLDPKSAAQNSKPRLSFSTKPTVL-ASRVESDTTINVMKW----KTVSTI-FLVVVLYLIIGATVFKALEQPHEI  74
K2P4_(TRAAK)    1  ---------------MTTAPQEPPARPLQAGSGAGPAPGRA---MRSTTL----LAL-LALVLLYLVSGALVFRALEQPHEQ  59
K2P10_(TREK-2)  1  MFFLYTDFFLSLVAVPAAAPVCQPKSATNGQPPAPAPTPRLSISSRATVVAR-MEGTSQGCLQTVMKW----KTVVAI-FVVVVVYLVTGGLVFRALEQPFES  99
K2P3_(TASK-1)   1  ---------------------------------------MKRQNVRT----LAL-IVCTFTYLLVGAAVFDALESEPEL  35
K2P9_(TASK-3)   1  ---------------------------------------MKRQNVRT----LSL-IVCTFTYLLVGAAVFDALESDHEM  35
K2P15_(TASK-5)  1  ---------------------------------------MRRPSVRA----AGL-VLCTLCYLLVGAAVFDALESEAES  35
K2P12_(THIK-2)  1  -----------------MSSRSPRPPPRRSRRRLPRPS-CCCCCCRRSHLNEDT-GRFVLL-AALIGLYLVAGATVFSALESPGEA  66
K2P13_(THIK-1)  1  ----------------------MAGRGFSWGP-----GHLNEDNARF----LLL-AALIVLYLLGGAAVFSALELAHER  47
K2P5_(TASK-2)   1  ---------------------------------------MVDRGP------LLT--SAIIFYLAIGAAIFEVLEEPHWK  32
K2P16_(TALK-1)  1  -----------------------------------MPSAGLCSCWG--GRVLPL-LLAYVCYLLLGATIFQLLERQAEA  41
K2P17_(TALK-2)  1  --------------------------------MYRP-RARAAPEGRVRGCAV----PSTVLL-LLAYLAYLALGTGVFWTLEGRAAQ  49
K2P18_(TRESK)   1  -------------------------------MEVSGHPQ--ARRCCPEALGKLFP----GLCFLCFLVTYALVGAVVFSAIEDGQVL  50
Kv1.2_1         1  -----------------------------------KGLQILGQTLKAS--MRELGLLIFFLFIGVILFSSAVYFAEADERD  44
KcsA            1  --------------------------MAPMLSGLLARLVKLLLGRHGSALHWRAAGAATVLLVIVLLAGSYLAVLAERGAPG  56
KIR2.2          1  ----------------------------------MFTTCVDIRWRYMLLLFSLAFLVSWLLFGLIFWLIALIHG  40
Kv1.2_2            ---------------------------------------------------------------------------------
```

E1   E2   Pore helix 1   M2

extracellular domain

filter

inner helix 1

* * ** *

```
K2P1_(TWIK-1)   51  LLRQE-LRKLKRRFLEEH-ECLSEQQLEQFLGRVLEASNYGVSVLSNASGNWN----WDFTSALFFASTVLSTTGYGH--TVPLSDGGKAFCIIYSVIGIPFTLLFLTA  151
K2P6_(TWIK-2)   35  RLRAE-LETLRAQLLQRS-PCVAAPALDAFVERVLAAGRLGRVVLANASGSANASDPAWDFASALFFASTLITTVGYGY--TTPLTDAGKAFSIAFALLGVPTTMLLLTA  140
K2P7            38  RLQAE-LRAELAAFQAEHRACLPPGALEELLGTALATQAHGVSTLGNSSEGRT-WDLPSALLFAASILTTTGYGH--MAPLSPGGKAFCMVYAALGLPASLALVAT  139
K2P2_(TREK-1)   75  SQRTT-IVIQKQTFISQH-SCVNSTELDELIQQIVAAINAGIIPLGNTSNQISH---WDLGSAFFFAGTVITTIGFGN--ISPRTEGGKIFCIIYALLGIPLFGFLLAG  176
K2P4_(TRAAK)    60  QAQRE-LGEVREKFLRAH-PCVSDQELGLLIKEVADALGGADPETNSTSNSSHS-AWDLGSAFFFAGTIITTIGYGN--VALRTDAGRLFCIIYALLGIPLFGFLLAG  163
K2P10_(TREK-2)  100 SQKNT-IALEKAEFLRDH-VCVSPQELETLIQHALDADNAGVSPICNSSNNSSH-AWDLGSAFFFAGTIITTIGYGN--IAPSTEGGKIFCILYAIFGIPLFGFLLAG  201
K2P3_(TASK-1)   36  IERQR-LELRQQELRARY-NLSQGGYEELERVVLRLKPHKAGVQ----WRFAGSFYFAITVITTIGYGH--AAPSTDGGKVFCMFYALLGIPLTLVMFQS  127
K2P9_(TASK-3)   36  REEEK-LKAEEIRIKGKY-NISSEDYRQLEVILQSEPHRAGVQ----WKFAGSFYFAITVITTIGYGH--AAPGTDAGKAFCMFYAVLGIPLTLVMFQS  127
K2P15_(TASK-5)  36  GRQRL-LVQKRGALRRKF-GFSAEDYRELERLALQAEPHRAGRQ----WKFPGSFYFAITVITTIGYGH--AAPGTDSGKVFCMFYALLGIPLTLVTFQS  127
K2P12_(THIK-2)  67  EARAR-WGATLRNFSAAH-GVAEPELRAFLRHYEAALAAGVRADALRPR----WDFPGAFYFVGTVVSTIGFGM--TTPATVGGKAFLIAYGLFGCAGTILFFNL  163
K2P13_(THIK-1)  48  QAKQR-WEERLANFSRGH-NLSRDELRGFLRHYEEATRAGIRVDNVRPR----WDFTGAFYFVGTVISTIGFGM--ITPATVGGKIFLIFYGLFGCPLCLTWISA  144
K2P5_(TASK-2)   33  EAKKN-YYTQKLHLLKEF-PCLGQEGLDKILEVVSDAAGQGVAITGNQTFNN---WNWPNAMIFAATVITTIGYGN--VAPKTPAGRLFCVFYGLFGVPLCLTWISA  132
K2P16_(TALK-1)  42  QSRDQ-FQLEKLRFLENY-TCLDQWAMEQFVQVIMEAWVKGVNPKGNSTNPSN---WDFGSSFFFAGTVITTIGYGN--LAPSTEAGQVFCVYALLGIPLNVIFLNH  142
K2P17_(TALK-2)  50  DSSRS-FQRDKWELLQNF-TCLDRPALDSLIRDVVQAYKGASLLSNTTSMGR---WELVGSFFFSVSTITTIGYGN--LSPNTMAARLFCIFFALVGIPLNLVVLNR  150
K2P18_(TRESK)   51  VAADD---GEFEKFLEEL--CRILNCSETVVEDRKQDLQGHLQKVKPQWFNRTTH-WSFLSSLFFCCTVFSTVGYGY--IYPVTRLGKYLCMLYALFGIPLMFLVLTD  150
Kv1.2_1         45  SQF----PSIPDAFWWAVVSMTTVGYGD--MVPTTIGGKIVGSLCAIAGVLTIALPVPV  97
KcsA            57  AQL----ITYPRALWWSVETATTVGYGD--LYPVTLWGRCVAVVVMVAGITSFGLVTAA  109
KIR2.2          41  DLENPG----GDDTFKPCVLQV-NGFVAAFLFSIETQTTIGYGFRCVTEECPLAVFMVVVQSIVGCIIDSFMIGA  110
Kv1.2_2            ---------------------------------------------------------------------------------
```

P domain 2 =>

M2   M3

inner helix 1 cont.

K2P1 (TWIK-1)	152 VVQRITVHVT----RRPVLYFHI-------RWGFSKQV---V	179
K2P6 (TWIK-2)	141 SAQRLSLLLT-----HVPLSWLSM-------RWGWDPRR---A	168
K2P7	140 LRHCLLPVLS-----RPRAWVAV-------HWQLSPAR---A	166
K2P2 (TREK-1)	177 VGDQLGTIFG--KGIAKVEDTFI-------KWNVSQTK---I	206
K2P4 (TRAAK)	164 VGDRLGSSLR--HGIGHIEAIFL-------KWHVPPEL---V	193
K2P10 (TREK-2)	202 IGDQLGTIFG----KSIARVEKVFR-------KKQVSQTK---I	231
K2P3 (TASK-1)	128 LGERINTLVR-----YLLHRAKK-------GLGMRRAD---V	154
K2P9 (TASK-3)	128 LGERMNTFVR-----YLLKRIKK-------CCGMRNTD---V	154
K2P15 (TASK-5)	128 LGERLNAVVR-----RLLLAAKC-------CLGLRWTC---V	154
K2P12 (THIK-2)	164 FLERIISLLAFIMRACRERQLRRSGLLPATFRRGSALSEADSLAGWKP	211
K2P13 (THIK-1)	145 FLERLITIIAYIMKSCHQRQLRRRGALPQESLKDAGQCEVDSLAGWKP	192
K2P5 (TASK-2)	133 LGKFFGGRAK-----RLGQFLT-------KRGVSLRK---A	158
K2P16 (TALK-1)	143 LGTGLRAHLA-------AIE-------RWEDRPRRSQVL	167
K2P17 (TALK-2)	151 LGHLMQQGVN-----HWASRLGG-------TWQDPDKA	176
K2P18 (TRESK)	151 TGDILATILSTSYNRFRKFPFFTRPLLSKWCPKSLFKKKPDPKPADEAVPQIIISAEELPGPKLGTCPSRPSCSMELFERSHALEKQNTLQLPPQAMERSNSCPELVLGR	260
Kv1.2_1	98 IVSNFNYFYHRET----------	110
KcsA	110 LATWFVGREQERRGH---------	124
KIR2.2	111 IMAKMARPK-----------	119
Kv1.2_2		

M3   Pore helix 2   M4

outer helix 2   filter   inner helix 2

*

K2P1 (TWIK-1)	180 -------AIVHAV---LLGFVTVSCFFFIPAAVFSVLEDDWNFLESFYFCFISLSTIGLGDYVPGEGY--NQKFRELYKIG---ITCYLLLGLIAMLVVLETF	267
K2P6 (TWIK-2)	169 -------ACWHLV---ALLGVVVTVCFLVPAVIFAHLEEAWSFLDAFYFCFISLSTIGLGDYVPGEAP--GQPYRALYKVL--VTVYLFLGLVAMVLVLQTF	256
K2P7	167 -------ALLQAV---ALGLLVASSFVLLPALVLWGLQGDCSLLGAVYFCFSSLSTIGLEDLLPGRGR--SLHPVIYHLGQLALLGYLLLGLLAMLLAVETF	256
K2P2 (TREK-1)	207 -------RIISTI--IFILFGCVLFVALPAIIFKHIE-GWSALDAIYFVVITLTTIGFGDYVAGGSD---IEYLDFYKPV--VWFWILVGLAYFAAVLSMI	292
K2P4 (TRAAK)	194 -------RVLSAM--LFLLIGCLLFVLTPTFVFCYME-DWSKLEAIYFVIVTLTTVGFGDYVAGADP--RQDSPAYQPL--VWFWILLGLAYFASVLTTI	279
K2P10 (TREK-2)	232 -------RVISTI--LFILAGCIVFVTIPAVFVFKYIE-GWTALESIYFVVVTLTTIGFGDFVAGGNA--GINYREWYKPL--VWFWILVGLAYFAAVLSMI	318
K2P3 (TASK-1)	155 -------SMANMV--LIGFFSCISTLCIGAAAFSHYE-HWTFFQAYYYCFITLTTIGFGDYVALQKD-QALQTPQPYVAF---SFVYILTGLTVIGAFLNLV	242
K2P9 (TASK-3)	155 -------SMENMV--TVGFFSCMGTLCIGAAAFSQCE-EWSFFHAYYYCFITLTTIGFGDYVALQTK-GALQKKPLYVAF---SFMYILVGLTVIGAFLNLV	242
K2P15 (TASK-5)	155 -------STENLV--VAGLLACAATLALGAVAFSHFE-GWTFFHAYYYCFITLTTIGFGDFVALQSG-EALQRKLPYVAF---SFLYILLGLTVIGAFLNLV	242
K2P12 (THIK-2)	212 -------SVYHVL--LILGLFAVLLSCCASAMYTSVE-GWDYVDSLYFCFVTFSTIGFGDLVSSQHA--AYRNQGLYRLG---NFLFILLGVCCIYSLFNVI	298
K2P13 (THIK-1)	193 -------SVYYVM--LILCTASILISCCASAMYTPIE-GWSYFDSLYFCFVAFSTIGFGDLVSSQNA--HYESQGLYRFA---NFVFILMGVCCIYSLFNVI	279
K2P5 (TASK-2)	159 -------QITCTV--IFIVWGVLVHLVIPPFVFMVTE-GWNYIEGLYYSFITISTIGFGDYVAGVNP--SANYHALYRYF---VELWIYLGLAWLSLFVNWK	245
K2P16 (TALK-1)	168 -------QVLGLA--LFLTLCTLVILIFPPMVFSHVE-GWSFSEGFYFAFITLSTIGFGDYVVGTDP--SKHYISVYRSL---AAIWILLGLAWLALILPLG	254
K2P17 (TALK-2)	177 -------RWLAGS--GALLSGLLLFLLLPPLLFSHME-GWSYTEGFYFAFITLSTVGFGDYVIGMNP--SQRYPLWYKNM--VSLWILFGMAWLALIIKLI	263
K2P18 (TRESK)	261 LSYSIISNLDEVGQQVERLDIPLPIIALIVFAYISCAAAILPFWETQLDFENAFYFCFVTLTTIGFGDTV------LEHPNFFLFF----SIYIIVGMEIVFIAFKLV	358
Kv1.2_1	-----------------------------	
KcsA	-----------------------------	
KIR2.2	-----------------------------	
Kv1.2_2	1 --------MRELGLLIFFLFIGVILFSSAVYFAEADERDSQFPSIPDAFWWAVVSMTTVGYGDMVPTTIGG-------------KIVGSLCAIAGVLTIALPVPVI 85	

C helix

proximal C-terminus

```
K2P1_(TWIK-1)   268 CELHELKKFRKMFYVKKDKDEDQVHIIEHDQ----------------LSFSSITDQAAGMKEDQKQNEPF-----VATQSSACVDGPANH------------- 336
K2P6_(TWIK-2)   257 RHVSDLHGLTELILLPPPCPASFNADEDDRVDILGPQP---------------ESHQQLSASSHTDYASIPR----------------------- 313
K2P7            257 SELPQVRAMGKFFRPSGPVTAEDQGGILCQDE---------------LALST-----------LPPAAPASGQAPAC------ 307
K2P2_(TREK-1)   293 GDWLRVISKKTKEEVGEFRAHAAEWTANVTAE---------------FKETRRRLSVEIY----------DKFQRATSIKRKLSAELAGNHNQE----LTPCRRTLSVNHL 374
K2P4_(TRAAK)    280 GNWLRVVSRRTRAEMGGLTAQAASWTGTVTAR---------------VTQRAGPAAPPP----------EKEQPLLPPPPCPAQPLGRPRSPSPPEKAQPPSPPTASALD 364
K2P10_(TREK-2)  319 GDWLRVLSKKTKEEVGEIKAHAAEWKANVTAE---------------FRETRRRLSVEIH----------DKLQRAATIRSMERRRLGLDQRAHSLDMLSPEKRSVFAALD 404
K2P3_(TASK-1)   243 VLRFMTMNAEDEKRDAEHRALLTRNGQAGGGGG--------GGSAHTTDTASSTAAAG----------GGGFRNVYAEVLHFQSMCSCLWYKSREKLQYSIPMIIPRDLST 335
K2P9_(TASK-3)   243 VLRFLTMNSEDERRDAEERASLAGNRRNSMVIHIP---------EEPRPSRPRYKADVPDLQSVCSCTCYRSQDYGGRSVAPQNSFS----------AKLA 323
K2P15_(TASK-5)  243 VLRFLVASADWPERAARPPSPRPPGAPESRGLWLPRR----------PARSVGSASVFCHVHKLERCARDN----LGFSPPSSPGVVRGG---------- 318
K2P12_(THIK-2)  299 SILIKQVLNWMLRKLSCRCCARCCPAPGAPLARRNAITPGS----------RLRRRLAALGADPAARDSDAEGRR----LSGELISMRDLTASN- 378
K2P13_(THIK-1)  280 SILIKQSLNWILRKMDSGCCPQCQRGLLRSRRNVVMPGS----------VRNRCNISIETDGVA-ESDTDGRR----LSGEMISMKDLLAAN- 356
K2P5_(TASK-2)   246 VSMFVEVHKAIKKRRRRKESFESSPHSRKALQVKGSTASKDVNIFSFLSKKEETYNDLIKQIG----------KKAMKTSGGGETGPGPGLGPQGGG----LPALPPSLV 342
K2P16_(TALK-1)  255 PLLLHRCCQLWLLSLRQGCGAKAAPGRRPRRGSTA----------ARGVQ----VTPQDFPISKKGLGS 309
K2P17_(TALK-2)  264 LSQLETPGRVCSCCHHSSKEDFKSQSWRQGP---------DREPESHSPQQGCYPEGPMGIIQH----LEPSAHAAGCGKDS- 332
K2P18_(TRESK)   359 QNRLIDIYKNVMLFFAKGKFYHLVKK---------- 384
Kv1.2_1             ----------
KcsA                ----------
KIR2.2              ----------
Kv1.2_2          86 VSNFNYFYHRET---------- 97
```

```
K2P2_(TREK-1)   375 TS----------------ERDVLPPLLKTESIYLNGLTP-HCAGEEIAVIENIK- 411
K2P4_(TRAAK)    365 YP---------------SENLAFIDESSDTQSERGCPLPRAPRGRRRPNPPRKPVRPRGPGPRDKGVPV- 419
K2P10_(TREK-2)  405 TGRFKA----------SSQESINNRPNNLRLKGPEQLNKHGQGASEDNIINKFGSTSR-LTKRKNKDLKKTLPEDVQKIYKTFRNYSLDEEKKEEETEKMCNSDNSSTA 502
K2P3_(TASK-1)   336 ----------SDTCVEQSHSSPGGGGRYS-DTPSRRCLCSGAPRSAISSVSTGLHSLSTFRGLMKRRSSV----------- 394
K2P9_(TASK-3)   324 PHYFHSISYKIEEISPSTLKNSLFPSPISSISPGLHSFTDHQRLMKRRKSV---------- 374
K2P15_(TASK-5)  319 ----------QAPRPGARWKS-I 330
K2P12_(THIK-2)  379 ----------KVSLALLQKQLSETANGYPRS-VCVNTRQNGFSGGVGALGIMNNRLAETSASR---------- 430
K2P13_(THIK-1)  357 ----------KASLAILQKQLSEMANGCPHQ-TSTLARDNEFSGGVGAFAIMNNRLAETSGDR---------- 408
K2P5_(TASK-2)   343 PLVVYSKNRV----------PTLEEVSQTLRSKGHVSRSPDEEAVARAPEDSSPAPEVFMNQ-LDRISEECEPWDAQDYHPLIFQDASITFVNTEAGLSDEETSKSSLE 440
```

```
K2P10_(TREK-2)  503 MLTDCIQQHAELENGMIPTDTKDREPENNSLLEDRN---------------------- 538
K2P5_(TASK-2)   441 DNLAGEESPQQGAEAKAPLNMGEFPSSSESTFTSTESELSVPYEQLMNEYNKANSPKGT 499
```

Figure 2.9: Alignment of human K_{2P} channels with rat $K_V1.2$, *S. lividans* KcsA and chicken $K_{IR}2.2$. Two copies of $K_V1.2$ are present in the alignment, one copy aligned to K_{2P} channel P domain 1 and a second aligned to P domain 2. Secondary structure of $K_{2P}1$ colored according to Figure 3.3. Red asterisks denote residues, which line the side portals of $K_{2P}1$, as referred to in the text. An orange box denotes the proximal C-terminus, which has been shown to be important for $K_{2P}2$ gating.
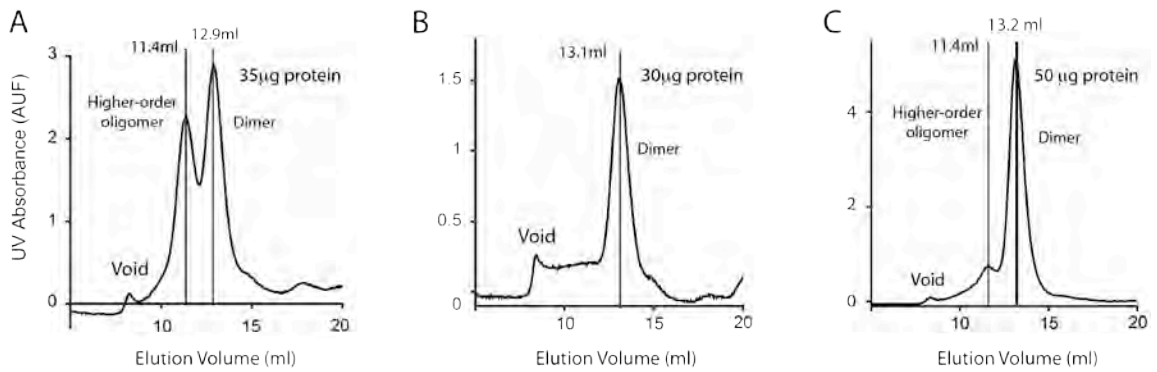
Figure 2.10: A higher-order oligomer of human $K_{2P}1$ N95Q $\Delta303$ EGEEF is formed by a non-specific disulfide bond. (A) Gel filtration profile of DDM-purified human $K_{2P}1$ N95Q $\Delta303$ after incubation for 6 hours at room temperature. (B) Gel filtration profile of DDM-purified human $K_{2P}1$ C10/22/288A N95Q $\Delta303$ after incubation for 6 hours at room temperature. (C) Gel filtration profile of DDM-purified $K_{2P}1$ C10A N95Q $\Delta303$, no incubation.

appeared that $K_{2P}1$ N95Q Δ303 was forming a higher-ordered oligomer through a non-specific disulfide bridge that is dependent on protein concentration as well as detergent alkyl chain length.

We turned our attention to identifying $K_{2P}1$ cytosolic cysteines. These residues are susceptible to forming non-specific disulfide bonds since they are within a reducing environment prior to detergent extraction. Three cytosolic cysteines, two located on the N-terminus (C10 and C22) and one located on the C-terminus (C268), were identified and individually mutated. Mutants were expressed in HEK293-GT cells, solubilized in DDM and evaluated by FSEC. A summary of the cysteine substitutions that were generated can be found in Table 2.5. All of the $K_{2P}1$ cysteine mutants appeared stable, eluting as a single peak by gel filtration. As a result, the cysteine mutations were combined as double and triple mutants, expressed in HEK293-GT cells and evaluated by FSEC. These combined mutants appeared as stable as wild-type human $K_{2P}1$.

The double and triple mutants (Table 2.5) were cloned into the N95Q Δ303 background for *P. pastoris* expression and large-scale purification. Both DDM-purified $K_{2P}1$ double (C10/22A) and triple (C10/22/268A) cysteine mutants eluted as a single population by gel filtration that did not form a higher-order oligomer over time (Figure 2.10). However, the gel filtration profile of the DDM-purified $K_{2P}1$ C10A single cysteine mutant appeared to have a small population of the higher molecular weight $K_{2P}1$ (Figure 2.10). These results suggest that, with concentrated purified protein, the cytosolic cysteines of human $K_{2P}1$ participate in disulfide bridge formation. In addition, elimination of C22 appears to be important for preventing formation of the higher-ordered oligomer, whereas C268 does not participate.

2.3.7. Expression of an N-terminal GFP-fusion construct improved $K_{2P}1$ protein yield

With purification of a stable human $K_{2P}1$ construct, we began crystallization trials with the

Single cysteine mutant

Residue	Mutant Residue(s)
C10	A, S
C22	A, S, Y
C268	A, S, Y

Double and triple cysteine mutants

Residue	Mutant Residue(s)
C10, C22	A
C10, C22, C268	A

Table 2.5: $K_{2P}1$ single and multiple cysteine mutants cloned and screened by FSEC. Residues are labeled in single letter amino acid code (A, Ala; C, Cys; S, Ser; Y, Tyr).

purified $K_{2P}1$ cysteine mutants. However, the overall yield from these purifications (< 0.5 mg) limited our ability to screen enough conditions to fully evaluate whether this construct was able to crystallize. Efforts were made to improve $K_{2P}1$ expression by modifying the *P. pastoris* induction conditions. K^+ channel overexpression can cause toxicity in *E. coli*, resulting in reduce cell viability, as has been documented for overexpression of the *Aeropyrum pernix* voltage-dependent K^+ channel (K_VAP) (Ruta et al., 2003). We reasoned that a similar phenomenon may also be occurring with overexpression of $K_{2P}1$ in *P. pastoris*. Modifying the induction conditions by altering the K^+ concentration in the media or by introducing a K^+ channel pore blocker could improve cell viability and, therefore, protein yield.

The total K^+ concentration in the original media recipes for *P. pastoris* growth and induction is 0.2 M, which is provided by potassium phosphate buffer. *P. pastoris* small-scale induction experiments with varying K^+ concentrations in the media, by either supplementing the media with KCl (0-1 M) or by removing K^+ (0-200 mM potassium phosphate) demonstrated that the ideal K^+ concentration for human $K_{2P}1$ expression was ∼ 200 mM, consistent with the original media recipe, as evaluated by YL1/2 western blot (see 2.2.4 Small- and large-scale growth and expression in *P. pastoris*) (Figure 2.11). Likewise, small-scale induction experiments were also performed in the presence of $BaCl_2$, a K^+ channel pore blocker. $BaCl_2$ (1 mM) addition to the *P. pastoris* induction media did not improve expression of human $K_{2P}1$, as evaluated by a FLAG western blot (Figure 2.11).

The location and the type of epitope tag used for affinity purification could affect protein stability and yield. Human $K_{2P}1$ constructs containing different affinity tags were generated, which included an N-terminal 8-His tag and a C-terminal FLAG (DYKDDDDK) tag. Purification of the His-tagged human $K_{2P}1$ construct was unsuccessful since I was not able to isolate a protein population by gel filtration. The FLAG affinity purification yielded approximately half the

A

0   0.25   0.5   1   KCl (M)

T S   T S   T S   T S

39 —
28 —
19 —

$K_{2P}1$ DC N95Q Δ303 EGEEF

B

0   10   100   200   KPhos (mM)

T S   T S   T S   T S

39 —
28 —

$K_{2P}1$ DC N95Q Δ303 EGEEF

C

-    + $BaCl_2$

T S   T S

39 —
28 —

$K_{2P}1$ TC N95Q Δ303 FLAG
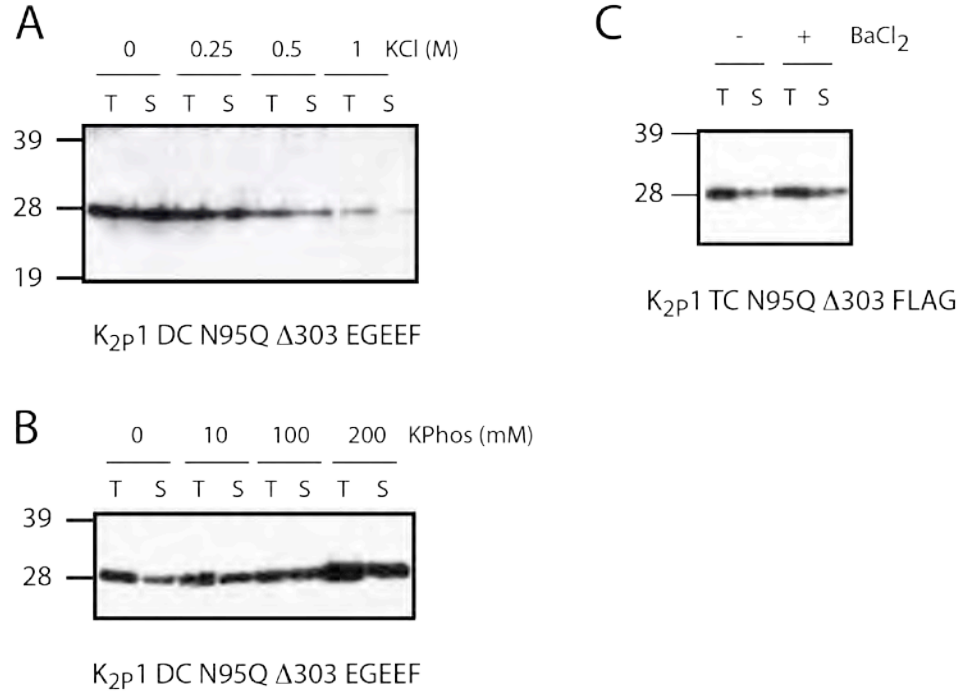
Figure 2.11: Modifications to the *P. pastoris* induction conditions do not improve $K_{2P}1$ expression. (A) YL1/2 western blot detecting $K_{2P}1$ C10/22A N95Q Δ303 ($K_{2P}1$ DC N95Q Δ303) expression in *P. pastoris*, supplemented with KCl in the growth and induction media (0-1 M). A total lysate (T) and a DDM-solubilized fraction (S) were collected for each sample (B) YL1/2 western blot detecting $K_{2P}1$ C10/22A N95Q Δ303 ($K_{2P}1$ DC N95Q Δ303) expression in *P. pastoris*, with varying concentrations of potassium phosphate (KPhos) in the growth and induction media (0-200 mM). A total lysate (T) and a DDM-solubilized fraction (S) were collected for each sample. (C) FLAG western blot detecting $K_{2P}1$ C10/22/288A N95Q Δ303 ($K_{2P}1$ TC N95Q Δ303) grown and induced in the absence (-) or presence (+) of $BaCl_2$.

81

amount of protein that I was able to purify from the original, EGEEF-tagged construct.

Generation of a fusion protein, which involves engineering the target protein with a stable, well-expressing soluble protein, is another strategy that has been used to improve recombinant protein expression. Human $K_{2P}1$ constructs were fused with either an 8-His tagged N-terminal GFP or an EGEEF tagged C-terminal GFP for expression in *P. pastoris*. Small-scale induction experiments were performed for N- and C-terminal GFP $K_{2P}1$ C10/22A N95Q Δ303 fusion constructs and were evaluated by FSEC. The expression level of the N-terminal GFP $K_{2P}1$ C10/22A N95Q Δ303 fusion construct was 5-fold greater than what was measured for the equivalent C-terminal GFP-fusion construct (Figure 2.12).

Large-scale purification of the N-terminal GFP $K_{2P}1$ C10/22A N95Q Δ303 construct was performed in DM using a similar two-step purification protocol as described for EGEEF-tagged $K_{2P}1$ with one additional step. After DDM extraction of the $K_{2P}1$ fusion from the membrane, the channel was purified using an immobilized metal affinity column (IMAC, cobalt resin). The IMAC-purified sample was proteolytically cleaved with PreScission protease to separate GFP from $K_{2P}1$, and this sample was further purified by gel filtration chromatography in buffer containing DM. The yield of this purification was 3- to 4-fold greater (> 1.5 mg) than the equivalent non-GFP tagged construct and was a sufficient amount of protein for comprehensive screening of crystallization conditions. Crystallization trials (~ 800 conditions) were initially set up with $K_{2P}1$ C10/22A N95Q Δ303 (>12 mg/ml) in hanging drop format, protein mixed 1:1 with well solution. Similarly, $K_{2P}1$ C10/22A N95Q Δ303 was purified by gel filtration in the presence of NM, a shorter-chain detergent, and brain total lipid extract. Unfortunately, under the purification and crystallization conditions tested, no crystals of $K_{2P}1$ C10/22A N95Q Δ303 were observed (Figure 2.13).
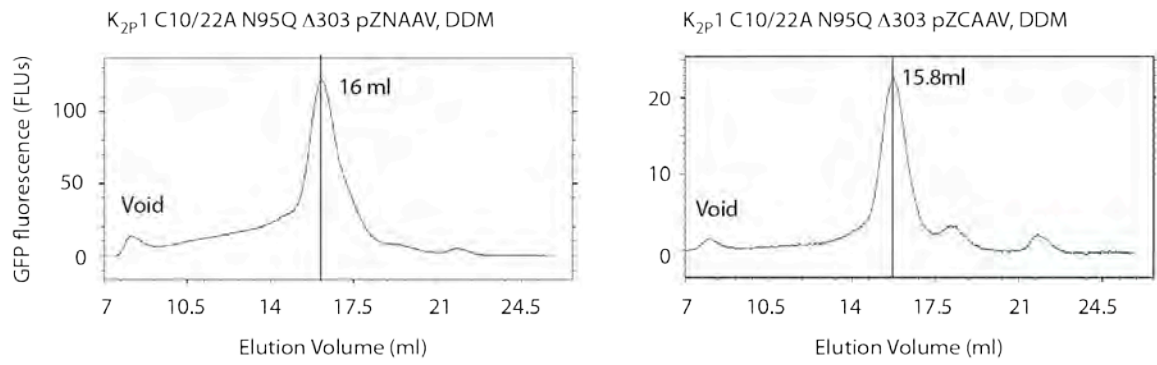
Figure 2.12: FSEC elution profiles for DDM-solubilzed human $K_{2P}1$ C10/22A N95Q Δ303 N-terminal (pZNAAV) and C-terminal (pZCAAV) GFP-fusion constructs expressed for 48 hours in HEK293-GT cells (Superose 6).
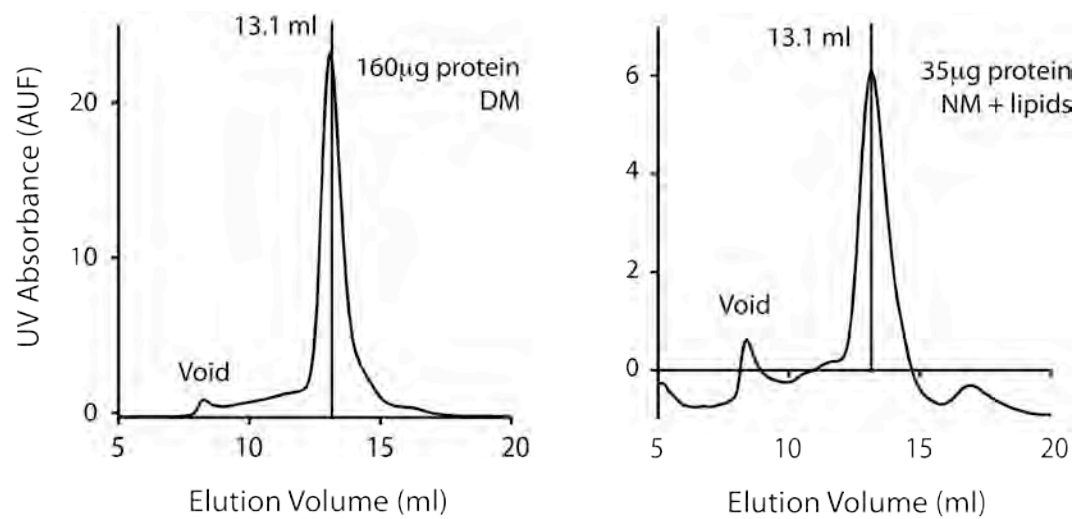
Figure 2.13: K$_{2P}$1 C10/22A N95Q Δ303 purifications in DM and NM. (A) Gel filtration profile of DM-purified K$_{2P}$1 C10/22A N95Q Δ303. (B) Gel filtration profile of K$_{2P}$1 C10/22A N95Q Δ303 purified in NM with brain total lipid extract.

2.3.8. Determining a structured 'core' of human $K_{2P}1$ – Part II

Since the $K_{2P}1$ C10/22A N95Q $\Delta303$ construct did not appear to crystallize, we hypothesized that there may be a smaller structured unit of human $K_{2P}1$ that had yet to be identified. As a first attempt to identify the smaller structured unit, sequences of the pore forming regions of KcsA and $K_V1.2$ were aligned to a $K_{2P}1$ multiple alignment. N-terminal deletion constructs ($\Delta10$, $\Delta16$, $\Delta19$ and $\Delta22$) were generated in the N95Q $\Delta303$ background based on 1) the human $K_{2P}1$ alignment to the outer helices of KcsA and $K_V1.2$ crystal sequences and 2) on the location of human $K_{2P}1$ N-terminal cysteines mutations. Both human $K_{2P}1$ 10-303 N95Q and 22-303 N95Q were purified in DM and crystallization trials were set up (Figure 2.14). Although no crystals of $K_{2P}1$ 10-303 N95Q were observed, the $K_{2P}1$ 22-303 N95Q construct yielded crystals in 20-30% PEG 400 in no salt, 150 mM NaCl or 150 mM KCl and 100 mM buffer ranging from pH 6.5-9.5 (see 3.4.2 Human $K_{2P}1$ crystal refinement and derivatization).

In addition to refining these crystals, a limited proteolysis experiment with human $K_{2P}1$ 22-303 N95Q DM-purified protein was performed with eight different proteases to address the question of whether the C-terminus could be further shortened while still retaining a structured unit of $K_{2P}1$ (Table 2.3). Overall, human $K_{2P}1$ 22-303 N95Q was resistant to most proteases tested with the exception of Asp-N and Glu-C (Figure 2.15). Asp-N selectivity cleaves peptide bonds N-terminal to Asp and Glu-C selectivity cleaves peptide bonds C-terminal to Glu. The human $K_{2P}1$ C-terminal sequence includes a cluster of Asp and Glu (residues 284-288), which is the region most likely being proteolytically cleaved (Figure 2.15). In addition to these results, other C-terminal deletion constructs were designed based on a human $K_{2P}1$ alignment to the inner helix of the $K_V1.2$ crystal sequence ($\Delta275$, $\Delta279$).

C-terminal deletion constructs were cloned into the $\Delta22$ N95Q N-terminal GFP-fusion background, transformed and expressed in *P. pastoris* and solubilized in DDM. The stability of
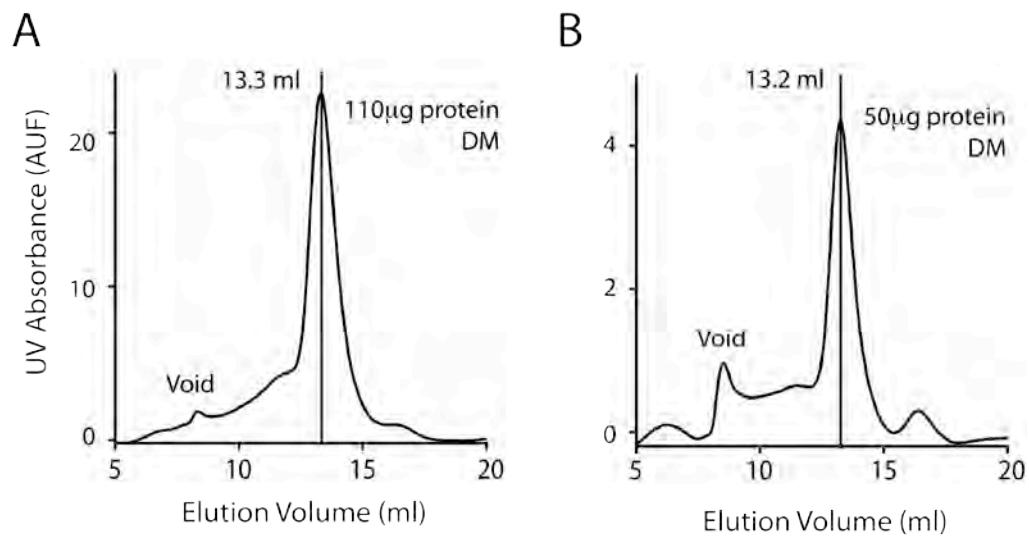
Figure 2.14: K$_{2P}$1 N-terminal deletion construct purifications in DM (A) Gel filtration profile of DM-purified K$_{2P}$1 10-303 N95Q. (B) Gel filtration profile of DM-purified K$_{2P}$1 22-303 N95Q.
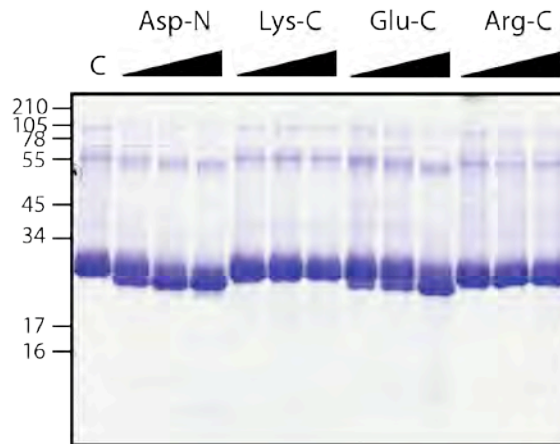
Figure 2.15: Limited proteolysis experiment with DM-purified K_2P1 22-303 N95Q. (A) Coomassie-stained gel of K_2P1 22-303 N95Q samples subjected to three concentrations of Asp-N, Lys-C, Glu-C and Arg-C, or no protease (C). Mapping of targeted residues by Asp-N and Glu-C (aspartates and glutamates, red) or Lys-C and Arg-C (lysine and arginines, blue) on the C-terminus. C-terminal deletion constructs generated from these results are highlighted in orange.

these constructs was evaluated by FSEC. Overall, the C-terminal deletion construct $\Delta 288$ appeared stable, whereas the $\Delta 275$ FSEC profile contained two oligomeric populations (monomer and dimer) (Figure 2.16). Large-scale purification of human $K_{2P}1$ 22-288 N95Q in DM yielded crystals in conditions similar to what was found for human $K_{2P}1$ 22-303 N95Q (see 3.4.2 Human $K_{2P}1$ crystal refinement and derivatization). Surprisingly, crystals were also observed for the $K_{2P}1$ 22-275 N95Q construct purified in DM. Although the human $K_{2P}1$ 22-279 N95Q construct did not crystallize, the protein yield after purification was low and, as a result, only a few crystallization conditions were tested. The human $K_{2P}1$ 22-279 N95Q construct would need to be further tested in order to fully evaluate its ability to crystallize.

2.4.   Discussion

K_{2P} channels are classified as background K^+ channels, essential for establishing and maintaining the resting potential in excitable cells. The first identified mammalian K_{2P} channel was named tandem of P domains in a weak inward rectifying K^+ channel (TWIK-1; $K_{2P}1$) based on its molecular architecture and electrophysiological properties (Lesage et al., 1996a). Since this initial work, a total of 15 human K_{2P} homologs have been identified in the K_{2P} channel subfamily (Table 1.2). In order to identify a stable, well-expressed K_{2P} channel that would be suitable for large-scale purification and crystallization, I cloned and screen 14 of the 15 human K_{2P} homologs and chose $K_{2P}1$ as the leading candidate based on its FSEC profile after extraction in a panel of detergents (Table 1.2) (Figure 2.3).

A published biochemical study of $K_{2P}1$ characterized several post-translational modifications which are located in a region between M1 and the first pore helix (Lesage et al., 1996b). It was shown, for instance, that wild-type $K_{2P}1$ separates at the approximate size of a dimer in non-denaturing conditions whereas a C69S mutant migrates as a monomer in the same conditions, suggesting that C69S forms an intermolecular disulfide bridge. My work addressed the question
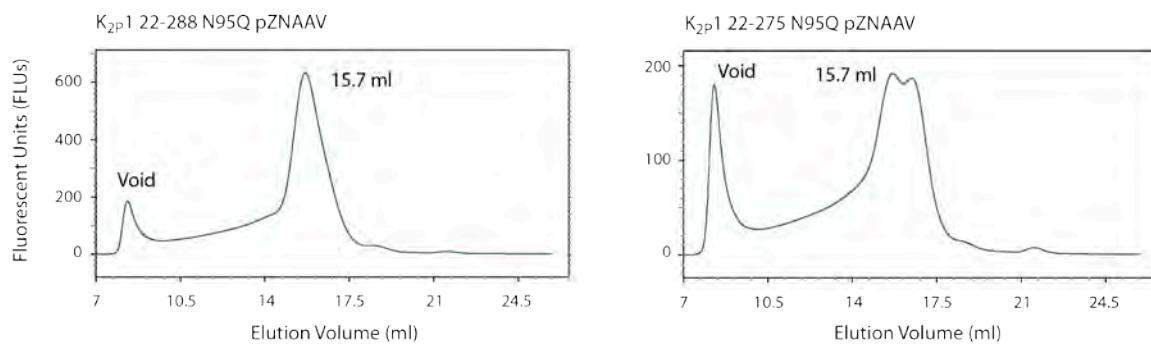
Figure 2.16: Comparison of FSEC elution profiles of DDM-solubilized $K_{2P}1$ C-terminal deletion constructs 22-288 and 22-275, cloned in the N95Q background (Superose 6).

of whether the C69 disulfide bridge is necessary for $K_{2P}1$ stability in detergent micelles. In low K^+ conditions (10 mM), wild-type $K_{2P}1$ elutes as a dimer by FSEC, whereas the $K_{2P}1$ C69S mutant, as well as DTT-exposed wild-type $K_{2P}1$, elute as a monomer (Figure 2.6). These results suggested that C69 is important for maintaining $K_{2P}1$ stability in DDM. Interestingly, 10 of the 15 human K_{2P} channel homologs contain the analogous C69 residue of $K_{2P}1$ (Figure 2.9). If the conserved cysteine was important for stabilization of K_{2P} channels in detergent, one would expect that the initial candidates selected based on FSEC screening in DDM ($K_{2P}1$, $K_{2P}6$, $K_{2P}13$ and $K_{2P}17$) would all contain the conserved cysteine. $K_{2P}13$ does not contain the cysteine. However, of the four candidates, $K_{2P}13$ is the least stable candidate, as evaluated by comparison of FSEC elution profiles in a panel of 13 detergents.

In addition to demonstrating that C69 forms a disulfide bridge, migration of $K_{2P}1$ at the approximate size of a dimer in non-denaturing conditions also suggested that $K_{2P}1$ assembles a dimer rather than a tetramer (Lesage et al., 1996b). Similar results have also been demonstrated for $K_{2P}2$ and $K_{2P}6$, two K_{2P} channels that also contain the conserved cysteine residue (Figure 2.9) (Maingret et al., 2000a; Patel et al., 2000). These results are not surprising since K_{2P} monomers contain 2 selectivity filter sequences and pore helices, whereas a functional tetrameric K^+ channels contains a total of 4 of these features, 1 per monomer. In support of this hypothesis, gel filtration purified human $K_{2P}1$ subjected to the crosslinking reagent DSS also separates as a dimer in denaturing conditions whereas the DMSO control migrates as a monomer (Figure 2.5). This experimental data, in addition to sequence analysis that identifies two selectivity filter sequences in one K_{2P} monomer, lends support to the hypothesis that K_{2P} channels assemble as dimers.

N95 was also identified as a post-translationally modified residue that harbors an N-linked glycan (Lesage et al., 1996a; Lesage et al., 1996b). Whereas separation of wild-type $K_{2P}1$ in denaturing conditions yielded two monomeric bands that differed by a few kilodaltons, the N95Q mutant

migrated as a single band, as evaluated by western blot. Furthermore, wild-type $K_{2P}1$ pre-exposed to PNGase F, an amidase that specifically cleaves N-linked glycans, also migrates as a single band, suggesting that wild-type $K_{2P}1$ is N-linked glycosylated and that N95 is the residue that is modified (Lesage et al., 1996b). DDM-purified $K_{2P}1$ also migrates as two bands that are separated by a few kilodaltons. Similar to the published biochemical experiments, addition of PNGase F to purified wild-type $K_{2P}1$, or purification of an N95Q mutant, results in a channel that separates as a single monomeric band by SDS-PAGE, further supporting the conclusion that N95 is typically N-linked to a glycan (Figure 2.7).

Protein glycosylation is known to play important roles in protein folding, stabilization and trafficking, as well as in cell-cell interactions and cell surface protection (Alberts, 2008). Although a direct study of glycosylation mediating $K_{2P}1$ trafficking or stability has not been performed, currents measured from wild-type and the N95 to alanine (N95A) mutant overexpressed in *Xenopus* oocytes are almost identical, suggesting that folding and trafficking are not affected by the substitution (Lesage et al., 1996b). It would be interesting to further characterize the N95Q mutant through electrophysiological studies to determine its functional role in $K_{2P}1$ channel function (e.g. role in extracellular acidification in $K_{2P}1$ gating).

Successful protein crystallization typically requires a high concentration ($\sim$ 5-15 mg/ml) of pure, stable and highly-ordered protein of interest. Human $K_{2P}1$ purifications in DDM typically yielded < 0.5 mg of protein from 24 g of *P. pastoris* ($\sim$1/3 of a L), which limited the number of crystallization conditions that could be evaluated. A number of modifications were made to the *P. pastoris* induction protocol that did not improve $K_{2P}1$ expression, as evaluated by YL1/2 and FLAG western blots. Several modifications were made to the construct itself, with the swapping of various affinity tags (EGEEF, His, FLAG), as well as the generation of a GFP fusion protein. GFP fused to the N-terminus of $K_{2P}1$ significantly improved expression (> 1.5 mg from 24 g of *P.*

pastoris) and, for each individual purification of the GFP-fused $K_{2P}1$ constructs, I was able to test ~ 800 crystallization conditions.

Conformationally homogeneous protein is also essential for protein crystal growth. Sequence analysis of K_{2P} channels suggests that the C-terminus is unstructured and an initial limited proteolysis experiment with purified $K_{2P}1$ N95Q suggests that this region is readily cleaved (Figure 2.8). A C-terminal deletion construct removing residues 304-331 was designed based on these results (Figure 2.8). Functional data supports a role for K_{2P} channel gating by the C-terminus since truncations and deletions to this region alter the electrophysiological properties of this channel family (Enyedi and Czirjak, 2010). In addition, the C-terminus appears to be an important region for interaction with a number of proteins such as kinases and trafficking proteins (Enyedi and Czirjak, 2010). Although truncation of the $K_{2P}1$ C-terminus is important for crystal growth, it also results in a loss of structural information that would be helpful for understanding how the C-terminus of K_{2P} channels is involved in gating. One potential avenue that could be explored using X-ray crystallography would be to identify a protein that binds to and stabilizes the C-terminus of $K_{2P}1$ (e.g. SUMO conjugation or proteins involved dynamin-mediated endocytosis), which could be used for co-crystallization trials (Rajan et al., 2005).

It was evident from subsequent purifications of $K_{2P}1$ N95Q Δ303 that the C-terminus prevented, or retarded the formation of a non-specific disulfide bridge between two channels. Removing the C-terminus accelerated this process, and the cysteine(s) that is participating in this covalent linkage is located on the N-terminus. Cysteine substitutions, or deletions of the N-terminus abolished the formation of the higher ordered oligomer (Figure 2.10). An experiment that could have been done to evaluate the accumulation of the higher-ordered oligomer prior to generating cysteine substitutions would have been to add a reducing agent (DTT, for instance) to the purified sample prior to or after the higher-ordered oligomer formed. Adding DTT immediately after $K_{2P}1$

N95Q Δ303 purification should prevent accumulation of higher-ordered oligomer, whereas adding the reducing agent after higher-ordered oligomer accumulation should shift the sample back to a dimer.

It is also clear that truncation to the N-terminus of $K_{2P}1$ was necessary for crystallization. This finding was not apparent from the limited proteolysis experiments that were performed, but was instead identified by protein alignment to the pore-forming regions of KcsA and Kv1.2 that had successfully crystallized. Removing the N-terminus had a two-fold effect of removing a region of $K_{2P}1$ that inhibited crystallization, and also of eliminating the cysteine residues, which were participating in non-specific disulfide bridge formation.

K_{2P} channels appear to assemble as dimers, as deduced from both sequence analysis (2 selectivity filter sequences in 1 protomer) and biochemical experiments (non-denaturing gels, crosslinking of purified $K_{2P}1$). A crystal structure of $K_{2P}1$ will give us insight into how the dimeric assembly of the K_{2P} channel family may accommodate structural features that distinguishes these channels from other types of K^+ channels. In addition, an alignment of K_{2P} channels reveals a conserved extracellular 'loop' of ~ 50-60 amino acids in length (Figure 1.3, Figure 2.9). It will be interesting to determine whether this extracellular loop forms a structured domain, especially since none of the previous tetrameric K^+ channel structures contain an extracellular domain. The $K_{2P}1$ residues (272-286), which align to the proximal C-terminus of $K_{2P}2$, are present in the $K_{2P}1$ C-terminal truncation constructs that crystallize (Figure 1.9, Figure 2.9). Since the proximal C-terminus has been shown to be important for $K_{2P}2$ gating, the $K_{2P}1$ crystal structure may provide additional evidence to support the role of this region in gating.

CHAPTER 3

3. CRYSTAL STRUCTURE OF HUMAN K$_{2P}$1

3.1. Summary

The human K$_{2P}$ 22-288 N95Q construct crystallized and diffracted to 3.4Å resolution. Unlike other K$^+$ channel structures, K$_{2P}$1 is dimeric and the crystal structure reveals a number of features that have not been previously observed. A 56 amino acid extracellular cap is positioned above the extracellular side of the selectivity filter and restricts K$^+$ ion access to the pore to two side portals. The extracellular cap may serve as a molecular shield against K$^+$ channel protein toxins and could be important for interaction with extracellular ligands or peptides. The coordination of K$^+$ ions within the K$_{2P}$1 selectivity filter recapitulates the four-fold symmetry that is present in other K$^+$ channel structures. However, the non-covalent interactions surrounding the K$_{2P}$1 filter deviate from what has been previously observed and is two-fold symmetric, which may facilitate outer pore gating. The K$_{2P}$1 ion pore is exposed to the lipid bilayer through openings in the intramembrane molecular surface, accommodating electron density that we attribute to lipid or detergent alkyl chains. The direct connection between the K$_{2P}$1 ion pore and the lipid bilayer may be important for accessibility of K$_{2P}$ channels to lipid compounds, inhibitors and possibly play a role in sensing mechanical tension. An amphipathic 'C-helix' runs parallel to the cytosolic side of the membrane and may be involved in inner helical gating. In support of this idea, substitution of residues within this region in other K$_{2P}$ channel paralogs results in alterations to gating. The human K$_{2P}$1 structure highlights the molecular architecture likely characteristic of the K$_{2P}$ channel family and also lays a foundation to further investigate how K$_{2P}$ channels are regulated by diverse stimuli. The results presented in this chapter have been published (Miller and Long, 2012).

3.2. Introduction

K_{2P} channels are regulated by a large variety of chemical and physical stimuli. How these inputs are translated to the conformational changes necessary for gate opening and closure is a topic of ongoing investigation (Cohen et al., 2009; Mathie et al., 2010). Initial studies of K_{2P} channel gating were performed with a *D. melanogaster* K_{2P} channel homolog, KCNK$\varnothing$ (Zilberberg et al., 2000; 2001). From these studies, several lines of evidence suggest that KCNK$\varnothing$ exhibits outer pore-like gating properties. Single channel recordings of KCNK$\varnothing$ revealed an increase in the open probability (P_O) to external K^+ concentration (comparing Na^+ versus K^+, 140 mM) as well as to extracellular application of tetraethylammonium (TEA). It has been previously shown that both K^+ ions and external TEA delay closure of the outer pore gate in K_V channels by preventing the collapse of the selectivity filter (Baukrowitz and Yellen, 1995; Choi et al., 1991; 1989a; Grissmer and Cahalan, 1989b; Lopez-Barneo et al., 1993; Marom and Levitan, 1994). In addition, a number of known analogous point mutations that alter C-type inactivation in the Shaker channel similarly modulate KCNK$\varnothing$ gating (Larsson and Elinder, 2000; Lopez-Barneo et al., 1993; MacKinnon and Yellen, 1990; Ortega-Saenz et al., 2000; Zilberberg et al., 2001).

Studies of a subset of mammalian K_{2P} channels that are modulated by changes in extracellular pH suggest that outer pore gating is most likely a general gating mechanism of K_{2P} channels (Cohen et al., 2008; Kang and Kim, 2004; Lopes et al., 2001; Morton et al., 2003; Niemeyer et al., 2007; Reyes et al., 1998; Sandoz et al., 2009; Yuill et al., 2007). At the whole cell level, $K_{2P}2$ and $K_{2P}3$ current amplitudes decrease with reduction in extracellular pH, with half maximal current at pH 7.5 in physiological conditions (extracellular K^+ concentration ~ 4-5 mM) (Cohen et al., 2009; Lopes et al., 2001; Morton et al., 2003). A higher extracellular K^+ concentration (100 mM) reduces the pH inhibition, shifting the half maximal current to ~6.5. Further study of $K_{2P}5$ at the single channel level revealed that extracellular pH affects channel P_O and not conductance (Kang

and Kim, 2004; Reyes et al., 1998). Finally, mutagenesis studies of $K_{2P}1$, $K_{2P}2$, $K_{2P}3$, $K_{2P}5$ and $K_{2P}9$ have identified residues surrounding the outer pore that are critical for sensing changes to extracellular pH (Cohen et al., 2008; Kim et al., 2000; Lopes et al., 2001; Ma et al., 2012b; Morton et al., 2003; Niemeyer et al., 2007; Sandoz et al., 2009; Yuill et al., 2007). These data suggest that extracellular pH can regulate outer pore gating in a mechanism similar to what has been described in K_v channels and that this may be a general gating property of K_{2P} channels.

Although there is initial evidence to support outer pore gating of K_{2P} channels, more recent studies have explored whether K_{2P} channels also possess a functional activation gate. K_{2P} channels contain the conserved gating hinge glycine in both the M2 and M4 segments (Figure 1.7). Substitution of either the M2 or M4 glycine to alanine in $K_{2P}9$ (G117, M2; G231, M4) reduces the P_O, stabilizing the closed state (Ashmole et al., 2009). Similarly, other point mutations within the inner helices of $K_{2P}9$, as well as within KCNK∅, alter the open and closed states of the channel (Ashmole et al., 2009; Ben-Abu et al., 2009). Interestingly, individual substitution of 3 glycine residues (G134, G139 or G141) to larger hydrophobic residues within M2 of KCNK∅ induces closure of both activation and inactivation gates, suggesting that these gates are positively coupled, in contrast to K_v channels where these two gates are negatively coupled (Baukrowitz and Yellen, 1995; 1996; Ben-Abu et al., 2009). Finally, to demonstrate function of the K_{2P} inner helical gate, a Shaker channel/KCNK∅ (K_v-K_{2P}) chimera was generated by replacing the Shaker channel pore domain with KCNK∅ pore domain 1. The K_v-K_{2P} chimera displayed voltage-dependent opening of the activation gate (Ben-Abu et al., 2009). However, it is worth noting that the K_v-K_{2P} chimera assembles as a homotetramer with its pore comprised of KCNK∅ pore domain 1 and, therefore, it is still unclear whether the presence of both KCNK∅ pore domains can form a functional activation gate. These results support the idea that K_{2P} channels possess a functional activation gate and suggest that this gate may be positively coupled

to the inactivation gate.

Additional studies of the K_{2P} channel activation gate had been hindered by the absence of a high-affinity pore blocker such as the quaternary ammonium (QA) cation TEA, which has proven to be a useful tool for probing K_V channel gating (Armstrong, 1969; Baukrowitz and Yellen, 1996; Choi et al., 1991; Holmgren et al., 1997). In K_V channels, internal application of TEA blocks K^+ conductance by binding within the K_V central cavity upon activation gate opening (Armstrong, 1966; 1971; Choi et al., 1993; Yohannan et al., 2007; Zhou et al., 2001a). Unlike K_V channels, K_{2P} channels are known to be fairly insensitive to intracellular TEA blockage (Enyedi and Czirjak, 2010; Lotshaw, 2007). However, a recent study demonstrated that extension of the QA alkyl chains improved the efficacy of the compound, with sub-micromolar range IC_{50} values of QA's with 5-7 carbon alkyl tails (TPenA, THexA and THepA), measured for 3 K_{2P} channels (Piechotta et al., 2011). Cysteine-scanning mutagenesis of the $K_{2P}2$ inner pore revealed key residues that reduce the TPenA blocking affinity and supports a model of QA binding within the K_{2P} central cavity, consistent to what has been observed for K_v channels (Choi et al., 1993; Zhou et al., 2001a). Surprisingly, $K_{2P}2$ activation gate studies using THexA revealed that the QA binding site is accessible regardless of whether $K_{2P}2$ is in an open- or closed-state. From these results, the authors conclude that the bundle-crossing gate for K_{2P} channel is constitutively open and that the inactivation gate is the functional K_{2P} channel gating apparatus (Piechotta et al., 2011).

If the K_{2P} channel activation gate is constitutively open, then gating by chemical or physical modulation to the intracellular C-terminus must be communicated to the external inactivation gate. Studies of $K_{2P}2$ outer pore gating by extracellular pH were performed in conjunction with C-terminal mutations to address the question of whether the C-terminus is capable of gating the outer pore (Bagriantsev et al., 2012). A glutamate (E306), located within the proximal C-terminus

($K_{2P}2$ 297-311, see Figure 1.9, Figure 2.9), has been shown to be critical for $K_{2P}2$ channel activation by intracellular pH (Figure 2.9) (Chemin et al., 2005b; Honore et al., 2002). Bagriantsev and colleagues report that outer pore gating of mouse $K_{2P}2$ by intracellular pH is inhibited with E306A substitution (Bagriantsev et al., 2012). However, it should be noted that this data opposes what has been reported for the human ortholog and may reflect either sequence divergence between species or different levels of $K_{2P}2$ expression in *Xenopus* oocytes (see Sandoz et al., 2009). $K_{2P}2$ channel gating modulation via the proximal C-terminus is believed to be associated with its interaction with the lipid bilayer (Honore, 2007). As a result, a $K_{2P}2$ mutant was generated to decouple the C-terminus from the membrane to further probe into C-terminal regulation of the outer pore gate (Bagriantsev et al., 2012). The predicted M4 and C-terminal linker (IGD) was mutated to three glycines (3G) or alanines (3A) to introduce or remove flexibility within this region. Both of these mutants appeared more sensitive to intracellular pH than the wild-type channel. Likewise, $K_{2P}2$ slow time-dependent channel inactivation, believed to reflect closure of the outer pore gate, was abolished by both of these mutants. From these results, the authors suggest that the C-terminus regulates gating at the extracellular mouth of the pore (Bagriantsev et al., 2012).

To further address the question of communication between the proximal C-terminus communication and the outer pore gate, a mouse $K_{2P}2$ gain of function M4 mutant (W275S), located on the extracellular side of the membrane, was identified and characterized (Bagriantsev et al., 2011). This mutation increased the P_O as measured from single channel studies and, as a result, decreases response to extracellular pH modulation. The $K_{2P}2$ W275S mutant is also less responsive to temperature changes and mechanical stretch, stimuli that act on the $K_{2P}2$ cytosolic C-terminus (Maingret et al., 1999b; Maingret et al., 2000a; Patel et al., 1998). However, an experimental pitfall is that temperature modulation and mechanical stretch perturb both sides of the membrane. In other words, it is difficult to conclude whether these stimuli are modulating the

activation gate via the C-terminus or if they are capable of doing so directly. Regardless, the authors conclude that gating modulation by extracellular pH, temperature, and mechanosensation converge at the inactivation gate (Bagriantsev et al., 2011).

3.3. Materials and Methods

3.3.1. Crystallization conditions, refinement, and heavy atom derivatization

$K_{2P}1$ 22-275, 22-279, 22-288 and 22-303 N95Q constructs were purified in buffer conditions containing 150 mM KCl, 20 mM Tris-HCl, pH 7.5 and detergent (anagrade) (see Table 2.2 for detergent concentrations used for large-scale purification) in the absence or presence of a 0.1 mg/ml of brain total lipid extract (Avanti Polar Lipids) and concentrated to ~ 5-13 mg/ml using a 50 kDa Vivaspin-2 concentrator (Sartorius Stedim Biotech). Purified protein was subsequently mixed 1:1 with well solution with volumes ranging from 100-300 nl (96 well) or 1-3 µl (24 well) and set up in hanging drop format over a reservoir containing 0.1 ml (96 well) or 0.5 ml (24 well) of well solution.

Initial conditions in which $K_{2P}1$ 22-303 N95Q crystallized contained: 26-30% PEG400 (v/v); no salt, 150 mM NaCl or 150 mM KCl; in a pH range between 6.6-9.0; at 17°C. $K_{2P}1$ 22-303 N95Q crystals also grew at 4°C in similar conditions in a PEG400 concentration range of 20-24% (v/v). Constructs of $K_{2P}1$ containing shorter C-termini, $K_{2P}1$ 22-275 N95Q and 22-288 N95Q also crystallized in similar conditions. The best diffracting crystals were of $K_{2P}1$ 22-288 N95Q purified in DM without brain total lipid extract, which grew in 18-20% PEG400 (v/v); 150 mM KCl; HEPES, pH 8.0 at 4°C and reached approximately 300 microns in size within 1-2 weeks. Crystals were cryo-protected and dehydrated in reservoir solution supplemented with 50% PEG400 (v/v), 5 mM DM and 20 mM HEPES, pH 8.0 in a step-wise manner (3.75% PEG400 increase each step, 2-5 minute intervals) and vitrified by flash-cooling in liquid nitrogen.

Crystallization trials with additives such as reducing agents (15-20 mM DTT, 10 mM tris(2-carboxyethyl)phosphine (TCEP)), ethylene glycol (EG; 5%), glycerol (5%), 2-methyl-2,4-pentanediol (MPD; 5%), xylitol (5%), sucrose (5%) and trehelose (5%) were manually pipetted into the reservoir prior to setting up crystallization trials. Detergent additives (NM, 8 mM; OM, 30 mM) were mixed with the protein prior to setting up crystal trays.

To obtain crystals containing the heavy atom thallium (Tl^+), cryo-protected native crystals were soaked by an initial transfer into a solution containing 42% PEG400, 150 mM KNO_3, 100 mM HEPES, pH 8.0, and 5 mM DM. The crystals were then transferred into a similar solution containing 75 mM KNO_3 and 75 mM $TlNO_3$ and left to soak for 24 hours. For co-crystallization experiments, the heavy atom compounds thimerosal, $KAu(CN)_2$, $GdCl_3$, ethyl mercury phosphate (EMP), and $K_2Pt(CN)_4$ (Hampton Research; 2 mM of each) were combined with the protein prior to crystallization and the derivatized crystals grew under the same condition as native protein.

3.3.2. X-ray crystallography data collection and analysis

Diffraction data were collected at beamline X25 (Brookhaven NSLS) and processed with the HKL2000 suite (Otwinowski and Minor, 1997). Initial thimerosal sites for experimental phase determination were located using two approaches. One approach, by Dr. Stephen Long, used molecular replacement (MR) and single wavelength anomalous dispersion Fourier methods (SAD) to find the two initial thimerosal sites with the program Phaser-EP (PHENIX suite) (Adams et al., 2010). The second approach, by myself, utilized the Patterson seeding of dual-space direct methods approach to find the two initial thimerosal sites with the program SHELXD, which were subsequently refined using multiple isomorphous replacement and anomalous dispersion (MIRAS) methods of phasing with the program SHARP (autoSHARP) (Vonrhein et al., 2007). Further heavy atom sites were obtained utilizing MIRAS methods with the programs

MLPHARE (CCP4 suite) and SHARP (Bricogne et al., 2003; Otwinowski, 1991; Winn et al., 2011).

The experimental phases were improved and extended to 3.4 Å resolution using solvent flattening, histogram matching, and four-fold non-crystallographic symmetry (NCS) averaging with the program DM (CCP4 suite) (Cowtan, 1994; Winn et al., 2011). A model was built into the density-modified map using the programs O and Coot and refined with CNS using tight NCS restraints throughout refinement (Emsley and Cowtan, 2004; Jones et al., 1990). The "mlhl" refinement target was used after "blurring" of the Hendrickson-Lattman coefficients (Brunger et al., 1998; Pannu et al., 1998). In addition, dihedral angle restraints on the peptide backbone within the assigned alpha helices, as well as harmonic restraints on the selectivity filter, were applied during refinement. The MolProbity webserver was used to assess the quality of the atomic model during both model building and refinement (Chen et al., 2010).

Figures were prepared with the program PyMOL (www.pymol.org). Angle between helices at the gating glycine hinge for MthK, KcsA and $K_{2P}1$ channels was calculated using the Angle Between Helices Python Module in PyMOL. The diameter of the pore was calculated using the program HOLE (Smart et al., 1996). Buried surface interface calculation of the hydrophobic core within the extracellular cap was calculated with PISA (CCP4 suite of programs) (Krissinel and Henrick, 2007).

3.3.3. $K_{2P}1$ reconstitution into vesicles

$K_{2P}1$ was purified as described above with slight modification. Following gel filtration, the protein was incubated with cobalt affinity resin to remove a small fraction of uncut protein. The supernatant from this rebinding step was collected and concentrated to 1.5 mg/ml. Rat $K_V1.2$ with the β2.1 subunit was purified (Long et al., 2007) and concentrated to 1.5 mg/ml. The purified

channels were reconstituted from DM into lipid vesicles following a published procedure (Heginbotham et al., 1998) with modifications. In brief, a POPE (1-palmitoyl-2-oleoyl-sn-glycero-3-phosphocholine) and POPG (1-palmitoyl-2-oleoyl-sn-glycero-3-phospho-(1'-rac-glycerol)) lipid mixture (7.5 mg/ml: 2.5 mg/ml) was prepared and solubilized with 8% OM. The protein was then mixed with the solubilized lipids to give a final protein concentration of 0.1 mg/ml (1:100 protein:lipid ratio). Detergent was removed by dialyzing against a solution containing 10 mM HEPES (pH 7.0) and 150 mM KCl at 4°C for 4 days. DTT (2 mM) was added to the dialysis solution for the $K_V 1.2$ sample. The resulting protein/lipid reconstitution was flash-cooled in liquid N_2 and stored at -80°C as small aliquots. Control vesicles ("empty vesicles") were prepared in the same manner without the addition of protein prior to dialysis.

3.3.4. K^+ flux assay

The flux assay was adapted from other such assays (Feng et al., 2010; Lee et al., 2009; Zhang et al., 1994). Briefly, vesicles were thawed, sonicated for 5 seconds and diluted 40-fold into flux assay buffer, which contained 150 mM NaCl, 10 mM HEPES, pH 7.0, 0.5 mg/ml bovine serum albumin, and 2 μM 9-amino-6-chloro-2-methoxyacridine (ACMA, Sigma-Aldrich, from a 2 mM stock in DMSO). This yielded a final K^+ concentration of ∼ 3.75 mM outside the vesicles. Data were collected on a SpectraMax M5 fluorometer (Molecular Devices) using the Softmax Pro 5 software package. Fluorescence intensity was measured every 30 sec for a total of 630 sec with excitation and emission settings at 410 nm and 490 nm, respectively. The H^+ ionophore carbonyl cyanide m-chlorophenyl hydrazone (CCCP, Sigma-Aldrich; 1 μM final concentration from a 0.1 mM stock in DMSO) was added after 150 sec and the sample was gently mixed with a pipette. Valinomycin (Sigma-Aldrich; 20 nM final concentration from a 2 μM stock in DMSO) was added at 450 sec to release K^+ from all vesicles. For experiments using Ba^{2+}, 1-10 mM $BaCl_2$ was added to the vesicles before sonication and to the flux assay buffer. The flux assay for these experiments was then performed as described above.

3.4.   Results

3.4.1.   Human $K_{2P}1$ channel crystal construct forms a functional channel

To assess the function of the purified protein, human $K_{2P}1$ was reconstituted into lipid vesicles and studied with a fluorescence-based flux assay (Figure 3.1) (Feng et al., 2010; Lee et al., 2009; Zhang et al., 1994). Vesicles loaded with 150 mM KCl (pH 7.0) were diluted 40-fold into an assay buffer containing 150 mM NaCl (pH 7.0). Under these conditions, K^+ efflux through $K_{2P}1$ would produce an electric potential across the vesicle membrane that is negative on the inside of the vesicle relative to the outside. Upon addition of the H^+ ionophore CCCP to the vesicles, the electric potential drives the uptake of H^+, which is used to quench the fluorophore ACMA. Valinomycin, a K^+ ionophore, was added at the end of each experiment to establish a minimum fluorescence baseline by releasing K^+ from all the vesicles. We validated this assay using the voltage-gated K^+ channel $K_V1.2$, which has been shown to be functional after purification and reconstitution into vesicles (Long et al., 2007). A robust decrease in fluorescence was observed upon addition of CCCP to vesicles reconstituted with $K_V1.2$ or $K_{2P}1$, but not to empty (control) vesicles, indicating the presence of K^+-selective pores (Figure 3.1). To confirm that the observed fluorescence decrease was due to K^+ flux through $K_{2P}1$, we performed the assay with the addition of barium ions (Ba^{2+}), which block K^+ channels including $K_{2P}1$ (Jiang and MacKinnon, 2000; Lesage et al., 1996a; Zhou et al., 2009). In the presence of $BaCl_2$ (1-10 mM), the fluorescence decrease measured for both $K_V1.2$- and $K_{2P}1$-reconstituted vesicles was reduced in a dose-dependent manner (Figure 3.1). However, Ba^{2+} had no effect on the minimum fluorescence baseline observed after the addition of valinomycin or on the fluorescence measured from control vesicles.
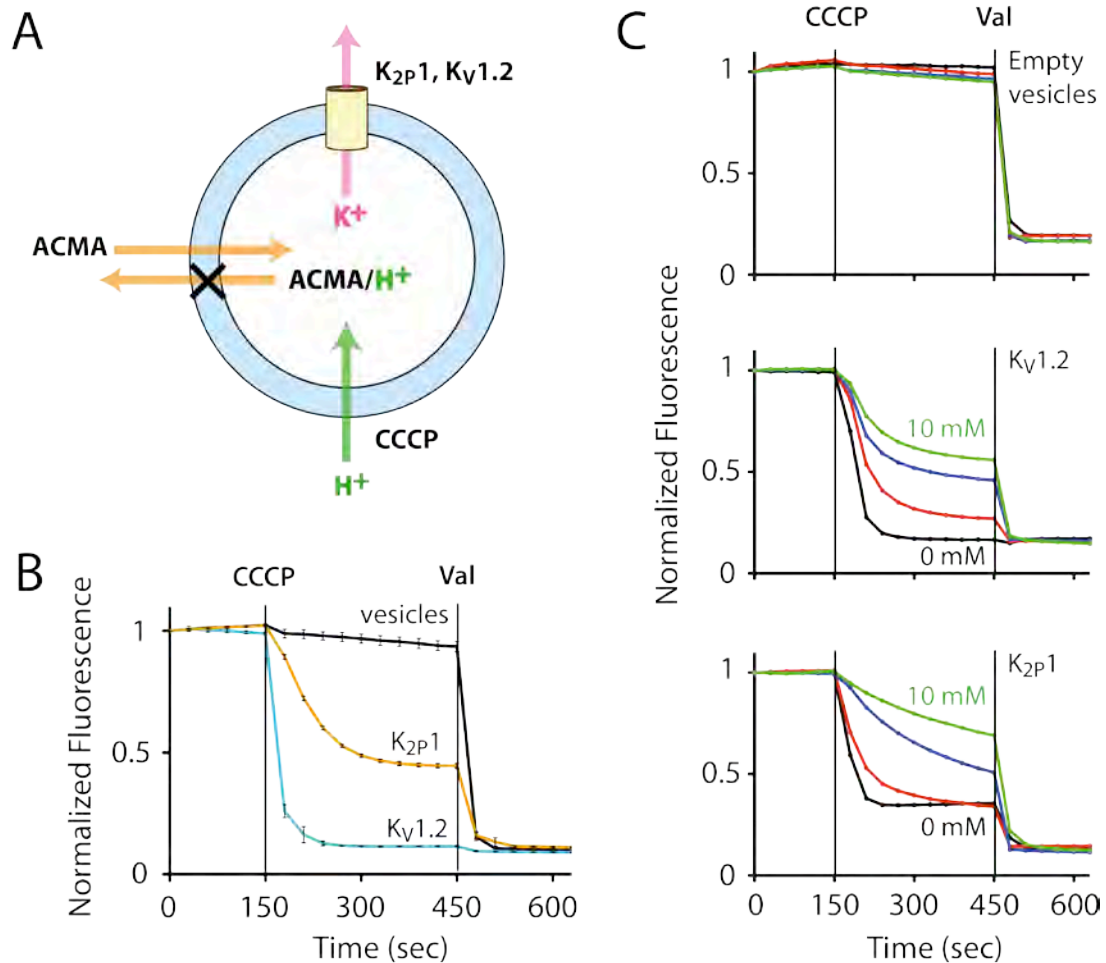
Figure 3.1: Reconstitution of $K_{2P}1$ activity. (A) Schematic of the fluorescent-based flux assay. Vesicles (blue) containing $K_{2P}1$ or $K_V1.2$ channels (yellow) were loaded with 150 mM KCl and diluted 40-fold into flux buffer containing the ACMA indicator and 150 mM NaCl to establish a K^+ gradient. After stabilization of the fluorescence signal (150 sec), CCCP, a proton ionophore was added to the sample, and an electrical potential arising from K^+ efflux was used to drive the uptake of protons into the vesicles through CCCP, which quenches the fluorescence of ACMA. The "X" indicates that ACMA is no longer membrane permeable and does not exit the vesicles in the protonated form. Valinomycin, a K^+ ionophore, was added at 450 seconds to render all vesicles permeable to K^+ and establish a minimum fluorescence baseline. Fluorescence was normalized by dividing by the initial value. (B) Fluorescence changes observed for $K_{2P}1$ (orange trace) and $K_V1.2$ (blue trace) compared with an empty vesicle control (black trace). Error bars indicate the standard error of three measurements from the mean. (C) Fluorescence changes in the presence of $BaCl_2$ (0, 1, 5 and 10 mM; black, red, blue and green traces, respectively) for $K_{2P}1$, $K_V1.2$, and empty vesicles.

3.4.2. Human $K_{2P}1$ crystal refinement and derivatization

$K_{2P}1$ 22-303 N95Q purified in DM initially crystallized in conditions containing 26-30% PEG400 (v/v); no salt, 150 mM NaCl or 150 mM KCl, in a pH range between 7.0-9.0 at 17°C. Refinement screens were made, which varied the percentage of PEG400 and pH and the best crystals, based on size and diffraction, grew in 26% PEG400, and 100 mM HEPES or Tris-HCl, pH 7.5-8.5. In addition, a number of purification and crystallization parameters were tested in order to improve crystal growth and diffraction. These parameters included purifying $K_{2P}1$ 22-303 N95Q in different detergents/lipids (OM with lipids, CYMAL-6, DM with lipids), addition of reducing agents (20 mM DTT, 10 mM TCEP), and varying protein concentration, well to drop ratios, and crystallization temperatures. From these tests, it appeared that larger crystals of $K_{2P}1$ grew at 4°C, most likely as a result of slower nucleation.

In addition, other constructs with shorter C-termini, such as $K_{2P}1$ 22-275 N95Q and $K_{2P}1$ 22-288 N95Q, were also capable of crystallizing in conditions similar to the $K_{2P}1$ 22-303 N95Q when purified in DM. In fact, $K_{2P}1$ 22-288 N95Q crystallized more readily than the other two constructs that were tested since a lower concentration of protein (5 mg/ml) was required for large crystal growth and because the construct crystallized in a greater variety conditions than the other two constructs. At 4°C, $K_{2P}1$ 22-288 N95Q purified in DM crystallized in 20-30% PEG400 with various salt additives: 200 mM calcium chloride, 200 mM ammonium sulfate, 50 mM magnesium acetate, 1 M ammonium formate, 2.3 M potassium phosphate, 100/50 mM sodium/lithium sulfate, 100 mM potassium sodium tartrate and 50 mM zinc acetate. The majority of these crystals were tested at the synchrotron and appeared to perform similarly to crystals grown in 150 mM KCl, with the exception of zinc acetate crystals (< 30 Å diffraction). All of the crystals tested, except for the zinc acetate crystals, indexed to the $P2_1$ space group, suggesting that the crystal packing was the same regardless of the salt conditions the crystal grew in. As a result, we

continued to pursue crystals that were grown in 150 mM KCl since these conditions had already been refined.

In addition to the crystallization parameters that were tested for purified $K_{2P}1$ 22-303 N95Q, detergent additives (NM, OM) and other additives (EG, glycerol, MPD, xylitol, sucrose, and trehelose) were tested for $K_{2P}1$ 22-288 N95Q. None of these additives or other modifications improved crystal diffraction, with the exception of temperature. The best-diffracting $K_{2P}1$ 22-288 N95Q crystals grew in 24 well trays (3 μl protein and 3 μl well solution) conditions containing 18-20% PEG400, 150 mM KCl, 100 mM HEPES, pH 8.0 at 4°C. During crystal harvesting, dehydration was tested as a method for improving crystal diffraction (Kuo et al., 2003). Crystals were simultaneously dehydrated and cryo-protected with reservoir solution supplemented with 50% PEG400, 5 mM DM and 20 mM Tris-HCl, pH 7.5 in a step-wise manner (see 3.3.1 Crystallization conditions, refinement, and heavy atom derivatization). Crystal dehydration dramatically improved crystal diffraction from ~ 6 Å to 4 Å resolution.

For heavy atom derivatization, both co-crystallization and soaking methods were performed. Tl^+-derivatized crystals were soaked by an initial transfer to a solution containing potassium nitrate, since thallium precipitates in the presence of chloride. These crystals were then transferred into a solution containing a mixture of 75 mM KNO_3 and 75 mM $TlNO_3$ (1 mM). For the other heavy atom tested, including thimerosal, $KAu(CN)_2$, $GdCl_3$, EMP, and $K_2Pt(CN)_4$, the heavy atom (2 mM) was combined with the purified protein prior to setting up the crystallization trials. $GdCl_3$ and EMP both inhibited crystal growth, while crystals were able to grow in the presence of thimerosal, $KAu(CN)_2$ and $K_2Pt(CN)_4$.

3.4.3. Human $K_{2P}1$ structural determination

Data collected from six $K_{2P}1$ 22-288 N95Q crystals were combined to generate a highly

	Native	**Derivative 1** thimerosal	**Derivative 2** $KAu(CN)_2$	**Derivative 3** $Tl(NO_3)$
Data collection	NSLS X25	NSLS X25	NSLS X25	NSLS X25
Wavelength (Å)	1.100	0.980	1.000	0.950
Space group	$P2_1$	$P2_1$	$P2_1$	$P2_1$
Cell dimensions:				
a, b, c (Å)	82.1, 123.2, 119.3	83.4, 124.4, 120.6	82.9, 123.2, 120.2	83.8, 124.6, 121.3
α, β, γ (°)	90, 94.9, 90	90, 94.3, 90	90, 94.5, 90	90, 94.0, 90
Resolution (Å)	50-3.4 (3.46-3.4)	50-4.4 (4.48-4.4)	50-4.1 (4.17-4.1)	50-4.3 (4.37-4.3)
No. of crystals	6	1	1	1
R_{sym} (%)	5.7 (>100)	8.8 (79.5)	5.7 (90.0)	5.4 (74.7)
I/σI	38.5 (2.1)	16.6 (1.4)	23.7 (1.2)	26.7 (1.7)
Completeness (%)	99.9 (100.0)	99.7 (99.9)	99.7 (99.9)	99.8 (100.0)
Redundancy	12.8 (12.0)	3.4 (3.5)	3.4 (3.3)	3.5 (3.7)
MIRAS Phasing				
No. of sites		14	12	19
Phasing power (acentric/centric)		1.23 / 0.70	0.94 / 0.55	0.89 / 0.54
R_{cullis} (iso/ano)		0.81 / 0.90	0.86 / 0.98	0.89 / 0.90
Figure of Merit (MLPHARE)	0.519 [50-6.0Å]			
Figure of Merit (DM)	0.779 [50-3.4Å]			
Refinement				
Resolution (Å)	20-3.4 Å			
Reflections $|F| > 0$ σF	29,136			
R_{work} (%)	27.3			
R_{free} (%)	27.9			
No. atoms/ B factor (Å^2)				
protein	7544 / 184.9			
K+	10 / 139.2			
acyl	44 / 137.8			
water	8 / 134.3			
Ramachandran (%) favored / outliers	94.1 / 0 [*]			
MolProbity score (percentile)	99th [*]			
r.m.s.d:				
bond lengths (Å)	0.009			
bond angles (°)	1.40			

Table 3.1: Data collection statistics are from HKL2000. Rsym $= \Sigma \, | \, Ii \, - <Ii> \, | \, / \, \Sigma \, Ii$, where $<Ii>$ is the average intensity of symmetry equivalent reflections. Phasing power = RMS $(|F|/\varepsilon)$, where $|F|$ is the heavy-atom structure factor amplitude and ε is the residual lack of closure error. Rcullis is the mean residual lack of closure error divided by the dispersive or anomalous difference. Rfactor $= \Sigma \, | \, Fobs - Fcalc \, | \, / \, \Sigma \, | \, Fobs \, |$, where Fobs and Fcalc are the observed and calculated structure factor amplitudes, respectively. Rfree = Rfactor calculated using a subset (~5%) of reflection data chosen randomly and omitted throughout refinement. Figure of merit is indicated from MIRAS analysis in MLPHARE and after density modification and phase extension starting from 6.0 Å in DM. R.m.s.d: root mean square deviations from ideal geometry. Numbers in parentheses indicate the highest resolution shells and their statistics. * The MolProbity and Ramachandran scores were also generated, for validation purposes, after refinement of the final coordinates without using secondary structure restraints. This yielded 92.0% of residues in Ramachandran favored regions and no outliers, and a MolProbity score of 95th percentile.

redundant native dataset in order to improve the final resolution of $K_{2P}1$ by the addition of weak reflections (Table 3.1) (Otwinowski and Minor, 1997). The crystals indexed to the space group $P2_1$, with systematic absences present at the expected Miller indices for this space group ((0k0), k = 2n + 1). The crystals contain four $K_{2P}1$ subunits, or two complete channels, in the asymmetric unit, with a solvent content of 74% and Matthew's coefficient (V_M) calculated to ~ 5 $Å^3$/Dalton, which is within the range expected for a crystallized, detergent-solubilized membrane protein (Schulz, 2011). In addition, datasets were collected for $K_{2P}1$ 22-288 N95Q crystals that were derivatized by either co-crystallization or soaking with thimerosal (2 mM, mercury derivative), $KAu(CN)_2$ (2 mM), $K_2Pt(CN)_4$ (2 mM), and $TlNO_3$ (75 mM) for obtaining experimental phases. An anomalous signal, based on 'anomalous measurability,' could be detected from the thimerosal, $KAu(CN)_2$, and $TlNO_3$ derivatized crystals, but not the $K_2Pt(CN)_4$ derivatized crystals, as evaluated using the program Xtriage (PHENIX suite) (Adams et al., 2010). The three datasets with anomalous measurability were also isomorphous to the native crystals with Rmerge values of 8.8% for thimerosal, 5.7% for $KAu(CN)_2$ and 5.4% for $TlNO_3$ (Table 3.1). These data sets were utilized for phase determination with a combination of isomorphous replacement and anomalous dispersion methods (MIRAS).

The initial phases could be obtained with two independent approaches. One approach involved the molecular replacement (MR) phasing method, using the Kv1.2 pore as a search model from the high-resolution Kv1.2-Kv-2.1 paddle chimera structure (PDB ID: 2R9R). With assistance from the MR phases, several thimerosal sites were located using single wavelength anomalous dispersion Fourier methods (SAD) with the program Phaser-EP (PHENIX suite) (Adams et al., 2010). The second approach utilized the Patterson seeding of dual-space direct methods approach with the program SHELXD, and two initial thimerosal sites were located and subsequently refined using MIRAS phasing with the program SHARP (autoSHARP) (Vonrhein et al., 2007). The phases calculated from the thimersol sites were used to identify sites in the $KAu(CN)_2$ and

TlNO$_3$ derivatives using MIRAS with the programs MLPHARE (CCP4 suite) and SHARP (Bricogne et al., 2003; Otwinowski, 1991; Winn et al., 2011). A total of 14 mercury, 12 gold, and 19 thallium were used in the MIRAS phase calculation (50-6.0 Å resolution) (Table 3.1).

The experimental phases were improved and extended to 3.4 Å resolution using solvent flattening, histogram matching, and four-fold non-crystallographic symmetry (NCS) averaging with the program DM (CCP4 suite) (Cowtan, 1994; Winn et al., 2011). With these improved phases, a model was built into the density-modified map using the programs O and Coot. Mercury and gold coordinated with cysteine residues in M2, M3 and M4 helices and assisted with model building. In addition, thallium sites were identified within the K$_{2P}$1 selectivity filter, as was expected since K$^+$ channels are typically permeant to thallium ions and because thallium has been previously utilized for crystallography studies of the KcsA selectivity filter (Zhou and MacKinnon, 2003).

The initial model was refined with CNS using tight NCS restraints throughout refinement (Emsley and Cowtan, 2004; Jones et al., 1990). The "mlhl" refinement target, which uses both structure factor amplitudes and experimental phases, was used after "blurring" of the Hendrickson-Lattman coefficients to minimize the overestimation of phase probability distribution that is introduced during density modification (Brunger et al., 1998; Pannu et al., 1998). This resulted in an inproved Rfree value and reduced the separation between the Rfree and Rwork values. This is in comparison to refinement strategies that used only the structure factor amplitudes ("mlf" or "mli") during refinement, which are more often used with MR solutions since they contain no experimental phase information. During refinement, the secondary structure of alpha helices was restrained by applying dihedral angle restraints on the peptide backbone within the helices. The regions in which the secondary structure restraints were applied were selected by inspection of the electron density, and test refinements without the restraints were

110

used to guide this selection. In addition, harmonic restraints were applied to the selectivity filter and initial modeling of this region was guided by the $K_V1.2$-K_V-2.1 chimera structure (Long et al., 2007). The use of these additional restraints yielded a model with a lower Rfree value. The quality of the atomic model was monitored throughout model building and refinement using the MolProbity webserver (Chen et al., 2010). The final structure yielded a model with good stereochemistry and an Rfree value of 27.9% (Table 3.1) (Figure 3.2).

The final model contains residues 22-281 of human $K_{2P}1$, excluding residues 94-99 and 169-174, which did not have well enough defined electron density to confidently direct model building. Likewise, residues following the C helix (282-288) were disordered. The atomic model includes 5 additional residues at the N-terminus from the vector, three of which are identical to $K_{2P}1$ sequence (residues 19-21). A number of side chains on solvent exposed surfaces of the channel were truncated in the atomic model because the electron density was not sufficient for placement, whereas all of the residues within the transmembrane region have fully modeled side chains.

3.4.4. One K_{2P} channel protomer contains two pore domains in tandem

Tetrameric K^+ channels, which include K_V and K_{IR} channels, are assembled from four protomers, each of which contains a structural region that form the ion conduction pore, called the pore (P) domain. The P domain is comprised of the outer transmembrane helix, pore helix, K^+ selectivity filter, and inner transmembrane helix (Figure 1.3, Figure 1.4). In the case of $K_{2P}1$ channels, one protomer consists of two P domains connected in tandem (P domains 1 and 2) and each K_{2P} channel protomer contain four transmembrane helices (Figure 1.3, Figure 3.3). Transmembrane helices 1 and 2 (M1, M2) comprise the outer and inner helices of P domain 1 and transmembrane helices 3 and 4 (M3, M4) comprise the P domain 2 outer and inner helices.
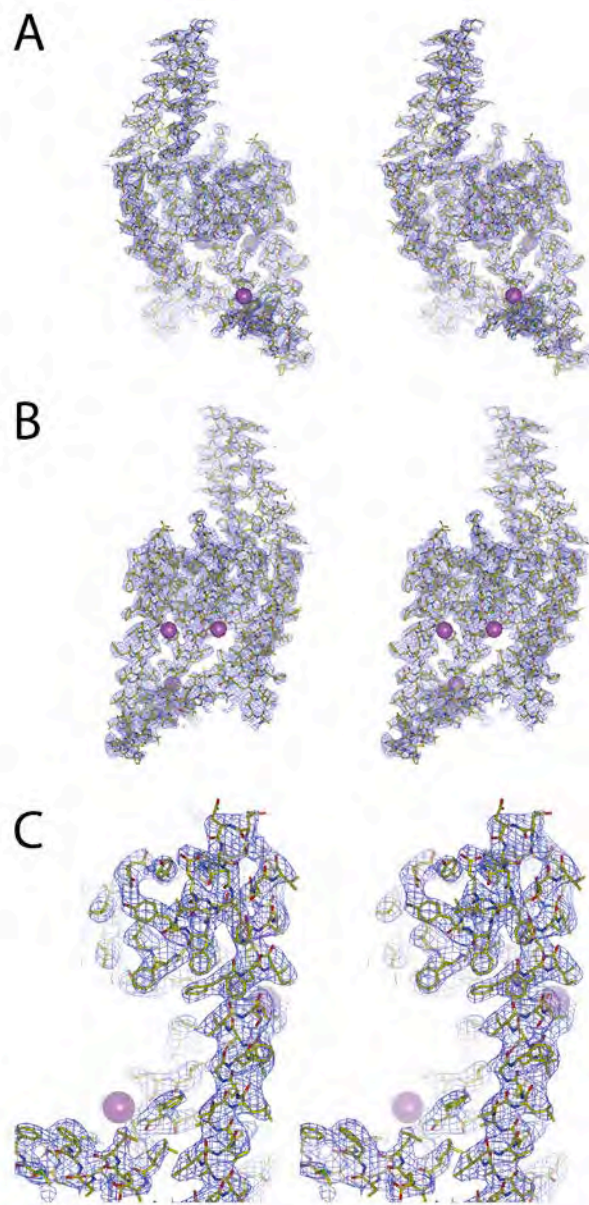
Figure 3.2: K$_{2P}$1 experimental electron density map. Stereo representations of the experimental electron density map (blue mesh) contoured at 1.5 σ for one protomer of the final model (stick representation). The map was calculated from 50 – 3.4 Å resolution using native, *B*-factor sharpened amplitudes and MIRAS solvent flattened, NCS averaged phases. Spheres represent the location of heavy atom binding sites (gold and mercury) adjacent to cysteine residues (cysteine 194, cysteine 251, and cysteine 268) that assisted with model building. (A) Side view of a complete subunit from the side, with the extracellular side above. The extracellular cap, selectivity filter and C-terminal helix are in the foreground. (B) View of the subunit rotated 180° relative to (A) with the extracellular solution above. The transmembrane helices are in the foreground. (C) Close up view of a portion of the electron density.
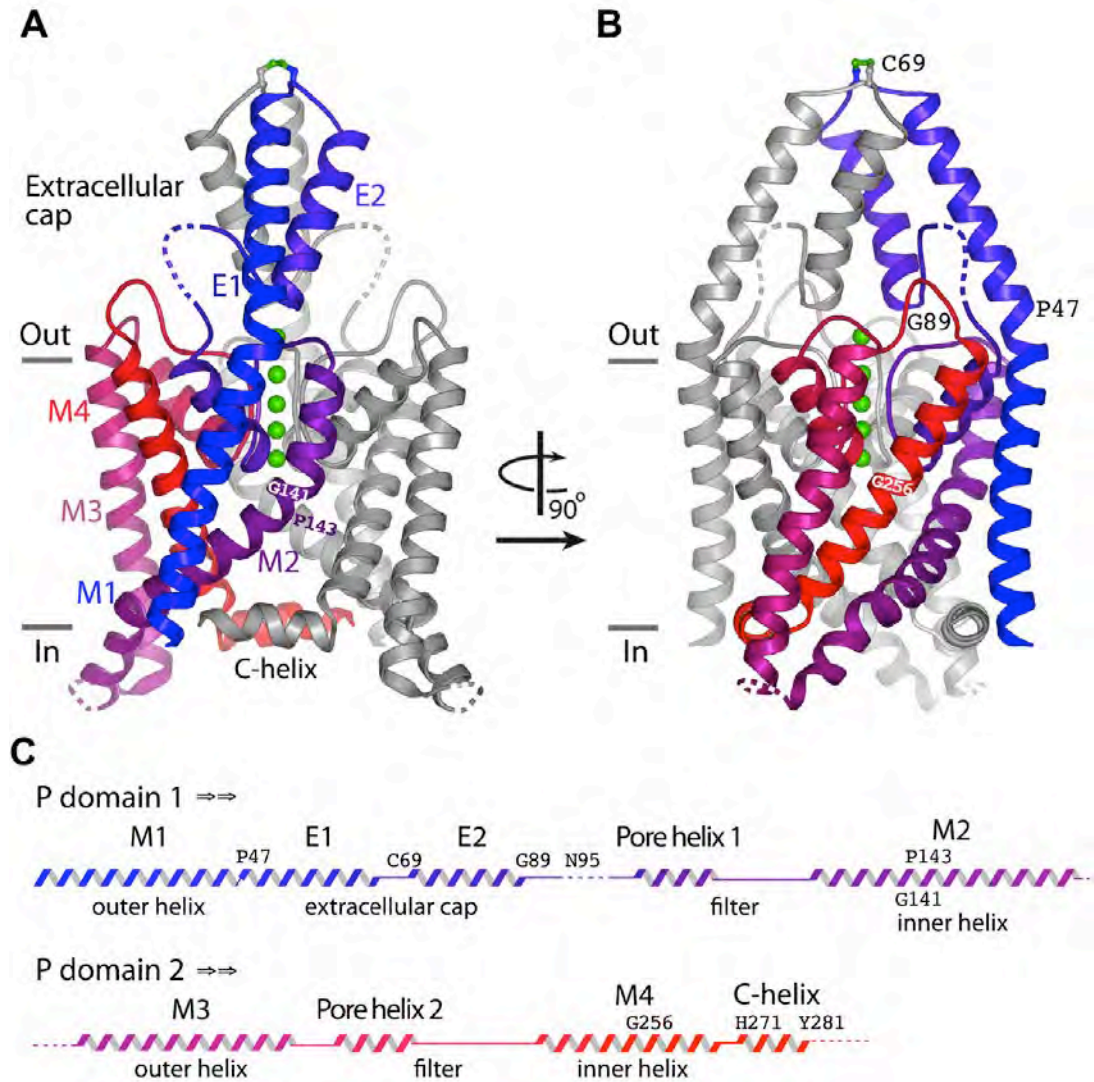
Figure 3.3: Tertiary and secondary structures of $K_{2P}1$. (A) Tertiary structure of $K_{2P}1$, showing a ribbon representation from the side. One protomer is colored blue-to-red from the N- to the C- terminus, and the other protomer is gray. K^+ ions are depicted as green spheres. Approximate boundaries of the lipid membrane are shown as horizontal lines with extracellular (out) and intracellular (in) sides denoted. The intersubunit disulfide bond (involving Cys69) at the apex of the extracellular cap is colored green. Loop regions not included in the final model are drawn as dashed lines. (B) An orthogonal view of the channel from the side. (C) Secondary structure of $K_{2P}1$ colored according to (A). Dashed lines indicate disordered regions. Residues discussed in the text are labeled.

3.4.5.   Human K$_{2P}$1 recapitulates the structural hallmarks of K$^+$ channels

The fundamental features observed in tetrameric K$^+$ channel structures are conserved in the human K$_{2P}$1 structure and include a K$^+$ selectivity filter, central cavity, and inner helices lining the channel pore (Figure 3.3). The selectivity filter in tetrameric K$^+$ channels is comprised of four filter signature sequences ('canonical' sequence: Thr-x-Gly-Tyr-Gly-Asp with x representing an aliphatic residue; TxGYGD) with backbone carbonyls or side-chain hydroxyl groups participating in K$^+$ coordination (see 1.3.1 K$^+$ channel selectivity) (Figure 1.4). The central cavity is an aqueous vestibule that is located directly below the selectivity filter in the center of the ion conduction pore. In the KcsA crystal structure, the central cavity contains a hydrated K$^+$ that is stabilized by electrostatic interactions with water and by the four pore helices with the negative ends of their helix dipole moments positioned toward the cavity (Figure 1.5) (Doyle et al., 1998; Roux and MacKinnon, 1999; Zhou and MacKinnon, 2004b). The inner helices of K$^+$ channels line the pore and form the activation gate (see 1.3.2 K$^+$ channel gating) (Figure 1.7). Although the structural hallmarks of tetrameric K$^+$ channels are preserved in the human K$_{2P}$1 structure, the dimeric architecture of K$_{2P}$1 accommodates a number of features that may be critical for function of this subfamily of K$^+$ channels.

3.4.6.   Network of non-covalent interactions surrounding the K$_{2P}$1 selectivity filter

Although human K$_{2P}$1 is dimeric, the ion coordination within the selectivity filter maintains four-fold symmetry and the residues within the filter sequence adopt a conductive conformation, at the limit at which the atomic coordinates could be determined (Figure 3.4). Conservation of the fold-fold symmetry is not surprising since the selectivity filter is the most conserved region of K$^+$ channels. Within each K$_{2P}$1 protomer however, residues that comprise the filter sequence of P domain 1 (Thr-Thr-Gly-Tyr-Gly-His; TTGYGH) and P domain 2 (Thr-Ile-Gly-Leu-Gly-Asp; TIGLGD) differ from one another and do not conform to the 'canonical' filter sequence. As a
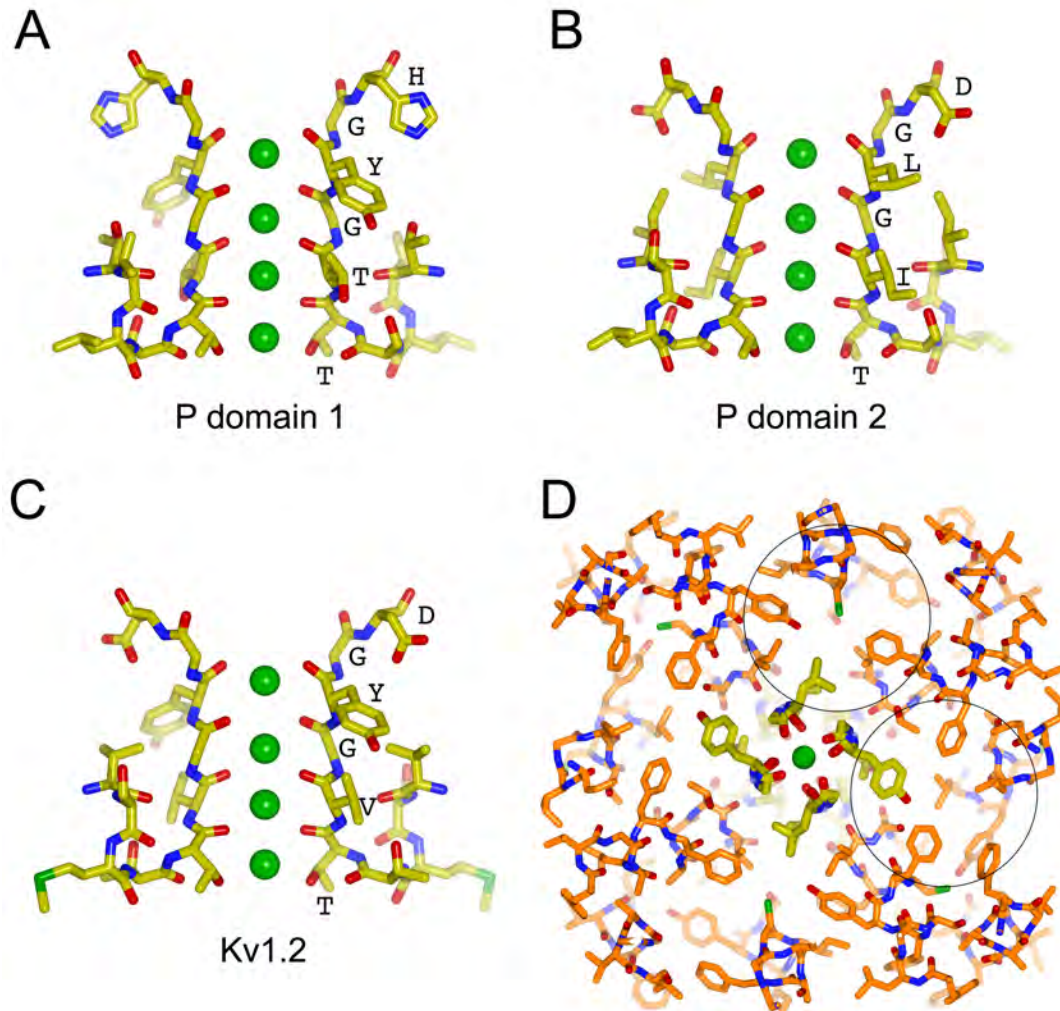
Figure 3.4: $K_{2P}1$ selectivity filter and residue packing surrounding the filter. Conformation of residues comprising the $K_{2P}1$ selectivity filter from P domain 1 (A) and P domain 2 (B) compared with the conformation of residues within the $K_V1.2$ selectivity filter (C) (PDB ID 2R9R). Two subunits are shown from the side, with the extracellular solution located above. The filter sequence is labeled in single letter amino acid code (D, Asp; G, Gly; H, His; I, Ile; L, Leu; T, Thr; V, Val; Y, Tyr). Residues are drawn as colored sticks (yellow, carbon; blue, nitrogen; red, oxygen; and green, sulfur), and K^+ ions are shown as green spheres. (D) Depiction of a ~10 Å-thick cross section of $K_{2P}1$, viewed from the extracellular side, showing the packing of residues (orange carbons) surrounding the selectivity filter (yellow carbons). Circles highlight differences in packing surrounding the selectivity filter residues of P domains 1 and 2.

result, the network of non-covalent interactions surrounding the selectivity filter which stabilize its configuration are two-fold symmetric (Figure 3.4).

The filter sequence of P domain 1 harbors two residues that deviate from the canonical pore sequence, threonine 118 (T118) and histidine 122 (H122) which replace the hydrophobic amino acid and aspartic acid, respectively. T118 is a residue that is unique to $K_{2P}1$ since it is not conserved in K_{2P} channels (Figure 2.9). T118 is typically an aliphatic residue (often valine or isoleucine) that makes a hydrophobic contact with the conserved tyrosine in the TxGYGD motif (Figure 3.5). Previous studies support the role of T118 in altering K^+ selectivity of human $K_{2P}1$ channels in a hypokalemic environment (low extracellular K^+, < 3 mM) (Ma et al., 2011; Ma et al., 2012a). In the human $K_{2P}1$ crystal structure, T118 γ oxygen forms a hydrogen bond with a main chain carbonyl of serine 222 (S222), located on the pore helix of P domain 2, and this interaction most likely introduces additional stability to this region of the filter (Figure 3.5).

In the crystal structures of KcsA, MthK and $K_V1.2$, the aspartic acid within the selectivity filter sequence (D375 δ2 oxygen in $K_V1.2$) forms a hydrogen bond with a tryptophan or tyrosine located in the pore helix of the same protomer (W362 ϵ nitrogen in $K_V1.2$) (Figure 3.6) (Long et al., 2007; Ye et al., 2010; Zhou et al., 2001b). Although the selectivity filter asparatic acid is not conserved within the K_{IR} family, it is typically substituted for a large hydrophobic residue such as phenylalanine or tyrosine. This residue is positioned toward the extracellular space and does not form a hydrogen bond with any other residues, as observed in the crystal structures of $K_{IR}2.2$ (F148) and $K_{IR}3.2$ (Y159) (Figure 3.6) (Tao et al., 2009; Whorton and MacKinnon, 2011). However, the subsequent arginine (R149 and R160 η nitrogens in $K_{IR}2.2$ and $K_{IR}3.2$, respectively) forms a salt bridge with a highly-conserved glutamic acid located within the pore helix (E139 and E150 ϵ2 nitrogen in $K_{IR}2.2$ and $K_{IR}3.2$, respectively) and mutations in this region

A   P1   P2

G121
Y120
S222   2.5Å   3.8Å   G119
3.5Å
2.9Å   T118
T117

K$_{2P}$1 P1

B   P2   P1

V124
F110   L228   G229
4.2Å
4.4Å
V114   4.1Å   G227
I226
T225

K$_{2P}$1 P2

C

G374
Y373
S367   2.5Å   3.7Å   G372
V371
3.1Å
T370
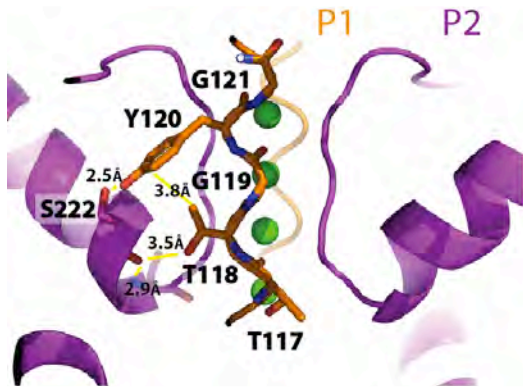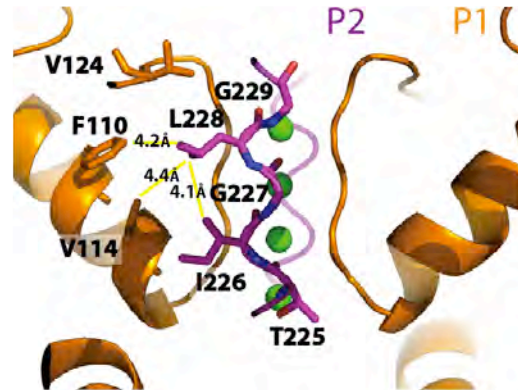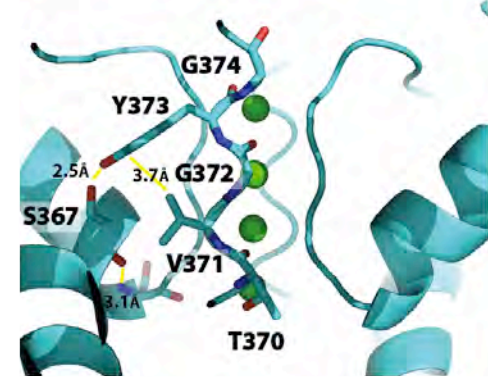
K$_{V}$1.2

Figure 3.5: Comparison of residue packing (threonine 118, leucine 228) surrounding the selectivity filter of $K_{2P}1$. Cutaway side views of $K_{2P}1$ (A-B) and $K_V1.2$ (C) (PDB ID: 2R9R) selectivity filters with extracellular solution above. (A) Packing of $K_{2P}1$ filter residues from P domain 1 (orange carbons) drawn in colored stick representation (blue, nitrogen; red, oxygen). P domain 2 residues (purple carbons) that participate in interactions with filter residues are drawn as sticks with similar coloring to P domain 1. Residue interactions are drawn with yellow lines. The remaining structure is depicted in ribbon representation with K^+ ions shown as green spheres. The filter sequence is labeled in single letter amino acid code (G, Gly; I, Ile; L, Leu; T, Thr; V, Val; Y, Tyr). (B) Packing of $K_{2P}1$ filter residues from P domain 2 with similar structural representation, coloring and labeling as in (A). (C) Packing of $K_V1.2$ filter residues (cyan carbons) drawn as sticks with coloring similar to (A). Residues from an adjacent pore helix that participate in interactions with filter residues are drawn are sticks.

A — K$_{2P}$1

P1
T123
3.1Å 4.3Å
G121   E235
H122
Y120
P2

B — K$_V$1.2

D375
G374   2.9Å
Y373
W362

C — K$_{IR}$2.2

F148
G147   R149
Y146   E139
2.4Å
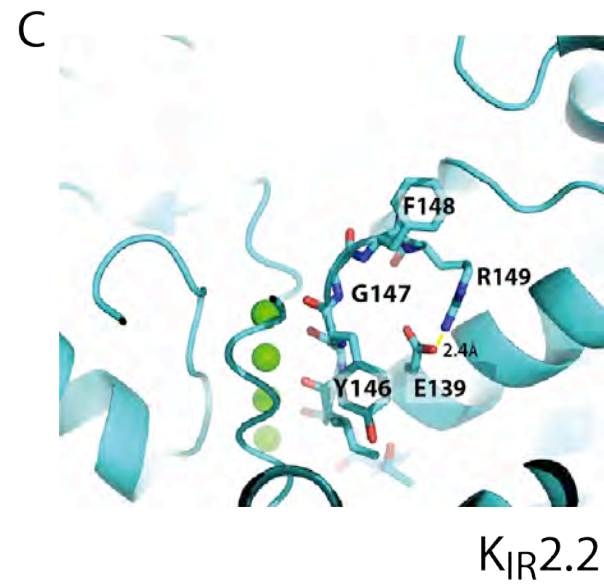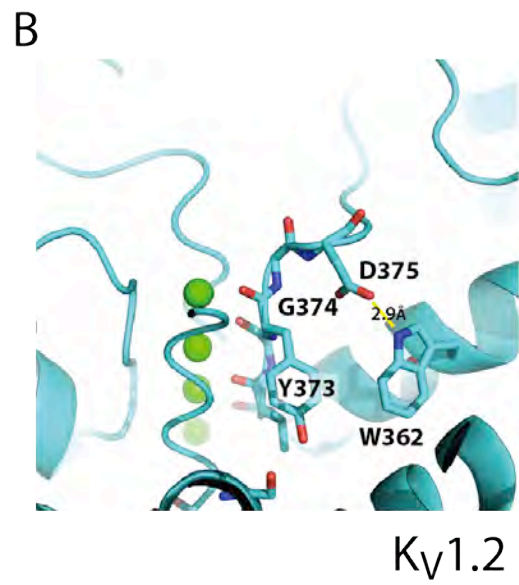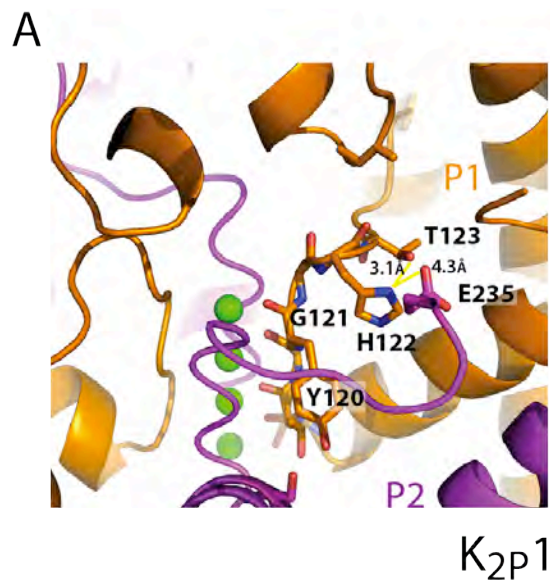
Figure 3.6: Comparison of residue packing (H122) surrounding the selectivity filter of $K_{2P}1$. Cutaway views of human $K_{2P}1$ (A), rat $K_V1.2$ (B) and chicken $K_{IR}2.2$ (C) selectivity filters viewed from the extracellular side. (A) Packing of $K_{2P}1$ filter residue H122 from P domain 1 (orange carbons) drawn in colored stick representation (blue, nitrogen; red, oxygen). P domain 2 residues (purple carbons) that participate in interactions with filter residues are drawn as sticks with similar coloring to P domain 1. Residue interactions are drawn with yellow lines. The remaining structure is depicted in ribbon representation with K^+ ions shown as green spheres. The filter residues, and residues involved in interactions, are labeled in single letter amino acid code (D, Asp; E, Glu; G, Gly; H, His; T, Thr; R, Arg; W, Trp; Y, Tyr). (B) Packing of $K_V1.2$ filter residue D375 (cyan carbons) drawn as sticks with coloring similar to (A). Packing of $K_{IR}2.2$ filter residue F148, and subsequent residue R149 (cyan carbons), drawn as sticks with coloring similar to (A).

are known to alter channel function (Figure 3.6) (Tao et al., 2009; Whorton and MacKinnon, 2011). Like K_{IR} channels, the selectivity filter aspartic acid in P domain 1 of K_{2P} channels is commonly replaced with histidine or asparagine (Figure 2.9, Figure 3.6). H122 of human $K_{2P}1$ forms a hydrogen bond with an adjacent residue, threonine 123 (T123) and, as a result, is not stabilized with contacts to the pore helix in P domain 1 (Figure 3.6). However, the analogous residue in P domain 2 of human $K_{2P}1$ is an aspartic acid (D230) which hydrogen bonds with the pore helix tyrosine (Y217) and both of these residues are fully conserved within the K_{2P} family (Figure 2.9).

The tyrosine residue within the P domain 2 selectivity filter sequences of K_{2P} channels is replaced with either a phenylalanine or leucine (Figure 2.9, Figure 3.5). This residue (Y373 η oxygen, $K_V1.2$) forms a hydrogen bond in tetrameric K^+ channels with a highly-conserved serine or threonine residue (S367 γ oxygen, $K_V1.2$) located in the pore helix of an adjacent protomer, in addition to contributing to a hydrophobic network of interactions (Figure 3.5) (Long et al., 2007; Tao et al., 2009; Zhou et al., 2001b). In contrast, the analogous residues to Y373 and S367 in the human $K_{2P}1$ structure are leucine 228 (L228) and valine 114 (V114), respectively, both of which are hydrophobic residues. This region of the channel, as a result, extends a hydrophobic network with isoleucine 221 (I221, pore helix residue) and isoleucine 226 (I226, filter residue) located within P domain 2, and phenylalanine 110 (F110, pore helix residue) and valine 124 (V124), both contributed from the adjacent protomer P domain 1 (Figure 3.5). A protein sequence alignment of K_{2P} channels confirms that V114, like L228, is a conserved non-polar residue in P domain 1, suggesting that L288 and V114 are residues that co-evolved, as has been previously observed for positions surrounding the K^+ selectivity filter (Lockless et al., 2007). Interestingly, the atomic distance between the L228 δ2 carbon atom and the V114 Cγ2 carbon atom in the $K_{2P}1$ structure is 4.4 Å, which is greater than the length of the hydrogen bond that is typically observed in this position (Figure 3.5). However, unlike the P domain 2 selectivity filter sequence, P domain 1

retains the consensus tyrosine residue (Y120 η oxygen) and forms a hydrogen bond with serine 222 (S222 γ oxygen), located within the pore helix of P domain 2 (Figure 3.5).

Overall, the asymmetry of hydrophobic and hydrogen bond interactions between $K_{2P}1$ channel P domains 1 and 2 are a consequence of filter sequence difference between the P domains. The deviation of the $K_{2P}1$ channel filter sequences from the canonical selectivity filter sequence also introduces an altered packing arrangement that may have K_{2P}-specific functional implications.

3.4.7.   Direct link between the lipid bilayer and the $K_{2P}1$ pore via the central cavity

The central cavity is another conserved feature of K^+ channels that is important for stabilizing the electrostatic charge of K^+ within the channel pore (Doyle et al., 1998; Roux and MacKinnon, 1999; Zhou and MacKinnon, 2004b). The central cavity of human $K_{2P}1$ has similarities with what has been observed in tetrameric K^+ channel structures. However, the two-fold symmetry of K_{2P} channels also introduces a feature that has not been reported previously. Two openings within $K_{2P}1$ transmembrane molecular surface directly expose the central cavity to the lipid bilayer. (Figure 3.7). These openings are formed at the interface between two subunits, whereas the molecular surface is sealed within a protomer (Figure 3.7). Proline 143 (P143), conserved in most K_{2P} channel family members, introduces a 20° helical bend within M2, the inner helix of P domain 1, which accommodates the intramembrane openings (Figure 3.7, Figure 3.8). Furthermore, electron density maps revealed tubes of density spanning across the intramembrane openings, parallel to the plane of the lipid bilayer (Figure 3.7). Although we were unable to unequivocally identify the molecule within the density, the size and shape of the density is consistent with two alkyl chains that are each approximately 11 carbons in length (Figure 3.7). We attribute this density to either lipid molecules that co-purified with human $K_{2P}1$ or with detergent molecules introduced throughout the purification (DDM or DM). The direct connection of the ion conduction pore to the lipid bilayer via these openings suggests a potential region for
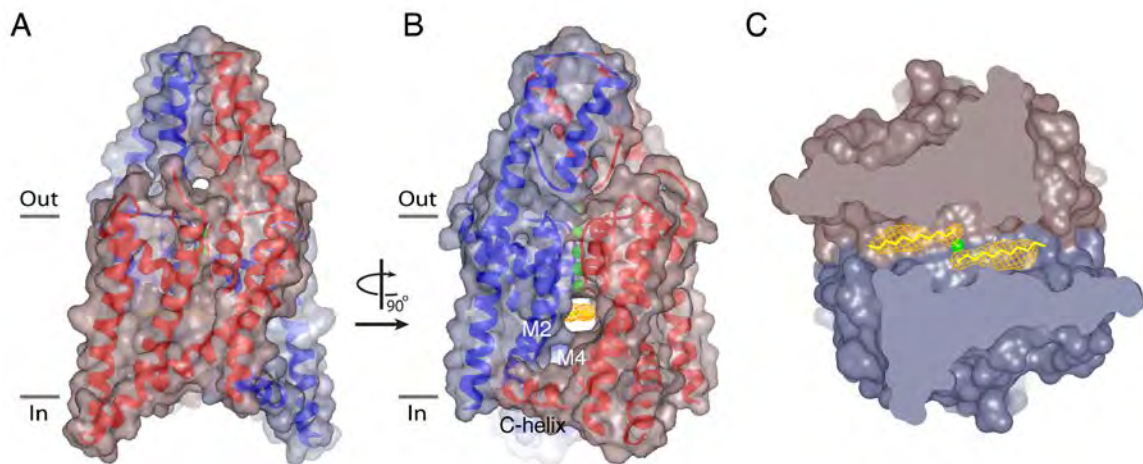
Figure 3.7: Molecular surface of $K_{2P}1$ introduces intramembrane openings within the interface between protomers. (A) View of the molecular surface with ribbon representation of the channel, from the side. One protomer is colored blue and the other red. K^+ ions in the selectivity filter are depicted as green spheres. (B) Orthogonal view from the side. Electron density (orange mesh, Fo-Fc simulated annealing omit map calculated from 20 to 3.4 Å resolution and contoured at 3 σ) is observed within an opening between the protomers. (C) Cutaway view of the molecular surface viewed from the intracellular side. Electron density (orange mesh), calculated as in (B), is shown with two 11 carbon alkyl chains modeled into the density (yellow sticks).
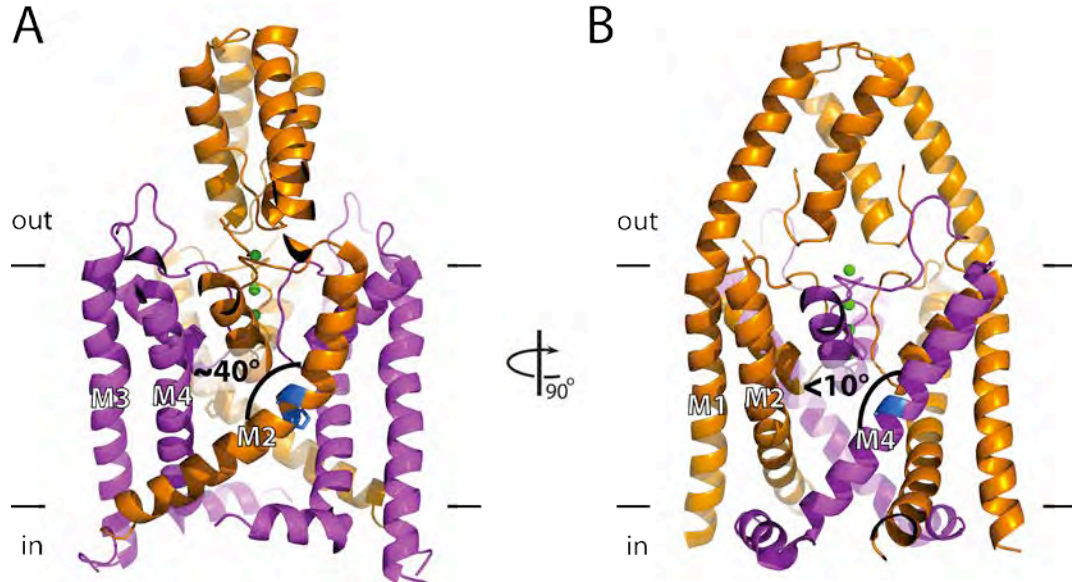
Figure 3.8: Bending observed in $K_{2P}1$ inner helices. (A) P domain 1 inner helix. Cutaway ribbon representation of $K_{2P}1$ viewed from the side, with approximate boundaries of the lipid membrane depicted as horizontal lines with extracellular (out) and intracellular (in) sides denoted. P domain 1 and 2 are colored orange and purple, respectively, in each protomer. Transmembrane helices (M1-4) from one protomer are labeled. Residues which accommodate inner helical bend are highlighted in blue. (B) P domain 2 inner helix. Orthogonal view of the channel from the side with coloring similar to (A). Transmebrane helix 4 (M4) from one protomer and transmembrane helices 1-2 (M1-2) from the adjacent protomer are labeled.

interaction with lipids and other hydrophobic molecules and also for sensing mechanical stress, as has been documented for the K_{2P} family member TREK-1 ($K_{2P}2$) (Patel et al., 2001).

3.4.8. Inner helix gating and an interfacial C helix

The inner helices (M2 and M4) of human $K_{2P}1$ are separated by >11 Å at the narrowest point, a distance which is greater than the diameter of a hydrated K^+ ion (~ 6 Å), suggesting that the channel is crystallized in an open conformation (Figure 3.9, Figure 3.10). Furthermore, the human $K_{2P}1$ inner helices are positioned closer to open (MthK and $K_V1.2$) versus closed (KcsA) inner helices when superimposed with other published K^+ channel structures (Figure 1.6, Figure 3.10). Conformational movements of inner helices in tetrameric K^+ channel are facilitated by a conserved gating hinge glycine within M2 (see 1.3.2 K^+ channel gating). This glycine is also observed in human $K_{2P}1$ (Gly 141 and Gly 256 located in M2 and M4, respectively; G141, G256) and is conserved within the K_{2P} family, as evaluated by an alignment of K_{2P} family members and $K_V1.2$ (Figure 2.9). In the human $K_{2P}1$ crystal structure, the degree of bending at the gating glycine hinges is different between P domains 1 and 2, with a ~20° helices kink at G141 and a shallower, < 10° bend at G256 (Figure 3.8). In addition to the 20° bend contributed by G141, an additional kink of ~20° is introduced by P143 of M2 and, as a result, creates a significant asymmetry between the inner helices within a K_{2P} protomer (total M2 bend of 40°, total M4 bend of 10°) that could have functional implications on the activation gate of K_{2P} channels.

Continuing from M4 of $K_{2P}1$ from a ~ 90° bend at histidine 271 (H271) is an amphipathic helix (C helix) that runs parallel to the cytosolic side of the membrane (Figure 3.9). Although interfacial cytosolic helices have been previously observed in crystal structures of prokaryotic NaK and eukaryotic K_V and K_{IR} channels, they have been connected to the outer helices of these channels (Jiang et al., 2003; Long et al., 2005; Nishida et al., 2007; Tao et al., 2009). The C helix
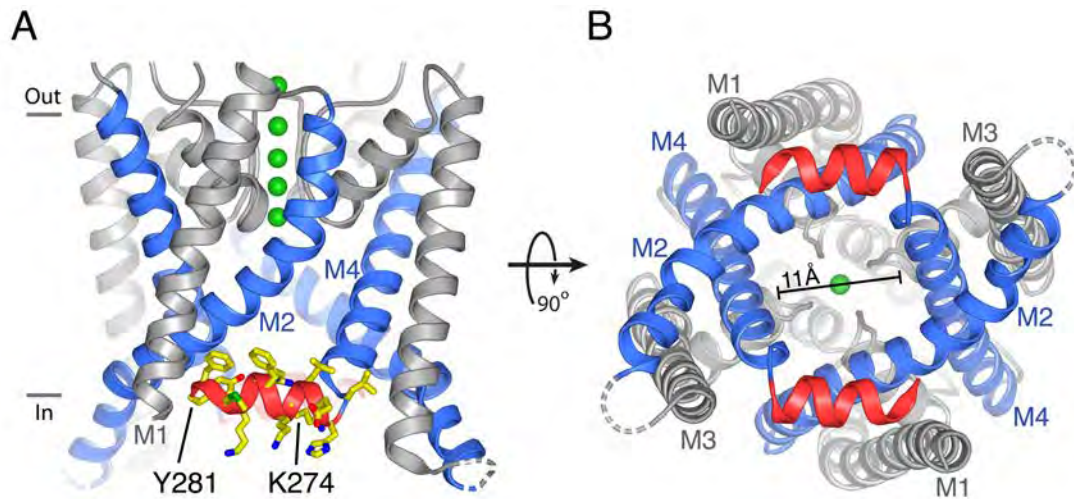
Figure 3.9: K$_{2P}$1 interfacial C helix. Ribbon representation of the transmembrane and intracellular regions of K$_{2P}$1 viewed from the membrane (A) and intracellular side (B). The inner helices are colored blue and labeled (M2, M4), the C helices are red, and the remaining portions are gray. K$^+$ ions are shown as green spheres. In (A), residues on the C helix in the foreground are drawn as sticks (yellow, carbon; blue, nitrogen; red, oxygen; green, sulfur). Two residues located within the C helix, lysine 274 (K274) and tyrosine 281 (Y281), are labeled.

A P domain 1 / Kv1.2

B P domain 2 / Kv1.2

C P domain 1 / P domain 2

D P domain 1 / P domain 2

E K2P1 / Kv1.2 / MthK

F K2P1 / KcsA
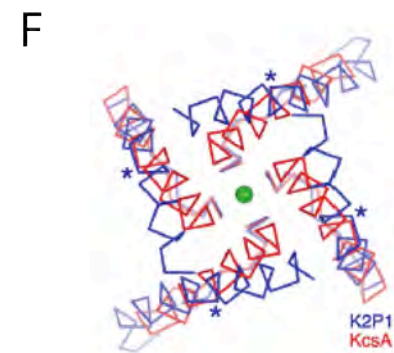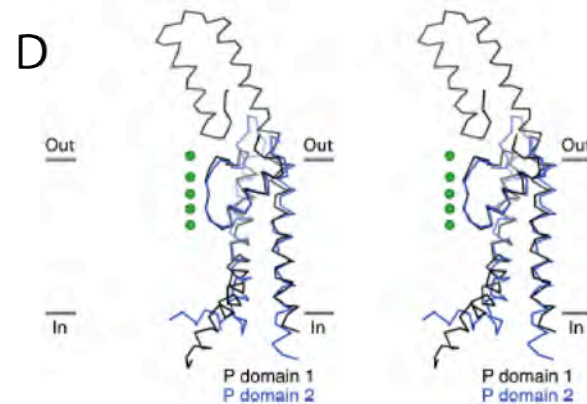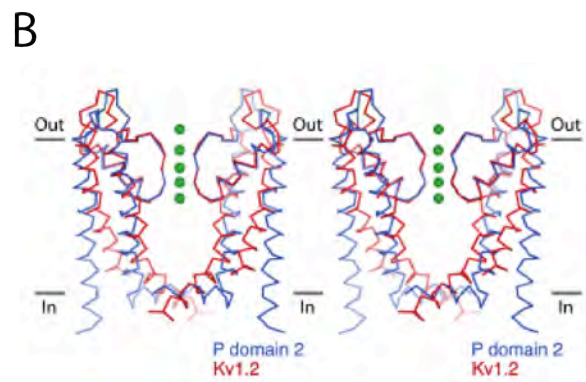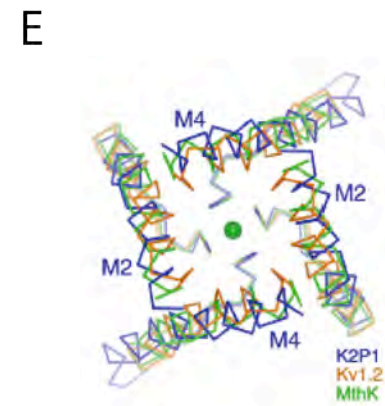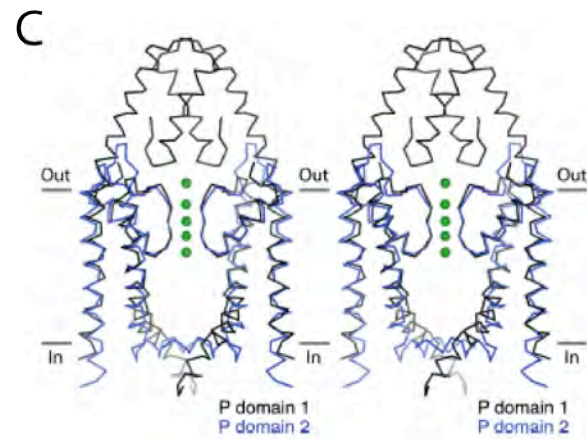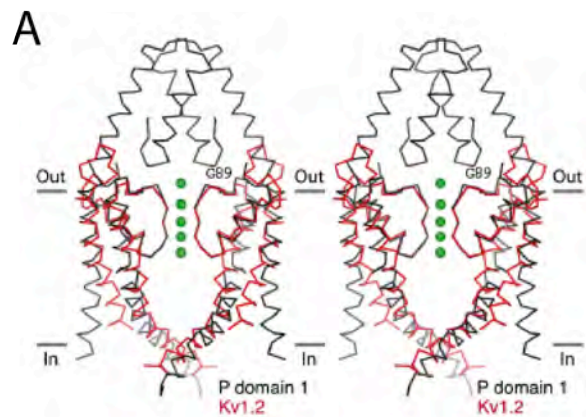
Figure 3.10: Comparison of $K_{2P}1$ inner helical gate with other tetrameric K^+ channel crystal structures. (A and B) Cα superpositions of $K_{2P}1$ (black and blue) with $K_V1.2$ (red, PDB ID 2R9R), in stereo. P domain 1 (black) is shown in (A); P domain 2 (blue) is shown in (B). The view is from the side with approximate boundaries of the bilayer depicted as horizontal lines with extracellular (out) and intracellular (in) sides denoted. K^+ ions are from the structure of $K_{2P}1$ and drawn as green spheres. The superposition was made by aligning the selectivity filters and pore helices. The position of Gly 89 of $K_{2P}1$ is indicated. (C and D) Cα superpositions comparing $K_{2P}1$ P domains 1 (black) and 2 (blue) to one another, in stereo. In (C) two subunits are shown and in (D) one subunit is shown. (E and F) The inner helices of K^+ channels with open (E) and closed (F) inner gates are shown in comparison to the inner helices of $K_{2P}1$. The view is from the intracellular side and the transmembrane portions of the inner helices are shown with the selectivity filters. In (E), $K_{2P}1$ (blue) is compared with the open inner gates of Kv1.2 (orange, PDB ID 2R9R), and MthK (green, PDB ID 3LDC). The M2 and M4 helices of $K_{2P}1$ are labeled. In (F), $K_{2P}1$ (blue) is compared with the closed inner gate of KcsA (red, PDB ID 1K4C) and shown in the same orientation as (E). Asterisks indicate the location of glycines 141 and 256 of $K_{2P}1$.

extends across the $K_{2P}1$ dimer interface and is positioned between M1 and M2 of the adjacent protomer (Figure 3.9). Mutation of a putative SUMOylation site within this region, lysine 274 to glutamate (K274E), increases the open probability of human $K_{2P}1$ (Figure 3.9) (Feliciangeli et al., 2007; Ma et al., 2011; Rajan et al., 2005).

In addition, a plethora of functional data supports the role of the proximal C-terminus in K_{2P} channel gating (Enyedi and Czirjak, 2010). For instance, TREK-1 and TREK-2 channels ($K_{2P}2$ and $K_{2P}10$, respectively) are gated by a variety of cell stimuli and pharmacological agents and the proximal C-terminus plays an important role (Figure 1.9, Figure 2.9). Residues within the proximal C-terminus appear to be involved since $K_{2P}2$ and $K_{2P}10$ C-terminal truncations and fusion constructs result in decreased response to mechanosensation, lipid stimulation, anesthetic modulation and intracellular acidosis (Chemin et al., 2005b; Honore et al., 2002; Kang et al., 2005; Kim et al., 2001b; Maingret et al., 1999b; Maingret et al., 2000a; Maingret et al., 2000b; Patel et al., 1999). In the case of $K_{2P}10$, a cluster of charged residues within the proximal C-terminus (residues 323-338) were implicated in channel gating by arachadonic acid (AA). Although mutagenesis of the 7 residues within this region did not alter the $K_{2P}10$ gating characteristics, deletion of these residues resulted in a significant reduction of channel activity in the presence of AA (Kim et al., 2001b). This suggested that the integrity of the predicted α-helix within this region is essential for AA stimulation. In the $K_{2P}1$ crystal structure, this region of $K_{2P}10$ aligns with residues within the C helix (Figure 2.9).

For the $K_{2P}2$ channel, mutation of 5 basic residues within the proximal C-terminus have been demonstrated to be to be essential for PIP_2 stimulation of $K_{2P}2$, as well as important for interaction with AKAP150 (AKAP79 in humans), a scaffolding protein expressed in the CNS (Figure 1.9, Figure 2.9) (Chemin et al., 2005b; Sandoz et al., 2006). Again, this region of $K_{2P}2$ aligns with the C helix of $K_{2P}1$ (Figure 2.9). Finally, a glutamate residue (E306) also located

within this region, has also been shown to play a role in intracellular pH 'sensing' (Honore et al., 2002). The analogous residue in the $K_{2P}1$ sequence is tyrosine 281 (Y281), which is positioned at the end of the C helix (Figure 2.9, Figure 3.9). This collection of functional data supports a role for the proximal C-terminus in K_{2P} channel gating. Furthermore, the proximity of the C helix to the inner helices (M2 of the adjacent subunit and its connection to M4) in the $K_{2P}1$ structure suggests that the C helix may be involved in inner helical gating.

3.4.9. The extracellular cap creates a restricted exit for hydrated K^+

Another unique feature observed in the $K_{2P}1$ crystal structure is a large 56 amino acid extracellular domain (extracellular cap), which extends 35 Å from the lipid bilayer and is positioned directly above the extracellular side of the selectivity filter (Figure 3.11). The extracellular cap connects M1 and pore helix 1 of P domain 1 in human $K_{2P}1$ (Figure 3.3). In tetrameric K^+ channels, residues within this region form what is called the 'turret', which is a short structured loop that has been observed in both K_V (6-8 residues) and K_{IR} (~20 residues) channel crystal structures. Therefore, the $K_{2P}1$ extracellular cap is a unique structural feature that appears to be conserved among K_{2P} channels based on a K_{2P} sequence alignment, and sequence analysis predicts that the majority of this region is helical and structured (Figure 2.9).

The extracellular cap resembles an A-frame formed by two helices (E1 and E2) from each protomer, bridged by a disulfide bond (cysteine 69; C69) at the apex (Figure 3.11). This disulfide bridge formed by C68 had been previously identified through biochemical studies of human $K_{2P}1$ (Lesage et al., 1996b). The E1 helix is an extension from M1, separated by a ~30° kink at a proline residue (P47) that is conserved among K_{2P} channels (Figure 3.11), and continues to the apex of the extracellular cap. The E2 helix is amphipathic, runs antiparallel to E1 and contributes non-polar residues that form a hydrophobic core (buried surface interface of ~750 Å^2) within the center of the extracellular cap (Figure 3.11). This hydrophobic core is also assembled from non-
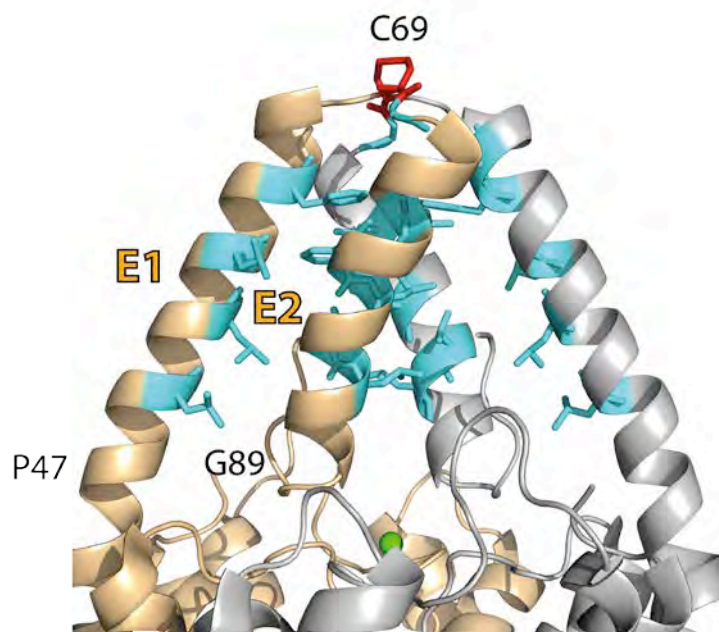
Figure 3.11: K$_{2P}$1 extracellular cap. Ribbon representation of the K$_{2P}$1 extracellular cap with protomers colored in gold and grey. Extracellular cap helices (E1 and E2) are highlighted. Residues referred to in the text are labeled in single letter amino acid code (C, Cys; G, Gly; P, Pro). Residues that form the hydrophobic core are shown in stick representation and are colored cyan. A disulfide bridge at the apex of the cap is highlighted in red and the K^{+} ion above the extracellular side of the selectivity filter is depicted as a green sphere.

polar residues provided by E1 from the same protomer and E2 from an adjacent protomer. The E2 helices are positioned with the negative ends of their helix dipole moments directly above the extracellular side of the selectivity filter. Following the E2 helix, a conserved glycine residue (G89) facilitates a sharp bend with four subsequent residues (residues 90 - 93) forming a short, extended loop that packs against the E2 helix (Figure 3.11). The remaining residues of the extracellular cap are positioned away from the selectivity filter and form an unstructured loop. Residues 94 - 99 are disordered and are, therefore, not modeled into the structure. It is worth noting that wild-type human $K_{2P}1$ contains a glycosylation site that has been removed from the crystallized $K_{2P}1$ construct (N95Q mutation). This residue is located at position 95 and it is possible that the addition of a glycan may stabilize this loop.

Since the extracellular cap is located directly above the channel pore, it restricts the movement of K^+ ions through two, funnel-shaped, side portals that meet above the selectivity filter (Figure 3.12). Measurement of the side portal diameter (between van der Waals surfaces) confirmed that it is wide enough to accommodate hydrated K^+ ions (Figure 3.12). Residues that line each side portal are polar, contributed from the E2 helix and short, extended loop of the cap (glutamate 84, serine 86, asparagine 87, tyrosine 88, serine 91) and from the extracellular connection between the filter sequence 2 and M4 (glutamate 235) (Figure 3.13). Surface residues positioned near the side portal are also polar, such as aspartate 208 and aspartate 209 from the extracellular connection between M3 and pore helix 2 and tyrosine 237, asparagine 238 and glutamine 239 from an unstructured loop at the connection between filter sequence 2 and M4. Although the crystallized $K_{2P}1$ construct does not contain a native glycosylation site, the N-linked oligosaccharide should also be located near the side portals. It is unclear how this sugar may interact with $K_{2P}1$; however, *N*-Acetylneuraminic acid (sialic acid) is commonly found at the end of N-linked oligosaccharide chains. Sialic acid is negatively charged in a physiological
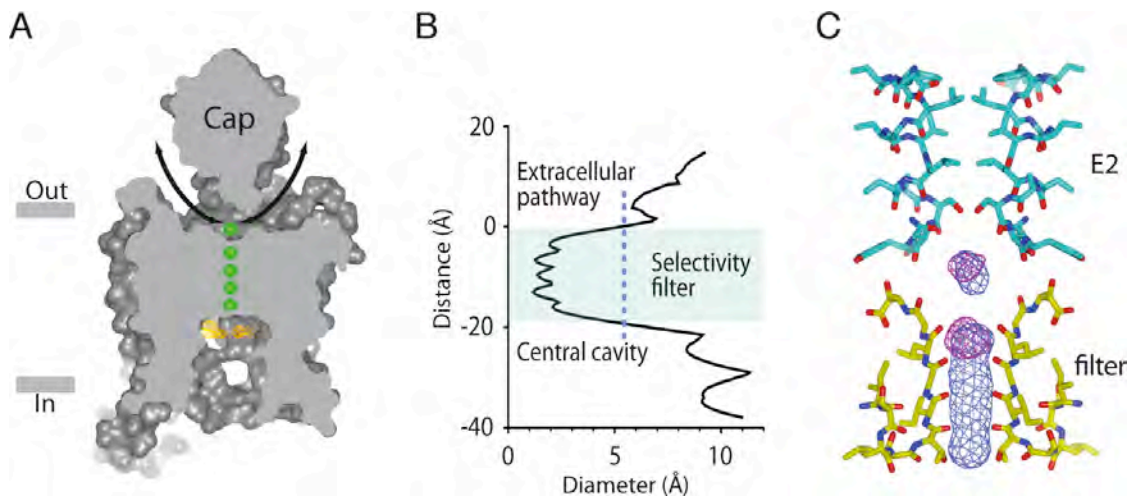
Figure 3.12: Extracellular ion pathway. (A) Cutaway view of the molecular surface of $K_{2P}1$ (gray) from the side with the approximate boundaries of the bilayer shown as horizontal lines with extracellular (out) and intracellular (in) sides denoted. K^+ ions (four sites in the selectivity filter and one external site) are shown as green spheres. Side portals (arrows) located beneath the extracellular cap connect the selectivity filter with the extracellular solution. Orange mesh depicts electron density assigned to alkyl chains. (B) Diameter of the pore (measured as the separation between van der Waals surfaces) as a function of distance along the ion conduction pathway. A dashed line indicates the diameter of a K^+-H2O complex. The 0 coordinate on the y-axis corresponds to the location of the external K^+ ion. (C) Ion binding in the extracellular pathway. Residues of the selectivity filter (yellow carbons, P domain 2) and E2 helices (cyan carbons) are shown as sticks. View is from the side, with a 90° rotation about the vertical axis with respect to (A). Electron density corresponding to K^+ ions is shown from a Fo-Fc simulated-annealing omit map (blue mesh, calculated from 20 to 3.4 Å resolution and contoured at 4 σ). A Tl^+ isomorphous difference Fourier map is also shown (red mesh, calculated from 20 to 6.2 Å resolution and contoured at 4 σ).

133
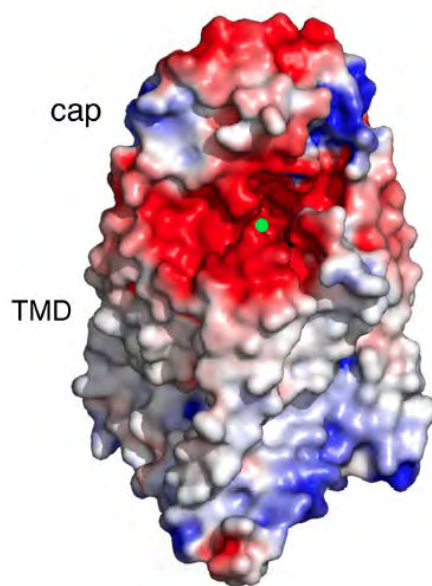
Figure 3.13: Molecular surface of $K_{2P}1$ colored according to the electrostatic potential, which was calculated with the APBS program using default parameters. Coloring is: blue (positive) and red (negative). The view is from the extracellular side, looking into a side portal. Green coloring represents the external K^+ ion. The extracellular cap (cap) and transmembrane domain (TMD) are labeled.

environment (pK_a 2.6) and could be positioned near the side portal as well, which raises the possibility that the identity of the sugar could have an effect on ion permeation.

The narrowest point of each funnel is directly above the selectivity filter and the diameter at this region is ~ 6 Å wide, as measured between van der Waals surfaces (or ~9 Å measured between atom positions) (Figure 3.12). A difference Fourier electron density map reveals a 6σ peak in the narrow region above the filter, calculated using diffraction data from a $K_{2P}1$ crystal soaked in Tl^+ (Figure 3.12). Tl^+ is a heavy atom surrogate for K^+, suggesting that an external K^+ site is located within this region (Figure 3.12, Figure 3.14) Furthermore, $2F_O$-F_C electron density maps revealed density within this region that is consistent with a K^+ ion coordinated with two water molecules (Figure 3.14). This K^+ ion may be stabilized by the positioning of E2 helices with negative ends of their helix dipole moments directly above the external K^+ site. This phenomenon has been documented for electrostatic stabilization of K^+ within the central cavity by pore helices (Doyle et al., 1998; Roux and MacKinnon, 1999; Zhou and MacKinnon, 2004b). In the case of central cavity, the pore helices have a significant contribution to stabilization since the electric field of their helix dipoles are less shielded due low dielectric environment of the membrane (Roux and MacKinnon, 1999). Likewise, the hydrophobic core of the extracellular cap may enhance the electrostatic effect of the E2 helices within the external K^+ site.

3.5.   Discussion

Our structure of human $K_{2P}1$ was published concurrently with a structure of human TRAAK ($K_{2P}4$), a K_{2P} channel within the TREK subfamily (Brohawn et al., 2012). As one would expect, many of the features that we observed in the $K_{2P}1$ crystal structure are also conserved within $K_{2P}4$. A comparison of the two structures will be discussed, as well as the potential functional
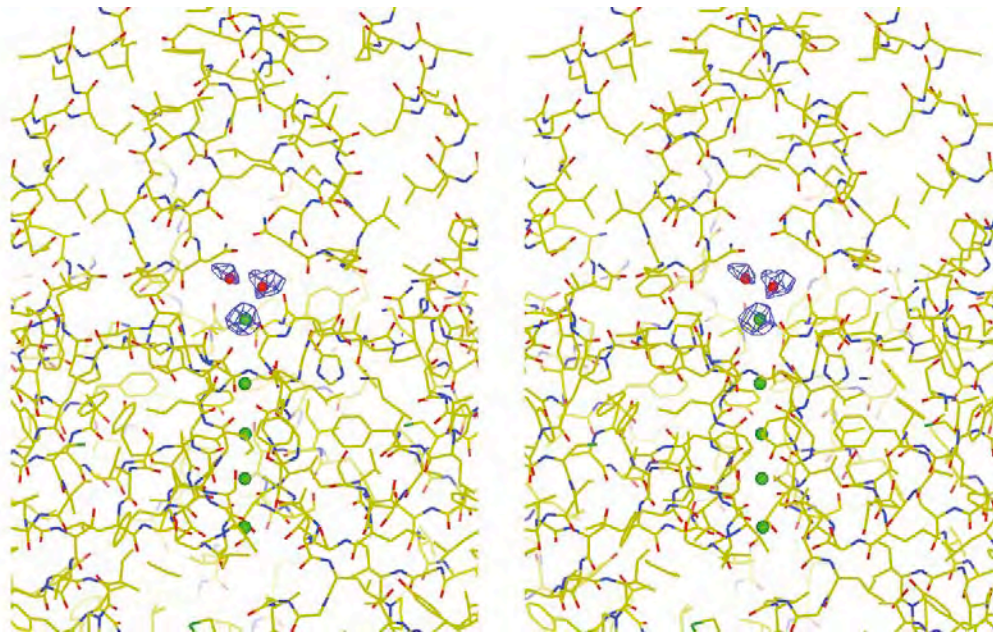
Figure 3.14: Ion hydration in the extracellular pathway. A stereo view of a portion of the channel (stick representation) depicts the region surrounding the selectivity filter and extracellular pathway. K^+ ions are shown as green spheres. The electron density (blue mesh, calculated from 50 - 3.4 Å using the experimental phases and contoured at 1.5 σ) is shown for the region near the external K^+ binding site and two coordinating waters (red spheres).

implications that we can hypothesize based on both channel structures and prior functional information.

### 3.5.1. The activation gate of K_{2P} channels

The molecular topology of $K_{2P}4$ is identical to $K_{2P}1$, with one subunit containing two pore domains in tandem (Figure 3.15). TM2 and 4 of $K_{2P}4$ are inner helices that line the ion conduction pore, and similar to $K_{2P}1$, the channel was crystallized in an open conformation based on the narrowest diameter of the inner helices (~12 Å measured between M2 helices; ~10 Å measured between M4 helices). The inner helices both contain the conserved gating glycine hinge (G153 and G268 in M2 and M4, respectively). In addition, the proline residue (P155) is also conserved in the pore domain 1 inner helix, which results in a ~20° kink in M2 and facilitates the intramembrane openings that are also visible in the $K_{2P}4$ crystal structure.

However, the contours at the cytosolic portions of the inner helices differ between the $K_{2P}1$ and $K_{2P}4$. For instance, significant curvature is observed within the cytosolic half of the $K_{2P}4$ M2 helix, with this helix almost parallel to the plasma membrane. This is particularly evident by comparing the C-terminal 8 residues of both $K_{2P}1$ and $K_{2P}4$ M2 helices, which are separated by ~10 Å (Figure 3.16). The curvature of M2 in the $K_{2P}4$ structure is facilitated by bends in glycine residues (G158, G163 and G165), which are conserved within the TREK subfamily of K_{2P} channels. These residues have been shown to be important for gating since substitution of these 3 glycine residues to larger hydrophobic residues in *D. melanogaster* KCNKØ decreases the channel P_O (Ben-Abu et al., 2009). Likewise, substitution of analogous $K_{2P}1$ residues (L146, A151 and V153) to glycine increased the whole cell current density, measured from *Xenopus* oocytes overexpressing the channel (Chatelain et al., 2012).
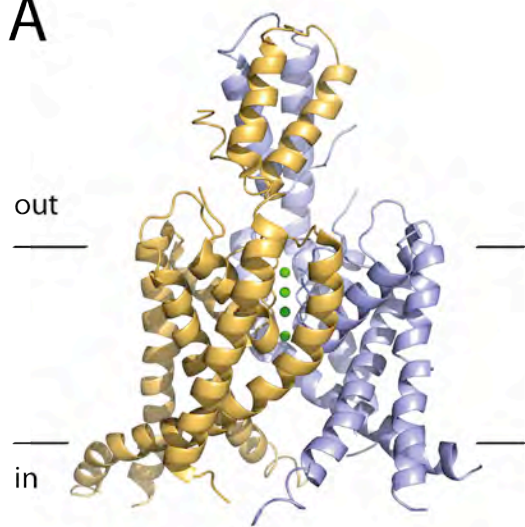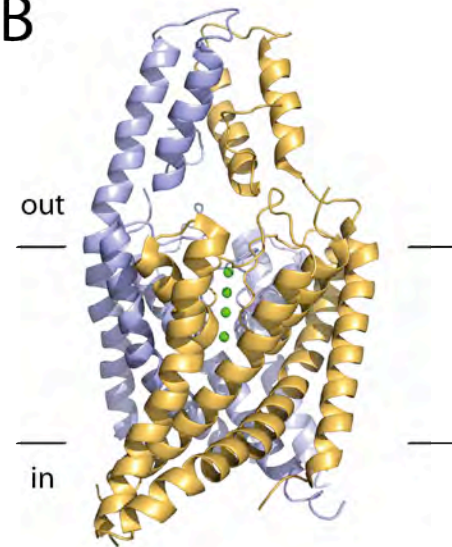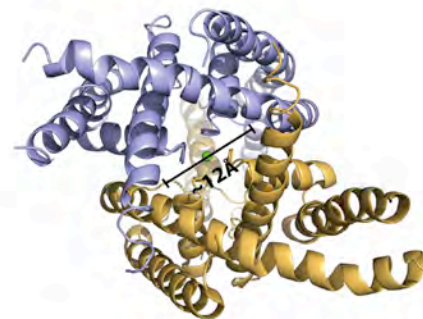
Figure 3.15: Overall structure of $K_{2P}4$ (TRAAK). (A) Tertiary structure of $K_{2P}4$ (PDB ID: 3UM7), showing a ribbon representation from the side. $K_{2P}4$ protomers are colored gold and light blue. K^+ ions are depicted as green spheres. Approximate boundaries of the lipid membrane are shown as horizontal lines with extracellular (out) and intracellular (in) sides denoted. (B) An orthogonal view of the channel from the side. (C) A view of $K_{2P}4$ from the intracellular side.
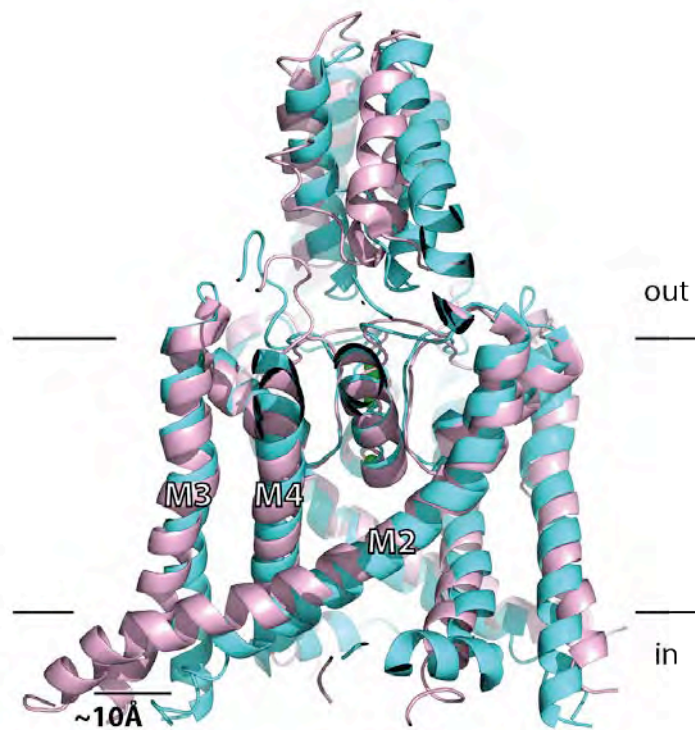
Figure 3.16: Cα superpositions of $K_{2P}1$ (cyan) with $K_{2P}4$ (pink, PDB ID: 3UM7). Cutaway ribbon representation of both channels viewed from the side, with approximate boundaries of the lipid membrane depicted as horizontal lines with extracellular (out) and intracellular (in) sides denoted. K^+ ions are from the structure of $K_{2P}1$ and drawn as green spheres. Transmembrane helices (M2-M4) from one protomer are labeled. The superposition was made by aligning the selectivity filters and pore helices.

The cytosolic region of $K_{2P}4$ M2 forms an amphipathic helix with hydrophobic residues pointing toward the membrane and basic residues positioned toward the cytosol. In conjunction with the flexibility at the glycine residues, it was suggested that this region of the channel may be important for chemical and mechanical activation of TREK channels (Brohawn et al., 2012). The glycine residues are not conserved in the other K_{2P} channel subfamilies (Figure 2.9). However, the residues that align to the M2 amphipathic helical region of $K_{2P}4$ are also hydrophobic and basic in other K_{2P} channels, yet the positions of these residues are not strictly conserved (Figure 2.9). It would be interesting to evaluate the contribution of this region to K_{2P} channel gating since mutagenesis studies of this region have not been performed currently.

The C-terminus observed in the $K_{2P}4$ crystal structure, which continues from the M4 helix, is the feature most different from $K_{2P}1$ since it does not form an interfacial C helix. Instead, the $K_{2P}4$ C-terminus extends into the cytosol (Figure 3.15). The observed differences between the $K_{2P}1$ and $K_{2P}4$ C-termini are not a result of packing in the crystal lattice since the C-termini do not participate in any direct crystal contacts. Therefore, the C-termini most likely adopt different physiological conformations, with $K_{2P}1$ forming an interfacial C helix and $K_{2P}4$ extending into the cytosol. The question remains whether the orientations of the $K_{2P}1$ and $K_{2P}4$ C-termini reflect inherent differences between the two channels or if these orientations represent two conformational states of the proximal C-terminus. In other words, does the proximal C-terminus of K_{2P} channels dynamically decouple and couple with the lipid bilayer and, if so, does this play a role in K_{2P} channel gating? In the case of $K_{2P}2$, gating by the C-terminus had been previously proposed to involve a process of membrane decoupling and coupling, which is suggested to be modulated by chemical and mechanical stimulation (Chemin et al., 2005b). This model was experimentally supported by fluorescence-based assays and a yeast viability SOS-recruitment assay studying $K_{2P}2$ C-terminal plasma membrane association (Chemin et al., 2005b; Sandoz et

al., 2011). Both the model and data suggest that association of the $K_{2P}2$ proximal C-terminus with the plasma membrane promotes $K_{2P}2$ channel opening.

It should be noted that although $K_{2P}4$ gating is potentiated by membrane stretch, AA and intracellular alkalization like other TREK family members, modifications to the proximal C-terminus do not alter chemical or mechanical stimulation of this channel (Kim et al., 2001a). Interestingly, residues within the proximal C-terminus are fairly conserved among the TREK subfamily, which raises the question of why there is a difference in regulation of $K_{2P}4$ compared to $K_{2P}2$ and $K_{2P}10$ (Figure 2.9). One hypothesis is that K_{2P} channel inner helical gating may involve a combination of protein interactions with the membrane at both the proximal C-terminus, as well as the M2 ampipathic helix located near the cytosolic side of the membrane and the adjacent loop connecting M2 and M3. In the case of $K_{2P}2$ and $K_{2P}10$, mutations to the proximal C-terminus are sufficient for abolishing the enhanced P_O from chemical and mechanical stimuli whereas $K_{2P}4$ may require combined perturbation to the proximal C-terminus and the M2 ampipathic helix/M2-M3 loop.

$K_{2P}1$ was crystalized in the open conformation, but unlike tetrameric K^+ channels, asymmetry is observed between the pore domain 1 and 2 inner helices. Whereas there is, in total, a ~40° bend contributed from both the gating glycine hinge G141 and P143 in pore domain 1, a shallow < 10° bend is observed at G256 in pore domain 2 (Figure 3.8). Likewise, the inner helix of $K_{2P}4$ pore domain 1 is bent ~25° greater than the inner helix of pore domain 2 (Brohawn et al., 2012). The shallow degree of bending at the M4 gating glycine hinge may be necessary to accommodate a membrane-associated C helix for positioning between M1 and M2 of an adjacent subunit, as observed in the $K_{2P}1$ structure.

3.5.2. Intramembrane openings provide an access point for lipids and lipophilic compounds?

The intramembrane openings in the $K_{2P}1$ structure expose the central cavity to the lipid bilayer. These openings are also observed in the $K_{2P}4$ crystal structure and, interestingly, a similar feature was identified in the crystal structure of a prokaryotic voltage dependent Na^+ channel, suggesting that these openings may be a feature that is common to other ion channels (Payandeh et al., 2011). Within the $K_{2P}1$ structure, two 11 carbon alkyl chains were modeled into electron density that was observed within this region, which are attributed to either detergent molecules or lipids that co-purified with $K_{2P}1$. The functional role of these openings and how they contribute to K_{2P} channel gating is not yet known.

However, a recent study identified TPenA, THexA and THepA as suitable, sub-micromolar QA pore blockers for 3 different K_{2P} channel family members, whereas TEA is ineffective at K_{2P} channel pore block (Piechotta et al., 2011). TPenA was demonstrated to bind to the central cavity of $K_{2P}2$ through a cysteine scanning mutagenesis study (Piechotta et al., 2011). By highlighting the analogous residues that are important for binding TPenA within the $K_{2P}1$ structure, it is clear that a number of these residues line the intramembrane openings (Figure 3.17). In addition, I have shown that THexA can inhibit $K_{2P}1$ K^+ flux through the K_{2P} flux assay, suggesting that larger hydrophobic QAs are capable of blocking all K_{2P} channels (see 4.4.2 Progress towards identifying the site of THexA binding through $K_{2P}1$ co-crystallization trials). The presence of the intramembrane openings in both the K_{2P} structures suggests that this feature is conserved within K_{2P} channels and begins to explain why QAs require longer alkyl chains to be effective K_{2P} channel blockers.

There is recent evidence to support the hypothesis that the activation gate of K_{2P} channels is constitutively open, with the primary mode of K_{2P} channel gating regulated by the outer pore gate
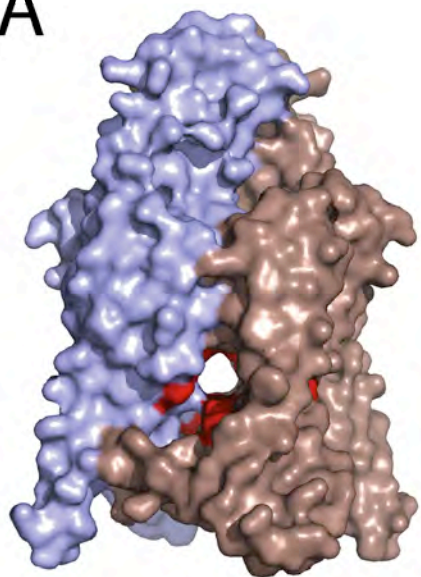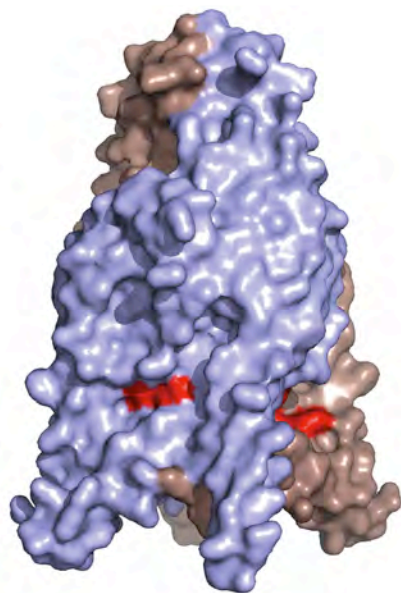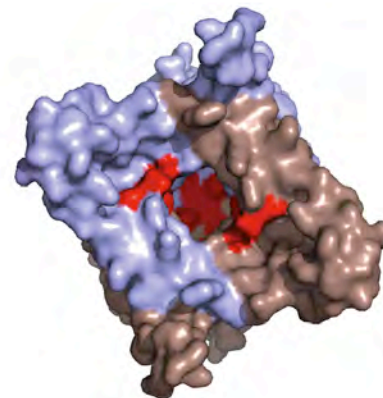
Figure 3.17: Molecular surface of $K_{2P}1$ with analogous residues highlighted from TPenA cysteine mutagenesis study of $K_{2P}2$ (A) View of the molecular surface from the side with the extracellular solution above. Protomer are colored blue and red. Residue that were critical for TPenA inhibition of $K_{2P}2$ are highlighted in red (B) Orthogonal view from the side. (C) Molecular surface viewed from the intracellular side.

(see 3.5.3 The K_{2P} channel selectivity filter) (Bagriantsev et al., 2011; Bagriantsev et al., 2012; Piechotta et al., 2011; Rapedius et al., 2012). The key experiment that addressed the question of K_{2P} inner helical gating demonstrated that THexA applied intracellularly could access the $K_{2P}2$ central cavity when the inner helices were opened and closed (Piechotta et al., 2011). In light of the K_{2P} crystal structures, an alternative hypothesis may be that THexA can access the central cavity through the intramembrane openings. In support of this idea, a previous study of QA hydrophobicity demonstrated that the partition coefficient of THexA is > 100 (octanol/water), suggesting that THexA would preferentially partition to the lipid bilayer instead remaining in an aqueous environment (Zhang et al., 1999).

To address this alternative hypothesis, a follow up study was performed to access the accessibility of 8-(Tributylammonium)octyl methanethiosulfonate (MTS-TBAO), a MTS-linked QA which is less hydrophobic than THexA, to the central cavity of $K_{2P}2$ (Rapedius et al., 2012). Sulfhydryl reactive MTS reagents have been used to evaluate pore accessibility within the Shaker channel through the introduction cysteine mutations in the central cavity (Karlin and Akabas, 1998; Liu et al., 1997). MTS compounds that successfully reach the inner cavity are able to react with the substituted cysteines and significantly reduce channel conductance. Like THexA, MTS-TBAO was shown in this study to be able to access the $K_{2P}2$ central cavity when the inner helices are opened or closed, as evaluated by electrophysiology recordings of a $K_{2P}2$ central cavity cysteine mutant (Rapedius et al., 2012). The authors interpret these data to mean that the $K_{2P}2$ inner helices are constitutively open or, in other words, that $K_{2P}2$ is not gated by the inner helices. However, one assumption that was made was that MTS-TBAO movement is restricted to the pore since this compound is less hydrophobic than THexA. However, it has been shown that 2-aminoethyl methanethiosulfonate hydrobromide (MTSEA), a small and positively charged MTS reagent (and less hydrophobic than MTS-TBAO) is able to cross a lipid bilayer rapidly, suggesting that MTS-TBAO should behave similarly (Holmgren et al., 1996). An experiment

utilizing a charged, hydrophilic MTS reagent could be performed to directly tackle the question of K_{2P} inner helical gating, as has been demonstrated for the Shaker channel (Liu et al., 1997).

The binding of larger, hydrophobic QA compounds to the central cavity and their interaction with residues in the intramembrane openings suggests that the openings may provide an entryway for lipids and lipophilic compounds. Characterization of $K_{2P}2$, $K_{2P}4$ and $K_{2P}10$ channel gating identified polyunsaturated fatty acids (PUFAs; e.g. AA), phospholipids (PL), and lysophospholipids (lysoPLs) as lipid moieties that enhance current amplitude (Bang et al., 2000; Chemin et al., 2005a; Chemin et al., 2005b; Fink et al., 1998; Lesage et al., 2000b; Maingret et al., 2000b; Patel et al., 1998). However, not all PUFAs, PLs and lysoPLs are able to activate this subfamily of K_{2P} channels, and this is determined by the length and saturation of the lipid acyl chain, as well as the size and charge of the lipid head group. For instance, saturated free fatty acids fail to increase $K_{2P}2$, $K_{2P}4$ and $K_{2P}10$ channel activity, whereas hydrocarbon saturation of lysoPLs has no effect (Bang et al., 2000; Fink et al., 1998; Lesage et al., 2000b; Maingret et al., 2000b; Patel et al., 1998) Although PUFAs and lysoPLs are differentially affected by acyl chain saturation, the length of the hydrocarbon chain in both cases has been shown to affect channel modulation (Bang et al., 2000; Maingret et al., 2000b).

Whereas large polar head groups of lysoPLs increase current amplitude in $K_{2P}2$, this is not a requirement for PL regulation (Chemin et al., 2005b; Chemin et al., 2007; Maingret et al., 2000b). This discrepancy may be due to differences in patch recordings. Whereas lysoPLs were applied to the extracellular bath and recorded in a whole-cell configuration, PLs were applied intracellularly and measured more directly by inside-out patch. In support of this point, lysophosphatidic acid (LPA), a lysoPL that does not contain a large polar head group, was later identified as a lysoPL that can activate $K_{2P}2$, $K_{2P}4$ and $K_{2P}10$ in an excised patch (inside-out) (Chemin et al., 2005a). LPA was not originally identified since currents were not measured in a whole-cell configuration

(Chemin et al., 2005a; Maingret et al., 2000b). The opposite was observed for lysophosphatidic choline (LPC), a lysoPL with a charged group, with robust currents measured from whole-cell patch that were not observed in an inside-out configuration (Maingret et al., 2000b). Moreover, The proximal C-terminus of $K_{2P}2$ has been shown to be important for LPC stimulation, as well as AA stimulation (PUFA) and PIP_2 regulation (PL), whereas LPA does not appear altered by modifications to this region (Chemin et al., 2005a; Chemin et al., 2005b; Chemin et al., 2007; Maingret et al., 2000b).

The differences observed between types of lipids (e.g. PUFAs and lysoPLs), as well as within the same lipid class (LPA versus LPC), suggest that $K_{2P}2$, $K_{2P}4$ and $K_{2P}10$ are able to discriminate lipids by size and charge. How these channels are selective for lipids is not clear, but the data suggest that the charged, proximal C-terminal may be involved in many instances (but not all; e.g. LPA) (Chemin et al., 2005a; Chemin et al., 2005b; Chemin et al., 2007; Maingret et al., 2000b). The location of this region (C helix) in the $K_{2P}1$ crystal structure is directly below the intramembrane openings, which suggests a possible functional coupling of the C terminus with the openings. It is also worth noting that conformational changes to the K_{2P} inner helices (M2, M4) and the C-terminus may affect the size and shape of the intramembrane openings, which could be essential for exposing and concealing a binding pocket for lipids and lipophilic compounds.

3.5.3. The K_{2P} channel selectivity filter

The selectivity filter within the $K_{2P}1$ and $K_{2P}4$ structures are four-fold symmetric and adopt a conductive conformation, within the limit at which the atomic positions could be determined at this resolution. However, the molecular packing which surrounds the selectivity filter sequence is two-fold symmetric, deviating from what has been observed in tetrameric K^+ channel structures. This is primarily a result of residue differences between the filter sequences of K_{2P} channel P

domains 1 and 2, with neither sequence strictly conforming to the 'canonical' K^+ channel filter sequence TxGYGD). For instance, the last position of the K_{2P} channel P domain 1 filter sequence (D) is substituted with histidine (e.g. $K_{2P}1$), asparagine (e.g. $K_{2P}4$), methionine or tyrosine (Figure 2.9). This aspartic acid residue in structures of KcsA, MthK and $K_V1.2$ forms a hydrogen bond with a conserved tyrosine or tryptophan in the pore helix (Long et al., 2007; Ye et al., 2010; Zhou et al., 2001a). Like K_{2P} channels, the filter aspartic acid is not conserved in K_{IR} channels. However, the residue following the filter aspartic acid is an arginine, which forms a salt bridge with a glutamate contributed from the pore helix (Tao et al., 2009; Whorton and MacKinnon, 2011). Both the arginine and glutamate residues are conserved with K_{IR} channels and mutations to either of these residues significantly diminished currents or produced non-functional channels (Dibb et al., 2003; Yang et al., 1997). Furthermore, a double substitution, which swapped the residues at these two positions, restored $K_{IR}2.1$ activity. However, the selectivity of the double mutant was altered with greater permeability to Na^+ (Yang et al., 1997). Although the selectivity filter sequence is critical for selection of K^+ ions over other types of cations, it is evident that residues surrounding the filter are also essential for K^+ selectivity since they appear to stabilize the filter structure.

In the $K_{2P}1$ and $K_{2P}4$ crystal structures, the last residue in the selectivity filter sequence of P domain 1 is His 122 (H122, $K_{2P}1$) or Asn 134 (N134, $K_{2P}4$), and this residue does not form a hydrogen bond(s) with residues in the pore helix (Figure 3.6, Figure 3.18). In addition, the residues which follow H122 and N134 do not form direct hydrogen bonds or salt bridges with the pore helix, as is observed in K_{IR} structures. In crystal structure of KcsA, a water is positioned behind the filter, which coordinates backbone amides provided by filter residues, as well as with side chains from residues along the pore helix (Cordero-Morales et al., 2006; Zhou et al., 2001b). Although not observed into the crystal structure, a water molecule could fit behind the $K_{2P}1$ filter and may coordinate with H122. This idea will be discussed in further detail below. Although
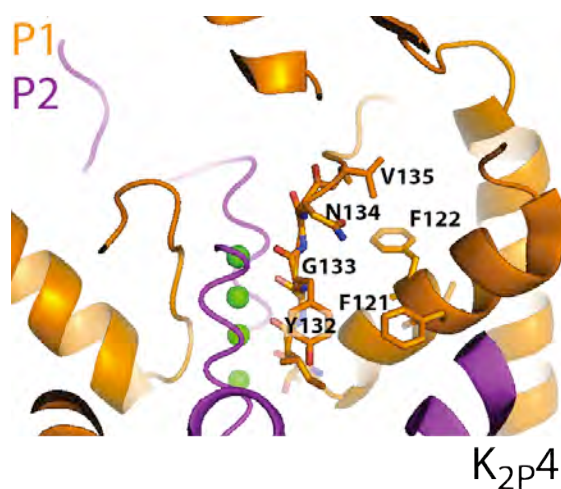
Figure 3.18: Residue packing (N134) surrounding the selectivity filter of K$_{2P}$4. Cutaway views of K$_{2P}$4 selectivity filter viewed from the extracellular side. (A) Packing of K$_{2P}$4 filter residue N134 from P domain 1 (orange carbons) drawn in colored stick representation (blue, nitrogen; red, oxygen). P domain 2 residues are colored purple. The remaining structure is depicted in ribbon representation with K$^+$ ions shown as green spheres. The filter residues, and residues surrounding N134, are labeled in single letter amino acid code (F, Phe; G, Gly; H, His; N, Asp; T, Thr; V, Val; Y, Tyr).

coordination of H122 with water could potentially stabilize this residue, the lack of non covalent bonds among the surrounding residues may introduce flexibility that could be important for selectivity and possibly outer pore gating of K_{2P} channels.

$K_{2P}1$ is modulated by extracellular acidification (pH_O), with decrease in current amplitude at positive membrane potentials (outward K^+ currents) as the pH is lowered from 8 to 6.2. H122 is implicated in sensing pH_O since the pH at which there is half block of current is 6.6, which is very close to the pKa of histidine, and because mutation to H122 results in a loss of pH_O sensitivity (Chatelain et al., 2012; Ma et al., 2012b; Rajan et al., 2005). These results recapitulate what has been reported for both $K_{2P}3$ and $K_{2P}9$, with both of these channels harboring the same histidine residue in the P domain 1 selectivity filter sequence (Figure 2.9) (Kim et al., 2000; Lopes et al., 2000; Lopes et al., 2001; Morton et al., 2003; Rajan et al., 2000). One hypothesis for why histidine protonation results in decrease $K_{2P}1$ current density, based on the $K_{2P}1$ structure, is that the additional positive charge may reduce channel conductance by introducing an energetic barrier at the extracellular side of the selectivity filter (Figure 3.12). In order to address this question, single channel studies of a $K_{2P}1$ H122 wild-type and mutant (H122N, D) channels will need to be performed with varying pH_O.

In whole cell recordings, it has been demonstrated that the reduction in $K_{2P}1$ outward currents at lower pH_O is associated with a shift of the reversal potential to more depolarized potentials than what is expected for a K^+ selective channel (near the E_K) (Chatelain et al., 2012; Ma et al., 2012b). These data suggest that that lower pH_O promotes Na^+ conduction and that Na^+ is contributing to the total current density measured. In support of this, whole-cell recordings of $K_{2P}1$ in extracellular solution containing $NMDG^+$, a cation that is not $K_{2P}1$ permeable and is used in place Na^+, at pH 6.0 are essentially identical to recordings at pH 7.4 in extracellular solution containing Na^+ (Chatelain et al., 2012; Ma et al., 2012b). These published results suggest that

histidine protonation could result in a conformational change(s) to the outer pore gate that alters K^+ selectivity, resulting in increased Na^+ influx.

In the case of $K_{2P}3$ and $K_{2P}9$, an increase in outward currents is also observed in the presence of extracellular $NMDG^+$ at acidic pH, suggesting that an Na^+ current also contributes to $K_{2P}3$ and $K_{2P}9$ whole-cell current measured (Ma et al., 2012b). However, the Na^+ contribution to the total current density is less than what is observed for $K_{2P}1$ since recordings in extracellular $NMDG^+$ only partially 'rescued' the reduced outward currents measured at acidic pH (Ma et al., 2012b). Why could this be happening? One explanation is that reduction $K_{2P}3$ and $K_{2P}9$ current amplitude in low pH, resulting in histidine (H98) protonation, could alter the channel outer pore gate. Alternatively, H98 protonation may affect both outer pore gating and conductance since the additional positive charge by the extracellular side of the filter may act as an energetic barrier. The $K_{2P}3$ and $K_{2P}9$ H98D mutant recorded at acidic pH restores the majority of outward currents recorded when compared with the same mutant at pH 7.4, supporting both possibilities (Ma et al., 2012b). However, single channel recordings of $K_{2P}9$ revealed no change in conduction between extracellular pH 6.0 and 7.2, but instead a significant reduction in a P_O, suggesting that histidine protonation most likely alters outer pore gating alone (Kim et al., 2000). It is tempting to speculate that the histidine protonation within the selectivity filter of the $K_{2P}1$, $K_{2P}3$ and $K_{2P}9$ may be a mechanism of outer pore gating regulation shared by these three channels, with $K_{2P}1$ exhibiting a greater alteration in channel selectivity compared to $K_{2P}3$ and $K_{2P}9$.

A hypothesis for the outer pore gating mechanism of pH_O regulation by $K_{2P}3$ H98 has been previously proposed based on both mutagenesis studies and $K_{2P}3$ homology modeling. In the homology model, a network of hydrogen bond interactions between selectivity filter backbone amides, residue(s) within the pore helix 1, H98 and a water molecule that is positioned in the homology model between pore helix 1 and selectivity filter was proposed (Stansfeld et al., 2008;

Yuill et al., 2007). In the case of $K_{2P}1$, the water molecule (not present in the structure) may be forming hydrogen bonds with the H122 side chain (proton acceptor in its deprotonated state), backbone amides (proton donors) and a conserved threonine side chain in the pore helix of P domain 1 (threonine 113 in $K_{2P}1$; T113 is a proton acceptor in this example). Protonation of the H122 at acidic pHs (< 6.0) would potentially destabilize the hydrogen bond network that is formed and consequently introduce flexibility within this region. In support of this hypothesis, a water molecule was found to stabilize the KcsA selectivity filter in this region as evaluated from a high-resolution crystal structure (Cordero-Morales et al., 2006). In addition, H122 in the $K_{2P}1$ crystal structure is positioned such that it could participate such a network (Figure 3.6). Interestingly, mutagenesis of the $K_{2P}3$ pore helix residue threonine 89 (analogous to T113 in $K_{2P}1$) to alanine or valine, but not serine, resulted in an increase in both Na^+ permeability and current amplitude in alkaline conditions (Figure 2.9) (Yuill et al., 2007). It would be interesting to see whether the mutagenesis of $K_{2P}1$ T113 could also result in a change to ion selectivity. Obtaining a high-resolution structure with $K_{2P}1$ crystals grown at an alkaline and acidic pHs could help elucidate the mechanism of pH_O regulation of $K_{2P}1$, as well as $K_{2P}3$ and $K_{2P}9$.

In the $K_{2P}1$ structure, two residues are in close proximity to H122, threonine 123 (T123) and glutamate 235 (E235), which are positioned within the loop connecting the filter and inner helices of P domains 1 and 2, respectively (Figure 3.6). Although T123 does form a hydrogen bond with H122, this interaction most likely does not play a crucial role in altered K^+ selectivity since T123 is not conserved in $K_{2P}3$ and $K_{2P}9$ channels (an alanine) (Figure 2.9). On the other hand, E235 and H122 are 4.3 Å apart in the $K_{2P}1$ structure and the analogous residue in $K_{2P}3$ and $K_{2P}9$ is a glutamine (Figure 3.6). If protonation H122 destablizes the hydrogen bond network that is formed with pore helix 1, backbone amides and water, this could allow for H122 to rotate to a position close enough to E235 to form a hydrogen bond. The loop connecting the filter to the inner helix of P domain 1 is not stabilized by a salt bridge or hydrogen bond, and could therefore

accommodate this movement, resulting in a conformational change to the selectivity filter. It is

also worth noting that the positions of H122 and E235 are on an adjacent side of the extracellular

side portals and an interaction between the two residues would not constrict the portals. However,

flipping of H122 would result in an alteration in the charge lining the portals, which could alter

K^+ affinity to this region. Similar to H122, an electrophysiology experiment could be performed

with an E235 mutant (substitution to an aspartic acid or alanine), which would address the

question of its role in $K_{2P}1$ pH_O regulation and selectivity.

In P domain 2 of K_{2P} channels, the 'canonical' tyrosine in the filter sequence is replaced with a

hydrophobic residue, such as Leu 228 (L288) in $K_{2P}1$ and Phe 241 (F241) in $K_{2P}4$. As a result, the

molecular interactions surrounding this portion of the selectivity filter are different from what is

observed in tetrameric K^+ channels. Typically the filter tyrosine residue makes a hydrogen bond

with a conserved serine or threonine residue contributed from a neighboring pore helix, and also

makes hydrophobic contacts with neighboring hydrophobic residues. In the case of K_{2P} channels,

the hydrogen bond is not present and, instead, a hydrophobic network is extended (Figure 3.5).

Residues that participate in the hydrophobic network are contributed by both pore helices, the

filter sequence and the loop connecting the filter and inner helix within P domain 1 (Figure 3.5).

In addition, the conserved serine or threonine, which contacts the canonical filter tyrosine in

tetrameric K^+ channels, is replaced with a non-polar residue in K_{2P} channels. The presence of two

hydrophobic residues in these highly conserved positions suggests that these residues co-evolved,

as has been reported for residues surrounding the K^+ selectivity filter (Lockless et al., 2007).

In K_{2P} channels, the hydrophobic contacts surrounding the filter in P domain 2 are most likely

critical for maintaining the structural integrity of the filter and perturbation to residues in this

region affect channel selectivity. A mutagenesis study of the analogous phenylalanine residue

(F202) in $K_{2P}3$ demonstrated that conservative substitutions of this residue alter K^+ selectivity

(Yuill et al., 2007). For instance, the most well tolerated substitution was to leucine (F202L), yet the reversal potential of this mutant shifted from -85 mV to -35 mV and the permeability ratio of Na^+ to K^+ (P_{Na}/P_K) increased from 0.04 to 0.28. Other substitutions that were made were to tyrosine, methionine, alanine and valine (F202Y, M, A and V, respectively). From these five mutations, it is evident that side chain length is important since the most severely altered mutants were F202A and F202V, with a shift in the reversal potential to -5 mV and an increase in the P_{Na}/P_K to 0.85 (Yuill et al., 2007). These mutagenesis studies suggest that the hydrophobic interactions between F202 and neighboring non-polar residues stabilize the filter and that the size of this residue is important for making contacts.

In the K_{2P} alignment, the equivalent filter residue to $K_{2P}3$ F202 is either a phenylalanine or leucine (Figure 2.9). Interestingly, leucine is only found at this position in the TWIK subfamily ($K_{2P}1$, $K_{2P}6$) and the analogous residue in $K_{2P}3$ (F202), when substituted to a leucine, results in a loss of K^+ selectivity (Yuill et al., 2007). In addition, residues that make hydrophobic contacts with L288 in the $K_{2P}1$ structure are conserved in $K_{2P}3$, suggesting that this portion of the $K_{2P}1$ filter may have more flexibility as a result of L288. It would be interesting to determine whether mutation of $K_{2P}1$ L288 to phenylalanine could stabilize the filter and result in a K^+ selective channel in hypokalemic conditions (Ma et al., 2011).

Studies of the Shaker K^+ channel in the 1990's identified the presence of two types of inactivation gates: a fast inactivation gate (N-type) which involves a physical block of the pore from the cytosolic side by the N-terminus (ball and chain model) and a slow inactivation gate (C-type; outer pore gating) that results in a conformational change to the filter (Yellen, 1998). C-type inactivation has been observed in a variety of K_{2P} channels (see 3.2 Introduction) and the deviations to the selectivity filter sequence may be important for introducing structural flexibility to the filter that is important for K_{2P} channel outer pore gating.

3.5.4. The extracellular cap is a conserved feature of K_{2P} channels

In tetrameric K^+ channel structures, the mouth of the selectivity filter is directly exposed to the extracellular environment. This is in contrast to the $K_{2P}1$ and $K_{2P}4$ crystal structures, in which a large extracellular cap is observed in this region (Figure 3.3, Figure 3.15). In the crystal structure of $K_{2P}4$, the extracellular cap is displaced and asymmetric as a result of a contact that is made in the crystal lattice (Brohawn et al., 2012). The cap in both $K_{2P}1$ and $K_{2P}4$ structures restricts access to the extracellular side of the selectivity filter to two side portals that can accommodate hydrated K^+ ions. In addition, K^+ ions at the extracellular side of the pore may be stabilized by the E2 helices, which are positioned with the negative ends of their helix dipole moments above the selectivity filter. These features are conserved between the $K_{2P}1$ and $K_{2P}4$ structures and suggest that the extracellular cap is a conserved K_{2P} channel domain.

Although the cap architecture is conserved between the $K_{2P}1$ and $K_{2P}4$ structures, the residues that line the side portals diverge. Interestingly, the majority of the analogous polar residues which contribute to the $K_{2P}1$ side portals are small and non-polar in $K_{2P}4$ (see 3.4.9 The extracellular cap creates a restricted exit for hydrated K^+) (Figure 2.9). In the case of $K_{2P}1$, the polarity of the residues within the side portals may be important for hydrogen bonding and electrostatic interactions with hydrated K^+ ions. Interestingly, residues that line the side portals of $K_{2P}4$ are both acidic and hydrophobic, which includes aspartic acid 93, leucine 95, glycine 96, glycine 97, aspartic acid 100 and alanine 248 (analogous residues to $K_{2P}1$) (Figure 2.9). A sequence alignment of all K_{2P} channels indicates that the residues lining the extracellular cap side portals are not well conserved and these differences could partially account for the different electrophysiological characteristics between K_{2P} channels (Figure 2.9). It would be interesting to swap the side portal residues between the $K_{2P}1$ and $K_{2P}4$ channels, or to generate side portal residue mutants in other well studied K_{2P} channels such as $K_{2P}2$ or $K_{2P}3$, to evaluate their contribution to channel function.

The limited accessibility to the external side of K_{2P} channels by the extracellular cap may also explain why these K^+ channels are insensitive to extracellular pore blocking inhibitors. Electrophysiological studies have demonstrated that the K^+ channel scorpin toxin charybdotoxin is unable to inhibit $K_{2P}1$ and $K_{2P}4$ channels, and the bee venom toxin apamin is ineffective and blocking $K_{2P}1$ (Fink et al., 1998; Lesage et al., 1996a). Likewise, K_{IR} channels are also insensitive to charybdotoxin and this has been attributed to the size and orientation of the turrets on the extracellular side of the $K_{IR}2.2$ channel (Tao et al., 2009). This is in contrast to extracellular entryway observed in the $K_V1.2$ structure, which provides a docking surface for charybtodoxin on the extracellular side of the channel (Long et al., 2007; Tao et al., 2009). Although insensitive to charybdotoxin, $K_{IR}1.1$ and $K_{IR}3.4$ channels are inhibited by the bee toxin tertiapin (Jin and Lu, 1998). Similar in structure and size to apamin, tertiapin is a 21 amino acid peptide that is likely able to dock onto the constricted extracellular entryway of K_{IR} channels since it is smaller in size than most peptide toxins. In the K_{2P} structures, the docking sites for the extracellular pore blocking toxins correspond to the location of the extracellular cap. This domain provides a physical barrier, restricting access of larger (charybdotoxin) and smaller (apamin) toxins to the pore. Thus the extracellular domain of K_{2P} channels likely confers resistance to these toxins.

A crystal structure of human $K_{2P}4$ was recently published in complex with a monoclonal antibody ($K_{2P}4$-Fab) solved to 2.75 Å resolution (Brohawn et al., 2013). The $K_{2P}4$-Fab crystal structure revealed a different connectivity of the channel along the extracellular cap when compared to the human $K_{2P}1$ and $K_{2P}4$ crystal structures. The domain swap occurs at the apex of the extracellular cap, where the two protomer M1 and extracellular cap helix E1 are swapped with one another (Figure 3.19). The electron density of $K_{2P}1$ at the apex of the cap cannot distinguish between these two possibilities and it is therefore conceivable that the $K_{2P}1$ structure may also exhibit a
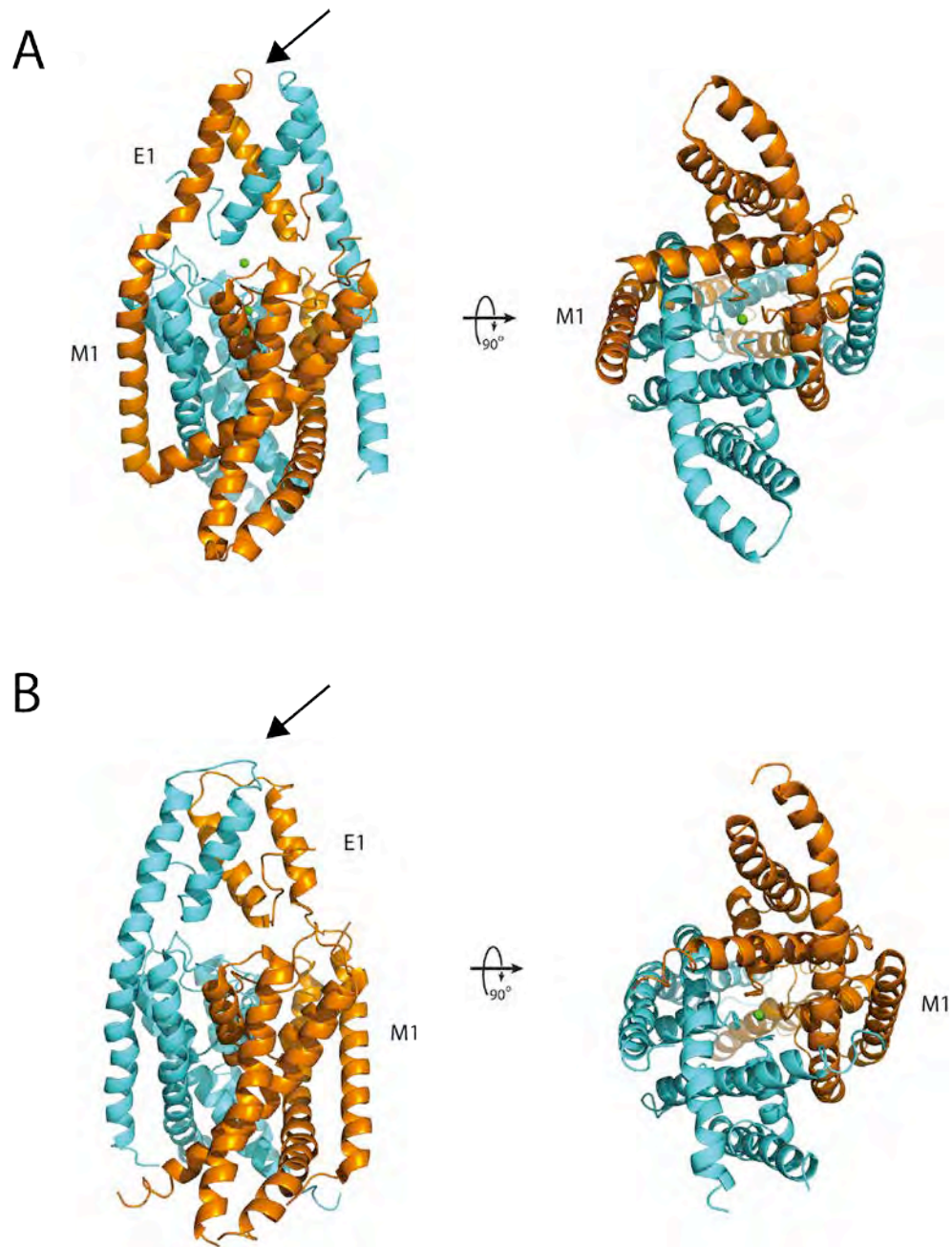
Figure 3.19: K$_{2P}$4-Fab complex crystal structure (A) (PDB ID: 4I9W) reveals a domain swap of transmembrane helix 1 (M1) and extracellular cap helix (E1) compared with K$_{2P}$4 crystal structure (B) (PDB ID: 3UM7). Ribbon diagrams of K$_{2P}$4, from the side and intracellular solution. Protomers are colored in orange and cyan. Arrow highlights the change in connectivity at the top of the extracellular cap.

similar domain-swapped architecture (Figure 3.19). The domain swapping of M1 and extracellular cap helix E1 should not change the overall interpretation of the $K_{2P}1$ structure since this channel, along with $K_{2P}4$, assembles as a homodimer.

The physiological role of the extracellular cap in K_{2P} channel function has not been explored. In addition to prohibiting extracellular toxins from binding and blocking K_{2P} channels, it is tempting to speculate that the extracellular cap may serve as a point of interaction for other extracellular proteins or ligands that may be important for channel activity. It is evident from the K_{2P} channel alignment that the connection between the E2 helix and pore helix 1 is the most diverse region of the extracellular cap in terms of amino acid conservation and length (Figure 2.9). Not surprisingly, this region is an unstructured loop in both $K_{2P}1$ and $K_{2P}4$ crystal structures that is in close proximity to the side portals (Figure 3.3, Figure 3.15). The location, flexibility and sequence variation within this loop suggest that this could be a region for a specific interaction with another protein or ligand. Pull down experiments with an overexpressed wild-type and extracellular cap deletion K_{2P} channel, followed by mass spectroscopy analysis of unique bands in the native K_{2P} sample is a potential approach for identifying interacting partners of K_{2P} channels.

CHAPTER 4

4. PROGRESS TOWARDS A HUMAN K$_{2P}$1 HIGH-RESOLUTION STRUCTURE

4.1. Summary

The crystal structure of human K$_{2P}$1 introduces features most likely important for gating and K$^+$ conductivity in K$_{2P}$ channels that have not been observed in tetrameric K$^+$ channel structures. However, a number of key questions still remain unanswered, such as the role of the K$_{2P}$1 selectivity filter in outer pore gating. For instance, how does extracellular pH modulate the K$_{2P}$1 outer pore gate and what is the role of H122 in extracellular pH 'sensing'? Is a water molecule present behind the selectivity filter and, if so, how does it stabilize a conformational state(s) of outer pore gating in K$_{2P}$1? In addition to outer pore gating, questions about the mechanism of K$_{2P}$ channels inhibition by QA compounds with longer alkyl tails also remain. A high-resolution human K$_{2P}$1 crystal structure could begin to address some of these outstanding questions. Several different approaches to improve human K$_{2P}$1 crystal diffraction were performed. Substitution of residues to strengthen or form new crystal contacts did not result in a new crystal form or improved crystal diffraction. Likewise, co-crystallization of human K$_{2P}$1 with THexA did not produce crystals with improved diffraction. K$_{2P}$1 exchanged into Na$^+$-containing solution did not improve crystal diffraction, and no significant changes to the K$_{2P}$1 structure were apparent at this resolution. Finally, mouse K$_{2P}$1 monoclonal antibodies were generated for future co-crystallization experiments with K$_{2P}$1.

4.2. Introduction

The diffraction of membrane protein crystals is often poor and, as a result, many published membrane protein structures are solved at low-resolution (> 3 Å). Membrane protein crystals are

typically associated with a high solvent content as a result of the detergent micelle, which is necessary to shield the transmembrane regions of the protein from the aqueous environment (Carpenter et al., 2008). The regions of the protein not sequestered by the detergent micelle are responsible for forming protein crystal contacts, and these contacts increase order in the crystal that is essential for high-resolution diffraction. Consequently, membrane proteins form fewer protein crystal contacts on average in comparison to water-soluble proteins, which contributes to their poor diffraction (Carpenter et al., 2008).

Strengthening, changing or increasing the number of protein crystal contacts that are present in the crystal can improve diffraction. Based on this idea, one strategy commonly explored is the growth of protein crystals in multiple crystallization conditions, since it is often found that crystals which grown in two unique conditions crystallize in different space groups and therefore, most likely have a different packing arrangement and crystals contacts. Another strategy is to modify the purification conditions to include a shorter chain detergent (e.g. DM in place of DDM or OM in place of DDM) or a detergent with a different head group (a maltopyranoside vs. glucopyranoside; e.g. DM vs. DG), since a smaller detergent micelle will expose a greater surface area of protein to the hydrophilic environment and the detergent head group could alter the detergent-mediated contacts (although, not ordered) in the crystal. However, substitution with a shorter chain detergent or a different detergent head group may also result in protein destabilization and, therefore, detergent selection is invariably a balance between protein stability and exposure.

With a crystal structure and knowledge of crystal packing, another strategy is to introduce substitutions in the protein in order to strengthen a protein crystal contact. Likewise, breaking a protein crystal contact through the introduction of a residue substitution(s) could also be advantageous since it may promote the formation of a new contact that is less favored to the

original contact, and this new contact could be strengthened by additional mutagenesis. Finally, a web server has been developed to predict a region(s) of the protein that will form a crystal contact(s), which can be particularly informative in the absence of a crystal structure, and subsequent mutagenesis studies can be performed to evaluate whether this substitution alters crystal growth (Goldschmidt et al., 2007). The surface entropy reduction prediction (SERp) server identifies residues within a protein that contribute significant surface entropy to the molecule (i.e. side chains with many rotamers, such as lysine), since it has been suggested that residues with high conformational entropy prevent crystallization (Derewenda and Vekilov, 2006). The server uses a surface entropy reduction approach by replacing these residues with low conformational entropy residues. Potential regions of modification are scored by residue conformational entropy, conservation and secondary structure prediction (Goldschmidt et al., 2007).

In the case of membrane protein crystal growth, complexes between membrane and soluble proteins have been successful for crystallization of novel membrane proteins, as well as for improving the diffraction of previously crystallized proteins. The addition of the soluble protein increases the total surface area exposed to aqueous environment, which increases the probability of forming crystal contacts. In particular, co-crystallization with a monoclonal antibody has proven successful for obtaining diffraction-quality crystals of channels, transporters and G protein-coupled receptors (GPCRs) (Hibbs and Gouaux, 2011; Jiang et al., 2003; Rasmussen et al., 2007; Rasmussen et al., 2011b). In addition, monoclonal antibodies have been used to improve crystal diffraction of KcsA and a bacterial ClC Cl$^-$ channel, by altering the packing of the crystal and crystal contacts formed (Dutzler et al., 2003; Zhou et al., 2001b). Other examples of membrane/soluble protein crystal structures in the literature include an endogenous complex of the voltage-gated K$^+$ channel, K$_V$1.2, and an auxiliary β subunit, as well as an unusual example of

β2 adrenergic GPCR and lysozyme fusion protein, with insertion of lysozyme into one of the GPCR intracellular loops (Long et al., 2005; Rosenbaum et al., 2007).

In addition to a lack of crystal contacts, poor diffraction of protein crystals can be a result of structural or sample heterogeneity as a result of protein flexibility or partial/heterogeneous modification(s) to the protein, respectively. In the context of membrane proteins and protein modification, glycosylated asparagines are routinely removed prior to (substitution of the asparagine to a glutamine) or after purification (addition of endoglycosidase PNGase F). Since the glycan chain itself is quite diverse with different compositions, structures and lengths, it can consequently inhibit protein crystallization.

One method of reducing protein flexibility is by introducing stabilizing residue substitutions or truncations. Other methods involved the addition of a co-factor(s), ligand(s) or chemical compound(s) that stabilizes one conformation of the protein. In addition, a protein-protein complex not only can change the landscape of surface residue contacts, but also can stabilize a flexible region of the protein, which would otherwise not crystallize, or a specific protein conformation that is not observed when crystallized alone (Rasmussen et al., 2011a; Uysal et al., 2011). Finally, in a native environment, membrane proteins are in contact with various types of lipid moieties and it has been previously demonstrated that lipid additives and mixtures can significantly improve crystal performance by stabilizing one conformation (Hunte and Richers, 2008). Furthermore, ion channels are often modulated by specific lipid moieties, such as PUFAs, PLs and lysoPLs in the case of the TREK family of K_{2P} channels (Bang et al., 2000; Chemin et al., 2005a; Chemin et al., 2005b; Fink et al., 1998; Lesage et al., 2000b; Maingret et al., 2000b; Patel et al., 1998). A number of groups have published membrane protein thermostability screening methods to identify a detergent or lipid additive that stabilizes the membrane protein at its temperature threshold (Alexandrov et al., 2008; Hattori et al., 2012; Mancusso et al., 2011).

The stabilizing detergent or lipid additives are typically included during purification, but can also be added prior to setting up crystallization trials.

4.3. Materials and Methods

4.3.1. Na$^+$ flux and K$^+$ flux inhibition by tetraammonium (TA) compounds

See 3.3.3 K$_{2P}$1 reconstitution into vesicles and 3.3.4 K$^+$ flux assay for more details on the setup of both K$_{2P}$1 reconstitution and the flux assay. For reconstitution of human K$_{2P}$1 for Na$^+$ flux studies, three dialysis solutions were prepared containing 10 mM HEPES (pH 7.0), 150 mM NaCl and 0, 1 or 10 mM KCl. Low concentrations of KCl were included in the dialysis buffer since we had previously demonstrated that detergent-purified human K$_{2P}$1 stability is dependent on the presence of K$^+$.

For the Na$^+$ flux study, two experiments were performed. Experiment 1: A Na$^+$ gradient was established by diluting vesicles reconstituted in 150 mM NaCl 40-fold into flux assay buffer containing 150 mM NMDG$^+$, a channel-impermeable cation. The Na$^+$ flux assay was performed as described for K$^+$ flux assay, but with the substitution of monensin (Sigma-Aldrich; 20 nM final concentration from a 20 μM stock in ethanol) for valinomycin, at 450 sec to release Na$^+$ from all vesicles. Experiment 2: K$_{2P}$1 reconstituted in 10 mM HEPES, pH 7.0 and 150 mM KCl were diluted 100-fold into flux assay buffer containing 150 mM NaCl, diluting K$^+$ to a concentration (1.5 mM) that permits Na$^+$ flux (Ma et al., 2011; Ma et al., 2012a). K$^+$ flux assay was performed.

For studies of QA compound inhibition, K$_{2P}$1 reconstituted in 10 mM HEPES, pH 7.0 and 150 mM KCl were briefly sonicated and incubated with TEA, tetrahexylammonium (THexA) or tetraoctylammonium bromide (TOctA) (Sigma-Aldrich; 0.1 mM final concentration from a 10 mM stock in DMSO). Samples were diluted 40-fold into flux assay buffer containing 150 mM NaCl and 0.1 mM QA compound (or DMSO as a control) and the K$^+$ flux assay was performed.

4.3.2. Na$^+$-soaked K$_{2P}$1 crystals and co-crystallization of K$_{2P}$1 with THexA

For exchange into Na$^+$-containing solution, K$_{2P}$1 22-288 N95Q crystals were first transferred to 150 mM NaCl reservoir solution, substituting KCl for NaCl, and supplemented with 5 mM DM and 20 mM Tris-HCl, pH 7.5 in a step-wise manner (30 mM K$^+$ decrease / Na$^+$ increase at each step, 2-5 minute intervals). Crystals were then dehydrated and cryo-protected with Na$^+$ containing reservoir solution, supplemented with 50% PEG400 (v/v), 5 mM DM and 20 mM Tris-HCl in a step-wise manner (3.75% PEG400 increase each step, 2-5 minute intervals).

For introduction of THexA to K$_{2P}$1 crystals, DM-purified K$_{2P}$1 22-288 N95Q was concentrated to ~ 6 mg/ml and incubated with 0.1- 0.2 mM THexA (dissolved in DMSO) or a DMSO control by rotation at 4°C, overnight. Sample was used the next day to set up crystallization trials. Crystals grown in the presence of THexA appeared at a slightly higher PEG400 range (24-26%), but otherwise similar conditions to the native K$_{2P}$1 22-288 N95Q crystals,

4.3.3. Purification of K$_{2P}$1 13-290 N95Q for K$_{2P}$1 monoclonal antibody project

Human K$_{2P}$1 22-288 N95Q, which is the construct that crystallized, contains N- and C- terminal residues that were contributed by the vector (7 on the N- and 2 on the C-termini). The K$_{2P}$1 13-290 N95Q, used for immunization, is a similar length to K$_{2P}$1 22-288 N95Q, but contains K$_{2P}$1 wild-type residues. This construct is a GFP-fusion, purified in DDM as described in Chapter 2 (2.2.6 Human K$_{2P}$1 protein purifications), but with small modifications. After collection of the peak, several steps of binding with high-affinity GFP monoclonal antibody resin were performed to remove residual GFP from the sample. Afterwards, GFP contribution to the sample was evaluated by FSEC. DDM-purified human K$_{2P}$1 13-290 N95Q (2 mg/ml) was used for immunization (200 μl) of five mice and four hamsters a total of 4x (performed by the MSKCC Monoclonal Antibody Core Facility), as well as for native and denaturing ELISAs.

4.3.4. ELISAs for K$_{2P}$1 monoclonal antibody selection

DDM-purified human K$_{2P}$1 13-290 N95Q or purified GFP was diluted (20 μg/ml) into regular or denaturing coating solution. The coating solution containing 150 mM KCl; 10 mM Tris, pH 7.5 and 0.5 mM DDM, with the addition of 0.2% SDS and 20 mM DTT to the denaturing coating solution. Diluted protein (50 μl) was pipetted into a 96 well maxisorb plates (Corning) and stored overnight at 4°C. Coating solution was removed the next day and the plate was washed 3x using 200 μl/well of buffer A, which contained: 150 mM KCl; 10 mM Tris, pH 7.5 and 0.5 mM DDM. A blocking solution (buffer A + 5% bovine serum albumin; BSA) was subsequently added to the plate (400 μl/well) and left to incubate for 1 hour at room temperature. Blocking solution was removed and the plate was washed 3x using 200 μl/well of buffer A. Primary antibody solution (100 μl/well) containing diluted test eye bleeds (4 serial dilutions between 1:100 and 1:100,000) or hybridoma/clone supernatents (1:200 dilution) in buffer A + 2% BSA was applied and incubated for 1 hour at room temperature, shaking. Primary antibody solution was removed and the plate was washed 3x using 200 μl/well of buffer A. Mouse IgG secondary antibody (1:10,000 dilution; Promega) was added to buffer A + 2% BSA and the solution (100 μl/well) was incubated for 1 hour at room temperature, shaking. Secondary antibody solution was removed and the plate was washed 5x using 200 μl/well of buffer A. TMB chromogenic ELISA substrate (100 μl/well, Thermo Scientific) was added to each plate and incubated for 15 min at room temperature. The reaction was quenched with 2 M sulfuric acid (100 μl/well) and absorbance values were recorded using a 96 well plate reader (SpectraMax Plus; Molecular Devices).

4.3.5. FSEC screening for K$_{2P}$1 monoclonal antibody selection

Samples of GFP-tagged human K$_{2P}$1 13-290 N95Q expressed in *P. pastoris* were prepared for FSEC screening. Briefly, human K$_{2P}$1 13-290 N95Q was extraction from lysed *P. pastoris* (fermentor) in buffer containing 150 mM KCl; 20 mM Tris, pH 7.5; 1:500 dilution of PI Mix III

and 40 mM DDM. Samples were rotated for 1 hour at 4°C, and then the sample was centrifugated for 1 hour at 4°C. The soluble fraction was collected, flash cooled and stored at -80°C.

GFP-tagged human $K_{2P}1$ Δ43-101 with VLEDD linker (extracellular cap deletion construct) was transfected and expressed in HEK293-GT cells. Cells were pelleted and flash cooled. For preparation of DDM-extracted sample, cells were thawed and the channel was extracted buffer containing 150 mM KCl; 20 mM Tris, pH 7.5; 1:500 dilution of PI Mix III and 40 mM DDM. Samples were rotated for 1 hour at 4°C, and then centrifugated for 1 hour at 4°C. The soluble fraction was collected.

For FSEC screening, $K_{2P}1$ was diluted in running buffer so that the peak height was ~ 20 fluorescence units ($K_{2P}1$ 13-290 N95Q ~ 1:100 dilution; $K_{2P}1$ extracelular cap deletion construct, ~ 1:5 dilution). Running buffer contained: 150 mM KCl; 20 mM Tris, pH 7.5; 1 mM DDM. Diluted $K_{2P}1$ (100 μl) was combined with hybridoma supernatant (50 μl) and incubated at room temperature for 15-20 min, shaking. Sample was separated (100 μl) by FSEC (Superose 6).

4.3.6. Antibody isotyping

$K_{2P}1$ 13-290 N95Q native ELISAs were performed for antibody isotyping of hybridomas with the ELISA protocol described above. Mouse IgG1, IgG2a, IgG2b and IgG3 secondary antibodies (1:3,000 dilution; Jackson Immunoresearch) substituted for the mouse IgG secondary antibody. For isotyping of clones picks, a rapid ELISA mouse antibody isotyping kit was used (Thermo Scientific).

4.4. Results

4.4.1. K$_{2P}$1 mutants generated to strengthen or create a new crystal contact

Attempts to crystallize K$_{2P}$1 C-terminal truncation mutants (e.g. Δ275) and purify K$_{2P}$1 in different detergent (CYMAL-6, OM in the presence of lipids) for the purpose of identifying new crystal conditions, did not yield different crystal packing or improve in crystal diffraction (see 3.4.2 Human K$_{2P}$1 crystal refinement and derivatization). Therefore, a direct strategy used to improve crystal diffraction was to alter the contacts that were being made in the crystal lattice by creating salt bridges that could strengthen and stabilize an interaction, potentially resulting in a more ordered crystals which could diffract to higher resolution. Four crystal contact mutant constructs were generated based on the arrangement of human K$_{2P}$1 22-288 N95Q in the crystal. The only ordered crystal contact that is made is at histidine 169 (H169), located on the loop connecting M2 and M3 (M2-M3 loop), which forms a hydrogen bond with H169 on a neighboring channel (Figure 4.1). Although the distance measured between the two histidine is 4.1 Å, a distance greater than one would expect for a hydrogen bond, the subsequent residues within this loop region are disordered and, in combination with the modest (3.4 Å) resolution of this structure, most likely produces some error in assigning the atomic coordinates for this residue. Since H169 is followed by isoleucine 170 (I170) and arginine 171 (R171), one strategy was to engineer a salt bridge utilizing R171. A double point mutation of H169 to glutamate (H169E) and I170 to alanine (I170A) was generated to promote the formation of a H169E-R171 salt bridge between neighboring channels. Likewise, leucine 166 (L166) is positioned on the channel surface towards the M2-M3 loop and a L166 to glutamate (L166E) was cloned to form a salt bridge between L166E and R171 (Figure 4.1).

Generating crystal contacts by mutagenesis of residues in close proximity with one another in the crystal was another strategy pursued. For instance, the N-terminal residue in the K$_{2P}$1 22-288
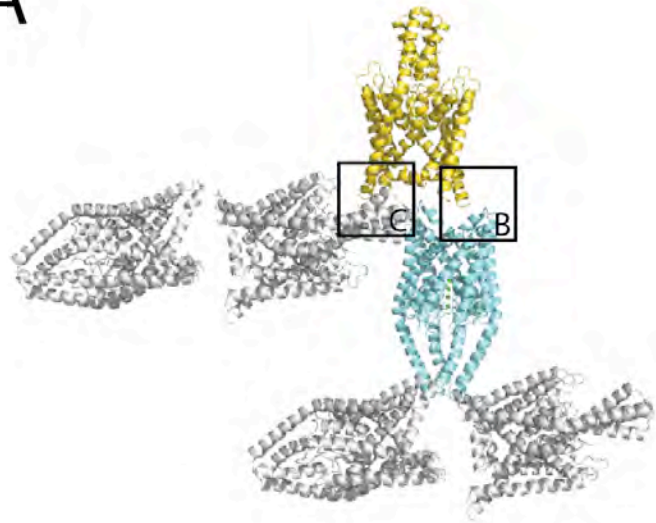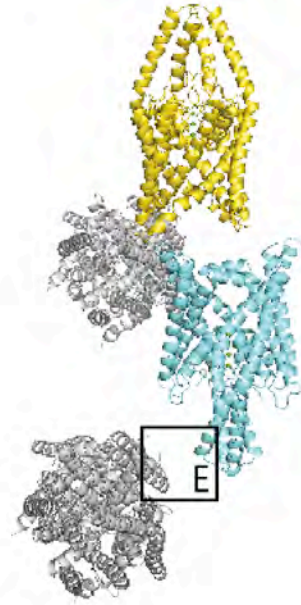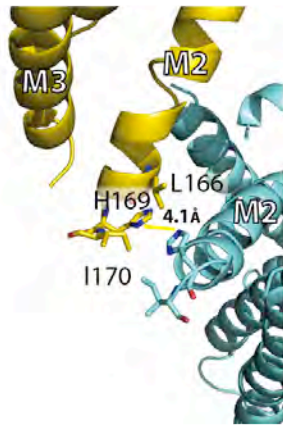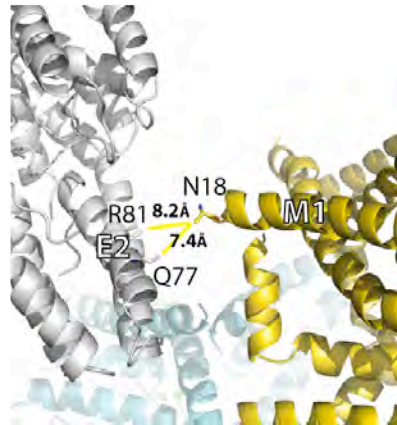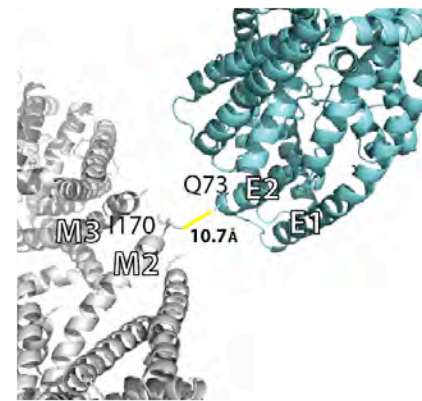
Figure 4.1: Crystal packing of K$_{2P}$1. (A) View of overall packing in K$_{2P}$1 in ribbon representation, crystallized in the space group P2$_1$. Four protomer, or two channels, are present in the asymmetric unit, and are colored in cyan and yellow. Additional K$_{2P}$1 channels are colored in gray. Boxes highlight regions in which residues are in close proximity to one another (boxes labeled B and C). (B) Close up view of the M2-M3 loop (box B from A). Coloring is the same as in (A). Residues labeled were mutated, as described in the text. They are drawn in colored stick representation (blue, nitrogen; red, oxygen). Distance between residues is drawn in yellow. Transmembrane helices (M2, M3) near this region are labeled. (C) Close up view of box C from (A). Coloring and labeling is the same as in (B). Helices (E2, M1) near this region are labeled. (D) Orthogonal view of (A). Box highlight regions in which residues are in close proximity to one another (box labeled E). (E) Close up view of box E from (D). Coloring and labeling is the same as in (B). Helices (E1, E2, M2, M3) near this region are labeled. Residues which are highlighted are labeled in single letter amino acid code (H, His; I, Ile; L, Leu; N, Asp; Q, Gln; R, Arg).

N95Q crystal structure, asparagine 18 (N18), is in close proximity (within 8.5 Å) to glutamine 77 (Q77) and arginine 81 (R81), residues within E2 of the extracellular cap (Figure 4.1). A triple mutant of these three residues, N18 to arginine, Q77 to glutamate and R81 to glutamate was generated to promote salt bridge formation. Likewise, glutamine 73 (Q73) is within the apex of the extracellular cap, is positioned on the surface of the channel and is reasonably near (within 11 Å) R171 on the M2-M3 loop (Figure 4.1). In addition, the crystal packing of $K_{2P}4$, which crystallized in a different space group (orthorhombic, $P2_12_12_1$) to $K_{2P}1$ (monoclinic, $P2_1$), is arranged with the extracellular cap making a crystal contact with the M2-M3 loop (Brohawn et al., 2012). Q73 was mutated to a glutamate to encourage the formation of a crystal contact between extracellular cap (Q73E) and the M2-M3 loop (R171). All mutants were generated in the $K_{2P}1$ 22-288 N95Q background.

All four crystal contact mutants were generated, expressed in *P. pastoris* and purified in buffer containing DM. Crystallization trials utilizing broad matrix screens, as well as a PEG400 and pH fine screen that was generated for optimizing $K_{2P}1$ 22-288 N95Q crystals, were set up. All constructs were able to crystallize in the fine screen and most were able to grow in a few of the broad matrix screen conditions, with 20% PEG400 being the common condition among all crystals. The crystals which performed the best, as evaluated by diffraction resolution, were harvested from the $K_{2P}1$ 22-288 N95Q fine screen. These diffracted to ~6-8 Å and indexed to the same space group as the original $K_{2P}1$ 22-288 N95Q crystals. Interestingly, unlike the $K_{2P}1$ 22-288 N95Q crystals, the crystal contact mutants did not improve with PEG400 dehydration.

4.4.2. Progress towards identifying the site of THexA binding through $K_{2P}1$ co-crystallization trials

K_{2P} channels are insensitive to TEA, an inhibitor of many tetrameric K^+ channels. However, a recent study demonstrated that longer alkyl length QA compounds such as tetrapentylammonium

(TPenA) and THexA are effective at inhibiting 3 different K_{2P} channels (Piechotta et al., 2011). To first evaluate whether longer alkyl length QA compounds are capable of inhibiting $K_{2P}1$, the K^+ channel flux was performed with vesicle-reconstituted human $K_{2P}1$ 22-288 N95Q (Figure 4.2). Of the three compounds that were tested, THexA and TOctA reduced the fluorescence drop observed for human $K_{2P}1$ 22-288 N95Q vesicles alone (Figure 4.2), suggesting that these two compounds are able to reduce $K_{2P}1$ K^+ flux.

In order to identify the site of THexA binding within K_{2P} channels, I set up crystallization trials with human $K_{2P}1$ in the presence of THexA. Crystals grew in conditions similar to the original crystals refined. A dataset was collected which diffracted to ~4.7 Å. It was clear from this trials that addition of THexA did not improve the diffraction. The crystals indexed to $P2_1$ with similar cell dimensions to the native $K_{2P}1$ crystals and the dataset was isomorphous to a native $K_{2P}1$ dataset (Rmerge = 18%). I performed rigid body refinement using the human $K_{2P}1$ crystal structure (Rfree = 33%). No significant differences to the structure were apparent at this resolution range and it could not be determined from the density if THexA was bound or not. In addition, no significant positive density was observed in a Fo-Fo difference map calculated from $K_{2P}1$ THexA and native datasets, with phase information contributed from the $K_{2P}1$ crystal structure (PDB ID: 3UKM) (Figure 4.3).

4.4.3. How does the concentration of extracellular K^+ affect $K_{2P}1$ selectivity?

Recent studies of $K_{2P}1$ demonstrated that ion selectivity is altered when the channel is exposed to low extracellular K^+ concentrations, a condition that resembles hypokalemia, which can result in heart arrhythmias and attacks in humans (Ma et al., 2011; Ma et al., 2012a). Na^+ contributes to the total current amplitude measured in CHO cells overexpressing $K_{2P}1$ K274E when extracellular K^+ concentrations fall below 3 mM. In addition, it has been shown that low
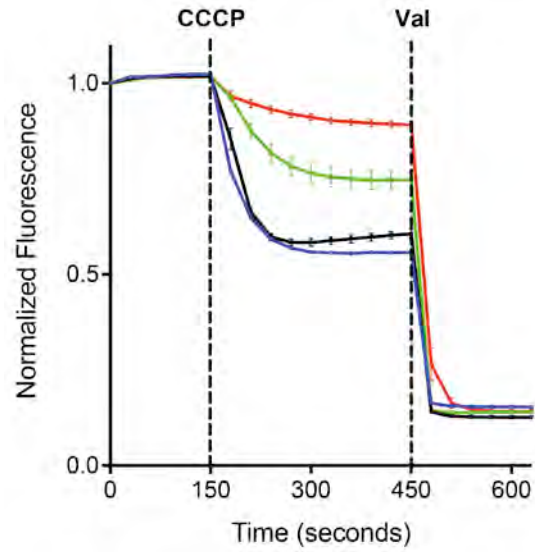
Figure 4.2: K$^+$ flux assay with QA compounds. Fluorescence changes observed for K$_{2P}$1 channels in the absence (DMSO, black) and presence of 100 µM QA compounds (TEA, blue; THexA, red; TOctA, green). Error bars indicate the standard error of three measurements from the mean.
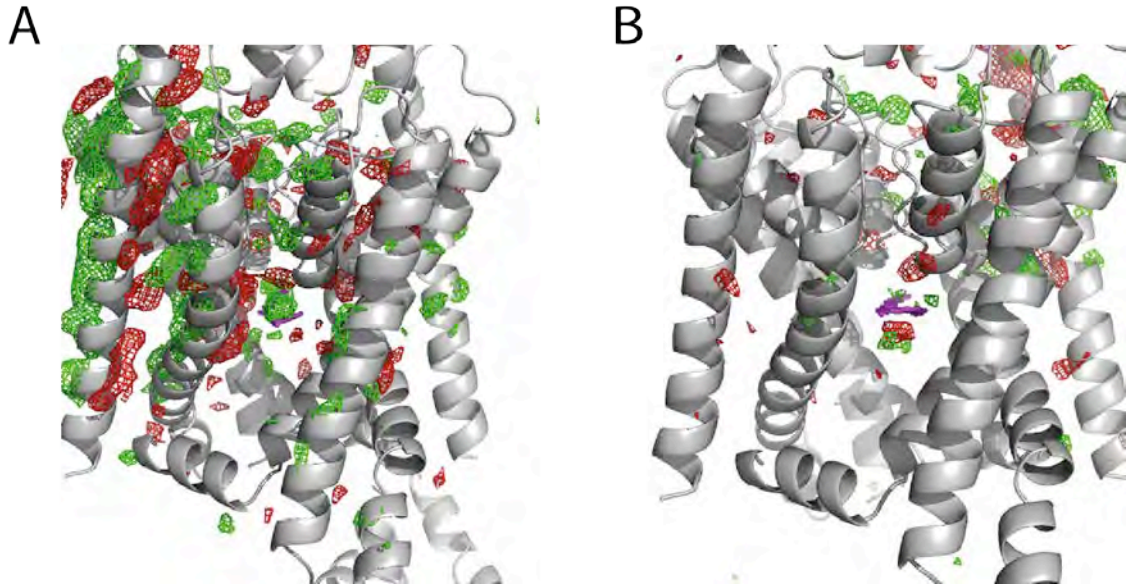
Figure 4.3: Positive electron density was not observed in K$_{2P}$1 crystals grown in the presence of the QA compound. (A) Ribbon representation of K$_{2P}$1 channel 1 in the asymmetric unit, viewed from the membrane, with intramembrane opening visible. Fo-Fo difference electron density map (positive density, green mesh; negative density, red mesh) was calculated from 20 to 3.4 Å resolution and contoured at 3 σ. (B) Ribbon representation of K$_{2P}$1 channel 2 in the asymmetric unit, viewed from the membrane, with intramembrane opening visible. Fo-Fo difference electron density map is colored as in (A).

extracellular pH results in altered selectivity and Na^+ influx through $K_{2P}1$ channels (Ma et al., 2012b). In order to evaluate Na^+ flux with purified $K_{2P}1$, I performed the flux assay using two experimental designs: a Na^+ gradient experiment and a K^+ 100-fold gradient experiment.

The first involves establishing a Na^+ gradient (3.75 mM outside, 150 mM inside) by diluting $K_{2P}1$ vesicles reconstituted in 150 mM NaCl into flux buffer containing 150 mM $NMDG^+$, a channel-impermeable cation. For this experiment, reconstitution of $K_{2P}1$ was performed in buffer containing 150 mM NaCl and 0, 1 or 10 mM KCl since lack of K^+ destabilizes detergent-purified $K_{2P}1$. Unfortunately, no fluorescence drop was observed after addition of CCCP for Na^+-reconstituted $K_{2P}1$ (Figure 4.4). The subsequent addition of monensin, a Na^+-selective ionophore, reduced fluorescence to baseline. We suspected that this result was not necessarily reflective of Na^+ flux through $K_{2P}1$, but more likely destabilization of $K_{2P}1$ during reconstitution, even in the presence of 10 mM KCl.

The second experimental setup involved creating a K^+ gradient that is representative of hypokalemia (low 'extracellular' K^+ concentration). A potassium gradient was established (1.5 mM outside, 150 mM inside) by diluting $K_{2P}1$ vesicles reconstituted in 150 mM KCl 100-fold into flux buffer containing 150 mM NaCl. This was compared to $K_{2P}1$ vesicles diluted 100-fold into flux buffer, supplemented with 6.5 mM KCl (7.5 mM total K^+, basal K^+ condition). The low 'extracellular' K^+ condition reduces the fluorescence drop that is measured for $K_{2P}1$ vesicles exposed to basal K^+ condition (Figure 4.4). For a K^+ selective channel, a steeper K^+ gradient should result in greater K^+ flux. $K_{2P}1$ exhibited the opposite effect, which corroborates with a change in $K_{2P}1$ ion selectivity.

In the high-resolution crystal structure of the KcsA, the selectivity filter adopts a collapsed, or
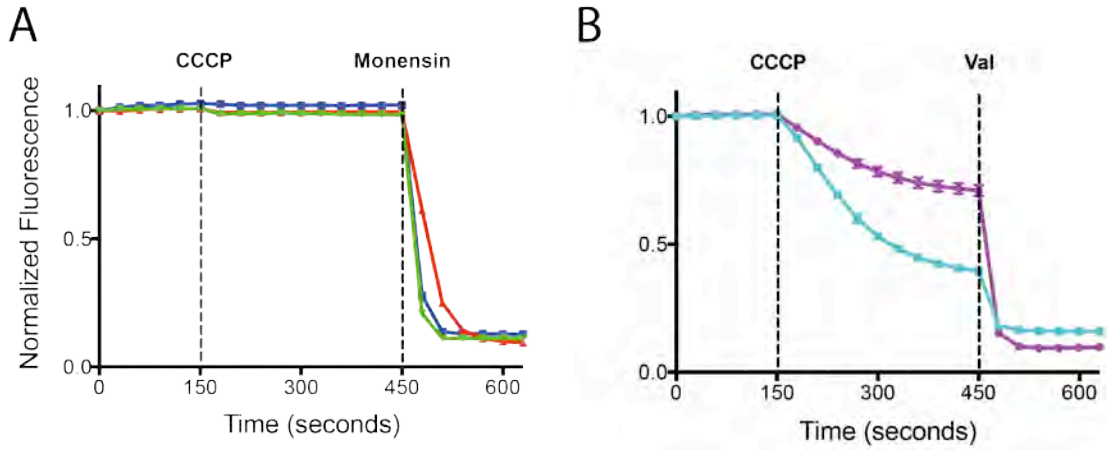
Figure 4.4: Na$^+$ flux studies with reconstituted K$_{2P}$1 (A) Na+ flux assay with vesicles reconstituted in buffer containing 150 mM NaCl and 0 mM (blue), 1 mM (red) or 10 mM (green) KCl. CCCP was added at 150 seconds and monensin at 450 sec, to render all vesicles Na$^+$ permeable. (B) Vesicles reconstituted in 150 mM KCl were diluted 100-fold into flux buffer containing 150 mM NaCl alone (magenta) or with 6 mM KCl (cyan). CCCP was added at 150 seconds and valinomycin (Val) at 450 sec, to render all vesicles K$^+$ permeable.

non-conductive, conformation when exposed to a low concentration of K^+ (3 mM) (Zhou et al., 2001b; Zhou and MacKinnon, 2003). However, a recent high-resolution crystal structure of MthK, does not adopt this conformation when exposed to similar conditions (Ye et al., 2010). To begin studying the effect of Na^+ on $K_{2P}1$, a dataset was collected from $K_{2P}1$ crystal soaked in NaCl (150 mM). This dataset diffracted to ~ 4.3 Å and was isomorphous to the original datasets that were collected (R_{merge} = 14%). I performed rigid body refinement (CNS) using the $K_{2P}1$ crystal structure but no significant changes to the human $K_{2P}1$ structure were apparent at this resolution (R_{free} = 32%).

4.4.4. Generation of $K_{2P}1$ monoclonal antibodies for co-crystallization with $K_{2P}1$

Another strategy for obtaining a high-resolution crystal structure of human $K_{2P}1$ involves co-crystallization of the channel with a $K_{2P}1$ interacting, soluble protein. A monoclonal antibody (mAb) against human $K_{2P}1$ would be an ideal candidate for co-crystallization since mAbs typically bind to their target with high-affinity and are structurally stable. The goal is to change the crystal packing and possibly improve the stability of human $K_{2P}1$ with the addition of the monoclonal antibody. The human $K_{2P}1$ construct that was purified and used for immunization ($K_{2P}1$ 13-290, N95Q) is 100% identical to the $K_{2P}1$ channel expressed in the host (mouse) and, as a result, we were not certain whether the mice would mount an immune response to human $K_{2P}1$. As a result, we chose to immunize both mice (x5) and hamsters (x4) to increase our chance of success.

Mice and hamsters were injected with 200 μl of $K_{2P}1$ 13-290, N95Q (2 mg/ml) a total of 4 times at 3 week intervals by the MSKCC Monoclonal Antibody Core Facility. One week after immunization, test eye bleeds were collected from the mice and hamsters and both human $K_{2P}1$ 13-290 N95Q native ELISAs were performed with 4 dilutions of each eye bleed to evaluate the response of the mice and hamsters to the $K_{2P}1$ antigen. GFP native ELISAs were also performed

to ensure that the animals were not mounting an immune response to residual GFP that could have remained in the purified human $K_{2P}1$ used for injections. The mice had a robust response to the $K_{2P}1$ antigen, with a clear response after the first immunization, which continued through the four immunizations. The response from the hamsters was not as robust initially, but was similar to the levels of the mouse response after the fourth immunization. However, the hamsters test bleeds also exhibited a response to GFP, suggesting that the hamsters were also producing antibodies against GFP. As a result, we chose to move forward with the best responding mouse for the generation of hybridomas.

Hybridomas were generated by fusion of mouse spleen cells with an immortal myeloma cell line, which was performed by the MSKCC Monoclonal Antibody Core Facility. Fused cells were selected for, diluted to yield ~ 1-3 hybridomas/well and grown in 96 well plates. Supernatent containing secreted $K_{2P}1$ antibody was collected from each hybridoma well and screened by human $K_{2P}1$ 13-290 N95Q native and denaturing ELISAs to evaluate the response from each well, as well as to distinguish antibodies which recognized structured and/or denatured human $K_{2P}1$. Initially, I performed GFP native ELISAs to ensure that the hybridomas were not producing antibodies against GFP, and from my initial tests, it was clear that none of the hybridomas responded to GFP. A total of 84 human $K_{2P}1$ 13-290 N95Q native ELISA positive and denaturing ELISA negative hybridomas were passaged, screened an additional x2 and flash cooled.

The native ELISA positive hybridomas were also mixed with GFP-tagged human $K_{2P}1$ 13-290 and screened by FSEC as a second measure of binding to the native protein. Antibodies which bound to human $K_{2P}1$ 13-290 shifted the elution volume of the human $K_{2P}1$ 13-290 peak to the left or reduced the size of the peak. The hybridomas were grouped into three categories: ones which caused a full peak shift (positive), ones which caused a partial shift (partial), and ones which appeared to have no effect (negative) (Figure 4.5). The 84 hybridomas initially identified
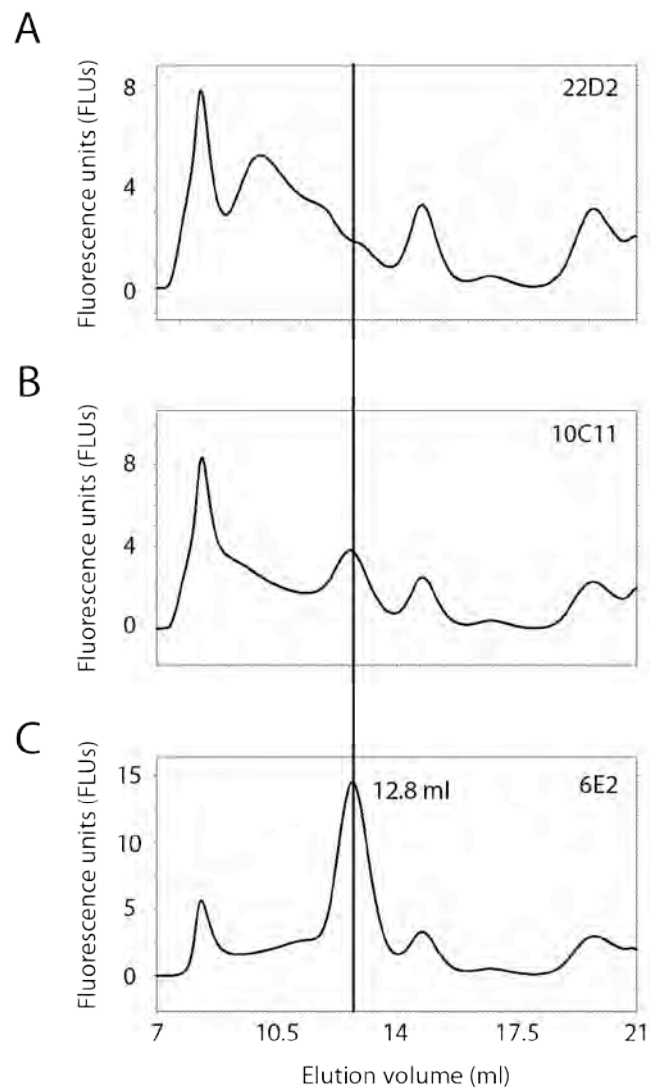
Figure 4.5: Representative FSEC traces of positive (A, hybridoma 22D2), partial (B, hybridoma 10C11) or negative (C, hybridoma 6E2) shifts of the $K_{2P}1$ peak in the presence of three ELISA positive hybridomas.

by $K_{2P}1$ native ELISA were categorized into 26 FSEC positive, 29 FSEC partial, and 29 FSEC negative hybridomas. In addition, a GFP-tagged human $K_{2P}1$ extracellular cap deletion construct was generated in order to identify the region(s) of antibody binding to human $K_{2P}1$. This was done for the purpose of $K_{2P}1$ antibody sub-classification, which would assist with choosing hybridomas for clonal selection. Incubation of the human $K_{2P}1$ extracellular cap mutant with the mouse terminal bleed, as well as test with hybridomas, did not cause a shift in the peak, suggesting that the all of the antibodies are targeted to the extracellular cap. The isotype of each native ELISA positive hybridoma was also identified at this stage by performing a human $K_{2P}1$ 13-290 native ELISA, using secondary antibodies against IgG 1, 2a, 2b or 3. Again, this was done to sub-classify the $K_{2P}1$ antibodies for the purpose of choosing hybridomas for clonal selection.

Overall, a total of 10 hybridomas, 5 FSEC positive, 3 FSEC partial, and 2 FSEC negative that grouped into IgG 1, 2a or 2b isotypes were chosen (Table 4.1). Individual clones were selected for (MSKCC Monoclonal Antibody Core Facility), screened by human $K_{2P}1$ 13-290 native ELISA a total of 2-3 times, and the isotype of each antibody was again characterized to validate the original results. A native ELISA positive clone for each antibody was identified and flash cooled. Future work will involve purification of the Fab fragments and set up of co-crystallization trials with human $K_{2P}1$.

4.5.   Discussion

With knowledge of the $K_{2P}1$ 22-288 N95Q crystal packing, one strategy to improve crystal diffraction was to manipulate the residues surrounding H169, the only protein crystal contact that formed. In addition, another strategy was to target residues that appear near each other as evaluated from the $K_{2P}1$ 22-288 N95Q crystal packing, which may be able to form a new salt bridge crystal contact with ideal residue substitutions. Knowledge of the crystal contacts made in the recently published $K_{2P}4$ structure also guided our crystal contact mutagenesis studies. A total

Hybridoma Name	FSEC (K$_{2P}$1 13-290 N95Q)			ELISA-1	ELISA-2	ELISA-3	Isotype
	Positive	Partial	Negative				
22D2	+			1.76	2.22	1.96	1
3B11	+			2.04	2.59	2.11	1
7B7	+			3.61	3.61	3.57	2a
8D11	+			3.45	3.63	4	2a
6A2	+			4	3.7	3.64	2b
7F10		+		0.88	1.24	1.33	1
10C11		+		3.38	3.6	3.46	2a
7G4		+		3.44	3.61	3.51	2b
6E2			+	1.84	1.29	1.06	1
2G11			+	2.34	1.58	1.43	2b

Table 4.1: Summary of the 10 K$_{2P}$1 hybridomas chosen for clonal selection and propagation. Hybridomas are sorted based on FSEC status (positive, partial or negative K$_{2P}$1 peak shift). Absorbance values are also provided from three independent K$_{2P}$1 native ELISAs (ELISA 1-3). Hybridoma isotypes are listed (IgG 1, 2a or 2b).

of four mutants were generated in the $K_{2P}1$ 22-288 N95Q background: H169E-R171, L166E, N18R/Q77E/R81E, and Q73E (Figure 4.1). All four mutants crystallized, although in similar conditions to what was observed for $K_{2P}1$ 22-288 N95Q native crystals (20% PEG400, various salt conditions, see 3.4.2 Human $K_{2P}1$ crystal refinement and derivatization). The crystals which performed the best, as evaluated by diffraction resolution (~6-8 Å resoltuion), were harvested from a $K_{2P}1$ 22-288 N95Q fine screen. Not surprisingly, all of the crystals indexed to the same space group of $P2_1$ as the original $K_{2P}1$ 22-288 N95Q crystals with similar unit cell dimensions, suggesting the packing had not changed significantly. Furthermore, unlike the $K_{2P}1$ 22-288 N95Q native crystals, the crystal contact mutants performed worse with PEG400 dehydration, as evaluated by diffraction resolution.

Design of the four crystal contact mutants tested was solely based on the packing information gained from the $K_{2P}1$ 22-288 N95Q crystal structure. In addition, the only substitutions that were made were to arginine or glutamate in order to promote the formation of a salt bridge, a strong non-covalent bond, which involves both electrostatic and hydrogen bond interactions. The loop connecting M2 and M3 in both $K_{2P}1$ and $K_{2P}4$ crystal structures are disordered, yet in both cases are important for forming crystal contacts. It is possible that additional mutagenesis to this region, either by shortening the loop or by introducing additional residues which can form crystal contacts or reduce conformational entropy (e.g. alanines) would improve protein stability and, thus, crystal diffraction. The only substitution that has currently been made to $K_{2P}1$ H169 was to a glutamate. Mutation to an alanine would not introduce surface entropy in this region and break the crystal contact, which could then promote the formation of a different crystal contact. In addition, the extracellular cap in the $K_{2P}4$ crystal structure is participating in the protein crystal contacts that are being made, where there is no participation of this region in the $K_{2P}1$ crystal structure. The extracellular cap is also the largest solvent-exposed region of the protein, making this an ideal target for formation of crystal contacts. Mutagenesis within this region could be

further explored. Finally, the SERp server predictions could be used in conjunction with our prior K$_{2P}$1 crystal packing knowledge to generate further crystal contact mutants.

QA compounds with longer alkyl tails, such as THexA, have been previously demonstrated to be potent inhibitors of three K$_{2P}$ channels: K$_{2P}$2, K$_{2P}$9 and K$_{2P}$18 (Piechotta et al., 2011). Using the K$^+$ flux assay, I demonstrated that that both THexA and TOctA are able to block K$^+$ flux through K$_{2P}$1-reconstituted channels, as evaluated by a reduction in fluorescence loss in the presence of THexA and TOctA, but not in the presence of TEA or the DMSO control (Figure 4.2). Further analysis of this could have been done by titrating different concentrations of THexA and TOctA to demonstrate that the QA block is dose-dependent. A second independent experiment utilizing whole-cell patch clamp could be performed with K$_{2P}$1 22-288 N95Q overexpressed in *Xenopus* oocytes to further validate this finding. Co-crystallization of K$_{2P}$1 22-288 N95Q with THexA did not appear to result in improved protein stability based on the crystal diffraction resolution. At this low resolution, it is difficult to determine whether THexA is bound, although the experimental evidence suggests that it is inhibiting K$^+$ flux through K$_{2P}$1 22-288 N95Q and that THexA binds within the central cavity of K$_{2P}$ channels (Piechotta et al., 2011). Since we observe density in the native K$_{2P}$1 22-288 N95Q crystal structure, THexA may be replacing the detergent or lipid molecule that is present in the native protein, suggesting a feasible reason for not observing a change in the F$_O$ (THexA) - F$_O$ (native) difference map (Figure 4.3).

In conditions which resemble hypokalemia, K$_{2P}$1 has been demonstrated to conduct Na$^+$, as evaluated by a shift in the reversal potential which is lost in the when NMDG$^+$ is substituted for Na$^+$ (Ma et al., 2011; Ma et al., 2012a). With the flux assay, I attempted to recapitulate these published findings utilizing K$_{2P}$1 22-288 N95Q reconstituted protein. Modification to the flux assay to monitor Na$^+$ flux by creating a Na$^+$ gradient without KCl, or in the presence of 1 mM or 10 mM KCl was unsuccessful (Figure 4.4). However, dilution of the K$_{2P}$1 vesicles reconstituted

in KCl by 100-fold (1.5 mM KCl outside) mimics the low extracellular K^+ concentration that resembles hypokalemia and reduces K^+ flux, as one would expect with opposing Na^+ flux (Figure 4.4). Furthermore, 100-fold dilution of $K_{2P}1$ vesicles and the subsequent addition of 6 mM KCl to the flux assay buffer (total of 7.5 mM extracellular KCl) restores K^+ flux to levels similar with a 20- or 40-fold dilution of $K_{2P}1$ (Figure 4.4). These results suggest that selectivity of $K_{2P}1$ is altered with low extracellular K^+ (<1.5 mM), leading to Na^+ permeation. An additional experiment that needs to be performed is 100-fold $K_{2P}1$ vesicle dilution into flux assay buffer containing 150 mM $NMDG^+$, which is $K_{2P}1$ impermeable. Although the kinetics may be altered, one would expect in this case, to observe an overall fluorescence drop similar to the 20- or 40-fold dilution of $K_{2P}1$ if Na^+ influx was preventing K^+ efflux through $K_{2P}1$.

$K_{2P}1$ 22-288 N95Q crystals soaked in 150 mM NaCl diffracted to a similar resolution as the native crystals, yet no major structural perturbations were observed to the selectivity filter at this resolution, as evaluated by rigid body refinement (CNS) using the $K_{2P}1$ crystal structure. The presence of Na^+ did not increase stability within this region since there was no significant improvement to the diffraction resolution, which is not surprising in retrospect since K^+ coordination is energetically favored to Na^+. In addition, it is not surprising that a major structural perturbation to the $K_{2P}1$ selectivity filter is not observed. The large conformational change that is observed in low K^+ conditions (3 mM) for KcsA results in a selectivity filter that is in a 'non-conductive' configuration (Zhou et al., 2001a). In contrast, a recent high-resolution crystal structure of MthK, does not adopt this conformation when exposed to similar conditions and it is further demonstrated that MthK is able to conduct Na^+ in the absence of K^+ (Ye et al., 2010). One could speculate, based on these published structures and experimental data, that the $K_{2P}1$ selectivity filter in low extracellular K^+ conditions will more likely resemble the MthK when exposed to low K^+ since it is, like MthK, able to conduct Na^+. However, a high-resolution

structure of $K_{2P}1$ in high (150 mM) and low (< 1.5 mM) KCl conditions is necessary to verify this hypothesis.

Another strategy to improve $K_{2P}1$ crystal diffraction is to alter the crystal packing and possibly improve $K_{2P}1$ stability by co-crystallization of $K_{2P}1$ with a mAb. We sought to generate and isolate individual human $K_{2P}1$ mAbs. Mice and hamsters were immunized with $K_{2P}1$ 13-290 N95Q a total of 4x at 3 week intervals for generation of $K_{2P}1$ mAbs. The best responding animal (mouse), as evaluated by $K_{2P}1$ 13-290 N95Q native ELISAs with test eye bleeds, was sacrified and hybridomas were generated. Through a native and denaturing ELISA screening process of > 1000 hybridoma supernatents, a total of 84 native ELISA positive hybridomas were identified (Table 4.1). They were further characterized by both FSEC screening and ELISA isotyping. A total of 10 hybridomas were picked for clonal selection and $K_{2P}1$ 13-290 N95Q native ELISAs were performed with the $K_{2P}1$ mAb-producing hybridoma clones in order to validate of the original ELISA results (Table 4.1). The $K_{2P}1$ monoclonal antibodies have to still be tested in co-crystallization experiments with $K_{2P}1$. Currently, co-crystallization with a $K_{2P}1$-Fab appears to be our best lead for obtaining a high-resolution structure of $K_{2P}1$. In support of this idea, MacKinnon and colleagues published a higher-resolution (2.75 Å) structure of $K_{2P}4$ in complex with a Fab (Brohawn et al., 2013). However, $K_{2P}4$ crystallized in a similar conformation to their original structure. Questions pertaining to K_{2P} outer pore gating have yet to be elucidated.

There are several other strategies for obtaining a high-resolution $K_{2P}1$ crystal structure. One strategy is based on experimental data suggesting that human $K_{2P}1$ is a target for SUMO conjugation (Rajan et al., 2005). Human SUMO1 and SUMO2/3 are structured, ~ 10 kDa protein, that could potentially stabilize a conformation of $K_{2P}1$ when K274 is conjugated with SUMO, and thus could alter and improve crystal growth and diffraction (Gareau and Lima, 2010). An *in vitro* SUMO conjugation assay can be performed to transfer mature, purified SUMO1 or SUMO2/3 to

purified $K_{2P}1$ prior to setting up crystallization trials (Yunus and Lima, 2009). Another strategy that could be tested is a membrane protein crystallization technique that has proven to be very successful for the crystallization of G protein-coupled receptors called lipidic cubic phase (LCP). This is particularly useful for membrane proteins that do not harbor a large extracellular or intracellular domain since crystal contacts that are made in LCP (Type I crystal packing of membrane proteins) are formed with both hydrophobic and hydrophilic regions (Caffrey, 2003; Caffrey et al., 2012; Cherezov, 2011). This is in contrast to traditional membrane protein crystals (Type II crystal packing of membrane proteins), which rely on the hydrophilic regions to form protein-protein crystal contacts due to the detergent micelle. One disadvantage of LCP matrix is the restriction for small, largely hydrophobic membrane proteins. One modification to the LCP technique that has been explored is to transform the LCP to a "sponge" phase with the addition of common additives (e.g. non-volatile alcohols, low molecular weight PEGs) which expands the LCP matrix to accommodate for larger hydrophilic regions or potentially interacting soluble proteins (Cherezov, 2011).

CHAPTER 5

5.   SUMMARY AND FUTURE DIRECTIONS

Summary:

This dissertation describes the first crystal structure of a K_{2P} family member, human $K_{2P}1$, solved to 3.4 Å resolution. Although a number of the fundamental structural features identified in tetrameric K^+ channels are also observed in this structure, $K_{2P}1$ is a dimer. As a result, $K_{2P}1$ confers two-fold symmetry of packing around the selectivity filter, which may be important for K_{2P} outer pore gating. In addition, this extracellular domain restricts access of K^+ ions to the extracellular side of the filter to two side portals. This feature has not been previously observed in other K^+ channels. It is a domain that is likely a hallmark of K_{2P} channels and so its function, although currently unknown, will most likely reflect on the family of K^+ channels. In addition to the inner helices, this C helix may also be involved in inner helical gating. Finally, the intramembrane openings which expose the ion conduction pore to the lipid bilayer could be important for sensing mechanical stress or for modulation by lipids.

Future Directions:

K_{2P} channels were originally described as background or leak channels, as predicted by the GHK current equation that was derived over 60 years ago (Goldman, 1943; Hodgkin and Katz, 1949). Although the electrophysiological properties of K_{2P} channels best represent K^+ leak channels, many family members diverge from the GHK prediction. The recently published crystal structures of two human K_{2P} channels, $K_{2P}1$ (TWIK-1) and $K_{2P}4$ (TRAAK), provide us with structural information to begin elucidating and exploring the gating and conduction properties

that distinguish this class of channels from other K^+ channels (Brohawn et al., 2012; Brohawn et al., 2013; Miller and Long, 2012).

Experimental strategy for evaluating function of extracellular cap

The extracellular cap is most likely a conserved feature of K_{2P} channels. The cap is present in both $K_{2P}1$ and $K_{2P}4$ channel structure (Figure 3.3, Figure 3.15). Although the residues within the structured regions of the extracellular cap are not identical among K_{2P} channels, the overall size of the cap and the charge of these residues (e.g. residues which contribute to the hydrophobic core) are conserved (Figure 2.9). Furthermore, the extracellular cap is a region that distinguishes the K_{2P} channel subfamilies from one another since conservation of cap size and residue charges is most conserved among subfamily members (Figure 2.9). The extracellular cap is a feature that has been only recently observed in the $K_{2P}1$ and $K_{2P}4$ crystals structures and, consequently, it has not been well studied and its physiological role in K_{2P} gating and conduction is not known.

The extracellular cap restricts access of hydrated K^+ ions to two side portals, which are lined with residues that are hydrophilic, but are not highly conserved among K_{2P} channels (Figure 2.9). It has been previously demonstrated that acidic residues located within the inner helices that line the ion conduction pore are important for the fast conduction properties of BK channels (Brelidze et al., 2003; Nimigean et al., 2003). Therefore, it is conceivable that the residues that line the extracellular cap side portals may contribute to differences in K_{2P} channel conduction. To address this question, a side portal mutagenesis study could be performed. This would involve swapping side portal lining residues between $K_{2P}2$ and $K_{2P}3$ channels, two of the most well characterized K_{2P} channels. Both individual and multiple substitutions could be introduced to evaluate the individual versus collective contribution of these residues towards $K_{2P}2$ and $K_{2P}3$ channel conduction. The wild-type and mutant $K_{2P}2$ and $K_{2P}3$ channels would be individually overexpressed in COS cells, and channels would be recorded in single channel inside-out patch

clamp mode. The single channel conductance of wild-type and mutant $K_{2P}2$ and $K_{2P}3$ channels would be calculated from an I-V curve (slope) of averaged single channel recordings for each channel.

In addition to a potential role of shaping differences in conductance between K_{2P} channels, the extracellular cap could have a direct or indirect role in gating. Although the majority of the cap is structured, residues subsequent to the loop that packs against E2 in an extended backbone conformation (94-99 in $K_{2P}1$, 104-111 in $K_{2P}4$) are not modeled into $K_{2P}1$ or $K_{2P}4$ crystal structures since the electron density could not be resolved in this region. This suggests that the loop in this region is flexible. The unstructured loop is the region within the extracellular cap that is least conserved between K_{2P} channels, but the length of the loop is fairly conserved between subfamily members. Interestingly, this loop is positioned near a side portal, so modification or movements to this loop could potentially alter K^+ movement through the side portals.

A crosslinking experiment could be performed to try to address questions of loop proximity to the side portal in solution. In $K_{2P}1$, this would involve performing a cysteine scanning of the loop (6 residues) in conjunction with cysteine substitutions to neighboring residues such as arginine 53 (R53) within E1 helix, that is pointing away from the side portal, or glutamate 235 (E235) within the loop between P domain 2 filter to M4, that is positioned near the side portal (Figure 5.1). Mutant channels would be overexpressed in COS cells and recorded in whole cell mode in the presence and absence of sulfhydryl crosslinking reagent (e.g. varying length maleimide reagents). One would expect cysteine mutants within the loop that crosslinked with E235 to result in reduced current amplitude. In contrast, one would expect the loop mutants crosslinked with R53 to result in either no change or an increase in current amplitude. If the crosslinking results suggest that the flexible loop within the extracellular cap can be positioned near the side portals, a second experiment could be performed by swapping extracellular cap flexible loops from different K_{2P}

189
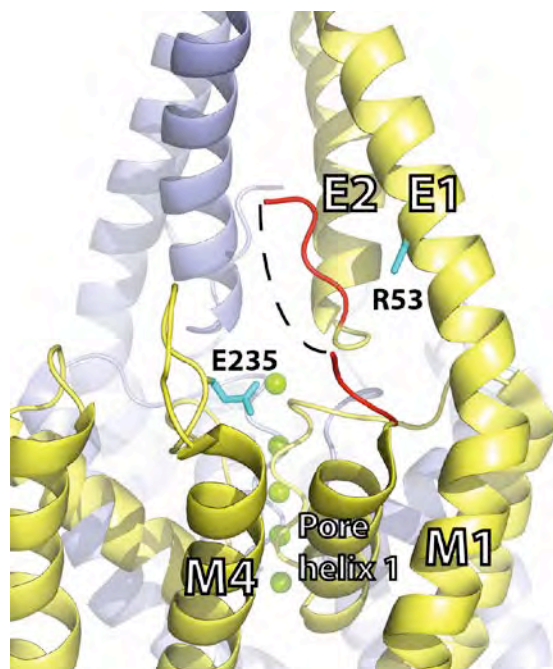
Figure 5.1: Mutagenesis scheme for studies of unstructured loop localization within the $K_{2P}1$ extracellular cap. $K_{2P}1$ crystal structure (PDB ID: 3KUM) with protomers colored in yellow and blue. Transmembrane and extracellular cap helices are labeled. Residues surrounding the unstructured loop are highlighted in red with the connection between these residues drawn as a dotted black line. Residues in close proximity to the loop that would be used for cysteine mutatgenesis studies are colored in cyan and labeled (R51, E235).

channel subfamilies and/or reducing or extending the size of the loop, to evaluate if these substitutions also alter measured current amplitudes.

Likewise, many K_{2P} channels have a putative glycosylation site(s) within this loop. In the case of $K_{2P}1$, I was able to demonstrate that asparagine 95 (N95) is glycosylated (Figure 2.7). In addition, the N-linked glycan is most likely positioned near the side portals, as evaluated from the $K_{2P}1$ crystal structure (Figure 2.9, Figure 3.11, Figure 3.12) To evaluate whether glycosylation of $K_{2P}1$ alters measured current amplitudes, wild-type and N95Q mutant $K_{2P}1$ could be overexpressed in COS cells and recorded in whole cell mode. For further evaluation of the contribution of N-glycan linked $K_{2P}1$ to conductance and/or gating, single channel recordings of wild-type and N95Q mutant $K_{2P}1$ could be measured from be performed in inside-out patch clamp mode to evaluate changes in the channel P_O, as well as $K_{2P}1$ conductance (slope of a current/voltage curve).

As mentioned above, the cysteine mutagenesis experiments to the flexible loop within the extracellular cap address the question of proximity and length of the loops in relation to channel current density. However, it is important to note that these experiments cannot distinguish between gating or conductance and do not demonstrate that this phenomenon is physiologically relevant. If the flexible loop were to be involved in gating, then an extracellular ligand or peptide or would need interact with this region of the cap to stabilize the loop and, therefore, increase or decrease the P_O of the channel. In order to identify extracellular cap interacting partners, one approach is to perform an immunoprecipitation experiment with $K_{2P}1$. Purified $K_{2P}1$ (22-288 construct, with and without the glycosylation mutation) could be pre-incubated with conditioned media collected from cultured glial cells and/or neurons. $K_{2P}1$ would be immunoprecipitated and remaining protein that was pulled down with $K_{2P}1$ would be separated on a Coomassie gel by SDS-PAGE. Bands that appear in the $K_{2P}1$ lanes, but not a control lane (unrelated channel control

or no $K_{2P}1$ control) could be excised and analyzed by mass spectrometry for peptide identification. In addition, an experiment could be performed by pre-incubating $K_{2P}1$ with a detergent-soluble fraction (membrane lysate) from glial cells and/or neurons, followed by immunoprecipitation. This experiment would be done to identify potential membrane-bound extracellular cap interacting proteins. Alternatively, a more selective approach would be to perform the same $K_{2P}1$ immunoprecipitation experiment, but with pre-incubation of the channel with known extracellular ligands or peptides in the CNS (e.g. neurotransmitters). If an interacting peptide or ligand is found through the immunoprecipitation approach, then studies of $K_{2P}1$ channel function could be performed. These studies would involve measuring $K_{2P}1$ single channel currents in a bilayer recording system (purified channel) to assess gating and conduction properties of $K_{2P}1$ in the absence and presence of ligand/peptide. Structural studies could also be performed by setting up co-crystallization trials of $K_{2P}1$ with ligand/peptide.

An alternative approach to studying the potential role of the extracellular cap in gating is through the identification of an inhibitor or activator of $K_{2P}1$ (see below). Similar to what was proposed above, $K_{2P}1$ bilayer recordings would be performed to assess the gating and conduction properties of the channel in the absence and presence of the inhibitor/activator. Furthermore, a mutagenesis experiment to identify the binding site for the inhibitor/activator could be done in whole-cell mode with wild-type and mutant $K_{2P}1$ overexpressed in COS cells. Residues that that are important for interaction with the inhibitor/activator could be identified from these experiments.

Screening for inhibitor or activators of $K_{2P}1$

K_{2P} channels are essential for establishing and maintaining the resting potential in eukaryotic cells. $K_{2P}2$ is the best-characterized member of the K_{2P} family, which is modulated by a variety of stimuli such as temperature, pH, lipids, mechanical stress and anesthetics. Knockdown of this channel in mice results in a number of neurological phenotypes such as loss of response to pain

perception and the hypnotic properties of anesthetics (Heurteaux et al., 2004). In addition, the $K_{2P}2$ knockout mice exhibit a depression-resistant phenotype (Heurteaux et al., 2006). Recently, missense mutations identified within a K_{2P} channel family member, $K_{2P}18$, were associated with typical familial migraine with aura in humans (Andres-Enguix et al., 2012; Lafreniere et al., 2010). The therapeutic potential for identifying both activators and inhibitors of K_{2P} channel is evident. Future work towards this goal with studies of human $K_{2P}1$ could be beneficial in finding K_{2P}-specific modulators, or for tailoring modulators to specifically target and modulate human K_{2P} paralogs. In addition, several isoforms of $K_{2P}2$ and $K_{2P}10$ have been identified, yet the physiological role(s) of the isoforms is unclear. Identification of K_{2P} modulators that recognize specific isoforms could begin to allow us to address these sorts of questions using *in vitro* or *in vivo* models.

An approach to identifying a $K_{2P}1$ inhibitor or activator could involve a high-throughput fluorescence based K^+ flux assay screening strategy with a small molecule library. The experimental design would be similar as what has been described for the K^+ fluorescence based flux assay (see 3.3.4 K^+ flux assay) but would be scaled to 96 well or 384 well format. Reconstituted $K_{2P}1$ 22-288 with and without the N-linked glycan (at ~ 4 μM) would be thawed and combined with a compound from the library (100 μM). Sample would incubate for several minutes prior to starting the assay. A reduction in fluorescence drop after addition of CCCP is indicative of channel inhibition whereas a fluorescence drop that is greater than the control (channel without compound) suggests that the small compound is stabilizing $K_{2P}1$ in an open state. Further characterization of the small molecule inhibitor or activator could be performed through whole-cell patch clamp in COS cells to identify the binding site of the compound and also to characterize the 'sidedness' of the compound. Since small molecule binding will most likely be located at either the extracellular cap or the intramembrane openings, extracellular cap deletion constructs could first be tested to identify the point of compound interaction with $K_{2P}1$.

Then a more detailed mutagenesis approach could be taken to identify $K_{2P}1$ residues that are important for compound interaction. For hydrophobic compounds that bind the intramembrane openings, addition of the compound to both the intracellular and extracellular sides of the membrane may result in channel inhibition/activation whereas extracellular cap-specific compounds will most likely be modulated with extracellular application of the compound only.

Conclusion

Overall, the crystal structure of human $K_{2P}1$ defines the molecular architecture of the K_{2P} channel family and also lays a foundation for further investigation of how K_{2P} channels are regulated by diverse stimuli. The structural features unique to K_{2P} channels, and in particular the presence of a large extracellular cap, provide possible targets for K_{2P}-specific therapeutics and an important direction for future work.

REFERENCES

1. Adams, P.D., Afonine, G., Bunkoczi, G., Chen, V.B., Davis, I.W., Echols, N., Headd, J.J., Hung, L.-W., Kapral, G.J., Gross-Kunstleve, R.W., McCoy, A.J., Moriarty, N.W., Oeffner, R., Read, R.J., Richardson, D.C., Richardson, J.S., Terwilliger, T.C., and Zwart, P.H. (2010). PHENIX: a comprehensive Python-based system for macromolecular structure solution. Acta Crystallographica Section D, Biological Crystallography *66, Part 2*, 213-21.

2. Adelman, J.P., Maylie, J., and Sah, P. (2012). Small-conductance Ca2+-activated K+ channels: form and function. Annu Rev Physiol *74*, 245-69.

3. Alberts, B. (2008). Molecular biology of the cell, 5th edn (New York: Garland Science).

4. Alexandrov, A.I., Mileni, M., Chien, E.Y., Hanson, M.A., and Stevens, R.C. (2008). Microscale fluorescent thermal stability assay for membrane proteins. Structure *16*, 351-9.

5. Alloui, A., Zimmermann, K., Mamet, J., Duprat, F., Noel, J., Chemin, J., Guy, N., Blondeau, N., Voilley, N., Rubat-Coudert, C., Borsotto, M., Romey, G., Heurteaux, C., Reeh, P., Eschalier, A., and Lazdunski, M. (2006). TREK-1, a K+ channel involved in polymodal pain perception. EMBO J *25*, 2368-76.

6. Andres-Enguix, I., Shang, L., Stansfeld, P.J., Morahan, J.M., Sansom, M.S., Lafreniere, R.G., Roy, B., Griffiths, L.R., Rouleau, G.A., Ebers, G.C., Cader, Z.M., and Tucker, S.J. (2012). Functional analysis of missense variants in the TRESK (KCNK18) K channel. Sci Rep *2*, 237.

7. Armstrong, C.M. (1966). Time course of TEA(+)-induced anomalous rectification in squid giant axons. J Gen Physiol *50*, 491-503.

8. Armstrong, C.M. (1969). Inactivation of the potassium conductance and related phenomena caused by quaternary ammonium ion injection in squid axons. J Gen Physiol *54*, 553-75.

9. Armstrong, C.M. (1971). Interaction of tetraethylammonium ion derivatives with the potassium channels of giant axons. J Gen Physiol *58*, 413-37.

10. Ashmole, I., Vavoulis, D.V., Stansfeld, P.J., Mehta, P.R., Feng, J.F., Sutcliffe, M.J., and Stanfield, P.R. (2009). The response of the tandem pore potassium channel TASK-3 (K(2P)9.1) to voltage: gating at the cytoplasmic mouth. J Physiol *587*, 4769-83.

11. Bagriantsev, S.N., Peyronnet, R., Clark, K.A., Honore, E., and Minor, D.L., Jr. (2011). Multiple modalities converge on a common gate to control K2P channel function. EMBO J *30*, 3594-606.

12. Bagriantsev, S.N., Clark, K.A., and Minor, D.L., Jr. (2012). Metabolic and thermal stimuli control K(2P)2.1 (TREK-1) through modular sensory and gating domains. EMBO J *31*, 3297-308.

13. Bang, H., Kim, Y., and Kim, D. (2000). TREK-2, a new member of the mechanosensitive tandem-pore K+ channel family. J Biol Chem *275*, 17412-9.

14. Baukrowitz, T., and Yellen, G. (1995). Modulation of K+ current by frequency and external [K+]: a tale of two inactivation mechanisms. Neuron *15*, 951-60.

15. Baukrowitz, T., and Yellen, G. (1996). Use-dependent blockers and exit rate of the last ion from the multi-ion pore of a K+ channel. Science *271*, 653-6.

16. Bayliss, D.A., and Barrett, P.Q. (2008). Emerging roles for two-pore-domain potassium channels and their potential therapeutic impact. Trends Pharmacol Sci *29*, 566-75.

17. Ben-Abu, Y., Zhou, Y., Zilberberg, N., and Yifrach, O. (2009). Inverse coupling in leak and voltage-activated K+ channel gates underlies distinct roles in electrical signaling. Nat Struct Mol Biol *16*, 71-9.

18. Berg, A.P., Talley, E.M., Manger, J.P., and Bayliss, D.A. (2004). Motoneurons express heteromeric TWIK-related acid-sensitive K+ (TASK) channels containing TASK-1 (KCNK3) and TASK-3 (KCNK9) subunits. J Neurosci *24*, 6693-702.

19. Berneche, S., and Roux, B. (2001). Energetics of ion conduction through the K+ channel. Nature *414*, 73-7.

20. Blaesse, P., Airaksinen, M.S., Rivera, C., and Kaila, K. (2009). Cation-chloride cotransporters and neuronal function. Neuron *61*, 820-38.

21. Blondeau, N., Lauritzen, I., Widmann, C., Lazdunski, M., and Heurteaux, C. (2002a). A potent protective role of lysophospholipids against global cerebral ischemia and glutamate excitotoxicity in neuronal cultures. J Cereb Blood Flow Metab *22*, 821-34.

22. Blondeau, N., Widmann, C., Lazdunski, M., and Heurteaux, C. (2002b). Polyunsaturated fatty acids induce ischemic and epileptic tolerance. Neuroscience *109*, 231-41.

23. Brelidze, T.I., Niu, X., and Magleby, K.L. (2003). A ring of eight conserved negatively charged amino acids doubles the conductance of BK channels and prevents inward rectification. Proc Natl Acad Sci U S A *100*, 9017-22.

24. Bricogne, G., Vonrhein, C., Flensburg, C., Schiltz, M., and Paciorek, W. (2003). Generation, representation and flow of phase information in structure determination: recent developments in and around SHARP 2.0. Acta Crystallogr D Biol Crystallogr *59*, 2023-30.

25. Brini, M., and Carafoli, E. (2011). The plasma membrane Ca(2)+ ATPase and the plasma membrane sodium calcium exchanger cooperate in the regulation of cell calcium. Cold Spring Harb Perspect Biol *3*.

26. Brohawn, S.G., del Marmol, J., and MacKinnon, R. (2012). Crystal structure of the human K2P TRAAK, a lipid- and mechano-sensitive K+ ion channel. Science *335*, 436-41.

27. Brohawn, S.G., Campbell, E.B., and Mackinnon, R. (2013). Domain-swapped chain connectivity and gated membrane access in a Fab-mediated crystal of the human TRAAK K+ channel. Proc Natl Acad Sci U S A *110*, 2129-34.

28. Brunger, A.T., Adams, P.D., Clore, G.M., DeLano, W.L., Gros, P., Grosse-Kunstleve, R.W., Jiang, J.-S., Kuszewski, J., Nilges, N., Pannu, N.S., Read, R.J., Rice, L.M., Simonson, T., and Warren, G.L. (1998). Crystallography and NMR system (CNS): A new software system for macromolecular structure determination. Acta Crystallographica Section D, Biological Crystallography, 905-21.

29. Caffrey, M. (2003). Membrane protein crystallization. J Struct Biol *142*, 108-32.

30. Caffrey, M., Li, D., and Dukkipati, A. (2012). Membrane protein structure determination using crystallography and lipidic mesophases: recent advances and successes. Biochemistry *51*, 6266-88.

31. Callahan, M.J., and Korn, S.J. (1994). Permeation of Na+ through a delayed rectifier K+ channel in chick dorsal root ganglion neurons. J Gen Physiol *104*, 747-71.

32. Carpenter, E.P., Beis, K., Cameron, A.D., and Iwata, S. (2008). Overcoming the challenges of membrane protein crystallography. Curr Opin Struct Biol *18*, 581-6.

33. Catterall, W.A., Perez-Reyes, E., Snutch, T.P., and Striessnig, J. (2005). International Union of Pharmacology. XLVIII. Nomenclature and structure-function relationships of voltage-gated calcium channels. Pharmacol Rev *57*, 411-25.

34. Chatelain, F.C., Bichet, D., Douguet, D., Feliciangeli, S., Bendahhou, S., Reichold, M., Warth, R., Barhanin, J., and Lesage, F. (2012). TWIK1, a unique background channel with variable ion selectivity. Proc Natl Acad Sci U S A *109*, 5499-504.

35. Chemin, J., Patel, A., Duprat, F., Zanzouri, M., Lazdunski, M., and Honore, E. (2005a). Lysophosphatidic acid-operated K+ channels. J Biol Chem *280*, 4415-21.

36. Chemin, J., Patel, A.J., Duprat, F., Lauritzen, I., Lazdunski, M., and Honore, E. (2005b). A phospholipid sensor controls mechanogating of the K+ channel TREK-1. EMBO J *24*, 44-53.

37. Chemin, J., Patel, A.J., Duprat, F., Sachs, F., Lazdunski, M., and Honore, E. (2007). Up- and down-regulation of the mechano-gated K(2P) channel TREK-1 by PIP (2) and other membrane phospholipids. Pflugers Arch *455*, 97-103.

38. Chen, V.B., Arendall, W.B., 3rd, Headd, J.J., Keedy, D.A., Immormino, R.M., Kapral, G.J., Murray, L.W., Richardson, J.S., and Richardson, D.C. (2010). MolProbity: all-atom structure validation for macromolecular crystallography. Acta Crystallogr D Biol Crystallogr *66*, 12-21.

39. Cherezov, V. (2011). Lipidic cubic phase technologies for membrane protein structural studies. Curr Opin Struct Biol *21*, 559-66.

40. Choi, K.L., Aldrich, R.W., and Yellen, G. (1991). Tetraethylammonium blockade distinguishes two inactivation mechanisms in voltage-activated K+ channels. Proc Natl Acad Sci U S A *88*, 5092-5.

41. Choi, K.L., Mossman, C., Aube, J., and Yellen, G. (1993). The internal quaternary ammonium receptor site of Shaker potassium channels. Neuron *10*, 533-41.

42. Christe, G. (1983). Effects of low [K+]o on the electrical activity of human cardiac ventricular and Purkinje cells. Cardiovasc Res *17*, 243-50.

43. Chudler, E.H., and Dong, W.K. (1995). The role of the basal ganglia in nociception and pain. Pain *60*, 3-38.

44. Cluzeaud, F., Reyes, R., Escoubet, B., Fay, M., Lazdunski, M., Bonvalet, J.P., Lesage, F., and Farman, N. (1998). Expression of TWIK-1, a novel weakly inward rectifying potassium channel in rat kidney. Am J Physiol *275*, C1602-9.

45. Coetzee, W.A., Amarillo, Y., Chiu, J., Chow, A., Lau, D., McCormack, T., Moreno, H., Nadal, M.S., Ozaita, A., Pountney, D., Saganich, M., Vega-Saenz de Miera, E., and Rudy, B. (1999). Molecular diversity of K+ channels. Ann N Y Acad Sci *868*, 233-85.

46. Cohen, A., Ben-Abu, Y., Hen, S., and Zilberberg, N. (2008). A novel mechanism for human K2P2.1 channel gating. Facilitation of C-type gating by protonation of extracellular histidine residues. J Biol Chem *283*, 19448-55.

47. Cohen, A., Ben-Abu, Y., and Zilberberg, N. (2009). Gating the pore of potassium leak channels. Eur Biophys J *39*, 61-73.

48. Coombs, J.S., Eccles, J.C., and Fatt, P. (1955). The specific ionic conductances and the ionic movements across the motoneuronal membrane that produce the inhibitory post-synaptic potential. J Physiol *130*, 326-74.

49. Cordero-Morales, J.F., Cuello, L.G., Zhao, Y., Jogini, V., Cortes, D.M., Roux, B., and Perozo, E. (2006). Molecular determinants of gating at the potassium-channel selectivity filter. Nat Struct Mol Biol *13*, 311-8.

50. Cowtan, K.D. (1994). 'dm': An automated procedure for phase improvement by density modification. Joint CCP4 and ESF-EACBM Newsletter on Protein Crystallography *31*, 34.

51. Cuello, L.G., Jogini, V., Cortes, D.M., Pan, A.C., Gagnon, D.G., Dalmas, O., Cordero-Morales, J.F., Chakrapani, S., Roux, B., and Perozo, E. (2010a). Structural basis for the coupling between activation and inactivation gates in K(+) channels. Nature *466*, 272-5.

52. Cuello, L.G., Jogini, V., Cortes, D.M., and Perozo, E. (2010b). Structural mechanism of C-type inactivation in K(+) channels. Nature *466*, 203-8.

53. Czirjak, G., Fischer, T., Spat, A., Lesage, F., and Enyedi, P. (2000). TASK (TWIK-related acid-sensitive K+ channel) is expressed in glomerulosa cells of rat adrenal cortex and inhibited by angiotensin II. Mol Endocrinol *14*, 863-74.

54. Czirjak, G., and Enyedi, P. (2002). Formation of functional heterodimers between the TASK-1 and TASK-3 two-pore domain potassium channel subunits. J Biol Chem *277*, 5426-32.

55. Davies, L.A., Hu, C., Guagliardo, N.A., Sen, N., Chen, X., Talley, E.M., Carey, R.M., Bayliss, D.A., and Barrett, P.Q. (2008). TASK channel deletion in mice causes primary hyperaldosteronism. Proc Natl Acad Sci U S A *105*, 2203-8.

56. Decressac, S., Franco, M., Bendahhou, S., Warth, R., Knauer, S., Barhanin, J., Lazdunski, M., and Lesage, F. (2004). ARF6-dependent interaction of the TWIK1 K+ channel with EFA6, a GDP/GTP exchange factor for ARF6. EMBO Rep *5*, 1171-5.

57. Dedman, A., Sharif-Naeini, R., Folgering, J.H., Duprat, F., Patel, A., and Honore, E. (2009). The mechano-gated K(2P) channel TREK-1. Eur Biophys J *38*, 293-303.

58. Demaurex, N. (2012). Functions of proton channels in phagocytes. WIREs Membr Transp Signal *1*, 3-15.

59. Derewenda, Z.S., and Vekilov, P.G. (2006). Entropy and surface engineering in protein crystallization. Acta Crystallogr D Biol Crystallogr *62*, 116-24.

60. Dibb, K.M., Rose, T., Makary, S.Y., Claydon, T.W., Enkvetchakul, D., Leach, R., Nichols, C.G., and Boyett, M.R. (2003). Molecular basis of ion selectivity, block, and rectification of the inward rectifier Kir3.1/Kir3.4 K(+) channel. J Biol Chem *278*, 49537-48.

61. Ding, S., Ingleby, L., Ahern, C.A., and Horn, R. (2005). Investigating the putative glycine hinge in Shaker potassium channel. J Gen Physiol *126*, 213-26.

62. Doyle, D.A., Morais Cabral, J., Pfuetzner, R.A., Kuo, A., Gulbis, J.M., Cohen, S.L., Chait, B.T., and MacKinnon, R. (1998). The structure of the potassium channel: molecular basis of K+ conduction and selectivity. Science *280*, 69-77.

63. Duprat, F., Lesage, F., Fink, M., Reyes, R., Heurteaux, C., and Lazdunski, M. (1997). TASK, a human background K+ channel to sense external pH variations near physiological pH. EMBO J *16*, 5464-71.

64. Duprat, F., Lesage, F., Patel, A.J., Fink, M., Romey, G., and Lazdunski, M. (2000). The neuroprotective agent riluzole activates the two P domain K(+) channels TREK-1 and TRAAK. Mol Pharmacol *57*, 906-12.

65. Dutzler, R., Campbell, E.B., and MacKinnon, R. (2003). Gating the selectivity filter in ClC chloride channels. Science *300*, 108-12.

66. Emsley, P., and Cowtan, K. (2004). Coot: model-building tools for molecular graphics. Acta Crystallogr D Biol Crystallogr *60*, 2126-32.

67. Enyedi, P., and Czirjak, G. (2010). Molecular background of leak K+ currents: two-pore domain potassium channels. Physiol Rev *90*, 559-605.

68. Feliciangeli, S., Bendahhou, S., Sandoz, G., Gounon, P., Reichold, M., Warth, R., Lazdunski, M., Barhanin, J., and Lesage, F. (2007). Does sumoylation control K2P1/TWIK1 background K+ channels? Cell *130*, 563-9.

69. Feliciangeli, S., Tardy, M.P., Sandoz, G., Chatelain, F.C., Warth, R., Barhanin, J., Bendahhou, S., and Lesage, F. (2010). Potassium channel silencing by constitutive endocytosis and intracellular sequestration. J Biol Chem *285*, 4798-805.

70. Feng, L., Campbell, E.B., Hsiung, Y., and MacKinnon, R. (2010). Structure of a eukaryotic CLC transporter defines an intermediate state in the transport cycle. Science *330*, 635-41.

71. Fink, M., Lesage, F., Duprat, F., Heurteaux, C., Reyes, R., Fosset, M., and Lazdunski, M. (1998). A neuronal two P domain K+ channel stimulated by arachidonic acid and polyunsaturated fatty acids. EMBO J *17*, 3297-308.

72. Flynn, G.E., Johnson, J.P., Jr., and Zagotta, W.N. (2001). Cyclic nucleotide-gated channels: shedding light on the opening of a channel pore. Nat Rev Neurosci *2*, 643-51.

73. Franks, N.P., and Lieb, W.R. (1988). Volatile general anaesthetics activate a novel neuronal K+ current. Nature *333*, 662-4.

74. Gadsby, D.C., and Cranefield, P.F. (1977). Two levels of resting potential in cardiac Purkinje fibers. J Gen Physiol *70*, 725-46.

75. Gareau, J.R., and Lima, C.D. (2010). The SUMO pathway: emerging mechanisms that shape specificity, conjugation and recognition. Nat Rev Mol Cell Biol *11*, 861-71.

76. Goldman, D.E. (1943). Potential, Impedance, and Rectification in Membranes. J Gen Physiol *27*, 37-60.

77. Goldschmidt, L., Cooper, D.R., Derewenda, Z.S., and Eisenberg, D. (2007). Toward rational protein crystallization: A Web server for the design of crystallizable protein variants. Protein Sci *16*, 1569-76.

78. Goldstein, S.A., Wang, K.W., Ilan, N., and Pausch, M.H. (1998). Sequence and function of the two P domain potassium channels: implications of an emerging superfamily. J Mol Med (Berl) *76*, 13-20.

79. Goldstein, S.A., Bockenhauer, D., O'Kelly, I., and Zilberberg, N. (2001). Potassium leak channels and the KCNK family of two-P-domain subunits. Nat Rev Neurosci *2*, 175-84.

80. Goldstein, S.A., Bayliss, D.A., Kim, D., Lesage, F., Plant, L.D., and Rajan, S. (2005). International Union of Pharmacology. LV. Nomenclature and molecular relationships of two-P potassium channels. Pharmacol Rev *57*, 527-40.

81. Grissmer, S., and Cahalan, M. (1989a). TEA prevents inactivation while blocking open K+ channels in human T lymphocytes. Biophys J *55*, 203-6.

82. Grissmer, S., and Cahalan, M.D. (1989b). Divalent ion trapping inside potassium channels of human T lymphocytes. J Gen Physiol *93*, 609-30.

83. Gurney, A., and Manoury, B. (2009). Two-pore potassium channels in the cardiovascular system. Eur Biophys J *38*, 305-18.

84. Hattori, M., Hibbs, R.E., and Gouaux, E. (2012). A fluorescence-detection size-exclusion chromatography-based thermostability assay for membrane protein precrystallization screening. Structure *20*, 1293-9.

85. Heginbotham, L., Kolmakova-Partensky, L., and Miller, C. (1998). Functional reconstitution of a prokaryotic K+ channel. J Gen Physiol *111*, 741-9.

86. Heurteaux, C., Guy, N., Laigle, C., Blondeau, N., Duprat, F., Mazzuca, M., Lang-Lazdunski, L., Widmann, C., Zanzouri, M., Romey, G., and Lazdunski, M. (2004). TREK-1, a K+ channel involved in neuroprotection and general anesthesia. EMBO J *23*, 2684-95.

87. Heurteaux, C., Lucas, G., Guy, N., El Yacoubi, M., Thümmler, S., Peng, X.D., Noble, F., Blondeau, N., Widmann, C., Borsotto, M., Gobbi, G., Vaugeois, J.M., Debonnel, G., and Lazdunski, M. (2006). Deletion of the background potassium channel TREK-1 results in a depression-resistant phenotype. Nat Neurosci *9*, 1134-41.

88. Hibbs, R.E., and Gouaux, E. (2011). Principles of activation and permeation in an anion-selective Cys-loop receptor. Nature *474*, 54-60.

89. Hibino, H., Inanobe, A., Furutani, K., Murakami, S., Findlay, I., and Kurachi, Y. (2010). Inwardly rectifying potassium channels: their structure, function, and physiological roles. Physiol Rev *90*, 291-366.

90. Hille, B. (1971). The permeability of the sodium channel to organic cations in myelinated nerve. J Gen Physiol *58*, 599-619.

91. Hille, B. (2001). Ion channels of excitable membranes, 3rd edn (Sunderland, Mass.: Sinauer).

92. Hodgkin, A.L., and Katz, B. (1949). The effect of sodium ions on the electrical activity of giant axon of the squid. J Physiol *108*, 37-77.

93. Hodgkin, A.L., and Huxley, A.F. (1952). A quantitative description of membrane current and its application to conduction and excitation in nerve. J Physiol *117*, 500-44.

94. Holmgren, M., Liu, Y., Xu, Y., and Yellen, G. (1996). On the use of thiol-modifying agents to determine channel topology. Neuropharmacology *35*, 797-804.

95. Holmgren, M., Smith, P.L., and Yellen, G. (1997). Trapping of organic blockers by closing of voltage-dependent K+ channels: evidence for a trap door mechanism of activation gating. J Gen Physiol *109*, 527-35.

96. Honore, E., Maingret, F., Lazdunski, M., and Patel, A.J. (2002). An intracellular proton sensor commands lipid- and mechano-gating of the K(+) channel TREK-1. EMBO J *21*, 2968-76.

97. Honore, E. (2007). The neuronal background K2P channels: focus on TREK1. Nat Rev Neurosci *8*, 251-61.

98. Hu, C., Rusin, C.G., Tan, Z., Guagliardo, N.A., and Barrett, P.Q. (2012). Zona glomerulosa cells of the mouse adrenal cortex are intrinsic electrical oscillators. J Clin Invest *122*, 2046-53.

99. Hunte, C., and Richers, S. (2008). Lipids and membrane protein structures. Curr Opin Struct Biol *18*, 406-11.

100. Jardetzky, O. (1966). Simple allosteric model for membrane pumps. Nature *211*, 969-70.

101. Jiang, Y., and MacKinnon, R. (2000). The barium site in a potassium channel by x-ray crystallography. J Gen Physiol *115*, 269-72.

102. Jiang, Y., Lee, A., Chen, J., Cadene, M., Chait, B.T., and MacKinnon, R. (2002). The open pore conformation of potassium channels. Nature *417*, 523-6.

103. Jiang, Y., Lee, A., Chen, J., Ruta, V., Cadene, M., Chait, B.T., and MacKinnon, R. (2003). X-ray structure of a voltage-dependent K+ channel. Nature *423*, 33-41.

104. Jin, W., and Lu, Z. (1998). A novel high-affinity inhibitor for inward-rectifier K+ channels. Biochemistry *37*, 13291-9.

105. Johnston, J., Forsythe, I.D., and Kopp-Scheinpflug, C. (2010). Going native: voltage-gated potassium channels controlling neuronal excitability. J Physiol *588*, 3187-200.

106. Jones, T.A., Bergdoll, M., and Kjeldgaard, M. (1990). O: A macromolecular modeling environment. . In Crystallographic and Modeling Methods in Molecular Design, C. Bugg, and S. Ealick, eds. (Springer-Verlag Press), pp. 189-95.

107. Jurkat-Rott, K., and Lehmann-Horn, F. (2005). Muscle channelopathies and critical points in functional and genetic studies. J Clin Invest *115*, 2000-9.

108. Kandel, E.R., Schwartz, J.H., Jessell, T.M., Siegelbaum, S.A., and Hudspeth, A.J. (2012). Principles of neural science, 4th edn (New York: McGraw-Hill, Health Professions Division).

109. Kang, D., Han, J., Talley, E.M., Bayliss, D.A., and Kim, D. (2004). Functional expression of TASK-1/TASK-3 heteromers in cerebellar granule cells. J Physiol *554*, 64-77.

110. Kang, D., and Kim, D. (2004). Single-channel properties and pH sensitivity of two-pore domain K+ channels of the TALK family. Biochem Biophys Res Commun *315*, 836-44.

111. Kang, D., Choe, C., and Kim, D. (2005). Thermosensitivity of the two-pore domain K+ channels TREK-2 and TRAAK. J Physiol *564*, 103-16.

112. Kang, D., and Kim, D. (2006). TREK-2 (K2P10.1) and TRESK (K2P18.1) are major background K+ channels in dorsal root ganglion neurons. Am J Physiol Cell Physiol *291*, C138-46.

113. Karlin, A., and Akabas, M.H. (1998). Substituted-cysteine accessibility method. Methods Enzymol *293*, 123-45.

114. Kawate, T., and Gouaux, E. (2006). Fluorescence-detection size-exclusion chromatography for precrystallization screening of integral membrane proteins. Structure *14*, 673-81.

115. Kilmartin, J.V., Wright, B., and Milstein, C. (1982). Rat monoclonal antitubulin antibodies derived by using a new nonsecreting rat cell line. J Cell Biol *93*, 576-82.

116. Kim, Y., Bang, H., and Kim, D. (1999). TBAK-1 and TASK-1, two-pore K(+) channel subunits: kinetic properties and expression in rat heart. Am J Physiol *277*, H1669-78.

117. Kim, Y., Bang, H., and Kim, D. (2000). TASK-3, a new member of the tandem pore K(+) channel family. J Biol Chem *275*, 9340-7.

118. Kim, Y., Bang, H., Gnatenco, C., and Kim, D. (2001a). Synergistic interaction and the role of C-terminus in the activation of TRAAK K+ channels by pressure, free fatty acids and alkali. Pflugers Arch *442*, 64-72.

119. Kim, Y., Gnatenco, C., Bang, H., and Kim, D. (2001b). Localization of TREK-2 K+ channel domains that regulate channel kinetics and sensitivity to pressure, fatty acids and pHi. Pflugers Arch *442*, 952-60.

120. Kollewe, A., Lau, A.Y., Sullivan, A., Roux, B., and Goldstein, S.A. (2009). A structural model for K2P potassium channels based on 23 pairs of interacting sites and continuum electrostatics. J Gen Physiol *134*, 53-68.

121. Korn, S.J., and Ikeda, S.R. (1995). Permeation selectivity by competition in a delayed rectifier potassium channel. Science *269*, 410-2.

122. Krissinel, E., and Henrick, K. (2007). Inference of macromolecular assemblies from crystalline state. J Mol Biol *372*, 774-97.

123. Krnjevic, K., and Schwartz, S. (1967). The action of gamma-aminobutyric acid on cortical neurones. Exp Brain Res *3*, 320-36.

124. Kuo, A., Bowler, M.W., Zimmer, J., Antcliff, J.F., and Doyle, D.A. (2003). Increasing the diffraction limit and internal order of a membrane protein crystal by dehydration. J Struct Biol *141*, 97-102.

125. Lafreniere, R.G., Cader, M.Z., Poulin, J.F., Andres-Enguix, I., Simoneau, M., Gupta, N., Boisvert, K., Lafreniere, F., McLaughlan, S., Dube, M.P., Marcinkiewicz, M.M., Ramagopalan, S., Ansorge, O., Brais, B., Sequeiros, J., Pereira-Monteiro, J.M., Griffiths, L.R., Tucker, S.J., Ebers, G., and Rouleau, G.A. (2010). A dominant-negative mutation in the TRESK potassium channel is linked to familial migraine with aura. Nat Med *16*, 1157-60.

126. Larsson, H.P., and Elinder, F. (2000). A conserved glutamate is important for slow inactivation in K+ channels. Neuron *27*, 573-83.

127. Latorre, R., Oberhauser, A., Labarca, P., and Alvarez, O. (1989). Varieties of calcium-activated potassium channels. Annu Rev Physiol *51*, 385-99.

128. Lauger, P. (1979). A channel mechanism for electrogenic ion pumps. Biochim Biophys Acta *552*, 143-61.

129. Lauritzen, I., Blondeau, N., Heurteaux, C., Widmann, C., Romey, G., and Lazdunski, M. (2000). Polyunsaturated fatty acids are potent neuroprotectors. EMBO J *19*, 1784-93.

130. Lee, S.Y., Letts, J.A., and MacKinnon, R. (2009). Functional reconstitution of purified human Hv1 H+ channels. J Mol Biol *387*, 1055-60.

131. LeMasurier, M., Heginbotham, L., and Miller, C. (2001). KcsA: it's a potassium channel. J Gen Physiol *118*, 303-14.

132. Lesage, F., Guillemare, E., Fink, M., Duprat, F., Lazdunski, M., Romey, G., and Barhanin, J. (1996a). TWIK-1, a ubiquitous human weakly inward rectifying K+ channel with a novel structure. EMBO J *15*, 1004-11.

133. Lesage, F., Reyes, R., Fink, M., Duprat, F., Guillemare, E., and Lazdunski, M. (1996b). Dimerization of TWIK-1 K+ channel subunits via a disulfide bridge. EMBO J *15*, 6400-7.

134. Lesage, F., and Lazdunski, M. (2000). Molecular and functional properties of two-pore-domain potassium channels. Am J Physiol Renal Physiol *279*, F793-801.

135. Lesage, F., Maingret, F., and Lazdunski, M. (2000a). Cloning and expression of human TRAAK, a polyunsaturated fatty acids-activated and mechano-sensitive K(+) channel. FEBS Lett *471*, 137-40.

136. Lesage, F., Terrenoire, C., Romey, G., and Lazdunski, M. (2000b). Human TREK2, a 2P domain mechano-sensitive K+ channel with multiple regulations by polyunsaturated fatty acids, lysophospholipids, and Gs, Gi, and Gq protein-coupled receptors. J Biol Chem *275*, 28398-405.

137. Levy, D.I., Velazquez, H., Goldstein, S.A., and Bockenhauer, D. (2004). Segment-specific expression of 2P domain potassium channel genes in human nephron. Kidney Int *65*, 918-26.

138. Lewis, R.S., and Cahalan, M.D. (1995). Potassium and calcium channels in lymphocytes. Annu Rev Immunol *13*, 623-53.

139. Linden, A.M., Aller, M.I., Leppa, E., Vekovischeva, O., Aitta-Aho, T., Veale, E.L., Mathie, A., Rosenberg, P., Wisden, W., and Korpi, E.R. (2006). The in vivo contributions of TASK-1-containing channels to the actions of inhalation anesthetics, the alpha(2) adrenergic sedative dexmedetomidine, and cannabinoid agonists. J Pharmacol Exp Ther *317*, 615-26.

140. Linden, A.M., Sandu, C., Aller, M.I., Vekovischeva, O.Y., Rosenberg, P.H., Wisden, W., and Korpi, E.R. (2007). TASK-3 knockout mice exhibit exaggerated nocturnal activity, impairments in cognitive functions, and reduced sensitivity to inhalation anesthetics. J Pharmacol Exp Ther *323*, 924-34.

141. Liu, Y., Jurman, M.E., and Yellen, G. (1996). Dynamic rearrangement of the outer mouth of a K+ channel during gating. Neuron *16*, 859-67.

142. Liu, Y., Holmgren, M., Jurman, M.E., and Yellen, G. (1997). Gated access to the pore of a voltage-dependent K+ channel. Neuron *19*, 175-84.

143. Lockless, S.W., Zhou, M., and MacKinnon, R. (2007). Structural and thermodynamic properties of selective ion binding in a K+ channel. PLoS Biol *5*, e121.

144. Long, S.B., Campbell, E.B., and Mackinnon, R. (2005). Crystal structure of a mammalian voltage-dependent Shaker family K+ channel. Science *309*, 897-903.

145. Long, S.B., Tao, X., Campbell, E.B., and MacKinnon, R. (2007). Atomic structure of a voltage-dependent K+ channel in a lipid membrane-like environment. Nature *450*, 376-82.

146. Lopatin, A.N., Makhina, E.N., and Nichols, C.G. (1994). Potassium channel block by cytoplasmic polyamines as the mechanism of intrinsic rectification. Nature *372*, 366-9.

147. Lopes, C.M., Gallagher, P.G., Buck, M.E., Butler, M.H., and Goldstein, S.A. (2000). Proton block and voltage gating are potassium-dependent in the cardiac leak channel Kcnk3. J Biol Chem *275*, 16969-78.

148. Lopes, C.M., Zilberberg, N., and Goldstein, S.A. (2001). Block of Kcnk3 by protons. Evidence that 2-P-domain potassium channel subunits function as homodimers. J Biol Chem *276*, 24449-52.

149. Lopez-Barneo, J., Hoshi, T., Heinemann, S.H., and Aldrich, R.W. (1993). Effects of external cations and mutations in the pore region on C-type inactivation of Shaker potassium channels. Receptors Channels *1*, 61-71.

150. Lorenz, J.N., Baird, N.R., Judd, L.M., Noonan, W.T., Andringa, A., Doetschman, T., Manning, P.A., Liu, L.H., Miller, M.L., and Shull, G.E. (2002). Impaired renal NaCl absorption in mice lacking the ROMK potassium channel, a model for type II Bartter's syndrome. J Biol Chem *277*, 37871-80.

151. Lotshaw, D.P. (2007). Biophysical, pharmacological, and functional characteristics of cloned and native mammalian two-pore domain K+ channels. Cell Biochem Biophys *47*, 209-56.

152. Lu, Z., and MacKinnon, R. (1994). Electrostatic tuning of Mg2+ affinity in an inward-rectifier K+ channel. Nature *371*, 243-6.

153. Ma, L., Zhang, X., and Chen, H. (2011). TWIK-1 two-pore domain potassium channels change ion selectivity and conduct inward leak sodium currents in hypokalemia. Sci Signal *4*, ra37.

154. Ma, L., Xie, Y.P., Zhou, M., and Chen, H. (2012a). Silent TWIK-1 Potassium Channels Conduct Monovalent Cation Currents. Biophys J *102*, L34-6.

155. Ma, L., Zhang, X., Zhou, M., and Chen, H. (2012b). Acid-sensitive TWIK and TASK Two-pore Domain Potassium Channels Change Ion Selectivity and Become Permeable to Sodium in Extracellular Acidification. J Biol Chem *287*, 37145-53.

156. MacKinnon, R., and Yellen, G. (1990). Mutations affecting TEA blockade and ion permeation in voltage-activated K+ channels. Science *250*, 276-9.

157. Magidovich, E., and Yifrach, O. (2004). Conserved gating hinge in ligand- and voltage-dependent K+ channels. Biochemistry *43*, 13242-7.

158. Maingret, F., Fosset, M., Lesage, F., Lazdunski, M., and Honore, E. (1999a). TRAAK is a mammalian neuronal mechano-gated K+ channel. J Biol Chem *274*, 1381-7.

159. Maingret, F., Patel, A.J., Lesage, F., Lazdunski, M., and Honore, E. (1999b). Mechano- or acid stimulation, two interactive modes of activation of the TREK-1 potassium channel. J Biol Chem *274*, 26691-6.

160. Maingret, F., Lauritzen, I., Patel, A.J., Heurteaux, C., Reyes, R., Lesage, F., Lazdunski, M., and Honore, E. (2000a). TREK-1 is a heat-activated background K(+) channel. EMBO J *19*, 2483-91.

161. Maingret, F., Patel, A.J., Lesage, F., Lazdunski, M., and Honore, E. (2000b). Lysophospholipids open the two-pore domain mechano-gated K(+) channels TREK-1 and TRAAK. J Biol Chem *275*, 10128-33.

162. Mancusso, R., Karpowich, N.K., Czyzewski, B.K., and Wang, D.N. (2011). Simple screening method for improving membrane protein thermostability. Methods *55*, 324-9.

163. Marom, S., and Levitan, I.B. (1994). State-dependent inactivation of the Kv3 potassium channel. Biophys J *67*, 579-89.

164. Mathie, A., Al-Moubarak, E., and Veale, E.L. (2010). Gating of two pore domain potassium channels. J Physiol *588*, 3149-56.

165. Matsuda, H., Saigusa, A., and Irisawa, H. (1987). Ohmic conductance through the inwardly rectifying K channel and blocking by internal Mg2+. Nature *325*, 156-9.

166. Meadows, H.J., Benham, C.D., Cairns, W., Gloger, I., Jennings, C., Medhurst, A.D., Murdock, P., and Chapman, C.G. (2000). Cloning, localisation and functional expression of the human orthologue of the TREK-1 potassium channel. Pflugers Arch *439*, 714-22.

167. Medhurst, A.D., Harrison, D.C., Read, S.J., Campbell, C.A., Robbins, M.J., and Pangalos, M.N. (2000). The use of TaqMan RT-PCR assays for semiquantitative analysis of gene expression in CNS tissues and disease models. J Neurosci Methods *98*, 9-20.

168. Medhurst, A.D., Rennie, G., Chapman, C.G., Meadows, H., Duckworth, M.D., Kelsell, R.E., Gloger, II, and Pangalos, M.N. (2001). Distribution analysis of human two pore domain potassium channels in tissues of the central nervous system and periphery. Brain Res Mol Brain Res *86*, 101-14.

169. Millar, I.D., Taylor, H.C., Cooper, G.J., Kibble, J.D., Barhanin, J., and Robson, L. (2006). Adaptive downregulation of a quinidine-sensitive cation conductance in renal principal cells of TWIK-1 knockout mice. Pflugers Arch *453*, 107-16.

170. Miller, A.N., and Long, S.B. (2012). Crystal structure of the human two-pore domain potassium channel K2P1. Science *335*, 432-6.

171. Morais-Cabral, J.H., Zhou, Y., and MacKinnon, R. (2001). Energetic optimization of ion conduction rate by the K+ selectivity filter. Nature *414*, 37-42.

172. Morton, M.J., O'Connell, A.D., Sivaprasadarao, A., and Hunter, M. (2003). Determinants of pH sensing in the two-pore domain K(+) channels TASK-1 and -2. Pflugers Arch *445*, 577-83.

173. Nicoll, R.A., and Madison, D.V. (1982). General anesthetics hyperpolarize neurons in the vertebrate central nervous system. Science *217*, 1055-7.

174. Nie, X., Arrighi, I., Kaissling, B., Pfaff, I., Mann, J., Barhanin, J., and Vallon, V. (2005). Expression and insights on function of potassium channel TWIK-1 in mouse kidney. Pflugers Arch *451*, 479-88.

175. Niemeyer, M.I., Gonzalez-Nilo, F.D., Zuniga, L., Gonzalez, W., Cid, L.P., and Sepulveda, F.V. (2007). Neutralization of a single arginine residue gates open a two-pore domain, alkali-activated K+ channel. Proc Natl Acad Sci U S A *104*, 666-71.

176. Nilius, B., Hess, P., Lansman, J.B., and Tsien, R.W. (1985). A novel type of cardiac calcium channel in ventricular cells. Nature *316*, 443-6.

177. Nimigean, C.M., Chappie, J.S., and Miller, C. (2003). Electrostatic tuning of ion conductance in potassium channels. Biochemistry *42*, 9263-8.

178. Nishida, M., Cadene, M., Chait, B.T., and MacKinnon, R. (2007). Crystal structure of a Kir3.1-prokaryotic Kir channel chimera. EMBO J *26*, 4005-15.

179. Noel, J., Zimmermann, K., Busserolles, J., Deval, E., Alloui, A., Diochot, S., Guy, N., Borsotto, M., Reeh, P., Eschalier, A., and Lazdunski, M. (2009). The mechano-activated K+ channels TRAAK and TREK-1 control both warm and cold perception. EMBO J *28*, 1308-18.

180. Ogielska, E.M., and Aldrich, R.W. (1998). A mutation in S6 of Shaker potassium channels decreases the K+ affinity of an ion binding site revealing ion-ion interactions in the pore. J Gen Physiol *112*, 243-57.

181. Orias, M., Velazquez, H., Tung, F., Lee, G., and Desir, G.V. (1997). Cloning and localization of a double-pore K channel, KCNK1: exclusive expression in distal nephron segments. Am J Physiol *273*, F663-6.

182. Ortega-Saenz, P., Pardal, R., Castellano, A., and Lopez-Barneo, J. (2000). Collapse of conductance is prevented by a glutamate residue conserved in voltage-dependent K(+) channels. J Gen Physiol *116*, 181-90.

183. Otwinowski, Z. (1991). Maximum likelihood refinement of heavy atom parameters. Darebury Study Weekend Proceedings.

184. Otwinowski, Z., and Minor, W. (1997). Processing of X-ray Diffraction Data Collected in Oscillation Mode. Methods in Enzymology *276*, 307- 26.

185. Pannu, N.S., Murshudov, G.N., Dodson, E.J., and Read, R.J. (1998). Incorporation of prior phase information strengthens maximum-likelihood structure refinement. Acta Crystallogr D Biol Crystallogr *54*, 1285-94.

186. Patel, A.J., Honore, E., Maingret, F., Lesage, F., Fink, M., Duprat, F., and Lazdunski, M. (1998). A mammalian two pore domain mechano-gated S-like K+ channel. EMBO J *17*, 4283-90.

187. Patel, A.J., Honore, E., Lesage, F., Fink, M., Romey, G., and Lazdunski, M. (1999). Inhalational anesthetics activate two-pore-domain background K+ channels. Nat Neurosci *2*, 422-6.

188. Patel, A.J., Maingret, F., Magnone, V., Fosset, M., Lazdunski, M., and Honore, E. (2000). TWIK-2, an inactivating 2P domain K+ channel. J Biol Chem *275*, 28722-30.

189. Patel, A.J., Lazdunski, M., and Honoré, E. (2001). Lipid and mechano-gated 2P domain K(+) channels. Curr Opin Cell Biol *13*, 422-8.

190. Payandeh, J., Scheuer, T., Zheng, N., and Catterall, W.A. (2011). The crystal structure of a voltage-gated sodium channel. Nature *475*, 353-8.

191. Piechotta, P.L., Rapedius, M., Stansfeld, P.J., Bollepalli, M.K., Ehrlich, G., Andres-Enguix, I., Fritzenschaft, H., Decher, N., Sansom, M.S., Tucker, S.J., and Baukrowitz, T. (2011). The pore structure and gating mechanism of K2P channels. EMBO J *30*, 3607-19.

192. Plant, L.D., Dementieva, I.S., Kollewe, A., Olikara, S., Marks, J.D., and Goldstein, S.A. (2010). One SUMO is sufficient to silence the dimeric potassium channel K2P1. Proc Natl Acad Sci U S A *107*, 10743-8.

193. Plaster, N.M., Tawil, R., Tristani-Firouzi, M., Canun, S., Bendahhou, S., Tsunoda, A., Donaldson, M.R., Iannaccone, S.T., Brunt, E., Barohn, R., Clark, J., Deymeer, F., George, A.L., Jr., Fish, F.A., Hahn, A., Nitu, A., Ozdemir, C., Serdaroglu, P., Subramony, S.H., Wolfe, G., Fu, Y.H., and Ptacek, L.J. (2001). Mutations in Kir2.1 cause the developmental and episodic electrical phenotypes of Andersen's syndrome. Cell *105*, 511-9.

194. Putney, J.W. (2011). The physiological function of store-operated calcium entry. Neurochem Res *36*, 1157-65.

195. Raghuraman, H., Cordero-Morales, J.F., Jogini, V., Pan, A.C., Kollewe, A., Roux, B., and Perozo, E. (2012). Mechanism of Cd2+ coordination during slow inactivation in potassium channels. Structure *20*, 1332-42.

196. Rajan, S., Wischmeyer, E., Xin Liu, G., Preisig-Muller, R., Daut, J., Karschin, A., and Derst, C. (2000). TASK-3, a novel tandem pore domain acid-sensitive K+ channel. An extracellular histiding as pH sensor. J Biol Chem *275*, 16650-7.

197. Rajan, S., Plant, L.D., Rabin, M.L., Butler, M.H., and Goldstein, S.A. (2005). Sumoylation silences the plasma membrane leak K+ channel K2P1. Cell *121*, 37-47.

198. Rapedius, M., Schmidt, M.R., Sharma, C., Stansfeld, P.J., Sansom, M.S., Baukrowitz, T., and Tucker, S.J. (2012). State-independent intracellular access of quaternary ammonium blockers to the pore of TREK-1. Channels (Austin) *6*.

199. Rasmussen, S.G., Choi, H.J., Rosenbaum, D.M., Kobilka, T.S., Thian, F.S., Edwards, P.C., Burghammer, M., Ratnala, V.R., Sanishvili, R., Fischetti, R.F., Schertler, G.F., Weis, W.I., and Kobilka, B.K. (2007). Crystal structure of the human beta2 adrenergic G-protein-coupled receptor. Nature *450*, 383-7.

200. Rasmussen, S.G., Choi, H.J., Fung, J.J., Pardon, E., Casarosa, P., Chae, P.S., Devree, B.T., Rosenbaum, D.M., Thian, F.S., Kobilka, T.S., Schnapp, A., Konetzki, I., Sunahara, R.K., Gellman, S.H., Pautsch, A., Steyaert, J., Weis, W.I., and Kobilka, B.K. (2011a). Structure of a nanobody-stabilized active state of the beta(2) adrenoceptor. Nature *469*, 175-80.

201. Rasmussen, S.G., DeVree, B.T., Zou, Y., Kruse, A.C., Chung, K.Y., Kobilka, T.S., Thian, F.S., Chae, P.S., Pardon, E., Calinski, D., Mathiesen, J.M., Shah, S.T., Lyons, J.A., Caffrey, M., Gellman, S.H., Steyaert, J., Skiniotis, G., Weis, W.I., Sunahara, R.K., and Kobilka, B.K. (2011b). Crystal structure of the beta2 adrenergic receptor-Gs protein complex. Nature *477*, 549-55.

202. Rastegar, A., and Soleimani, M. (2001). Hypokalaemia and hyperkalaemia. Postgrad Med J *77*, 759-64.

203. Reyes, R., Duprat, F., Lesage, F., Fink, M., Salinas, M., Farman, N., and Lazdunski, M. (1998). Cloning and expression of a novel pH-sensitive two pore domain K+ channel from human kidney. J Biol Chem *273*, 30863-9.

204. Reyes, R., Lauritzen, I., Lesage, F., Ettaiche, M., Fosset, M., and Lazdunski, M. (2000). Immunolocalization of the arachidonic acid and mechanosensitive baseline traak potassium channel in the nervous system. Neuroscience *95*, 893-901.

205. Rosenbaum, D.M., Cherezov, V., Hanson, M.A., Rasmussen, S.G., Thian, F.S., Kobilka, T.S., Choi, H.J., Yao, X.J., Weis, W.I., Stevens, R.C., and Kobilka, B.K. (2007). GPCR engineering yields high-resolution structural insights into beta2-adrenergic receptor function. Science *318*, 1266-73.

206. Roux, B., and MacKinnon, R. (1999). The cavity and pore helices in the KcsA K+ channel: electrostatic stabilization of monovalent cations. Science *285*, 100-2.

207. Ruta, V., Jiang, Y., Lee, A., Chen, J., and MacKinnon, R. (2003). Functional analysis of an archaebacterial voltage-dependent K+ channel. Nature *422*, 180-5.

208. Sabbadini, M., and Yost, C.S. (2009a). Molecular biology of background K channels: insights from K(2P) knockout mice. Journal of Molecular Biology *385*, 1331-44.

209. Sabbadini, M., and Yost, C.S. (2009b). Molecular biology of background K channels: insights from K(2P) knockout mice. J Mol Biol *385*, 1331-44.

210. Sandoz, G., Thummler, S., Duprat, F., Feliciangeli, S., Vinh, J., Escoubas, P., Guy, N., Lazdunski, M., and Lesage, F. (2006). AKAP150, a switch to convert mechano-, pH- and arachidonic acid-sensitive TREK K(+) channels into open leak channels. EMBO J *25*, 5864-72.

211. Sandoz, G., Douguet, D., Chatelain, F., Lazdunski, M., and Lesage, F. (2009). Extracellular acidification exerts opposite actions on TREK1 and TREK2 potassium channels via a single conserved histidine residue. Proc Natl Acad Sci U S A *106*, 14628-33.

212. Sandoz, G., Bell, S.C., and Isacoff, E.Y. (2011). Optical probing of a dynamic membrane interaction that regulates the TREK1 channel. Proc Natl Acad Sci U S A *108*, 2605-10.

213. Schagger, H. (2006). Tricine-SDS-PAGE. Nat Protoc *1*, 16-22.

214. Schulz, G.E. (2011). Validation of the detergent micelle classification for membrane protein crystals and explanation of the Matthews Graph for soluble proteins. Protein Sci *20*, 1765-70.

215. Seyfarth, E.A. (2006). Julius Bernstein (1839-1917): pioneer neurobiologist and biophysicist. Biol Cybern *94*, 2-8.

216. Sirois, J.E., Lei, Q., Talley, E.M., Lynch, C., 3rd, and Bayliss, D.A. (2000). The TASK-1 two-pore domain K+ channel is a molecular substrate for neuronal effects of inhalation anesthetics. J Neurosci *20*, 6347-54.

217. Skou, J.C. (1957). The influence of some cations on an adenosine triphosphatase from peripheral nerves. Biochim Biophys Acta *23*, 394-401.

218. Smart, O.S., Neduvelil, J.G., Wang, X., Wallace, B.A., and Sansom, M.S. (1996). HOLE: a program for the analysis of the pore dimensions of ion channel structural models. J Mol Graph *14*, 354-60, 76.

219. Stanfield, P.R., Davies, N.W., Shelton, P.A., Sutcliffe, M.J., Khan, I.A., Brammar, W.J., and Conley, E.C. (1994). A single aspartate residue is involved in both intrinsic gating and blockage by Mg2+ of the inward rectifier, IRK1. J Physiol *478 (Pt 1)*, 1-6.

220. Stansfeld, P.J., Grottesi, A., Sands, Z.A., Sansom, M.S., Gedeck, P., Gosling, M., Cox, B., Stanfield, P.R., Mitcheson, J.S., and Sutcliffe, M.J. (2008). Insight into the mechanism of inactivation and pH sensitivity in potassium channels from molecular dynamics simulations. Biochemistry *47*, 7414-22.

221. Starkus, J.G., Kuschel, L., Rayner, M.D., and Heinemann, S.H. (1997). Ion conduction through C-type inactivated Shaker channels. J Gen Physiol *110*, 539-50.

222. Starkus, J.G., Kuschel, L., Rayner, M.D., and Heinemann, S.H. (1998). Macroscopic Na+ currents in the "Nonconducting" Shaker potassium channel mutant W434F. J Gen Physiol *112*, 85-93.

223. Steinmeyer, K., Ortland, C., and Jentsch, T.J. (1991). Primary structure and functional expression of a developmentally regulated skeletal muscle chloride channel. Nature *354*, 301-4.

224. Talley, E.M., Solorzano, G., Lei, Q., Kim, D., and Bayliss, D.A. (2001). Cns distribution of members of the two-pore-domain (KCNK) potassium channel family. J Neurosci *21*, 7491-505.

225. Talley, E.M., and Bayliss, D.A. (2002). Modulation of TASK-1 (Kcnk3) and TASK-3 (Kcnk9) potassium channels: volatile anesthetics and neurotransmitters share a molecular site of action. J Biol Chem *277*, 17733-42.

226. Tao, X., Avalos, J.L., Chen, J., and MacKinnon, R. (2009). Crystal structure of the eukaryotic strong inward-rectifier K+ channel Kir2.2 at 3.1 A resolution. Science *326*, 1668-74.

227. Uysal, S., Cuello, L.G., Cortes, D.M., Koide, S., Kossiakoff, A.A., and Perozo, E. (2011). Mechanism of activation gating in the full-length KcsA K+ channel. Proc Natl Acad Sci U S A *108*, 11896-9.

228. Vergara, C., Latorre, R., Marrion, N.V., and Adelman, J.P. (1998). Calcium-activated potassium channels. Curr Opin Neurobiol *8*, 321-9.

229. Vonrhein, C., Blanc, E., Roversi, P., and Bricogne, G. (2007). Automated structure solution with autoSHARP. Methods Mol Biol *364*, 215-30.

230. Wehland, J., Schroder, H.C., and Weber, K. (1984). Amino acid sequence requirements in the epitope recognized by the alpha-tubulin-specific rat monoclonal antibody YL 1/2. EMBO J *3*, 1295-300.

231. Werman, R., Davidoff, R.A., and Aprison, M.H. (1968). Inhibitory of glycine on spinal neurons in the cat. J Neurophysiol *31*, 81-95.

232. Whorton, M.R., and MacKinnon, R. (2011). Crystal structure of the mammalian GIRK2 K+ channel and gating regulation by G proteins, PIP2, and sodium. Cell *147*, 199-208.

233. Wible, B.A., Taglialatela, M., Ficker, E., and Brown, A.M. (1994). Gating of inwardly rectifying K+ channels localized to a single negatively charged residue. Nature *371*, 246-9.

234. Winn, M.D., Ballard, C.C., Cowtan, K.D., Dodson, E.J., Emsley, P., Evans, P.R., Keegan, R.M., Krissinel, E.B., Leslie, A.G., McCoy, A., McNicholas, S.J., Murshudov, G.N., Pannu, N.S., Potterton, E.A., Powell, H.R., Read, R.J., Vagin, A., and Wilson, K.S. (2011). Overview of the CCP4 suite and current developments. Acta Crystallogr D Biol Crystallogr *67*, 235-42.

235. Wright, S.H. (2004). Generation of resting membrane potential. Adv Physiol Educ *28*, 139-42.

236. Wu, R.S., and Marx, S.O. (2010). The BK potassium channel in the vascular smooth muscle and kidney: alpha- and beta-subunits. Kidney Int *78*, 963-74.

237. Yang, J., Yu, M., Jan, Y.N., and Jan, L.Y. (1997). Stabilization of ion selectivity filter by pore loop ion pairs in an inwardly rectifying potassium channel. Proc Natl Acad Sci U S A *94*, 1568-72.

238. Ye, S., Li, Y., and Jiang, Y. (2010). Novel insights into K+ selectivity from high-resolution structures of an open K+ channel pore. Nat Struct Mol Biol *17*, 1019-23.

239. Yellen, G., Sodickson, D., Chen, T.Y., and Jurman, M.E. (1994). An engineered cysteine in the external mouth of a K+ channel allows inactivation to be modulated by metal binding. Biophys J *66*, 1068-75.

240. Yellen, G. (1998). The moving parts of voltage-gated ion channels. Q Rev Biophys *31*, 239-95.

241. Yohannan, S., Hu, Y., and Zhou, Y. (2007). Crystallographic study of the tetrabutylammonium block to the KcsA K+ channel. J Mol Biol *366*, 806-14.

242. Yuill, K.H., Stansfeld, P.J., Ashmole, I., Sutcliffe, M.J., and Stanfield, P.R. (2007). The selectivity, voltage-dependence and acid sensitivity of the tandem pore potassium channel TASK-1: contributions of the pore domains. Pflugers Arch *455*, 333-48.

243. Yunus, A.A., and Lima, C.D. (2009). Purification of SUMO conjugating enzymes and kinetic analysis of substrate conjugation. Methods Mol Biol *497*, 167-86.

244. Zhang, J., Feng, Y., and Forgac, M. (1994). Proton conduction and bafilomycin binding by the V0 domain of the coated vesicle V-ATPase. J Biol Chem *269*, 23518-23.

245. Zhang, L., Gorset, W., Dresser, M.J., and Giacomini, K.M. (1999). The interaction of n-tetraalkylammonium compounds with a human organic cation transporter, hOCT1. J Pharmacol Exp Ther *288*, 1192-8.

246. Zhao, Y., Yarov-Yarovoy, V., Scheuer, T., and Catterall, W.A. (2004). A gating hinge in Na+ channels; a molecular switch for electrical signaling. Neuron *41*, 859-65.

247. Zhou, M., Morais-Cabral, J.H., Mann, S., and MacKinnon, R. (2001a). Potassium channel receptor site for the inactivation gate and quaternary amine inhibitors. Nature *411*, 657-61.

248. Zhou, M., and MacKinnon, R. (2004a). A mutant KcsA K(+) channel with altered conduction properties and selectivity filter ion distribution. J Mol Biol *338*, 839-46.

249. Zhou, M., Xu, G., Xie, M., Zhang, X., Schools, G.P., Ma, L., Kimelberg, H.K., and Chen, H. (2009). TWIK-1 and TREK-1 are potassium channels contributing significantly to astrocyte passive conductance in rat hippocampal slices. J Neurosci *29*, 8551-64.

250. Zhou, Y., Morais-Cabral, J.H., Kaufman, A., and MacKinnon, R. (2001b). Chemistry of ion coordination and hydration revealed by a K+ channel-Fab complex at 2.0 A resolution. Nature *414*, 43-8.

251. Zhou, Y., and MacKinnon, R. (2003). The occupancy of ions in the K+ selectivity filter: charge balance and coupling of ion binding to a protein conformational change underlie high conduction rates. J Mol Biol *333*, 965-75.

252. Zhou, Y., and MacKinnon, R. (2004b). Ion binding affinity in the cavity of the KcsA potassium channel. Biochemistry *43*, 4978-82.

253. Zilberberg, N., Ilan, N., Gonzalez-Colaso, R., and Goldstein, S.A. (2000). Opening and closing of KCNKO potassium leak channels is tightly regulated. J Gen Physiol *116*, 721-34.

254. Zilberberg, N., Ilan, N., and Goldstein, S.A. (2001). KCNKO: opening and closing the 2-P-domain potassium leak channel entails "C-type" gating of the outer pore. Neuron *32*, 635-48.